Title
Exploring the Crossover of Attractive Gelation and Repulsive Jamming in Dense Soft Materials

Author
Xu, Yixuan

Publication Date
2023

UNIVERSITY OF CALIFORNIA
Los Angeles

Exploring the Crossover of Attractive Gelation and Repulsive Jamming in Dense Soft Materials

A dissertation submitted in partial satisfaction
of the requirements for the degree
Doctor of Philosophy in Materials Science and Engineering

by

Yixuan Xu

2023

ABSTRACT OF THE DISSERTATION

Exploring the Crossover of Attractive Gelation and Repulsive Jamming in Dense Soft Materials

by

Yixuan Xu
Doctor of Philosophy in Materials Science and Engineering
University of California, Los Angeles, 2023
Professor Thomas G. Mason, Co-Chair
Professor Bruce S. Dunn, Co-Chair

Dense colloidal emulsions represent a captivating category of soft materials, boasting a vast range of practical applications in industry and consumer goods. To design and tailor the mechanical properties of concentrated emulsions for specific applications, a comprehensive quantitative understanding of emulsion rheology is essential. In practice, colloidal emulsions are not typically monodisperse with nearly hard repulsive interactions between droplets; instead, they often exhibit depletion attractive interactions induced by excess ionic surfactant molecules, other additives, or even polydispersity. In this dissertation, we outline the advancements we have achieved in quantitatively describing the linear plateau elastic shear modulus, G'_{p}, of depletion attractive emulsions and extremely bidisperse colloidal emulsions, coupled with their optical transport and dynamic properties. Our investigation also encompasses the unjamming behavior and the exploration of potential molecular-probing platforms for microrheology, employing a combination of experimental, analytical, and computational approaches with a primary focus on oil-in-water (O/W) nanoemulsions.

Our first focus is on the quantitative microrheology of attractive emulsions. We employ diffusing wave spectroscopy (DWS) microrheology analysis for quantifying the rheological properties, particularly G'_{p}, of depletion-induced attractive emulsions having various attractive potential at contact $|U_{\mathrm{d}}|$; and at each given $|U_{\mathrm{d}}|$, we investigate G'_{p} over a wide range of droplet volume fraction, ϕ. We show that on top of correcting for collective light scattering effects present in highly scattering concentrated colloidal systems through an empirically determined average structure factor, it is necessary to apply an effective scattering probe size factor associated with the resulting corrected mean square displacements (MSDs) in the generalized Stoke-Einstein relation (GSER) of passive microrheology, and thereby lead to accurate values of G'_{p} for attractive emulsions. By developing the sophisticated decorated core-shell network (DCSN) model for strongly attractive emulsions and the extended DCSN model for intermediately attractive emulsions, along with our discovery of moderately attractive emulsions, we systematically and self-consistently understand the effective probe size that depends on both ϕ and the depletion attractive strength.

To broaden our investigation of the rheology of attractive emulsions, we explore highly bidisperse mixtures of microscale emulsions and nanoemulsions. In these polydisperse mixtures, nanodroplets form repulsively jammed glasses while simultaneously acting as depletion agents, which can lead to the formation of attractive gels by microscale droplets. We demonstrate that at lower microscale droplet volume fractions, ϕ_{EM}, far below its jamming point, nanodroplets predominantly contribute to the bulk shear elasticity. In this condition, microscale droplets serve as elastic inclusions residing within the jammed matrix of nanodroplets without weakening the system's elasticity. At higher ϕ_{EM}, near yet below jamming, the nanodroplet-induced depletion attractions cause larger droplets to form percolating gel networks, which contribute to the macroscopic shear rigidity.

Motivated by advances in DWS microrheology for a diverse range of colloidal emulsions, we explore the potential of applying molecule-probing techniques to microrheology. Experimentally, we demonstrate the unjamming behavior of customized ^{19}F-laden nanoemulsions,

stabilized by non-fluorinated ionic surfactants, using ^{19}F pulsed-field gradient nuclear magnetic resonance (PFG-NMR) measurements. Our findings reveal dramatic changes in NMR magnetization decays at high field-gradient strengths as ϕ is lowered through dilution. We show that this dramatic change coincides with the loss of low-frequency shear elasticity of the nanoemulsion, which occurs at the ϕ associated with Lindemann melting criterion. Moreover, we present a trajectory-based simulation study that illustrates passive microrheology by analyzing the MSDs of a Brownian probe molecule confined within a droplet undergoing harmonically bound Brownian motion. Our simulation approach highlights the significance of small colloid size and high contrast between the viscosities of the dispersed and continuous phases for extracting accurate MSDs of the droplets, thus yielding quantitative microrheological results.

The dissertation of Yixuan Xu is approved.

Mark S. Goorsky

Jaime Marian

Bruce S. Dunn, Committee Co-Chair

Thomas G. Mason, Committee Co-Chair

University of California, Los Angeles

2023

To my family, friends, and people who have supported me.

TABLE OF CONTENTS

LIST OF FIGURES

LIST OF TABLES

ACKNOWLEDGMENTS

The completion of this dissertation would not have been possible without the support I have received from my family and friends. I wish to take this opportunity to express my wholehearted appreciation to all those who have assisted me in the pursuit of my Ph.D. at UCLA.

First and foremost, I am deeply grateful to my Ph.D. advisor, Prof. Thomas G. Mason, who has been the most influential figure in shaping my growth as a proficient scientist over the past four years. His wealth of knowledge, expertise, and practical skills in addressing scientific research challenges have been invaluable, as has his ability to foster my curiosity and critical thinking. Tom has not only been an exceptional mentor but also a dear friend, consistently offering support, motivation, and crucial career guidance throughout my Ph.D. journey. His mentorship and encouragement have been indispensable in the completion of this dissertation, and I would like to express my heartfelt appreciation once again.

I am also extremely grateful to my Ph.D. committee members, Prof. Bruce S. Dunn, Prof. Jaime Marian, and Prof. Mark S. Goorsky, for their insightful feedback, constructive criticism, and continuous support, leading to the success of this dissertation.

I would like to extend my appreciation to Prof. Frank Scheffold for his invaluable collaboration on the diffusing wave spectroscopy experiments focused on highly scattering colloidal emulsions, and for his visit to UCLA, where we engaged in the endeavor of developing a quantitative rheological model for microgels. I would also like to thank Dr. Madison L. Nelson and Prof. Joseph D. Seymour for their contributions to the PFG-NMR experiments and the fruitful discussions we had. I would like to thank Mr. Thai Dinh and Prof. Thomas Cubaud for their collaborative efforts on the microfluidics of nanoemulsions. Additionally, I am thankful to Ms. N. Stephanie Kawecki and Prof. Amy C. Rowat for offering me the unique opportunity to take part in the fascinating project focused on marbled cultured meat.

Working with the remarkable members of the Mason group over the past four years has been a delightful experience. I am grateful to Dr. Ha Seong Kim for initially introducing me to Tom's group and for sharing his valuable expertise on emulsions and microrheology. I would like to thank Dr. Matthew Pagenkopp for his generous assistance in setting up the initial synthesis apparatus and for sharing his insights on teaching the biochemistry laboratory course. Additionally, I will always cherish the memories and enjoyable moments shared with Mr. Tianren Yu in our group, who not only offered technical support and collaboration but also contributed to a stimulating and engaging work environment. Their friendship and encouragement have made my time in the lab truly memorable.

I would like to thank my dearest friends Ms. Changling Zhao, Ms. Yanan Yu, and Dr. Jia Han. Their unwavering friendship, support, and understanding throughout this journey have been invaluable. Sharing countless memorable moments, laughter, and encouragement with them has made my time in the program not only more enjoyable but also more enriching. I am truly grateful for their companionship and support during all these years. I would also like to take this opportunity to express my heartfelt gratitude towards my steadfast friend, Ms. Bingqing Sun. While geographical distances may separate us, her emotional support has been unflagging and ever-present, forming a stronghold in my academic pursuit. Over a span of twelve years, she has been an unwavering pillar of strength, persistently cheering me on from afar. Her belief in me has fueled my resilience, underlining the power of a friendship that transcends physical boundaries. Bingqing, thank you for your ceaseless support and companionship, your presence is deeply felt, regardless of the miles between us. I am thrilled by our reunion in the near future.

Last but not least, I owe a special debt of gratitude to my parents and grandmother, who have been a constant source of love, encouragement, and inspiration. Their unwavering belief in my abilities and their sacrifices have laid the foundation for my academic journey. This accomplishment would not have been possible without their support.

Thank you all for being a part of my Ph.D. journey and for making it a rewarding and enriching experience.

The following chapters have been adapted from the versions of the corresponding journal publications: Chapter 2, Xu, Yixuan, Frank Scheffold, and Thomas G. Mason. (2020). Diffusing wave microrheology of strongly attractive dense emulsions. *Physical Review E* **102**(6): 062610. DOI: 10.1103/PhysRevE.102.062610; Chapter 3, Xu, Yixuan and Thomas G. Mason. (2023). Complex optical transport, dynamics, and rheology of intermediately attractive emulsions. *Scientific Reports* **13**(1): 1791. DOI: 10.1038/s41598-023-28308-6; Chapter 5, Xu, Yixuan, Madison L. Nelson, Joseph D. Seymour, and Thomas G. Mason. (2023). Signatures of nanoemulsion jamming and unjamming in stimulated-echo NMR. *Physical Review E* **107**(2): 024605. DOI: 10.1103/PhysRevE.107.024605. The contents of Chapter 4 and Chapter 6 have not yet been published, with their current statuses being *accepted by Science Advances* and *submitted to Physical Review E*, respectively. Portions of this thesis have been previously copyrighted by the authors in the listed works and are used here with permission. Anyone seeking to reproduce any portion of this dissertation that also appears in one of these works, including any portion of this dissertation in submitted and accepted works mentioned above, should contact the respective journals and/or authors to obtain appropriate permission. Symbols assigned to certain variables in Chapters 1, 2, 3, 4, 5, 6, 7, 8, and 9 may differ according to the specific chapter in which they appear.

VITA

2017	Bachelor of Engineering, Polymer Materials and Engineering, University of Science and Technology of China (USTC), Hefei, Anhui, China.
2017–2018	UCLA Graduate Division Fellowship Award.
2017–2019	Graduate Student Researcher, Department of Materials Science and Engineering, University of California, Los Angeles (UCLA), California, USA.
2019–2022	Teaching Assistant, Department of Chemistry and Biochemistry, University of California, Los Angeles (UCLA), California, USA.
2019–2023	Graduate Student Researcher, Department of Chemistry and Biochemistry, University of California, Los Angeles (UCLA), California, USA.

PUBLICATIONS AND PRESENTATIONS

1. **Xu, Y.** and Mason, T.G. "Double-bound Brownian motion of molecular probes in concentrated emulsions and nanoemulsions", submitted to *Phys. Rev. E* (2023).

2. Kawecki, N.S., Norris, S.C.P., **Xu, Y.**, Wu, Y., Davis, A.R., Fridman, E., Chen, K.K., Crosbie, R.H., Garmyn, A.J., Li, S., Mason, T.G., Rowat, A.C.. "Engineering multicomponent tissue by spontaneous adhesion of myogenic and adipogenic microtissues cultured with customized scaffolds", resubmitted to *Food Res. Int.* (2023).

3. **Xu, Y.** and Mason, T.G. "Jamming and depletion in extremely bidisperse mixtures of microscale emulsions and nanoemulsions", *Sci. Adv.*, In Press (2023).

4. **Xu, Y.**, Nelson, M.L., Seymour, J.D., Mason, T.G. “Signatures of nanoemulsion jamming and unjamming in stimulated-echo NMR”, *Phys. Rev. E*, **107**(2), 024605 (2023).
5. **Xu, Y.** and Mason, T.G. “Complex optical transport, dynamics, and rheology of intermediately attractive emulsions”, *Sci. Rep.*, **13**(1), 1791 (2023).
6. Dinh, T., **Xu, Y.**, Mason, T.G., Cubaud, T. “Microflow of nanoemulsion threads in surfactant solutions”, *Phys. Rev. E*, **107**(1), 015101 (2023).
7. Kim, H.S., **Xu, Y.**, Scheffold, F., Mason, T.G. “Self-motion and heterogeneous droplet dynamics in moderately attractive dense emulsions”, *J. Phys.: Condens. Matter*, **33**(17), 175101 (2021).
8. **Xu, Y.**, Scheffold, F., Mason, T.G. “Diffusing wave microrheology of strongly attractive dense emulsions”, *Phys. Rev. E*, **102**(6), 062610 (2020).
9. Li, J., Wei, K., Zuo, S., **Xu, Y.**, Zha, Z., Ke, W., Chen, H., Ge, Z. “Light-Triggered Clustered Vesicles with Self-Supplied Oxygen and Tissue Penetrability for Photodynamic Therapy against Hypoxic Tumor”, *Adv. Funct. Mater.*, **27**(33), 1702108 (2017).
10. Li, J., Xiao, S., **Xu, Y.**, Zuo, S., Zha, Z., Ke, W., He, C., Ge, Z. “Smart Asymmetric Vesicles with Triggered Availability of Inner Cell-Penetrating Shells for Specific Intracellular Drug Delivery”, *ACS Appl. Mater. Interfaces*, **9**(21), 17727-17735 (2017).
11. **Xu, Y.**, Scheffold, F., Mason, T.G. “Passive Microrheology of Strongly Attractive Dense Emulsions using Diffusing Wave Spectroscopy.” *APS March Meeting Abstracts*, Oral presentation (2021).

Chapter 1 - Introduction

Colloidal systems are ubiquitous in nature and hold substantial importance across diverse fields such as materials science, biophysics, and soft matter physics[1–4]. These systems are comprised of particles, droplets, or macromolecules dispersed within a continuous medium, and their properties and behaviors are dictated by the interplay between the particles, the medium, and external forces exerted upon them. Gaining a comprehensive understanding and control over the properties of colloidal systems is crucial for the development of novel materials and technologies in various sectors, including food science[5], pharmaceuticals[6,7], energy[8], and environmental[9] applications. The properties of colloidal systems encompass a broad spectrum, dependent on factors such as the size, shape, and material attributes of the dispersed particles, as well as on the characteristics of the continuous medium. This dissertation primarily explores dense colloidal materials and particularly emphasizes on emulsions and nanoemulsions.

Recent advancements in the study of dense colloidal emulsions have led to an improved understanding of their rheological properties and interactions[10]. Nevertheless, there is room for further exploration in comprehensively grasping the quantitative rheological properties across various interaction regimes and size distributions, as well as the potential for alternative molecular detection techniques in passive microrheology. Passive microrheology[11,12] is a technique used to measure the mechanical properties of complex fluids by tracking the random motion of microscale colloids, such as particles and droplets, suspended within the material, which is primarily driven by thermal fluctuations. It provides insight into the viscoelastic properties of these materials, including elasticity and viscosity, based on the statistical analysis of colloidal trajectories.

This dissertation contributes to these ongoing efforts by investigating the interplay between droplet volume fractions ϕ, interactions, polydispersity, and overall emulsion properties. Through our research, we aim to reveal the underlying mechanisms that govern the optical transport, dynamics, and rheology of emulsions in different regimes. Additionally, we seek to accurately interpret diffusing wave spectroscopy (DWS) data for emulsions with various interaction strengths and extreme bidispersity using opto-microrheological models. Lastly, we explore the potential of employing molecular detection techniques for passive microrheology, which may open up new avenues for understanding dense colloidal emulsions.

1.1 Rheology of monodisperse emulsions and nanoemulsions

Emulsions are mixtures of two immiscible fluids with one dispersed as deformable droplets in the other. Many common emulsions consist of oil droplets in water (O/W)[13]. With the addition of surfactants, they are used in various applications such as enhanced oil recovery, paints, lubricants, coatings, food, cosmetics, and pharmaceuticals[14–19]. Rheological properties are essential to their practical applications, as they can exhibit properties ranging from liquid viscosity to solid elasticity. As a type of complex fluid, emulsions possess colloidal structures with length scales larger than atomic or simple molecular scales, yet smaller than macroscopic scales[20]. Emulsions exhibit similarities with other complex fluids: in the dilute limit, they resemble suspensions of nondeformable spheres as droplets maintain their spherical shape due to Laplace pressure; in the highly compressed limit, their interfacial structure is comparable to gas foams, with thin liquid films separating the deformed droplets[21].

Emulsions are typically prepared through an emulsification process, during which an externally applied energetic flow works against the interfacial tension, σ, prompting larger droplets to elongate and rupture into smaller ones through capillary instability[22]. Under extreme high-flow conditions, this results in the formation of nanoemulsions, which have an average droplet radius $a < 100$ nm[23–25]. The process also leads to increased interfacial surface area to volume ratio and Laplace pressure $\Pi_{\mathrm{L}} = 2\sigma/a$ for undeformed droplets. As a result, emulsions and nanoemulsions become thermodynamically metastable dispersions, susceptible to droplet coalescence. To achieve long-lasting emulsions and nanoemulsions with consistent droplet size distribution, droplet coalescence is typically suppressed by incorporating strong stabilizers, such as amphiphilic surfactants[26]. Ostwald ripening is generally mitigated by using oils with a sufficiently high molecular weight, which effectively reduces their solubility in the continuous phase[27].

To better comprehend the relationship between microscopic structure, forces between droplets, and macroscopic properties, researchers use monodisperse or highly size-fractionated emulsions with highly uniform droplet sizes[11,21,24,28]. These emulsions have a controllable droplet radius and are highly stable, making them suitable for exploring the full range of rheological behavior. Depletion flocculation is a suitable approach for size-fractionating larger colloidal droplets[29], while for nanoemulsions with a radius smaller than 100 nm, ultracentrifugal droplet fractionation is generally more practical and efficient, as long as a mass density disparity exists between the dispersed and continuous phase to facilitate droplet sedimentation or creaming[30,31].

A diverse array of rheological properties of stable model concentrated emulsions have been previously studied, spanning different regimes of excitations from linear viscoelasticity to nonlinear viscoelasticity[32,33]. The latter includes yielding and shear ordering - disordering in the moderate flow conditions, as well as droplet rupturing and coalescence in the extreme flow conditions. In this dissertation, we primarily consider the linear shear viscoelastic response of disordered concentrated emulsions subjected to a small strain, below the yield strain, during oscillatory rheological tests.

For highly concentrated emulsions, the frequency-dependent complex linear modulus, $G^*(\omega) = G'(\omega) + iG''(\omega)$, can be used to quantify the linear shear elasticity, where $G'(\omega)$ represents the storage shear modulus, $G''(\omega)$ denotes the loss shear modulus, and ω is the angular frequency. A mechanical rheometer is often used to measure $G^*(\omega)$ by conducting linear oscillatory frequency sweeps at a small strain amplitude, γ_0. During these frequency sweeps, the rheometer applies a small-amplitude sinusoidal strain, $\gamma(t) = \gamma_0 \sin(\omega t)$, to the emulsion and records the sample's response to the perturbation in the form of a sinusoidal stress, $\tau(t)$, which exhibits a phase lag, δ, relative to the input strain signal. The sinusoidal stress is related to the applied strain through $\tau(t) = \gamma_0[G'(\omega)\sin(\omega t) + G''(\omega)\cos(\omega t)]$, allowing the extraction of non-negative $G'(\omega)$ and $G''(\omega)$. In concentrated emulsions, $G'(\omega)$ demonstrates a dominant plateau significantly exceeding $G''(\omega)$ at intermediate ω, making it possible to define a plateau elastic shear modulus, G'_{p}.

In a less concentrated regime, viscoelastic response of emulsions begins to exhibit ω-dependence, complicating the definition of plateau shear elasticity from frequency-sweep measurements. Typically, G'_{p} can be identified at an inflection point in $|G^*(\omega)|$, if there is a low-frequency viscous relaxation. Alternatively, the G'_{p} can be obtained by performing oscillatory strain sweeps at a given intermediate ω using a mechanical rheometer. Each strain sweep yields the linear and nonlinear shear storage modulus, $G'(\gamma)$, and its small-strain plateau value, G'_{p}, corresponding to the linear viscoelastic regime, can be extracted where γ is below the yield strain.

Experimental investigations of G'_{p} in monodisperse oil-in-water emulsions have provided insights into the jamming of disordered soft colloidal spheres[21,28,34]. The concept of random close packing (RCP) was introduced by J.D. Bernal and J. Mason[35], with a droplet volume fraction $\phi_{\mathrm{RCP}} \approx 0.64$. Subsequently, the concept of maximal random jamming (MRJ) was developed by S. Torquato *et al.*[36], with a volume fraction $\phi_{\mathrm{MRJ}} = 0.646$. By contrast, O/W nanoemulsions have a very low effective jamming ϕ for predominantly water compositions[30]. Short-range repulsive interactions in O/W nanoemulsions result in pronounced downward shifts in the effective ϕ associated with jamming, as Debye screening layers of neighboring nanodroplets strongly overlap. The entropic-electrostatic-interfacial (EEI) model[37] was developed to explain linear shear elasticity measurements in microscale and nanoscale emulsions. The model considers jamming at high ϕ, screened-charge repulsion from an ionic surfactant, and an entropic term[38]. It accurately predicts $G'_{\mathrm{p}}(\phi)$ for emulsions above and below jamming, and describes uniform size-fractionated O/W emulsions stabilized by an ionic surfactant over a range of average droplet radii.

Expanding beyond the short-range repulsive interactions and the monodispersity in disordered O/W emulsions, here we investigate the linear viscoelasticity of short-range attractive emulsions. Furthermore, we explore the crossover between repulsive jamming of nanodroplets and attractive gelation of microscale droplets in extremely bidisperse mixtures of microscale emulsions and nanoemulsions.

1.2 Linear viscoelasticity of attractive emulsions

While considerable progress has been made in understanding the viscoelasticity of attractive colloidal systems[39–43], significant challenges remain, particularly in optical microrheological measurements and interpretation. The intricacies of passive microrheology can lead to potential artifacts in data interpretation arising from inappropriate scattering techniques, such as issues related to non-ergodicity and collective scattering effects in dense attractive emulsions. The droplet size distribution is a critical factor, as smaller droplets can induce attraction through depletion effects, profoundly influencing the emulsion's viscoelastic behavior. Moreover, depletion attractions can lead to the formation of clusters or gels, complicating the rheological profile of the emulsion. Although additives like polymers and micelles can be incorporated to modify an emulsion's structure, these changes may not straightforwardly correlate with the viscoelastic properties due to complex interactions and phase behavior. Thus, a more comprehensive understanding of these issues is needed to improve the predictability and control of the linear viscoelastic properties of attractive emulsions.

The depletion force, an entropic force originally predicted by Asakura and Oosawa[44], results from the system's tendency to increase entropy per the second law of thermodynamics. When larger and smaller colloidal particles coexist, larger particles approach each other, overlapping exclusion volumes and increasing available space for smaller particles. In colloidal emulsions, larger particles are referred to microscale emulsion droplets, while smaller particles typically refer to surfactant micelles[28,29,45,46] or polymers[47–49]. The droplet size distribution of an emulsion is a significant factor to consider, as it has been demonstrated in idealized binary emulsion systems[50] that smaller droplets can lead to attractive forces through depletion effects. When secondary attractions, such as those induced by depletion effects, are significantly greater than $k_\mathrm{B}T$, where k_B is Boltzmann's constant and T is temperature, the translational entropy gain of micelles outweighs the entropy loss from flocculation of droplets, leading to spontaneous colloidal flocculation or even gel without coalescing. Such gelation can significantly alter the emulsion's rheological properties. It is important to note that incorporating other additives, such as salts, into emulsions can also result in significant interdroplet attractions by altering electrostatic interaction potentials[51,52]. However, this dissertation primarily focuses on attractive emulsions with entropic depletion attractive interactions between droplets.

In our series of studies on attractive monodisperse emulsions, we systematically vary the magnitude of the depletion attractive potential $|U_\mathrm{d}|$ between droplets at contact, induced by surfactant micelles, covering the regimes of moderate attraction ($\sim$2.4 $k_\mathrm{B}T$), intermediate attraction ($\sim$5.6 $k_\mathrm{B}T$), and strong attraction ($\sim$14.5 $k_\mathrm{B}T$). In our separate study on extremely bidisperse emulsions in the absence of micelles, we show that a nanodroplet-induced $|U_\mathrm{d}|$ between microscale droplets can become large enough compared to $k_\mathrm{B}T$ to cause attractive gelation.

1.3 Quantitative microrheology using diffusing wave spectroscopy

Microrheology is a powerful technique that enables researchers to probe the rheological properties of complex fluids and soft materials at the microscale. Particle tracking microrheology has gained significant attention due to its ability to measure local rheological properties of anisotropic and inhomogeneous viscoelastic systems, which are often inaccessible to conventional macroscopic rheology methods[12,53,54]. In particle tracking microrheology, the motion of tracer particles embedded in the colloidal system is monitored, and their mean square displacements (MSDs) are used to deduce the viscoelastic response of the material. Moreover, passive microrheology has been explored through optical diffusing wave spectroscopy (DWS)[11,55,56]. DWS is a non-invasive technique that enables the investigation of complex fluids and soft materials at the microscopic level by analyzing the fluctuations in the intensity of scattered light in a high multiple-scattering regime. In passive microrheology with DWS, the Brownian motion of tracer particles embedded in the colloidal system is exploited, and the temporal correlation of scattered light intensity is measured. This information is then used to extract the MSDs of the tracer particles, allowing researchers to determine the local viscoelastic properties of the system. This technique is particularly advantageous for probing systems with strong optical scattering and it offers a complementary approach to particle tracking microrheology for studying the rheological properties of complex fluids.

In previous research, monodisperse emulsion passive microrheology with DWS has been investigated using microscale emulsions featuring nearly hard droplet interactions[57]. In this dissertation, we broaden our DWS quantitative microrheology study to the various complex emulsion models mentioned above, attaining quantitative agreement between the DWS microrheologically determined G'_p and the mechanically measured macroscopic G'_p for all examined systems. This is achieved by coupling the optical transport, dynamics, and rheological properties of the system. We offer a sophisticated interpretation of the inhomogeneous microstructures within the droplet network, and demonstrate the effective DWS scattering probe size for performing quantitative passive microrheology each of these systems.

1.4 Towards molecular probe microrheology

To explore the potential of using other techniques, which can detect probe-molecule dynamics at a smaller molecular scale for passive microrheology, we present the first studies of ^{19}F-laden molecular diffusion within the droplets of nanoemulsions using pulsed-field gradient nuclear magnetic resonance (PFG-NMR). From probe-molecule motion we can infer droplet motion over a limited range of ϕ. Additionally, we have conducted a trajectory-based simulation study of droplet-confined Brownian molecular diffusion, where droplets experience harmonic Brownian bound motion in dense emulsions.

1.5 Overview

In the following chapters, we present a series of studies aimed at gaining a deeper quantitative understanding of the rheology of dense colloidal emulsions by exploring their properties and interactions using experimental, analytical, and simulation methods.

In Chapter 2, we investigate diffusing wave microrheology in strongly attractive dense emulsions. We induce an attractive depletion interaction potential energy between two oil droplets near contact with a magnitude of 14.5 $k_{\mathrm{B}}T$, much stronger than the thermal energy $k_{\mathrm{B}}T$. We develop a comprehensive opto-microrheological model, the decorated core-shell network (DCSN) model, which accounts for collective light scattering effects as well as the effective optical scattering probe size.

From prior advances in DWS microrheology on emulsions with nearly hard interactions[57], it is known that in jammed, dense emulsions, collective light scattering effects must be considered. This is related to the average structure factor of the system and depends on the droplet volume fraction. In the strongly attractive limit, droplets form lubricated bonds with other droplets through slippery diffusion-limited cluster aggregation (S-DLCA)[51,58], leading to local optical inhomogeneity for different droplets with varying numbers of nearest neighbors. In the DCSN model, we deduce a ϕ-independent effective probe-size factor of 2.0, meaning the effective scattering probe radius is twice the droplet radius, by fitting the measured optical transport properties of the emulsion, specifically the ϕ-dependent inverse optical transport mean free path, $1/\ell^*(\phi)$. The $1/\ell^*(\phi)$ in the strongly attractive limit is noticeably asymmetric and exhibits two bending knees, which is remarkably different than the symmetric, inverse parabolic $1/\ell^*(\phi)$ for the emulsions having nearly hard interactions. When fitting $1/\ell^*(\phi)$, we also involve the measured dynamical properties of the emulsions (*i.e.* the MSDs), associated with the scattering probe. By applying the effective probe size and the low-frequency plateau MSD after correcting for collective scattering to the generalized Stokes-Einstein relation (GSER)[11], we determine the linear plateau elastic shear modulus, G'_p, at each ϕ using only the optical properties. We present quantitative microrheological agreement between the optically determined G'_p and mechanically measured G'_p over the full range of ϕ explored. The analysis of the experimental data helps elucidate the microstructure of droplets subjected to strongly attractive interactions and its role in both the optical and viscoelastic properties of these systems.

Initial work by Kim, Xu, Scheffold, & Mason examined moderately attractive emulsions (2.4 $k_\mathrm{B}T$)[59]. We demonstrate that inducing a moderate depletion attraction creates a secondary decay-to-plateau in the DWS intensity autocorrelation functions, which we hypothesize to be a result of the heterogeneous dynamics of a sub-population of droplets that still experience bound motion yet with significantly larger displacements than the average. By analyzing the early- and intermediate-time MSDs associated with the primary rise-to-plateau, we show that these MSDs, when interpreted using the GSER of passive microrheology, yield quantitative agreement with macroscopic mechanical measurements of G'_p. This finding highlights the complexities involved in interpreting DWS MSDs in moderately attractive dense colloidal systems, as such attractions can lead to additional dynamics (*i.e.* the excess MSDs at long times) involving a sub-population of colloids exhibiting heterogeneous collective dynamics in more heterogeneous local structures caused by the moderate attraction, as compared to nearly hard interaction and strongly attraction. Additionally, we find that single emulsion droplets still effectively serve as scattering probes, namely, there is a ϕ-independent effective scattering probe-size factor of 1.0 for this moderate depletion attractive strength of 2.4 $k_\mathrm{B}T$.

In Chapter 3, we delve into the complex optical transport, dynamics, and rheology of intermediately attractive emulsions, having a micelle-induced depletion attractive interaction energy of approximately 5.6 $k_{\mathrm{B}}T$, situated between the strongly and moderately attractive regimes. In addition to the asymmetrical shape of $1/\ell^*(\phi)$ as found in strongly attractive emulsions, we uncover a striking notch in the measured $1/\ell^*(\phi)$ between the hard-sphere glass transition, ϕ_{g}, and maximal random jamming, ϕ_{MRJ}. This notch feature indicates the existence of a greater population of compact dense clusters of droplets, as compared to tenuous networks of droplets in strongly attractive emulsion gels. Moreover, the overall magnitude of $1/\ell^*(\phi)$ for ϕ below ϕ_{MRJ} is reduced in comparison to strongly attractive emulsions, implying a lower surface-to-volume ratio of attractive networks and constituent clusters. Furthermore, we observe the existence of excess MSDs at long times in the intermediately attractive emulsions, suggesting additional complexity in the local heterogeneous structure of droplets compared to the strongly attractive emulsions. Therefore, we develop an extended decorated core-shell network (E-DCSN) model to couple the measured ϕ-dependent self-motion plateau MSDs to the measured $1/\ell^*(\phi)$ by incorporating dense non-percolating clusters that do not contribute to shear rigidity in the prior DCSN model designed for strongly attractive colloidal systems. Using this E-DCSN model, we demonstrate a ϕ-dependent effective scattering probe-size factor ranging from 1.0 in the low-ϕ limit to 2.0 in the high-ϕ limit. This implies that the DWS scattering probes are effectively individual droplets at low ϕ, akin to moderately attractive emulsions at lower depletion strength; whereas, the scattering probes are effectively local dense clusters of droplets with an average radius twice the droplet radius at high ϕ, similar to the strongly attractive emulsions at higher depletion strengths.

In Chapter 4, we explore the extreme bidispersity in a droplet size distribution of a concentrated colloidal emulsion, which can be a source of emergent effects in that emulsion's optical transport properties, droplet dynamics, and bulk linear rheological response to shear. Our investigation of well-controlled binary mixtures of size-fractionated microscale emulsions and nanoemulsions reveals that these effects can stem from an additionally complex scenario of droplet jamming, and alternatively from entropic depletion attractions between microscale droplets, induced by nanoscale droplets functioning as a depletion agent. The binary emulsion mixtures exhibit notably distinct optical transport properties compared to a microscale emulsion alone, as the small dimensions of nanodroplets result in less scattering of visible light than those of microscale droplets. We deduce the effective scattering probe size by using the measured $1/\ell^*$ of mixtures and reference microscale-only emulsions, as well as accounting for the effective refractive index difference. We correct for collective scattering effects and apply the GSER to determine the G'_p using only optical properties. This approach yields quantitative microrheological agreement between optically and mechanically determined G'_p.

To understand the main factors influencing the shear rheological response of the binary mixture, we define the volume fraction of the nanoemulsion within an effective continuous phase, where all water volume is associated with nanodroplets. In this context, microscale emulsion droplets serve as weaker elastic inclusions in a primarily elastic matrix resulting from nanodroplet jamming. When the microscale droplet volume fraction in the final mixture is far below the jamming point of the microscale emulsion, or ϕ_MRJ, nanodroplet jamming dominantly governs the shear rigidity. However, at a higher microscale droplet volume fraction below but near ϕ_MRJ, nanodroplet-induced depletion attractions between microscale droplets begin to influence the shear rheological response. The results shed light on the interplay between the size ratio of droplets and their interactions in determining the overall properties of the emulsion system.

In Chapter 5, we undertake a preliminary exploration of employing nuclear magnetic resonance (NMR) for quantitative microrheology, with a specific focus on detecting the unjamming transition of elastic concentrated nanoemulsions into viscous dilute nanoemulsions. This process presents intriguing possibilities for pulsed-field gradient (PFG) NMR, especially when the nanoemulsion is engineered to exploit the nuclear specificity provided by ^{19}F-NMR. We study size-fractionated oil-in-water nanoemulsions formulated with a perfluorinated co-polymer silicone oil, which is highly insoluble in the aqueous continuous phase, to preclude any contribution from the aqueous continuous phase containing non-fluorinated ionic surfactants. Our findings reveal a significant change in the ^{19}F stimulated-echo (StE) PFG-NMR decays at high field-gradient strengths as the droplet volume fraction is reduced through dilution. We demonstrate that this dramatic change, a systematic progression from decay-to-plateau behavior in the jammed regime of nanodroplets to a simple decay in the unjammed regime, corresponds with the loss of low-frequency shear elasticity of the nanoemulsion by comparing it to bulk mechanical rheometry.

In Chapter 6, we focus on a simulation study to explore the feasibility of alternative techniques for passive microrheology of dense colloidal systems using molecular probes similar to ^{19}F-laden oils. We develop a two-dimensional oil-in-water emulsion model with perfectly confined molecular probe molecules and simulate the free diffusion of the probe molecule within a droplet, as well as the droplet's harmonically bound Brownian motion. Through our analysis, we demonstrate the potential for extracting droplet self-motion MSDs, which are essential for microrheology, and examines the thresholds for performing microrheology based on various material properties and detection limits. By understanding the mechanics and material parameters involved, we envision the potential application of methods such as NMR and electron paramagnetic resonance (EPR) spectroscopy, which inherently detect the molecular dynamics at a smaller scale.

In Chapter 7, we present a comprehensive comparison of optical transport properties of short-range attractive emulsions, which can serve as a useful road map of the presence of strong attractions relative to $k_{\mathrm{B}}T$. In addition to the moderately attractive (MA), intermediately attractive (IA), and strongly attractive (SA) emulsions that have been thoroughly studied by far, we perform measurements on attractive emulsions with very similar droplet size distributions to the earlier ones at a moderately-to-intermediately attractive (MA-IA) strength of approximately 3.3 $k_{\mathrm{B}}T$, as well as an intermediately-to-strongly attractive (IA-SA) strength of approximately 7.3 $k_{\mathrm{B}}T$, induced by surfactant micellar depletion. We compare the $1/\ell^*(\phi)$ features of all these attractive emulsions, spanning a broad range of attractive strength with detailed intervals, with one other and compare these with $1/\ell^*(\phi)$ of emulsions having nearly hard interactions. We display an *isoskedastic* point near ϕ_{MRJ} at which the optical scattering intensity does not depend on the interaction strength for all the emulsion systems explored.

In Chapter 8, we seek to develop another strategy of performing passive microrheology using molecular probe techniques, such as ^{19}F-NMR, with higher ratios of droplet MSD relative to total probe MSD, $\xi = \left\langle \Delta \boldsymbol{r}^2_{\mathrm{drop}} \right\rangle_{\mathrm{p}} / \left\langle \Delta \boldsymbol{r}^2_{\mathrm{pr,tot}} \right\rangle_{\mathrm{p}}$, than those shown in Chapter 6. We demonstrate 2D trajectory-based simulations of a surface-bound molecular probe conducting harmonically bound Brownian motion on the droplet surface. This approach resembles the use of irreversibly adsorbed fluorinated surfactant molecules at a high density on the droplet interfaces in emulsions and nanoemulsions. The molecular probe motion on droplet surface is highly localized, resulting in a high percentage of the total probe MSDs that arises from the droplet MSDs. Ultimately, this approach provides a high ξ for extracting colloidal dynamics from molecular dynamics and therefore, offers the potential of extending the passive microrheology of nanoemulsions using molecular probe techniques to the dense, elastic regime.

In conclusion, this dissertation presents a multidisciplinary approach to characterizing and understanding the optical and rheological properties of dense colloidal systems, particularly emulsions, taking into account various types and strengths of interactions between droplets and considering the presence of extreme bidispersity in droplet size distribution. We develop opto-microrheological models for quantitative DWS passive microrheology, providing insights into the local microstructures of dense emulsions under each of these conditions. By combining experimental techniques, analytical methods, and simulation models, we have investigated the potential application of molecular detection techniques to passive microrheology of emulsions and nanoemulsions.

Chapter 2 - Diffusing wave microrheology of strongly attractive sense emulsions

Reprinted/Adapted from "Diffusing wave microrheology of strongly attractive dense emulsions." *Phys. Rev. E* 102(6), pages 062610 by Xu, Y., Scheffold, F., and Mason, T. G. (2020), with permission from American Physical Society (APS).

2.1 Abstract

We advance the microrheological interpretation of optical diffusing wave spectroscopy (DWS) measurements of strongly attractive emulsions at dense droplet volume fractions, ϕ. Beyond accounting for collective scattering, we show that measuring the mean free path of optical transport over a wide range of ϕ is necessary to quantify the effective size scale of the DWS probes, which we infer to be local dense clusters of droplets through a decorated core-shell network model. This approach yields microrheological elastic shear moduli that are in quantitative agreement with mechanical rheometry.

2.2 Introduction

Gelation of uniform colloids in a continuous liquid phase through strongly attractive interactions leads to interesting arrested systems that have different kinds of network morphologies and physical properties[60,61]. These morphologies and properties can depend on the shapes and deformability of the colloids, the specific nature of the intercolloidal attractions, and even the history of preparation[62,63]. Theoretical and numerical studies of short-range attractive colloidal systems[41, 42, 64–67] have focused mainly on structural characteristics and mechanics of spherical particles interacting through central-force potentials at colloid volume fractions ϕ that are below the hard-sphere jamming-point[35, 36, 68, 69]. Dynamic light scattering measurements on attractive gel-like systems of solid colloidal particles[40, 70–74], have revealed plateau behavior in correlation functions reflecting the existence of low-frequency elasticity, yet an accurate quantitative passive microrheological comparison with mechanical measurements has remained elusive. Some non-equilibrium colloidal gel systems age and evolve[67, 75–77], whereas others do not if the short-range attractions are sufficiently strong compared to thermal energy, which sets an average scale for quiescent Brownian excitations. Even when aging and evolution can effectively be neglected, prior attempts to connect optical and mechanical properties of colloidal gels through passive microrheology, which involved the multiple light-scattering technique of diffusing wave spectroscopy (DWS)[55], did not yield accurate quantitative agreement[78]. However, this does not necessarily imply that any problem exists with the basic notions of passive microrheology; instead, it suggests that the assumptions related to interpreting DWS signals in terms of the self-motion of scattering-probes need to be re-examined for strongly attractive dense colloidal systems.

A recent advance has enabled the quantitative microrheological interpretation of DWS measurements of colloidal droplets having nearly hard interactions in dense, jammed, elastic emulsions by accounting for collective light scattering effects, related to the system's average structure factor, which depends on ϕ[57]. This study showed that apparent droplet mean square displacements (MSDs), obtained by routine DWS analysis, must first be converted into self-motion MSDs before applying the generalized Stokes-Einstein relation (GSER) of thermal-entropic passive microrheology[11]. This conversion involves multiplying the apparent MSD by factor proportional to the measured inverse mean free path of optical transport, $1/\ell^*$, at high ϕ relative to the slope of $1/\ell^*(\phi)$ of isolated droplets as $\phi \to 0$. By using droplet self-motion MSDs, not apparent MSDs, in the GSER, the linear plateau elastic shear modulus, G'_p, determined microrheologically was found to match macroscopic mechanical measurements over a wide range of ϕ.

While demonstrated for dense emulsions having nearly hard interdroplet interactions[57], this advance does not guarantee that treating DWS MSDs in the same manner would yield quantitative microrheological predictions of G'_{p} for strongly attractive emulsion systems, because such attractive droplets typically form lubricated bonds with other droplets through slippery diffusion-limited cluster aggregation (S-DLCA)[51,58]. Slippery aggregation leads to local dense clusters (LDCs) of droplets that form heterogeneous elastic networks for ϕ well below the hard jamming-point[46]. In S-DLCA, strongly attractive droplets are not isolated even at low ϕ; instead LDCs and aggregates of LDCs are present. Such strongly attractive emulsion systems have been previously created using depletion attractions[44] caused by nanoscale surfactant micelles[45,46,79]; despite this attraction, droplets do not coalesce as a consequence of screened-charge repulsion at shorter range, provided by ionic amphiphiles which coat the droplets' surfaces. So, ascertaining if passive microrheology can be performed quantitatively using DWS on elastic emulsion systems having strong attractions at high ϕ is a remaining challenge. If demonstrated, this would overcome a major existing conceptual hurdle and potentially enable DWS microrheology to be performed on other strongly attractive dense colloidal systems, including particulate systems.

Here, we show that quantitative passive microrheology of a dense emulsion system, which has been made strongly attractive using micellar depletion, can be performed using DWS, yet through an interpretation that is quite different than the one applied to the same emulsion having nearly hard interactions. While MSDs are still modified to account for collective scattering, this modification still does not provide quantitative microrheological agreement with mechanical measurements of G'_{p}. We resolve this problem by hypothesizing that the scattering probes associated with DWS MSDs in strongly attractive colloidal emulsions are not necessarily single droplets, but instead are LDCs of several droplets held together by slippery attractions. By measuring ϕ-dependent plateau MSDs and fitting the measured $1/\ell^*(\phi)$ using an opto-mechanical colloidal gel model, which we call the decorated core-shell network (DCSN) model, we show that the average radius of the dominant scattering-probes from $\phi \approx 0.5$ to $\phi \approx 0.8$ is about twice the radius of a droplet, corresponding to tetrahedral LDCs. With these advances in interpreting DWS, we show that passive microrheology yields accurate G'_{p} for this strongly attractive dense emulsion system, as we demonstrate through comparison with macroscopic rheometry.

2.3 Experimental

2.3.1 Size-fractionated attractive emulsions

A uniform oil-in-water (O/W) microscale emulsion has been prepared using trimethylsiloxy terminated poly-dimethylsiloxane oil (PDMS, Gelest Inc.; kinetic viscosity: $\nu_{\mathrm{o}} = 350$ cSt; mass density: $\rho_{\mathrm{o}} = 0.97$ g cm^{-3}; average molecular weight: $\mathrm{MW}_{\mathrm{o}} = 13{,}650$ g mol^{-1}; refractive index: $n_{\mathrm{o}} = 1.4031$), sodium dodecyl sulfate (SDS, Fisher Scientific; electrophoresis grade 99% purity), and deionized water (Millipore Milli-Q Academic; resistivity: 18.2 MΩ cm). To highlight differences between emulsion systems caused by strong interdroplet attractions, as compared to nearly hard interactions, we use the same size-fractionated emulsion prepared by Kim *et al.*[57] (*i.e.* the same droplet size distribution); yet, we set [SDS] to be much higher, 80 mM, in the final master stock emulsion sample in order to generate strong interdroplet depletion attractions, as opposed to the nearly hard interdroplet interactions at lower [SDS] = 10 mM used by Kim *et al.*[57]. Primary characteristics of the droplet radial size distribution, determined by dynamic and static light scattering, are: average radius $\langle a \rangle = 459 \pm 15$ nm and polydispersity $\delta a / \langle a \rangle \simeq 0.18$, where δa is the standard deviation. These characteristics are the same as those of Kim *et al.*[57], who investigated nearly hard interactions between droplets; fixing $\langle a \rangle$ and δa facilitates meaningful comparisons of physical properties that change as a result of the strong depletion attraction. The refractive index of the 80 mM aqueous SDS solution, the continuous phase, is $n_{\mathrm{c}} = 1.3340$ at temperature $T = 20$ °C[80].

Strong lubricated depletion attractions between droplets, which give rise to a secondary potential minimum in their pair interaction potential, in the fractionated PDMS O/W emulsion are induced by setting [SDS] = 80 mM in the continuous phase, well above SDS's critical micelle concentration of $C^{*} \approx 8.1$ mM. To generate depletion attractions in this fractionated emulsion, we centrifuge the emulsion using a swinging bucket rotor (Beckman L8-55 ultracentrifuge, SW-28 swinging bucket rotor, 10,000 rpm, 1.25 h) to form concentrated elastic plugs at the tops of the thick-wall polycarbonate centrifuge tubes without inducing droplet coalescence, separate and combine these concentrated plugs, and dilute the combined recovered plugs to $\phi \approx 0.1$ using an aqueous solution at [SDS] = 80 mM. This process is repeated two additional times to set the SDS concentration, yielding a large volume of concentrated stock emulsion that is elastic at high ϕ. This master concentrated stock emulsion is mixed thoroughly, at sufficiently low strain rates that preclude droplet rupturing, in order to exclude any size-separation that potentially could be induced by centrifugation. To reduce the potential evolution of ϕ by evaporation-condensation of water vapor onto the lid and walls of the container as well as loss of water vapor when opening and re-sealing the container, we store this master sample in a temperature-controlled chamber set at 20 °C. We also select a container that has a volume only slightly larger than that of the master sample, which allows only a very small volume of water vapor in the gas above the emulsion; this also reduces water loss from the master sample over time. We measure the oil droplet volume fraction of this master stock emulsion to be $\phi_{\mathrm{m}} = 0.771 \pm 0.008$, determined through a previously developed gravimetric evaporation method[80].

Emulsion samples at lower ϕ are obtained by diluting this master stock emulsion with an aqueous solution at [SDS] = 80 mM using an analytical balance (Denver Instruments APX-200, 0.1 mg precision). Each diluted sample having $\phi < \phi_{\mathrm{m}}$ has been mixed in a 3 mL vial to ensure that it is well and homogeneously dispersed before loading into an optical cuvette or the mechanical rheometer. For $\phi \geq 0.62$, the diluted emulsion samples are stirred with a small spatula for 3 minutes, and for $\phi < 0.62$, emulsions are stirred with a spatula, capped, and shaken. Each diluted sample after mixing is split into two portions: 1.5 mL for DWS and 0.5 mL for mechanical rheometry. This ensures that exactly the same sample ϕ has been used for both DWS and mechanical rheometry. We find that using exactly the same sample ϕ is necessary in order to make accurate comparisons between light scattering and mechanical measurements. We estimate the magnitude of the attractive depletion interaction potential energy between two oil droplets near contact, U_{attr}, by combining Asakura-Oosawa's theory for larger and smaller hard spheres with Vrij's linear micellar model[46]: $|U_{\mathrm{attr}}| = 4\pi a a_{\mathrm{m}}^2 N_0 k_{\mathrm{B}} T \left(C - C^*\right)/\nu_{\mathrm{m}}$, where the radius of the emulsion droplets is $a = \langle a \rangle$, a_{m} is the effective radius of a micelle ($a_{\mathrm{m}} \sim 2$ nm for SDS), N_0 is Avogadro's number, k_{B} is Boltzmann's constant, T is the temperature, C is the bulk concentration of SDS (in moles per volume), and ν_{m} represents the aggregation number of amphiphilic molecules in a micelle ($\nu_{\mathrm{m}} \approx 70$ for SDS). This formula implicitly assumes that the shape and size of the micelles are independent of C. For the fractionated emulsion at [SDS] = 80 mM, we calculate $|U_{\mathrm{attr}}| \approx 14.5\ k_{\mathrm{B}}T$, much stronger than thermal energy $k_{\mathrm{B}}T$. Beyond providing a micellar depletion attraction, adsorbed dodecyl sulfate anions (DS^-) on the droplet surfaces, as well as DS^- and Na^+ in the continuous phase, also give rise to a strong short-range Debye-screened-charge repulsion between droplets, thereby precluding their coalescence. Thus, the preservation of a layer of aqueous continuous phase between droplets in this strongly attractive system makes the interdroplet attraction lubricated and slippery; this is quite different than the nature of bonding between solid colloids that have been destabilized in a manner that causes them to fuse together in a shear-rigid manner as a consequence of extremely strong Van der Waals attractions.

2.3.2 Diffusing wave spectroscopy

DWS measurements are made using a Rheolab 3 light scattering instrument (LS Instruments, Fribourg CH, equipped with backscattering option, light wavelength $\lambda = 685$ nm). Each emulsion is loaded into a clean glass optical cuvette having a thickness (*i.e.* pathlength) of $L = 5$ mm and a width of 10 mm. This pathlength is large enough to guarantee that the optical transport mean free path ℓ^* is always significantly less than L over all ϕ corresponding to mean square displacements (MSDs) that we report. A sufficiently large volume of emulsion is loaded to ensure that the emulsion's upper surface is at least 15 mm high relative to the bottom surface of the cuvette; this ensures that the region of light scattering around the incident laser beam is symmetric and uniform. Centrifugation at low speed for a short duration removes stray air bubbles in loaded cuvettes having $\phi \geq 0.62$ without generating gradients in ϕ. The maximum centrifugal speed does not exceed 1500 rpm, and the total duration, including acceleration and deceleration, does not exceed 60 s. For $\phi < 0.62$, this brief centrifuging step is omitted, since it creates noticeable gradients in ϕ visible in the cuvette. For $0.537 \leq \phi \leq 0.595$, we load the emulsion samples into the cuvettes using a syringe with a stainless-steel needle tip having an inner diameter I.D. = 0.84 mm. Initially, we fully insert the syringe-tip to the bottom of the glass cuvette, and the syringe is slowly withdrawn while injecting the emulsion and ensuring that the tip remains below the emulsion's surface. For $\phi \leq 0.520$, the emulsion's yield stress is sufficiently low that we simply pour the emulsion into the optical cuvette along one wall to ensure that no air bubbles are introduced. After loading, we use Parafilm to seal the capped optical cuvettes and all the emulsion samples are stored in a temperature-controlled chamber and allowed to equilibrate for 24 hours before making DWS measurements. For all measurements, the sample temperature in the Rheolab 3 is maintained and controlled at $T = 20 \pm 0.1$ °C. The completion of loading an emulsion into the cuvette for DWS sets the start of its reported waiting time. This effective invariance on waiting time in the elastic dense emulsion limit facilitates microrheological comparisons; aging and gravity-induced droplet compaction[81] do not significantly influence our measurements.

While we report dynamic DWS MSD measurements only in this effectively time-invariant range of ϕ, we measure and report $1/\ell^*$ down to even lower ϕ, using a technique that measures scattering properties of clusters of strongly attractive droplets but is not unduly influenced by gravitational compaction. After diluting a portion of the master stock emulsion and mixing to set $\phi \leq 0.3$ at [SDS] = 80 mM, we let the attractive emulsion sample rest 24 hours; then, a sample at $\phi \leq 0.3$ is loaded in cuvette, and the cuvette is gently inverted for 5 times and finally righted. We place the cuvette into the Rheolab 3 and then wait 1,200 s before measuring $1/\ell^*$. We estimate the characteristic doubling time, based on colloidal diffusion of droplets in water, to be ≈1.4 s at the lowest $\phi = 0.05$, corresponding to the longest doubling time. So, a waiting duration of 1,200 s is over two orders of magnitude larger than this longest doubling time. Thus, local dense clusters of droplets have ample time to form through slippery diffusion limited cluster aggregation[51,58] at all $0.05 \leq \phi \leq 0.3$ we report using this procedure, yet evidence of gravitational compaction is not seen. At each ϕ, $1/\ell^*$ is measured and averaged from 11 trials at intervals of 380 s; the trial-to-trial standard deviation is less than 1.5%. No visible phase separation or systematic trend in the measured $1/\ell^*$ is observed as a function of trial number.

In order to facilitate a meaningful microrheological comparison between light scattering and mechanical measurements, we first assess the regime of ϕ over which time-invariant light scattering measurements can be made, such that aging and gravitational compaction of the dense attractive emulsion are effectively negligible over at least one day. For a given waiting time after loading, the optical mean free path ℓ^*_{attr} of each dense attractive emulsion is measured and averaged from at least 8 trials, yielding $1/\ell^*_{\mathrm{attr}}(\phi)$. At each ϕ, we also obtain the DWS transmission autocorrelation function, expressed as $g_2(t)-1$, where t is the correlation time, averaged from at least 8 trials; the multi-tau duration is 300 s, and the echo duration is 60 s.

For each ϕ, having measured $g_2(t)-1$ and ℓ^*_{attr}, we extract the apparent mean squared displacement $\langle \Delta \boldsymbol{r}_{\mathrm{a}}^2(t) \rangle$ by solving the classic transcendental equation of DWS[57,82,83]. To correct for collective light scattering effects, each apparent MSD is converted into a probe self-motion MSD $\langle \Delta \boldsymbol{r}^2(t) \rangle$ by multiplying the apparent MSD with a dimensionless ratio given by the actual measured scattering strength at that ϕ, reflected by $1/\ell^*_{\mathrm{attr}}(\phi)$, divided by a scattering strength that ignores collective scattering and is given by the linear extrapolation of low-ϕ

scattering: $[1/\ell^*_{\mathrm{attr}}(\phi)]/[(1/\ell^*_{\mathrm{LDC,attr}})\phi]$, where $1/\ell^*_{\mathrm{LDC,attr}}$ is the slope of the measured $1/\ell^*_{\mathrm{attr}}$ versus ϕ in the dilute limit as $\phi \to 0$. This ratio lowers the overall magnitude of the MSDs by different amounts that depend on ϕ.

2.3.3 Mechanical shear rheometry

We use a controlled-strain mechanical shear rheometer (RFS-II, Rheometric Scientific, 25 mm diameter stainless steel cone-and-plate geometry, equipped with a vapor trap) to measure plateau elastic shear moduli, $G'_{\mathrm{p,mech}}$, at low strains corresponding to the linear viscoelastic regime. At each ϕ, a strain sweep, yielding the linear and non-linear shear storage modulus, expressed as $G'(\gamma)$, is performed at room temperature $T = 20$ °C and a frequency of $\omega = 1$ rad/s. This frequency is within the range of time scales that correspond to the plateau associated with DWS MSD measurements. Strains down to $\approx 2 \times 10^{-4}$ can be reached; this limit is set by the resolution of the RFS-II's motor. For the lowest ϕ, such small strains are needed to identify the true linear regime.

2.4 Model

To explain the complex shape of $1/\ell^*_{\mathrm{attr}}(\phi)$ for the heterogeneous attractive emulsion system in the limit of strong slippery attractions, we propose a model that takes into account scattering contributions from droplets in different local regions of a gel-like network that have different numbers of nearest neighbors, reflected through the local coordination number N. We simplify the continuous distribution of N[58] using only three principal scattering components from different local regions of the network: surface decorating droplets (SDDs) that have $\langle N \rangle \approx 3$ and are found at the boundary between the network and the void region; shell droplets that have $\langle N \rangle \approx 5$ to 6, reflecting loose connections between small clusters in the gel-like network that do not support shear stresses elastically; and core droplets that have $\langle N \rangle \approx 10$ to 12, reflecting core regions of the network, inside the shell regions, that are more highly compact and can support shear stresses elastically. Each of these different components of the network scatter light to different degrees because droplets with higher N effectively scatter less than droplets with lower N, since crowding reduces the scattering cross section for the droplet sizes considered. The dominant contribution to the scattering is from SDDs at very low ϕ, from the shell at intermediate ϕ as SDDs are effectively converted into shell droplets through osmotic compression, and from the core towards the highest ϕ as the shell droplets are converted into core droplets. Ultimately at very high ϕ, the system's structure resembles a defected disordered solid composed mostly of core droplets. We call this model the decorated core-shell network (DCSN) model, and it goes beyond earlier, simpler gel-void models[84] by categorizing droplets in the attractive network gel into these three different categories according to their different effective scattering strengths, which reflect different local $\langle N \rangle$. Also, the DCSN model couples optical and mechanical properties of the system, since only core regions of the network with the highest N contribute significantly to the macroscopic G'_{p}. Strong slippery bonding between droplets implies that no individual droplets or LDCs detach from the network as a result of Brownian excitations.

At very low ϕ, we assume that the volume fraction of SDDs, ϕ_{SDD}, grows linearly with ϕ, reflecting the formation of LDCs, while the volumes of core and shell droplets remain negligible. However, for larger ϕ, as SDDs are converted into shell droplets, ϕ_{SDD} decreases rapidly above a threshold ϕ. A simple function that captures these key features is a linear rise multiplied by a Fermi function:

$$\phi_{\mathrm{SDD}}(\phi) = \frac{\phi}{1 + \exp[(\phi - \phi_{\mathrm{SDD,F}})/\Delta\phi_{\mathrm{SDD}}]}, \tag{2.1}$$

where $\phi_{\mathrm{SDD,F}}$ restricts the growth of $\phi_{\mathrm{SDD}}(\phi)$ towards higher ϕ and $\Delta\phi_{\mathrm{SDD}}$ is related to how rapidly $\phi_{\mathrm{SDD}}(\phi)$ decreases. Moreover, the GSER of thermal-entropic passive microrheology implies that the macroscopic shear elastic modulus of the attractive system varies as: $G'_{\mathrm{p,attr}} \sim 1/\left\langle \Delta \boldsymbol{r}^2 \right\rangle_{\mathrm{p}}$. We hypothesize that the core regions are characterized by an average droplet volume fraction, $\phi_{\mathrm{net,core}}$, which lies above the hard jamming-point, so the repulsive part of the interdroplet potential is dominant. The average elastic shear modulus within only these core regions can therefore be determined using an entropic, electrostatic, and interfacial (EEI) model[37]: $G'_{\mathrm{p,EEI}}(\phi_{\mathrm{net,core}})$. For $\phi < \phi_{\mathrm{net,core}}$, we reason that the volume fraction of core droplets in the attractive system, ϕ_{core}, is proportional to $G'_{\mathrm{p,attr}}$:

$$\phi_{\mathrm{core}}(\phi) = \phi_{\mathrm{net,core}} \frac{G'_{\mathrm{p,attr}}(\phi)}{G'_{\mathrm{p,EEI}}(\phi_{\mathrm{net,core}})}. \tag{2.2}$$

Because the size of DWS scattering-probes is not known *a priori* in the attractive system, we introduce an effective probe-size factor, α, in the GSER, which in the plateau region yields:

$$G'_{\mathrm{p,attr}} = \frac{k_{\mathrm{B}}T}{\pi\alpha\langle a\rangle \left\langle \Delta \boldsymbol{r}^2\right\rangle_{\mathrm{p}}}, \tag{2.3}$$

where $G'_{\mathrm{p,attr}}$ and $\left\langle \Delta \boldsymbol{r}^2\right\rangle_{\mathrm{p}}$ depend on ϕ. Thus, $\phi_{\mathrm{core}}(\phi)$ is inversely proportional to $\left\langle \Delta \boldsymbol{r}^2\right\rangle_{\mathrm{p}}(\phi)$. Volume conservation of droplets implies that the volume fraction of shell droplets is:

$$\phi_{\mathrm{shell}}(\phi) = \phi - [\phi_{\mathrm{SDD}}(\phi) + \phi_{\mathrm{core}}(\phi)]. \tag{2.4}$$

Since ϕ_{shell} is determined entirely by ϕ_{SDD} and ϕ_{core}, no independent fit parameters are associated with it.

Furthermore, at a given ϕ, we assume that the scattering contributions to $1/\ell^*_{\mathrm{attr}}$ of SDD, shell, and core regions are simply linearly proportional to the droplet volume fractions in those regions:

$$1/\ell^*_{\mathrm{attr}} = (1/\ell^*_{\mathrm{SDD}})(\phi_{\mathrm{SDD}} + r_{\mathrm{shell}}\phi_{\mathrm{shell}} + r_{\mathrm{core}}\phi_{\mathrm{core}}), \tag{2.5}$$

where r_{shell} and r_{core} are fit parameters that indicate the relative scattering intensity from a shell or core droplet, respectively, with respect to a SDD droplet, and $1/\ell^*_{\mathrm{SDD}}$ is the linear coefficient of $1/\ell^*_{\mathrm{attr}}(\phi) \sim \phi_{\mathrm{SDD}}$ for SDDs in the low-ϕ limit. By varying the DCSN model's parameters, subject to the constraints that ϕ_{shell} vanishes with zero slope and zero curvature as $\phi \to 1$ and χ^2 of the nonlinear least squares fit to $1/\ell^*_{\mathrm{attr}}(\phi)$ is minimized, the optimal parameters $\phi_{\mathrm{SDD,F}}$, $\Delta\phi_{\mathrm{SDD}}$, $1/\ell^*_{\mathrm{SDD}}$, r_{shell}, and r_{core} can be determined. In addition, the values of α and $\phi_{\mathrm{net,core}}$ can be varied and the above process can be repeated in order to find the optimized model parameters $\widetilde{\alpha}$ and $\phi_{\mathrm{net,core}}$ that minimize χ^2 of the fit to the measured $1/\ell^*_{\mathrm{attr}}(\phi)$.

2.5 Results

2.5.1 Diffusing wave spectroscopy

For dense $\phi \geq 0.4$, we observe that both $1/\ell^*_{\mathrm{attr}}$ and $\langle \Delta \boldsymbol{r}^2 \rangle_{\mathrm{p}}$ of the strongly attractive emulsion system are effectively time-invariant over 24 hours [see Figures 2.1(a) and 2.1(b), respectively]. Likewise, visual observations of the loaded cuvettes confirm the absence of any macroscopic phase separation. Additional assessments of time-invariance include: $< 2\%$ change in $1/\ell^*$ and $< 14\%$ change in plateau MSD $\langle \Delta \boldsymbol{r}^2 \rangle_{\mathrm{p}}$ after 88 h at $\phi = 0.595$; after 8 days at $\phi = 0.501$; and after 20 days at $\phi = 0.537$; and $< 1\%$ change in $1/\ell^*$ and $< 18\%$ change in $\langle \Delta \boldsymbol{r}^2 \rangle_{\mathrm{p}}$ after 88 h at $\phi = 0.301$. However, more highly diluted emulsions below this range behave differently, and their plateau MSDs become time-varying as samples evolve. This evolution is largely a consequence of gravity-induced compaction arising from the mismatch

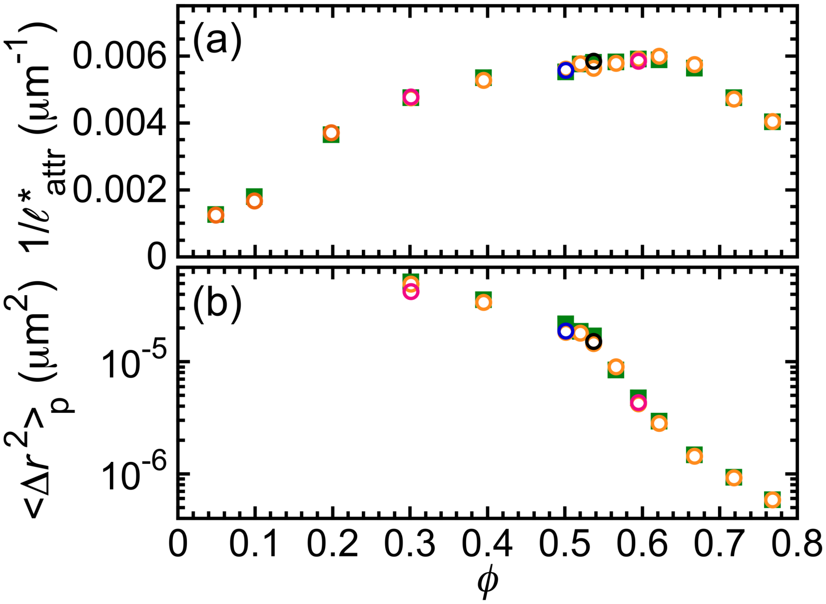

Figure 2.1. Light scattering measurements of (a) inverse mean free path of optical transport, $1/\ell^*_{\mathrm{attr}}$, and (b) DWS plateau probe MSDs $\langle \Delta \boldsymbol{r}^2 \rangle_{\mathrm{p}}$, for the strongly attractive dense emulsion at [SDS] = 80 mM as a function of droplet volume fraction ϕ for different waiting times after sample loading into the optical cuvette: 20 minutes (green solid squares); 24 hours (orange open circles); 88 hours (magenta open circles); 8 days (blue open circles); 20 days (black open circle).

between the mass densities of the oil phase ($\rho_{\mathrm{o}} = 0.97$ g cm^{-3}) and the continuous aqueous phase ($\rho_{\mathrm{c}} = 1.00$ g cm^{-3}). In order to obtain reproducible DWS results for dense gel-like emulsions that do not age or compact appreciably over at least 24 hours, which are more amenable for microrheological comparisons with mechanical rheometry measurements, we report DWS MSDs only for the time-invariant dense regime corresponding to $\phi \gtrsim 0.4$.

To facilitate comparison with the nearly hard emulsion system, we fit the measurements of $1/\ell^*_{\mathrm{hard}}(\phi)$ made by Kim *et al.*[57] to a semi-empirical functional form that we introduce here, which provides excellent agreement [see Figure 2.2(a)]:

$$1/\ell^*_{\mathrm{hard}}(\phi) = (1/\ell^*_{\mathrm{ISA,hard}})\phi[1 - (\phi/\phi_{\mathrm{trans}})^2], \tag{2.6}$$

where $1/\ell^*_{\mathrm{ISA,hard}} = 0.0197 \pm 0.0001$ μm^{-1} reflects the slope at low ϕ, corresponding to the independent scattering approximation (ISA), and $\phi_{\mathrm{trans}} = 0.853 \pm 0.002$ is the ϕ associated with optical transparency, extrapolated beyond the measurement range ($\mathrm{R}^2 = 0.998$). This fit is based on data of the nearly hard emulsion system up to a maximum volume fraction of $\phi \approx 0.73$ and should not be interpreted as being a strictly accurate description for significantly higher ϕ. A Mie-scattering calculation of an ideal isolated sphere, using n_{c} and n_{o}, yields a slope $1/\ell^*_{\mathrm{ISA,Mie}} = 0.0208$ μm^{-1} [Figure 2.2(a)][57] that is within about 10% of $1/\ell^*_{\mathrm{ISA,hard}}$.

In Figure 2.2(a), we plot $1/\ell^*_{\mathrm{attr}}(\phi)$ for the strongly attractive emulsion system and compare it with $1/\ell^*_{\mathrm{hard}}(\phi)$ for the same droplet size distribution yet nearly hard interactions. We find that $1/\ell^*_{\mathrm{attr}}(\phi)$ is noticeably asymmetric and remarkably different than the peaked and much more symmetric $1/\ell^*_{\mathrm{hard}}(\phi)$. In particular, $1/\ell^*_{\mathrm{attr}}(\phi)$ exhibits a first knee at $\phi \approx 0.3$, corresponding to a pronounced change in upward slope, and a second knee at $\phi \approx 0.65$, corresponding to a drop towards higher ϕ. Also, at intermediate ϕ between the first and second knee, $1/\ell^*_{\mathrm{attr}}$ is lower than $1/\ell^*_{\mathrm{hard}}$, indicating that the attractions lead to a reduction in scattering there. The attractive and hard systems have about the same $1/\ell^*$ at ϕ_{eq} just above 0.6. For larger ϕ up to the limit of our exploration near 0.77, the heterogeneous strongly attractive system actually scatters more than homogeneous jammed hard system of

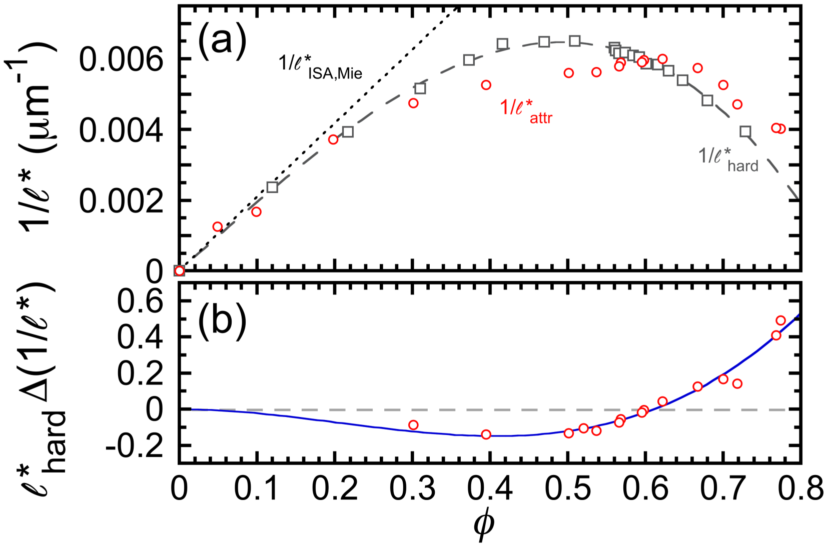

Figure 2.2. Inverse mean free path of optical transport, $1/\ell^*_{\mathrm{attr}}$, for fractionated oil-in-water emulsions that have strong depletion attractions at fixed [SDS] = 80 mM. (**a**) Measured $1/\ell^*_{\mathrm{attr}}$ as a function of droplet volume fraction ϕ (red circles). For comparison: measured $1/\ell^*_{\mathrm{hard}}$ for the same emulsion size distribution but for nearly hard interactions between droplets at much lower [SDS] = 10 mM (gray squares from[57]) and corresponding fit using equation (2.6) (gray dashed line). Black dotted line: isolated scattering approximation (ISA) of the hard system based on Mie scattering: $1/\ell^*_{\mathrm{ISA,Mie}}$. (**b**) Difference in scattering caused by the attraction, $\Delta(1/\ell^*) = 1/\ell^*_{\mathrm{attr}} - 1/\ell^*_{\mathrm{hard}}$, normalized by $1/\ell^*_{\mathrm{hard}}$ beyond the low-ϕ linear region. Fit using equation (2.7) (blue solid line; square of correlation coefficient, $\mathrm{R}^2 = 0.966$.)

droplets. To quantify this, we subtract the fit to $1/\ell^*_{\mathrm{hard}}(\phi)$ from the measured $1/\ell^*_{\mathrm{attr}}(\phi)$ and normalize this by $1/\ell^*_{\mathrm{hard}}$, yielding a dimensionless difference in scattering as a consequence of strong interdroplet attractions [see Figure 2.2(b)]. We fit this to:

$$\frac{\Delta(1/\ell^*)}{1/\ell^*_{\mathrm{hard}}} = P\phi^2(\phi - \phi_{\mathrm{eq}}), \tag{2.7}$$

yielding: $P = 4.4 \pm 0.3$, reflecting the strength of the depletion attraction, and $\phi_{\mathrm{eq}} = 0.611 \pm 0.007$.

To compensate apparent DWS MSDs for collective light scattering effects, resulting from the close proximity of the probes, we determine accurate probe self-motion MSDs $\langle\Delta \boldsymbol{r}^2(t)\rangle$ using the measured $\ell^*_{\mathrm{attr}}(\phi)$ [see Figure 2.3(a) and chapter 2.3.2]. We fit the measured $1/\ell^*_{\mathrm{attr}}(\phi)$ for $\phi \leq 0.22$ to $(1/\ell^*_{\mathrm{LDC,attr}})\phi$, yielding $1/\ell^*_{\mathrm{LDC,attr}} = 0.0187 \pm 0.0004$ μm^{-1}. This

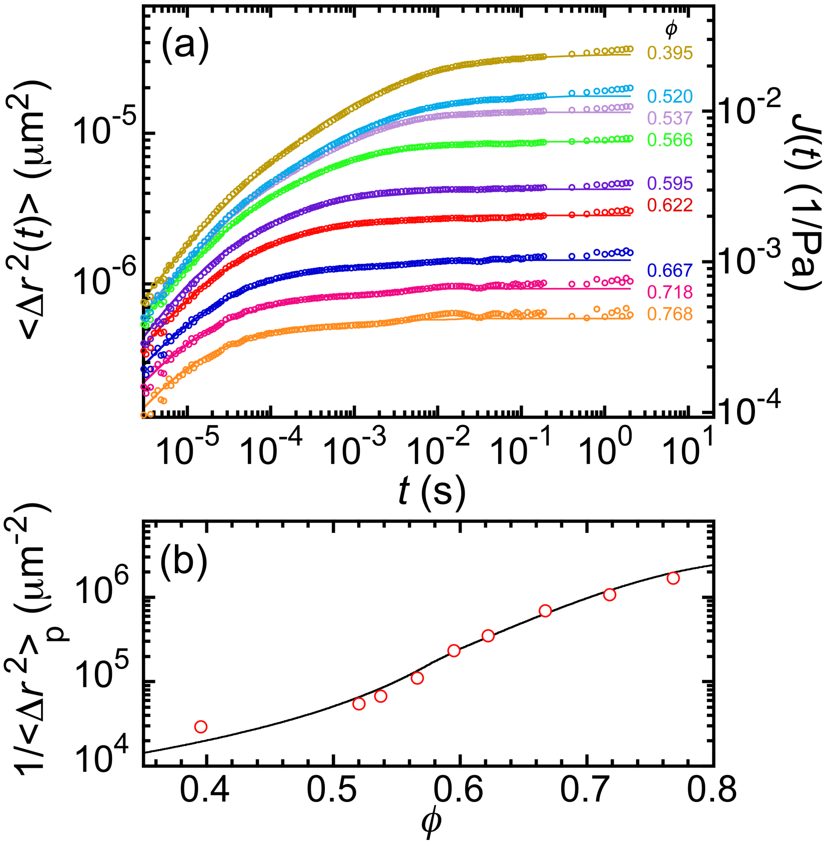

Figure 2.3. (a) **Ensemble-averaged time-dependent self-motion mean square displacements (MSDs), $\langle \Delta \boldsymbol{r}^2(t) \rangle$, measured using diffusing wave spectroscopy (DWS), in strongly attractive emulsions at [SDS] = 80 mM for different ϕ** (colored circles, see legend at right). Correlator data: $t < 0.2$ s. Echo data: $t > 0.2$ s. MSDs have been corrected for collective scattering using $1/\ell^*_{\text{attr}}(\phi)$ (see text). Solid lines: fits capture the early-time rise, the crossover regime, and the long-time plateau behavior. Right axis: corresponding shear creep compliance $J(t)$ obtained via passive microrheology using the DCSN model (see text). (b) **Inverse plateau MSDs, $1/\langle \Delta \boldsymbol{r}^2 \rangle_{\text{p}}$, from the fits in part (a) versus ϕ.** Solid line: smooth analytical interpolation.

represents a measured effective ISA for the probes, which we hypothesize to be local dense clusters of droplets in the strongly attractive emulsion system, and this value is very close to the ISA of droplets in the nearly hard emulsion system having the same size and size distribution obtained by Kim *et al.*[57]: $1/\ell^*_{\text{LDC,attr}}$ is within about 20% of both $1/\ell^*_{\text{ISA,hard}}$ and $1/\ell^*_{\text{ISA,Mie}}$.

The self-motion probe MSDs $\langle \Delta \boldsymbol{r}^2(t) \rangle$ exhibit an early-time near-linear rise up to $t \approx 10^{-5}$

s, next a gradual bending, and then a long-time plateau behavior beyond $t \approx 10^{-1}$ s. We find that a dense-emulsion MSD model, originally created for jammed emulsions with nearly hard droplet interactions[57], can also be used to fit probe MSDs of strongly attractive emulsions [see Figure 2.3(a)]. In order to obtain more accurate plateau MSD values, any minor periodic vibrational noise (evidenced by a small oscillation in the MSD in the plateau region at longer times) and all data in the echo region are excluded from the fits. From the fits, we extract the inverse self-motion plateau MSDs, $\langle \Delta \boldsymbol{r}^2 \rangle_{\mathrm{p}}$, the time scales, τ, associated with the gradual bend and high-frequency square-root contribution to the complex shear modulus, and the high frequency viscosities, η_∞, consistent with the optimal effective size-shape parameter $\widetilde{\alpha}$ of the probes as local dense clusters of droplets in the strongly attractive system. From these fits, we determine the inverse plateau probe MSDs, $1/\langle \Delta \boldsymbol{r}^2 \rangle_{\mathrm{p}}(\phi)$, as well as a smooth analytical interpolation useful for DCSN model calculations, are shown in Figure 2.3(b). We

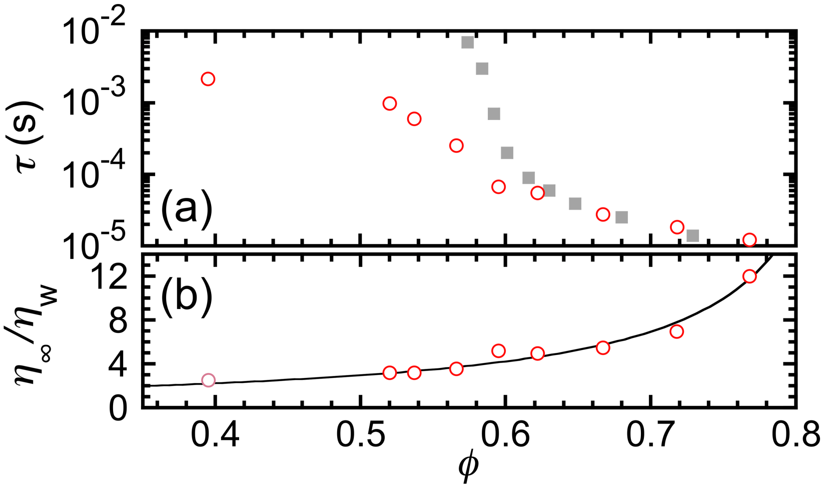

Figure 2.4. Characteristic time scale τ and high-frequency viscosity η_∞ determined by fitting DWS probe self-motion MSDs of strongly attractive dense emulsions at [SDS] = 80 mM. (**a**) Red open circles: τ obtained by fitting $\langle \Delta \boldsymbol{r}^2(t) \rangle$ in Figure 2.3(a), as a function of ϕ for the attractive emulsion. Gray solid squares: $\tau(\phi)$ for the same droplet size distribution but nearly hard interactions at [SDS] = 10 mM (see Kim *et al.*[57]). (**b**) η_∞, normalized by the viscosity of water η_{w}, versus ϕ; η_∞ depends most sensitively on early-time MSD data. Solid line: semi-empirical fit using $\eta_\infty(\phi)/\eta_{\mathrm{w}} = 1 + S\phi/(\phi_{\mathrm{div}} - \phi)$, where $S = 1.5 \pm 0.2$ is the initial linear slope at low ϕ and $\phi_{\mathrm{div}} = 0.87 \pm 0.02$ corresponds to the effective divergence in η_∞ ($\mathrm{R}^2 = 0.963$).

point out here that in colloidal systems with strong slippery attractions, these self-motion DWS MSDs may not necessarily be associated with individual droplets, but instead could be associated with larger effective scattering-probes[51,78], such as LDCs. This is particularly important when the average size of the colloids is near or smaller than the wavelength of light, as is the case for droplets in this emulsion system. We also show the high-frequency fit parameters $\tau(\phi)$ and $\eta_\infty(\phi)$ for the strongly attractive emulsion system in Figures 2.4(a) and 2.4(b), respectively. For $\phi > 0.62$, $\tau(\phi)$ for the attractive emulsion system at [SDS] = 80 mM exhibits a decrease which is almost identical to that of the nearly-hard system at 10 mM[57]. By contrast, for $\phi < 0.62$, $\tau(\phi)$ for the attractive emulsion system increases much less rapidly towards lower ϕ than for the nearly-hard emulsion system. This major difference in the behavior of $\tau(\phi)$ towards low ϕ, below the jamming point of hard spheres, is an additional prominent signal of strong attractions in the dense emulsion system. We find that $\eta_\infty(\phi)$ normalized by the viscosity of water can be fit using a relatively simple semi-empirical equation [see Figure 2.4(b) and its caption].

2.5.2 Optimized fits using the DCSN model

We use the following procedure to obtain optimal model parameters $\widetilde{\alpha}$ and $\phi_{\text{net,core}}$. In Figure 2.5, we show that varying α affects the point at which the best fit to calculated $\phi_{\text{shell}}(\phi)$ vanishes towards high ϕ. For values of α that are significantly less than 2, ϕ_{shell} becomes negative and unphysical for ϕ below $\phi_{\text{net,core}}$ in our measurement range; by contrast, if α becomes significantly greater than 2, then ϕ_{shell} only reaches zero for unphysical ϕ beyond unity. For each trial value of α that does not generate negative ϕ_{shell}, we fit the volume fraction in the shell region to the semi-empirical formula:

$$\phi_{\text{shell}}(\phi) = \frac{\beta_1(\phi_{\text{shell,z}} - \phi)^4}{1 + \exp[((\phi_{\text{shell,z}} - \phi) - \phi_{\text{h}})/\Delta\phi_{\text{h}}]}. \tag{2.8}$$

This procedure yields the point at which ϕ_{shell} vanishes as a function of trial α: $\phi_{\text{shell,z}}(\alpha)$. To determine optimal $\widetilde{\alpha}$, we fit $\phi_{\text{shell,z}} - 1$ to $\beta_2(\alpha - \widetilde{\alpha})$, where the parameters for $\phi_{\text{net,core}} = 0.78$

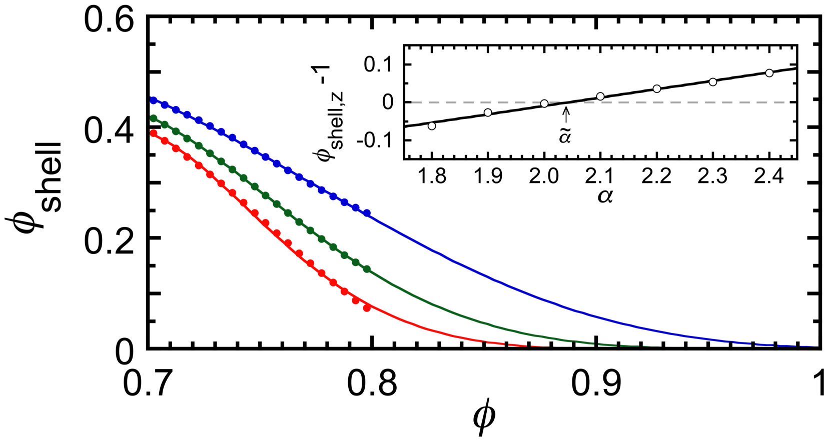

Figure 2.5. Complete conversion of shell to core droplets constrains the behavior of $\boldsymbol{\phi_{\text{shell}}}$ as $\boldsymbol{\phi \to 1}$, yielding optimal parameter $\boldsymbol{\widetilde{\alpha}}$ characterizing the effective scattering cluster probe size relative to the droplet size. Volume conservation of droplets yields ϕ_{shell} for different trial values of size parameter α [points: 1.8 (red); 2.0 (green); 2.4 (blue)]. Solid lines: semi-empirical fits of ϕ_{shell} versus ϕ for different α yield ϕ values where ϕ_{shell} vanishes with zero slope and curvature: $\phi_{\text{shell,z}}$ [equation (2.8)]; χ^2 is minimized for $\alpha \approx 2.0$. Inset: linear fit of $\phi_{\text{shell,z}} - 1$ versus α identifies optimal $\widetilde{\alpha} = 2.04 \pm 0.01$ at the zero-crossing ($\text{R}^2 = 0.987$).

are: $\beta_1 = 104 \pm 4$, $\phi_{\text{h}} = 0.301 \pm 0.003$, $\Delta\phi_{\text{h}} = 0.0536 \pm 0.0008$ ($\text{R}^2 = 0.999$); and $\beta_2 = 0.22 \pm 0.01$, $\widetilde{\alpha} = 2.04 \pm 0.01$ ($\text{R}^2 = 0.987$). If $\phi_{\text{net,core}}$ is varied in either direction away from 0.78, then χ^2 of the fit of $1/\ell^*(\phi)$ increases, indicating a non-optimal fit. The optimal $\widetilde{\alpha}$ is not highly sensitive to different $\phi_{\text{net,core}}$; $\widetilde{\alpha}$ varies over a relatively narrow range from $\approx$2.2 at $\phi_{\text{net,core}} = 0.77$ to $\approx$1.8 at $\phi_{\text{net,core}} = 0.80$. Thus, this optimized fitting procedure yields values of model parameters $\widetilde{\alpha} \approx 2.0$ and $\phi_{\text{net,core}} \approx 0.78$ that provide the minimized χ^2-fit to the measured $1/\ell^*(\phi)$ constrained by the measured trend in $1/\left\langle \Delta \boldsymbol{r}^2 \right\rangle_{\text{p}}(\phi)$ that sets the behavior of $\phi_{\text{core}}(\phi)$. We determine the optimal parameters $\phi_{\text{SDD,F}} = 0.339$, $\Delta\phi_{\text{SDD}} = 0.0904$, $1/\ell^*_{\text{SDD}} = 0.0198\ \mu\text{m}^{-1}$, $r_{\text{shell}} = 0.509$, and $r_{\text{core}} = 0.150$ ($\text{R}^2 = 0.992$). The separated contributions to $1/\ell^*(\phi)$ from SDDs, shell, and core are shown in Figure 2.6(a). This optimized fit also yields ϕ_{SDD}, ϕ_{shell}, and ϕ_{core} [Figure 2.6(b)]. The knees in the measured $1/\ell^*_{\text{attr}}(\phi)$ correspond to peaks in ϕ_{SDD} and then ϕ_{shell} as ϕ increases. The outcome of $\widetilde{\alpha} \approx 2.0$ over $0.5 \leq \phi \leq 0.77$, where scattering from shell droplets dominates, is particularly important

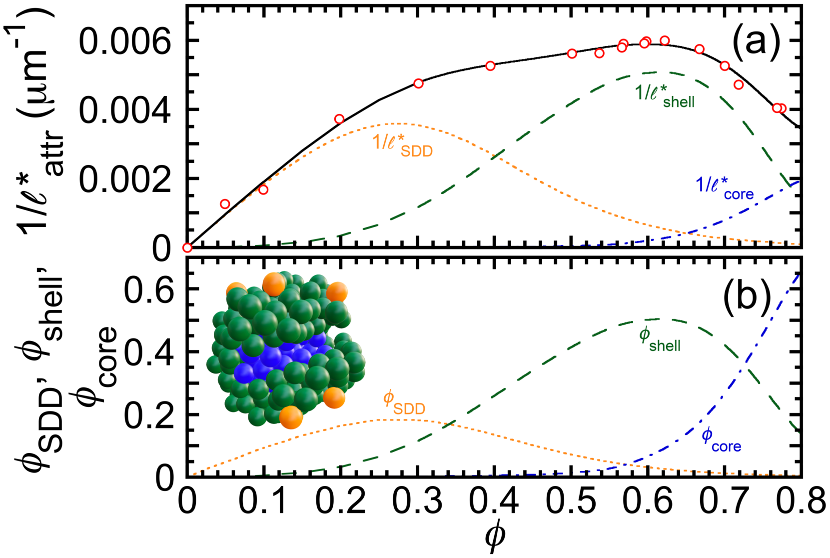

Figure 2.6. Fitting the measured $1/\ell^*_{\mathrm{attr}}(\phi)$ using a decorated core-shell network (DCSN) model. (**a**) Scattering contributions from surface decorating droplets (SDDs), $1/\ell^*_{\mathrm{SDD}}$ (orange dotted line); network shell droplets, $1/\ell^*_{\mathrm{shell}}$ (green dashed line); and network core droplets, $1/\ell^*_{\mathrm{core}}$ (blue dashed-dotted line), result from least-squares fitting the measured $1/\ell^*_{\mathrm{attr}}(\phi)$ (red open circles) and optimizing DCSN parameters [fit to equation (2.5): solid black line, subject to the constraints imposed by equations (2.1)-(2.4)]. (**b**) Optimized fitting results yield component droplet volume fractions: ϕ_{SDD}, ϕ_{shell}, and ϕ_{core} [line colors and types as in part (a)]. Inset: simplified schematic illustrating the DCSN model having core $\langle N \rangle \approx 10.6$ (blue spheres), shell $\langle N \rangle \approx 6.5$ (green spheres), and SDD $\langle N \rangle \approx 3$ (orange spheres), corresponding to $\phi \approx 0.65$. Shell droplets have been removed from a 20° region to display the core droplets.

from a microrheological perspective, since it implies that the scattering-probes corresponding to DWS MSDs are larger than the droplets themselves and correspond to tetrahedral LDCs of droplets on average. Moreover, $\phi_{\mathrm{net,core}} \approx 0.78$ effectively corresponds to the maximum osmotic compression experienced by the attractive system at $\phi_{\mathrm{m}} \approx 0.77$ of the master emulsion, which serves as the same starting point for preparing all attractive emulsions at lower ϕ (see chapter 2.3.1).

2.5.3 Mechanical shear rheometry

At a given ϕ, we fit the measured $G'(\gamma)$ [see Figure 2.7(a)] to obtain the linear $G'_{\mathrm{p,mech}}$, given by the low-γ-plateau:

$$G'(\gamma) = G'_{\mathrm{p,mech}} / \left[\left(\gamma/\gamma_{\mathrm{y}}^{*} \right)^{\kappa} + 1 \right] , \tag{2.9}$$

where γ_{y}^{*} is a yield strain associated with the knee in $G'(\gamma)$ and κ is a power law exponent associated with the non-linear response of $G'(\gamma)$ towards higher strains. At each ϕ, we also determine a yield strain, γ_{y}, defined slightly differently by a classic method involving the intersection of lines associated with linear low-strain behavior and power-law high strain behavior of the shear stress amplitude τ_{mech} as a function of the shear strain amplitude γ [Figure 2.7(b)]. Since yield strains in attractive systems at low ϕ can become very small, for strongly attractive emulsions at lower ϕ, accurate measurements of $G'_{\mathrm{p,mech}}$ become difficult using mechanical rheometry as a consequence of practical limitations imposed by the minimum strain that the motor can produce and the resolution of the torque-transducer. Strongly attractive emulsions may still be weakly elastic at lower ϕ than we can measure mechanically using this rheometer and geometry, given their very low yield strains and also sample volume limitations. So, we only report mechanical $G'_{\mathrm{p,mech}}$ where the plateau in $G'(\gamma)$ at low γ, corresponding to the linear elastic regime, can be accurately determined by fitting $G'(\gamma)$ using equation (2.9).

We apply two common yet different analyses on strain sweep measurements in Figure 2.7 to determine the yield strains of the attractive emulsion system as a function of ϕ [see Figure 2.8(a)]: γ_{y}^{*} by fitting $G'(\gamma)$ in Figure 2.7(a) using equation (2.9), and γ_{y} from intersecting lines through the measured stress-strain amplitude curves in the log-log plot in Figure 2.7(b). While both analyses yield similar trends with respect to ϕ, we find that γ_{y}^{*} is systematically about 1.4× larger than γ_{y} on average. For the attractive system, the yield strain increases dramatically about two orders of magnitude from $\sim 10^{-3}$ near $\phi \approx 0.5$ to about $\sim 10^{-1}$ for $\phi \gtrsim 0.7$. The non-linear high-strain power-law fitting parameter κ, associated with the decrease in $G'(\gamma)$-fit in Figure 2.7(a), increases from about 1 near $\phi \approx 0.5$ to about 1.7 near

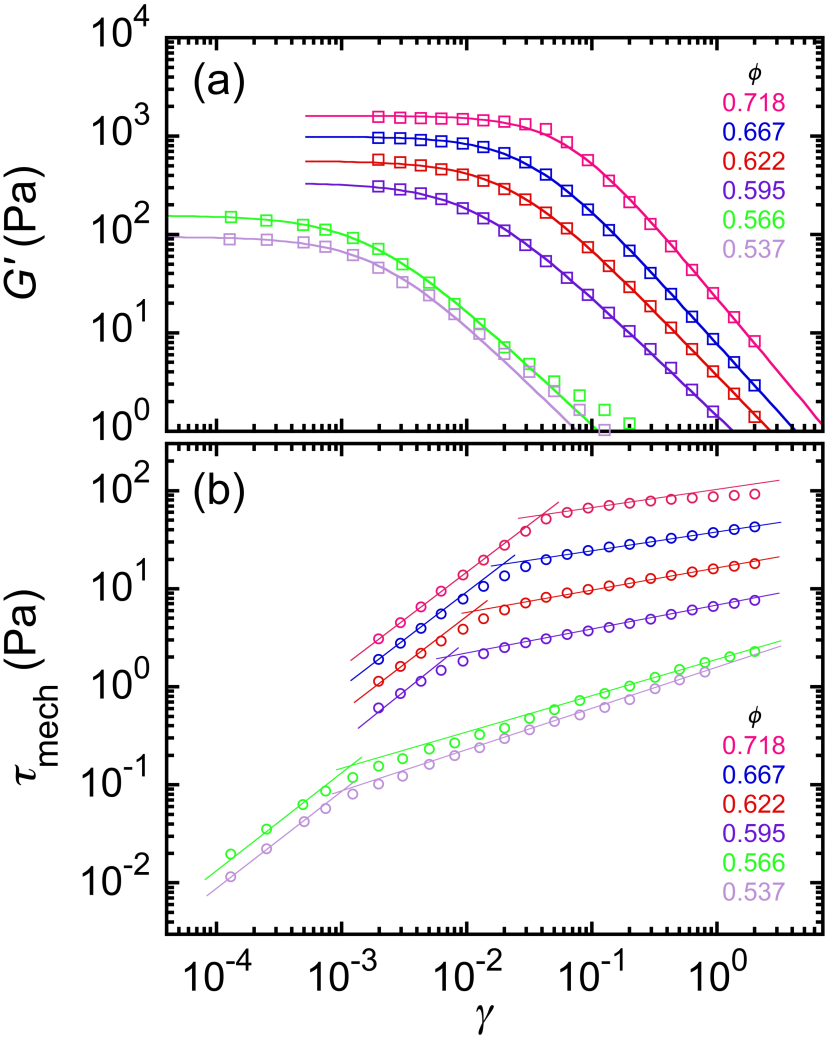

Figure 2.7. Mechanical shear oscillatory measurements of the storage modulus G' and the peak stress amplitude τ_{mech} as a function of the applied peak strain amplitude γ for strongly attractive dense emulsions at [SDS] = 80 mM and frequency $\omega = 1$ rad/s. (**a**) Data for $G'(\gamma)$ are fit using equation (2.9) yielding: the plateau shear modulus $G'_{\mathrm{p,mech}}$; position of the knee that defines yielding, γ_{y}^{*}; and high-strain power law parameter κ describing the decrease in the non-linear G' well beyond yielding. (**b**) Classical method of extracting yield strain γ_{y} from stress-strain amplitude measurements. At each ϕ, γ_{y} is determined by the intersection of power-law lines on a log-log plot of τ_{mech} versus γ. A line having slope one is extrapolated through the data at low γ until it intersects with a line of lower slope passing through the data at higher γ.

$\phi \approx 0.77$ [see Figure 2.8(b)]. For comparison, $\kappa \approx 2$ for a nearly-hard emulsion system at [SDS] = 10 mM for ϕ well above the droplet jamming point. The reported yield strains here

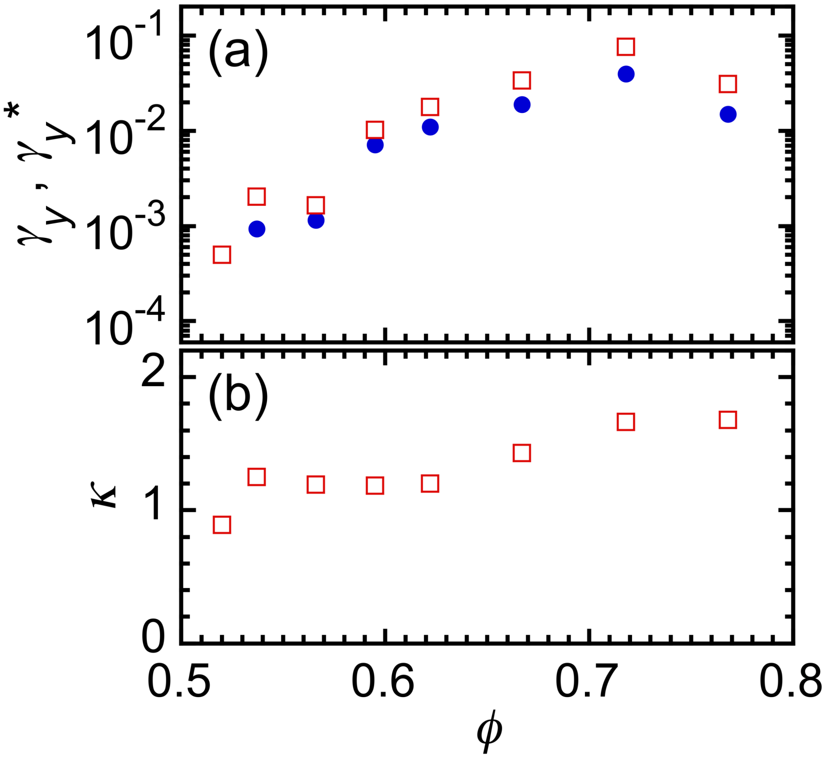

Figure 2.8. Dependence on droplet volume fraction ϕ of the yield strains γ_{y} and γ_{y}^* and of the non-linear high-strain power-law exponent κ for strongly attractive size-fractionated emulsions at [SDS] = 80 mM. (**a**) Red open squares: $\gamma_{\mathrm{y}}^*(\phi)$ obtained from fits in Figure 2.7(a); blue solid circles: $\gamma_{\mathrm{y}}(\phi)$ obtained from intersections of lines in Figure 2.7(b). (**b**) $\kappa(\phi)$ obtained from fits in Figure 2.7(a).

correspond to the large scale drop in $G'(\gamma)$ and onset of non-linear flow of the attractive emulsion, not to more subtle increases in the loss modulus $G''(\gamma)$ which can occur at even lower strains[46].

2.5.4 Comparison of DWS microrheology with mechanical macrorheology

Using the optimal $\widetilde{\alpha}$, we display $G'_{\mathrm{p,attr}}(\phi)$ from the modified GSER in Figure 2.9. For comparison, mechanical rheometry measurements of exactly the same attractive emulsions are shown for $\phi \geq 0.5$; accurate mechanical measurements of G'_{p} were precluded at lower ϕ by very small yield strains and limitations of the rheometer's torque transducer. The

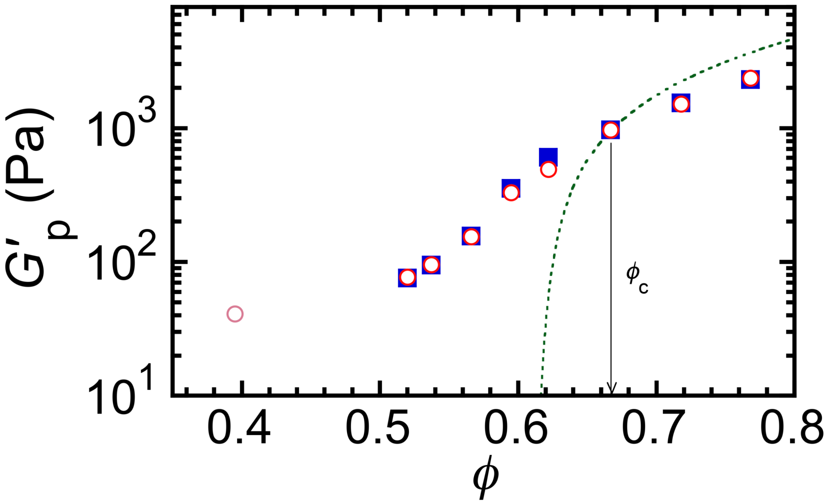

Figure 2.9. Comparison of mechanical measurements of plateau elastic shear moduli $G'_{\mathrm{p,mech}}(\phi)$ (blue solid squares) with DWS microrheological moduli, $G'_{\mathrm{p,attr}}(\phi)$ (red open circles), obtained using the DCSN model's $\widetilde{\alpha} \approx 2.0$ and plateau MSDs from Figure 2.3(b) for the strongly attractive emulsion. For reference: EEI model calculations of $G'_{\mathrm{p,EEI}}(\phi)$ for a non-attractive emulsion at an ionic strength of 80 mM (dotted line). Arrow: volume fraction where G'_{p} for non-attractive and attractive systems coincide: $\phi_{\mathrm{c}} = 0.668$ (see text).

comparison between the mechanical $G'_{\mathrm{p,mech}}$ and microrheological $G'_{\mathrm{p,attr}}$ yields a quantitative match, given uncertainties in both measurements, for the entire range of ϕ over which both measurements could be performed reliably. We also infer the corresponding shear creep compliance, $J(t)$ [see Figure 2.3(a), right axis].

2.5.5 Effect of strong attractive interactions on plateau elastic shear moduli

To contrast the plateau mechanical behavior of disordered, heterogeneous, strongly-attractive emulsion system with the corresponding disordered, homogeneous, nearly-hard emulsion system having the same size distribution, we determine the difference in their plateau elastic shear moduli as a function of ϕ. We calculate plateau elastic shear moduli for uniform ionic emulsions having nearly hard interactions using the entropic, electrostatic, interfacial (EEI) model, which has been shown to provide accurate values of G'_{p} over a wide range of ϕ^{37}. Parameters used in the EEI model are: interfacial tension σ = 9.8 mN/m, effective surface charge density $|\psi_0| = 270$ mV, and dimensionless EEI parameters $\alpha_{\mathrm{EEI}} = 0.85$ and $\xi_{\mathrm{EEI}} = 0.15$. The Debye screening length[1] used in the EEI model is $\lambda_{\mathrm{D}} = 1.1$ nm for [SDS] = 80 mM. In Figure 2.9, we compare $G'_{\mathrm{p,attr}}(\phi)$ with $G'_{\mathrm{p,EEI}}(\phi)$ as captured through the EEI model[37] of non-attractive emulsion shear elasticity at monovalent ionic strength of 80 mM. For lower ϕ, $G'_{\mathrm{p,attr}}$ is dominant, a crossover occurs at $\phi_{\mathrm{c}} = 0.668$, and for higher ϕ, $G'_{\mathrm{p,EEI}}$ is slightly larger. As a measure of the additional elasticity in the attractive emulsion system that is primarily a consequence of the depletion attraction at [SDS] = 80 mM, as compared to the elasticity of the same emulsion yet for a nearly hard interaction potential that includes only the screened-charge short-range repulsion at [SDS] = 10 mM, provided by the EEI model, we calculate $\Delta G'_{\mathrm{p}}(\phi)$ for $\phi < \phi_{\mathrm{c}}$, as shown in Figure 2.10(a). This can be described reasonably well by the semi-empirical function:

$$\frac{\Delta G'_{\mathrm{p}}(\phi)}{G'_{\mathrm{p,EEI}}(\phi_{\mathrm{c}})} = \frac{\epsilon_1(\phi_{\mathrm{c}} - \phi)}{1 + [(\phi_{\mathrm{c}} - \phi)/\epsilon_2]^4}, \tag{2.10}$$

where $\epsilon_1 = 14.6 \pm 0.9$, and $\epsilon_2 = 0.061 \pm 0.002$ ($\mathrm{R}^2 = 0.976$). The shape and magnitude of this trend provide a measure of how structural changes and spatial heterogeneity, a consequence of locally dense droplet regions and void regions arising from strong micellar depletion in the attractive emulsion, cause the attractive emulsion to remain rigid for ϕ well below that associated with maximal random jamming of hard spheres, even after accounting for Debye screened-charge repulsions. Any future fundamental theory that describes attractive emulsion systems could be compared with the magnitude and shape of this curve. For $\phi > \phi_{\mathrm{c}}$ in the range we measure, the values of $\Delta G'_{\mathrm{p}}$ are negative, implying that the strong attraction, which leads to void-defects, actually reduces the shear elasticity of the emulsion system somewhat at least for ϕ immediately above ϕ_{c}. We anticipate that G'_{p} of emulsion systems having strongly attractive and nearly hard interactions will ultimately converge towards the same values at very high ϕ in the biliquid foam limit, since there the void-regions disappear and interfacial deformation of the droplets will dominate the free energy of both systems similarly.

Beyond comparing $G'_{\mathrm{p,attr}}(\phi)$ with $G'_{\mathrm{p,EEI}}(\phi)$, we also compare $G'_{\mathrm{p}}(\tau)$ for strongly attrac-

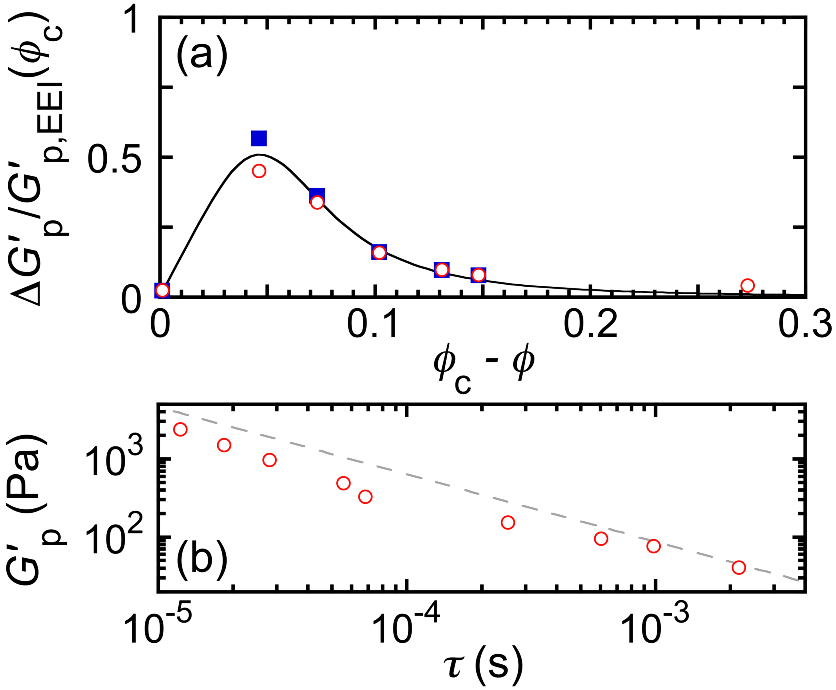

Figure 2.10. (a) **Difference between G'_p and calculated $G'_{p,EEI}$ at [SDS] = 80 mM, normalized by the crossover value, $\Delta G'_p/G'_{p,EEI}(\phi_c)$, versus $\phi_c - \phi$ for $\phi < \phi_c$.** Here $\phi_c = 0.668$ is the cross-over volume fraction where G'_p of the EEI model calculation equals the DWS and mechanical measurements of G'_p (see Figure 2.9). Line: fit using a two-parameter semi-empirical function [equation (2.10)] capturing excess normalized G'_p arising from the strong depletion attraction after accounting for Debye screened-charge repulsions at very short range. (b) **Plateau elastic storage modulus G'_p from DWS of the strongly attractive emulsion in Figure 2.9 versus τ in Figure 2.4(a).** Dashed line: power law $G'_p(\tau) \sim \tau^{-\chi}$, where $\chi = 0.86$, which describes the nearly-hard emulsion system accurately[57].

tive and nearly hard interactions, measured using the same emulsion size distribution, in Figure 2.10(b). For $\tau \geq 10^{-3}$ s, corresponding to lower ϕ, the strongly attractive emulsion system exhibits the same magnitude as the nearly hard system[57]. However, for $\tau < 10^{-3}$ s, corresponding to higher ϕ, $G'_p(\tau)$ of the strongly attractive emulsion system exhibits a small reduction in magnitude from the power law trend observed for the nearly hard emulsion system. However, for $\tau \leq 3 \times 10^{-4}$, the strongly attractive emulsion system appears to retain a similar scaling $G'_p(\tau) \sim \tau^{-\chi}$, where $\chi = 0.86$[57], although a slightly lower magnitude.

2.6 Discussion and conclusion

Our findings indicate that measuring an asymmetrically shaped $1/\ell^*(\phi)$ for disordered systems of uniform dielectric colloidal spheres is likely to be a useful indicator of the presence of strong attractions relative to thermal energy. This initial qualitative identification is important because it significantly influences how to perform passive microrheology quantitatively using DWS. The DCSN model provides a simplified way of representing and coupling optical and mechanical properties of the dense heterogeneous system of droplets that interact through strong slippery attractions. Only light scattering measurements, namely $\ell^*_{\mathrm{attr}}(\phi)$ and self-motion $\left\langle \Delta \boldsymbol{r}^2 \right\rangle_{\mathrm{p}}(\phi)$, are used in combination with the DCSN model to infer the optimal $\widetilde{\alpha}$ in a modified GSER which permits LDCs to serve as DWS scattering-probes. Our approach also handles collective scattering of probes in the attractive system by converting DWS apparent MSDs into self-motion scattering-probe MSDs, appropriate for microrheology, using the measured slope of $1/\ell^*_{\mathrm{attr}}(\phi)$ in the limit of low ϕ. Inherent in the DCSN model is the assumption of strong coupling (*i.e.* bonding) between the shell and the core; this is reasonable for the strong attraction used in our study but it could break down as the strength of the attraction is reduced. Considering other types of colloidal systems, if strong attractions between solid colloids are not slippery or if the colloids are highly non-spherical in shape, then the DCSN model may not directly apply. We anticipate that our approach, results, and interpretations for dense attractive colloidal emulsions will motivate other exciting future directions, both experimental and theoretical.

While the application of the DCSN model to light scattering data in this strong attraction limit provides quantitative microrheological agreement with mechanical data for attractive emulsions over a limited range of dense ϕ, the DCSN model may or may not work as successfully at even higher ϕ than we have probed. At very high ϕ, one would expect $1/\ell^*$ for both attractive and hard systems of droplets to approach zero, although in different ways; thus, we emphasize that the semi-empirical fitting equation describing normalized $\Delta(1/\ell^*)$ of the droplets would not necessarily be expected to remain valid for $\phi > 0.8$. At such very high ϕ, droplets would begin to deform significantly as the applied osmotic pressure begins to dominate the energy density associated with attractive interactions, and isolated void-regions in the disordered solid would act as vacancy-like defects which could dominant the scattering. The meaning of the scattering probes in DWS could change in this limit, such that using a single optimal $\widetilde{\alpha}$ value might not provide very good microrheological agreement at significantly higher ϕ than we have explored; instead it may become necessary to describe α as a function of ϕ. Thus, understanding how to interpret DWS correlation functions in the very high ϕ limit of strongly osmotically compressed attractive emulsions, where droplet deformation is much more significant, represents a different and ongoing challenge.

In future experiments, it would be interesting to explore the change in $1/\ell^*(\phi)$ and DWS MSDs associated with the crossover between the strong attractive limit and the weak attractive limit, where the secondary well depth begins to approach $k_\mathrm{B}T$, which has not been examined in this work. In such systems, temporal evolution over a wider range of ϕ can be important; so, we anticipate that both DWS as well as mechanical rheology, starting from comparable starting structural states after loading, would have to be performed rapidly at the same waiting times in order to make meaningful microrheological comparisons. Beyond this, real-space 3D confocal microscopy studies of larger fractionated monodisperse emulsions that have been density-matched, index-matched, and fluorescently-stained[85], which improved on a prior confocal structural approach[86], if combined with a suitable depletion agent and similarly prepared in the dense-ϕ limit, could potentially be used to identify and map out the primary types of heterogeneous regions, particularly the core and shell regions, that are inherent to the DCSN model. Moreover, If 3D confocal imaging methods, including those involving shear[87,88], could be made fast enough, average motion of both droplets and tetrahedra of droplets could be considered and then microrheological comparisons involving plateau MSDs of each could be made with mechanical measurements to more stringently test the DCSN model. Likewise, it would be useful for simulations to be extended in order to predict optical properties of materials of strongly attractive deformable colloids, including

$1/\ell^*(\phi)$ of droplets, over a comparably wide range of ϕ as we have measured. We know of no such prediction at present, particularly in the limit when the droplet radius is comparable to or less than then wavelength of visible light. More sophisticated simulations could potentially also treat the full distribution in N in heterogeneous attractive systems without having to resort to the simplified view of SDD, shell, and core droplets in the DCSN model. Such simulations could show more explicitly where the approximations and assumptions inherent in the DCSN model would work reasonably and also when these would break down. While the level of structural complexity in such strongly attractive dense systems of colloidal droplets poses a particularly different challenge from the standpoint of fundamental theory, advancing a theoretical meaning of what probes actually mean for DWS in such strongly attractive systems would be a worthwhile goal.

Chapter 3 - Complex optical transport, dynamics, and rheology of intermediately attractive emulsions

Reprinted by permission from Springer Nature: Springer *Scientific Reports* “Complex optical transport, dynamics, and rheology of intermediately attractive emulsions.” *Sci. Rep.* 13(1), 1791 by Xu, Y. and Mason, T. G. (2023).

3.1 Abstract

Introducing short-range attractions in Brownian systems of monodisperse colloidal spheres can substantially impact their structures and consequently their optical transport and rheological properties. Here, for size-fractionated colloidal emulsions, we show that imposing an intermediate strength of attraction, well above but not much larger than thermal energy ($\approx 5.6\ k_{\mathrm{B}}T$), through micellar depletion leads to a striking notch in the measured inverse mean free path of optical transport, $1/\ell^*$, as a function of droplet volume fraction, ϕ. This notch, which appears between the hard-sphere glass transition, ϕ_{g}, and maximal random jamming, ϕ_{MRJ}, implies the existence of a greater population of compact dense clusters of droplets, as compared to tenuous networks of droplets in strongly attractive emulsion gels. We extend a prior decorated core-shell network model for strongly attractive colloidal systems to include dense non-percolating clusters that do not contribute to shear rigidity. By constraining this extended model using the measured $1/\ell^*(\phi)$, we improve and expand the microrheological interpretation of diffusing wave spectroscopy (DWS) experiments made on attractive colloidal systems. Our measurements and modeling demonstrate richness and complexity in optical transport and shear rheological properties of dense, disordered colloidal

systems having short-range intermediate attractions between moderately attractive glasses and strongly attractive gels.

3.2 Introduction

Imposing short-range attractive interactions between colloids in a continuous liquid phase can dramatically alter a wide range of Brownian colloidal systems, both equilibrium and non-equilibrium, leading to different structural morphologies, dynamics, and physical properties[21, 28, 46, 60, 61, 89–91]. In particular, for higher colloidal volume fractions, ϕ, beyond the dilute limit and for attractive interactions that are much stronger than thermal energy, $k_\mathrm{B}T$, where k_B is Boltzmann's constant and T is the temperature, networks of colloids can form, yielding colloidal gels[39, 60, 75, 92, 93]. The shape, size distribution, and deformability of the colloids, the history of preparation and flow imposed on the system, and the type, range, and strength of the intercolloidal attractions are all factors that can affect the structure, dynamics, and properties of colloidal gels[62, 63]. For instance, short-range strongly attractive systems that are formed through slippery bonding[51, 58], arising from a deep secondary attractive well in the interaction potential, can have different distributions of local coordination numbers than solid-particulate systems that are formed through shear-rigid bonding[51, 58, 63], arising from an extremely deep primary attractive well[89, 94]. Strongly attractive colloidal gels represent one specific type of colloidal system having locally disordered structure, yet for which a characteristic length scale associated with an average mesh-size can emerge through the process of diffusion-limited cluster aggregation (DLCA)[90, 95]. By contrast, in the other limit of very weak colloidal attractions, approaching nearly hard (NH) interactions, disordered colloidal glasses can be formed through rapid osmotic compression to dense ϕ. Further osmotic compression of a colloidal glass to even higher ϕ can lead to a jammed colloidal glass.

Although colloidal gels and colloidal glasses are both disordered and can exhibit low-frequency plateau shear elasticity, they represent two different types of soft elastic systems that are distinguished primarily by the strength of colloidal attractions relative to $k_\mathrm{B}T$. We refer to dense colloidal systems that have interactions ranging from weakly attractive to hard and that lack a long-time relaxation as colloidal glasses, since classical concepts of the ergodic-nonergodic transition for hard spheres apply in this limit of vanishing attractive strength. For ϕ just above the glass transition volume fraction of hard monodisperse spheres, $\phi_\mathrm{g} \approx 0.56$ - 0.58[96–98], such hard-sphere glasses exhibit a zero-frequency elastic plateau shear storage modulus, G'_p, as a consequence of nonergodicity and very limited accessible translational microstates per colloid on average; yet, the magnitude of G'_p remains finite even as ϕ is increased somewhat above ϕ_g. For example, classic mode-coupling theory (MCT)[99,100] describes glassy dynamics in glass-forming liquids as well as in hard-interacting colloidal systems[101]; MCT predicts a divergence in the relaxation time of density fluctuations as ϕ is raised towards ϕ_g. However, for even larger ϕ, colloidal glasses of hard rigid spheres approach the maximal random jamming (MRJ) point[36], $\phi_\mathrm{MRJ} \approx 0.646$ (an insightful refinement of the earlier concept of random close packing[35]), where the zero-frequency G'_p effectively diverges when the ideally rigid colloids jam and touch. By contrast, colloidal gels, which consist of space-filling networks, can have substantial zero-frequency G'_p for ϕ well below ϕ_g. In both cases, if the colloidal objects are soft, rather than highly rigid solid spheres, this softness can modify the behavior, and G'_p does not diverge at ϕ_MRJ[37]. In addition, the strengths of short-range attractions and also stabilizing repulsions, which may be present at even shorter range than the attractions, can influence both the onset and ϕ-dependence of G'_p[10,30]. For low enough ϕ and intermediate attractive strengths, two-phase coexistence between a gas-like monomer phase and a liquid-like non-percolating cluster phase can occur[42,60,102]; yet, for ϕ well below ϕ_g, owing to the absence of shear-rigid percolating networks, the shear rheology of such gas-cluster systems is dominantly viscous, not elastic.

While prior simulations[67,73,85,103], theories[41,64], and experiments, such as dynamic light scattering (DLS)[40,71,72,74,104,105] and three-dimensional (3D) high-resolution confocal microscopy[85,86,106,107], have addressed various aspects of short-range attractive colloidal systems, interesting questions still remain. In particular, the connections between colloidal dynamics and structures to observable macroscopic properties, such as optical transport and rheological properties, have not been systematically explored experimentally and explained self-consistently for intermediate attractive strengths. This is particularly true regarding passive microrheological interpretations of complex dense colloidal systems having short-range slippery attractions. Recently, in a key advance, Kim *et al.*[57] has shown how to correct diffusing wave spectroscopy (DWS)[55, 56, 108, 109] measurements of mean square displacements (MSDs) for collective scattering that occurs in dense, nearly hard interacting, size-fractionated, colloidal emulsions at high ϕ using measurements of the inverse scattering mean free path, $1/\ell^*(\phi)$. This advance has yielded quantitative agreement between $G'_\mathrm{p}(\phi)$ measured using mechanical rheometry and $G'_\mathrm{p}(\phi)$ derived from DWS MSDs through the generalized Stokes-Einstein relation (GSER) of passive microrheology[11]. Using a modern form of DWS that is suitable for non-ergodic samples[82, 110–114] and that provides reproducible plateau MSDs and also performing collective scattering corrections, amounting to factors that can be well over 2 for dense ϕ, are both extremely important in order to measure accurate DWS MSDs in dense elastic colloidal systems, irrespective of interactions. Thus, performing and interpreting the DWS experiments properly are both necessary for ensuring quantitatively accurate passive microrheology using the GSER.

Going beyond nearly hard interactions, this improved DWS technique has also been applied to size-fractionated colloidal emulsions that are subjected to short-range micellar depletion attractions. Kim *et al.*[59] have explored the moderately attractive (MA) regime, where $|U_\mathrm{d}| \approx 2$ - $3\ k_\mathrm{B}T$; by contrast, Xu *et al.*[115] have investigated the strongly attractive (SA) regime, where $|U_\mathrm{d}| \gg k_\mathrm{B}T$ (*i.e.* specifically $|U_\mathrm{d}| \approx 15\ k_\mathrm{B}T$). For dense MA emulsions, the existence of excess MSDs at long times, related to heterogeneous larger-scale motion of a minor subset of droplets in the system, have been observed and identified; yet, quantitative passive microrheological agreement can still be obtained for $G'_\mathrm{p}(\phi)$ using plateau MSDs at intermediate times, which accurately reflect the average motion of droplets in shear-stress bearing regions when interpreted using the GSER. At least over the limited range of dense ϕ explored, the measured $1/\ell^*(\phi)$ of MA emulsions effectively equals that of emulsions having NH interactions[57]. By contrast, for dense SA emulsions, excess MSDs are effectively suppressed by the strong attractions, and the intermediate-time plateaus in MSDs extend to long times. However, the asymmetric shape of the $1/\ell^*(\phi)$ for SA emulsions substantially differs from the highly symmetric shape of the $1/\ell^*(\phi)$ associated with the same emulsion having NH interactions. Moreover, the meaning of the scattering probe associated with DWS MSDs requires a more sophisticated interpretation; rather than simply being a droplet, the DWS scattering probe in the strongly attractive limit has been identified to be effectively a local dense cluster (LDC) of droplets, which has an average size similar to a tetrahedral cluster. Therefore, the effective radius of the relevant DWS scattering probe, appropriate for use in the GSER, is increased by a ϕ-independent factor of ≈ 2. To arrive at this effective DWS probe-size and interpretation of an average DWS probe as approximately similar to tetrahedral cluster in this strongly slippery-attractive colloidal system, Xu *et al.* have introduced a decorated core-shell network (DCSN) model, which provides a self-consistent means of deducing the relative fractions of surface decorating droplets, shell droplets, and core-network droplets from the measured $1/\ell^*(\phi)$. However, a colloidal emulsion system in the intermediately attractive (IA) regime, which lies between the moderately and strongly attractive regimes, has not yet been systematically investigated using this improved DWS technique. If performed, a new study on IA emulsions could potentially give rise to additional quantitative insights beyond an earlier DWS study on attractive polymer-emulsion systems[48]. In particular, this new DWS study could provide a ϕ-dependent quantitative comparison of passive microrheological measurements, made optically, with macroscopic rheology measurements. Moreover, the results of this new DWS study could be compared directly to previously published studies of NH, MA, and SA emulsions.

Here, we show that passive DWS microrheology can be performed quantitatively on a dense IA emulsion system having a short-range, slippery interdroplet attraction ($\approx 5.6\ k_{\mathrm{B}}T$)

induced by micellar depletion, provided that the substantial complexities in the DWS correlation functions are identified and interpreted without oversimplification. Our measurements of optical transport properties, DWS correlation functions, and macroscopic mechanical properties of dense IA emulsions cover a much larger range of ϕ than prior studies in which the dense emulsion systems were formed through gravitational creaming of larger droplets and in which different experimental techniques were used[81,93]. Our measurements reveal a ϕ-dependent richness, both in optical transport properties and DWS MSDs, that has not been previously observed for either MA or SA emulsion systems. Most strikingly, the overall magnitude of $1/\ell^*(\phi)$ for $\phi \leq 0.65$ is reduced compared to SA emulsions, indicating a lower surface-to-volume ratio of attractive networks and constituent clusters, and a notch-like depression is also observed for $\phi_{\mathrm{g}} \leq \phi \leq \phi_{\mathrm{MRJ}}$. In addition to applying the essential MSD correction for collective light scattering in DWS[57], we extract the true self-motion MSDs of scattering probes in shear-supporting regions of the attractive emulsion at intermediate times and disregard long-time excess MSDs that are known to arise from a small sub-population of droplets having higher mobility[59]. Moreover, we hypothesize that the scattering probes associated with DWS MSDs are neither solely single droplets throughout the entire range of ϕ as in MA emulsions[59], nor solely LDCs of tetrahedra of droplets throughout the entire range of ϕ as in SA emulsions[115]. Instead, for IA emulsions, our measurements suggest that the effective average radius of the DWS probes is dominated by droplets below the cluster-jamming point at lower dense ϕ, varies continuously through a transition region between droplets and tetrahedral LDCs for ϕ in the notch, and then is dominated by LDCs at higher dense ϕ above the cluster-jamming limit near ϕ_{MRJ}. To quantify this transition of DWS probes and link it to our experimental measurements, we develop an extended decorated core-shell network (E-DCSN) model that couples the measured ϕ-dependent self-motion plateau MSDs to the measured $1/\ell^*(\phi)$, thereby enabling us to infer the effective average radius of the dominant scattering probes for different ϕ. We then deduce the microrheological G'_{p} from solely optical measurements via the GSER. With these advances in interpreting DWS, passive microrheology delivers accurate G'_p for this highly complex, intermediately attractive dense emulsion system, as evidenced by comparisons with macroscopic rheometry, noting that the zero-frequency shear rigidity of the system effectively vanishes at ϕ corresponding to the minimum in the notch of $1/\ell^*(\phi)$. In addition, we predict trends in the probability distributions of local coordination number over a wide range of ϕ for IA emulsions through a principal-component fit to $1/\ell^*(\phi)$ based on the E-DCSN model.

3.3 Methods

3.3.1 Attractive emulsion preparation, handling, and characterization

We prepare a uniform, size-fractionated emulsion having a short-range intermediately attractive depletion interaction ($|U_\mathrm{d}| \approx 5.6\ k_\mathrm{B}T$) using trimethylsiloxy terminated polydimethylsiloxane oil (PDMS, Gelest Inc.; kinetic viscosity: $\nu_\mathrm{o} = 350$ cSt; mass density: $\rho_\mathrm{o} = 0.97$ g cm^{-3}; average molecular weight: $\mathrm{MW}_\mathrm{o} = 13{,}650$ g mol^{-1}; refractive index: $n_\mathrm{o} = 1.4031$), sodium dodecyl sulfate (SDS, Fisher Scientific; electrophoresis grade 99% purity), and deionized water (Millipore Milli-Q Academic; resistivity: 18.2 MΩ cm). We follow the protocol of emulsification, homogenization, and size-fractionation developed by Kim *et al.*[57], but here fix [SDS] = 35 mM and thereby obtain a 4× size-fractionated, concentrated master emulsion. A small portion of this master emulsion is diluted in a 10 mM aqueous SDS solution to $\phi \approx 10^{-4}$ and then characterized using dynamic and static light scattering, yielding an average radius $\langle a \rangle = 484 \pm 12$ nm and polydispersity $\delta a / \langle a \rangle \simeq 0.15$, where δa is the standard deviation of the droplet radial size distribution. The emulsion in the present study of intermediate attractions (IA) at [SDS] = 35 mM has been purposefully made to be as close to the same as possible when compared to the emulsion used in recent prior DWS studies of nearly hard (NH)[57] at [SDS] = 10 mM, moderate attractions (MA)[59] at [SDS] = 20 mM, and strong attractions (SA)[115] at [SDS] = 80 mM. These NH, MA and SA emulsions have been made from PDMS having the same molecular weight as we used for the

IA emulsions; moreover, the NH, MA and SA emulsions all have the same average radius $\langle a \rangle = 459 \pm 15$ nm and polydispersity $\delta a / \langle a \rangle \simeq 0.18$. So, the measured characteristics of the size distributions are very close, confirming that the IA emulsion is nearly the same as the emulsion used in prior NH, MA, and SA studies. Based on results of a prior optical study[80], the refractive index of the continuous phase of the IA emulsion at [SDS] = 35 mM is calculated to be $n_\mathrm{c} = 1.3320$ at room temperature $T = 20.0$ °C.

Setting [SDS] = 35 mM in the continuous phase, well above SDS's critical micelle concentration of $C^* \approx 8.1$ mM, induces lubricated depletion attractions between droplets in the fractionated PDMS O/W emulsion, resulting in a secondary minimum in the pair interaction potential. By combining Asakura-Oosawa's theory for larger and smaller hard spheres with Vrij's linear micellar model[46], the magnitude of this potential minimum is calculated to be $|U_\mathrm{d}| \approx 5.6\ k_\mathrm{B}T$. In addition to providing micellar depletion attractive interactions, adsorbed dodecyl sulfate anion (DS^-) on the droplet surfaces, as well as DS^- and Na^+ in the continuous phase, also lead to a strong short-range Debye-screened-charge repulsion between droplets, which precludes their coalescence. The interdroplet attraction is lubricated and slippery as a result of the retention of an aqueous continuous phase layer between droplets; this is dissimilar to bonding between solid colloids that have been destabilized in a way that allows them to fuse together in a shear-rigid fashion as a result of exceedingly strong Van der Waals attractions. The Debye screening length at $T = 20.0$ °C is $\lambda_\mathrm{D} \approx 1.64$ nm at [SDS] = 35 mM in the IA emulsion, as compared to $\lambda_\mathrm{D} \approx 3.04$ nm at [SDS] = 10 mM for the NH emulsion and to $\lambda_\mathrm{D} \approx 1.08$ nm at [SDS] = 80 mM for the SA emulsion. These changes in Debye screening length influence the shape and location of the rapid rise in the stabilizing repulsion between droplets, at shorter range than that corresponding to the secondary minimum cause by depletion effects. So, changing [SDS] alters not just $|U_\mathrm{d}|$ but also λ_D, which plays an important role in repulsive droplet jamming at higher applied osmotic pressures.

We concentrate the emulsion by centrifugation using a swinging bucket rotor (Beckman L8-55 ultracentrifuge, SW-28 swinging bucket rotor, 10,000 rpm, 1.25 h) without inducing droplet coalescence. We then separate and combine the concentrated elastic plugs formed at the top of centrifuge tubes; next, we dilute these combined recovered plugs to $\phi \approx 0.1$ using 35 mM SDS solution. We repeat this process twice more to set the SDS concentration and acquire a large volume of concentrated stock emulsion that is elastic at high ϕ. To avoid any size separation that could be caused by centrifugation, this concentrated master emulsion is thoroughly mixed at sufficiently low strain rates to prevent droplet rupturing. To reduce water loss from the master sample, we store this master sample in a temperature-controlled chamber set at a temperature of 20.0 °C to minimize the possible evolution of ϕ due to evaporation-condensation of water vapor into the cap and walls of the container, as well as water vapor leakage when opening and re-sealing the container. The oil droplet volume fraction of this concentrated master emulsion is measured to be $\phi_{\mathrm{m}} = 0.793 \pm 0.003$, determined using a gravimetric evaporation method[80].

We make IA emulsions at lower ϕ by diluting this concentrated master emulsion with an aqueous 35 mM SDS solution using an analytical balance (Denver Instruments APX-200, 0.1 mg precision). We stir each diluted sample having $\phi < \phi_{\mathrm{m}}$ using a small spatula, imposing an estimated 50 s^{-1} average shear flow-rate, for 3 minutes in a 3 mL vial to ensure that the resulting emulsion is homogeneously dispersed before loading into an optical cuvette or the mechanical rheometer. After mixing, each diluted sample is split into two portions: 1.5 mL for optical transport and DWS measurements and 0.5 mL for mechanical rheometry. This guarantees that exactly the same sample with identical ϕ has been used for both DWS and mechanical rheometry measurements, which is necessary in order to make accurate microrheological comparisons.

3.3.2 Optical transport and diffusing wave spectroscopy measurements

Optical transport and DWS measurements are performed with a Rheolab 3 light scattering instrument (LS Instruments, Fribourg CH), equipped with backscattering option. Laser light (wavelength $\lambda = 685$ nm), transmitted from a rotating ground-glass diffuser, is subsequently collimated to illuminate the sample. At a given ϕ, each emulsion is loaded into a clean glass optical cuvette with a width of 10 mm and a thickness (*i.e.* pathlength) of $L = 5$ mm. This pathlength is large enough to ensure that the ℓ^* is always at least a factor of 4 smaller than L for all ϕ corresponding to the MSDs that we report. To avoid artifacts that could occur because of an inadequate sample volume, we ensure that the upper surface of the loaded emulsion is at least 15 mm high relative to the bottom surface of the cuvette.

The protocols that we have developed for loading emulsion samples into the cuvette and for setting the waiting time, which starts at the completion of sample loading and ends at the beginning of measurements, depend on how viscous or elastic each sample is and therefore on ϕ. For dilute viscous samples having $\phi \leq 0.3$, we only measure and report optical transport ℓ^*, not DWS MSDs, using the following protocol that has been designed to not be excessively influenced by gravitational compaction leading to phase separation, which is known for dilute attractive emulsions[81]. After dilution and mixing, we pour the sample into the cuvette over one wall, cap and seal the cuvette with Parafilm, and allow the sample to rest for 24 hours at 20.0 °C. Then, the cuvette is gently inverted for 5 times and finally righted. After placing the cuvette into the Rheolab 3, we wait 1,200 s before measuring ℓ^*. This waiting time of 1,200 s is significantly larger than the longest doubling time $\approx$1.7 s for the lowest $\phi = 0.052$, calculated on basis of colloidal diffusion of droplets in water. Therefore, local dense clusters of droplets have adequate time to form through S-DLCA[51,58] for all presented $0.052 \leq \phi \leq 0.30$. At each ϕ, the reported $1/\ell^*$ is averaged from 11 trials and the trial-to-trial standard deviation is less than 4%. No noticeable creaming, which would create a systematic trend in the measured ℓ^*, is observed as a function of trial number.

We measure both ℓ^* and DWS $g_2(t) - 1$ for all samples having $\phi \geq 0.401$ after loading the sample in the following manner to avoid introducing air bubbles into the cuvette. For 0.401 $\leq \phi \leq$ 0.541, the yield stress of the emulsion is still low enough that we can simply pour the emulsion into the cuvette over one wall. For $0.571 \leq \phi \leq 0.630$, we use a syringe with a stainless-steel needle (inner diameter I.D. = 0.84 mm) to load the samples. We begin by completely inserting the syringe tip into the bottom of the cuvette, then slowly withdrawing the syringe while injecting the emulsion and ensuring that the tip stays below the emulsion's surface. For $\phi \geq 0.64$, we transfer the emulsion with a small spatula into the cuvette as close as possible to its bottom; then, we use low speed ($<$ 1,500 rpm) centrifugation for a total duration less than 60 s to eliminate stray air bubbles in loaded cuvettes without generating gradients in ϕ. After loading, the capped optical cuvettes are sealed with Parafilm, and all of the emulsion samples are stored in a temperature-controlled chamber for 24 hours to equilibrate before measurements. The sample temperature in the Rheolab 3 is maintained at $T = 20.0 \pm 0.1$ °C for all measurements. For each $\phi \geq 0.401$, we measure ℓ^* followed by DWS $g_2(t) - 1$ in transmission geometry for 11 trials; and then we measure DWS $g_2(t) - 1$ in backscattering geometry for 11 trials. Each trial of $g_2(t) - 1$ measurements contains 300 s of multi-tau duration and 60 s of echo duration. The reported $1/\ell^*$ and $g_2(t) - 1$ at each ϕ are obtained by averaging. The standard deviations of $1/\ell^*$ for all ϕ explored over $\phi \geq 0.4$ and also the standard deviations of the long-time $g_2 - 1$ for all ϕ explored over $\phi \geq 0.61$ are less than 2% of the corresponding average values.

At each ϕ, using the measured $g_2(t) - 1$ and ℓ^*, we extract the apparent $\langle \Delta \boldsymbol{r}_{\mathrm{a}}^2(t) \rangle$ by solving the classic transcendental equation of DWS[57,82,83], and then each apparent MSD is converted into the probe self-motion $\langle \Delta \boldsymbol{r}^2(t) \rangle$ to correct for collective light scattering. The apparent MSD is multiplied by a dimensionless ratio, less than unity, given by the actual measured scattering strength at that ϕ, reflected by $1/\ell^*(\phi)$, divided by the Mie scattering strength that ignores collective scattering at low-ϕ: $[1/\ell^*(\phi)]/[(1/\ell^*_{\mathrm{ISA,Mie}})\phi]$, where $1/\ell^*_{\mathrm{ISA,Mie}} = 0.0207\ \mu\mathrm{m}^{-1}$ is the slope of the calculated $1/\ell^*$ versus ϕ in the dilute limit as $\phi \to 0$, based on independent scattering approximation. As a result, the overall magnitude of the apparent MSDs at different ϕ are reduced by various amounts to obtain the probe self-motion MSDs, as this dimensionless ratio is ϕ-dependent.

To ensure that the number of droplets per scattering volume is time-invariant within during our DWS measurements of concentrated IA emulsions at higher ϕ, we have also performed Rheolab 3 measurements after only a 10-minute waiting time, which serves as a reference for the reported results at a much longer 24-h waiting time. For all $\phi \geq 0.401$, changes in the DWS count rate are less than 3%, and changes in the measured $1/\ell^*$ are less than 4%. Moreover, no distinct layer of cream, which would scatter light more strongly at the top of the cuvette, has been observed visually after the 24-h waiting time. We report dynamic DWS MSD measurements only in the effectively time-invariant range of $\phi \geq 0.541$, over which aging and gravity-induced droplet compaction do not significantly influence our measurements and over which the measured DWS $g_2(t) - 1$ do not fully decay to baseline in the long-time limit. For $\phi \geq 0.64$, a slight decrease in the decay rate of long-time $g_2(t) - 1$ beyond $t \approx 2 \times 10^{-1}$ s is observed in measurements after the 24-h waiting time, which is an indication of very slow aging. This slow aging is not the subject of our study, and our microrheological comparisons are based on plateau MSDs that are at intermediate correlation times, not at long correlation times which show some evidence of slight aging through changes in relaxation. Thus, the primary plateau MSDs, used in the GSER of passive microrheology, occur at shorter times $t \lesssim 2 \times 10^{-2}$ s and are time-invariant over at least 24 h for all $\phi \geq 0.541$ that we report. Microrheological comparisons are facilitated by this effective time-invariance of the plateau feature in the MSD over 24-h long waiting time for the elastic dense emulsions. Our purpose in the present study is to make microrheological comparisons of elastic plateau moduli, not to study long-term aging.

3.3.3 Mechanical shear rheometry

We use a 25 mm diameter cone-and-plate geometry (stainless steel) in a controlled-strain mechanical shear rheometer (RFS-II, Rheometric Scientific, equipped with a vapor trap) to measure the plateau elastic shear moduli, $G'_{\mathrm{p,mech}}$, at low strains corresponding to the linear viscoelastic regime. After the same 24-h waiting time also used for DWS, we pre-shear the sample at $50\ \mathrm{s}^{-1}$ shear rate for 30 s by stirring with a spatula and load the sample into the rheometer. Measurements are commenced two minutes after lowering the cone to the appropriate pre-set gap with respect to the plate and adjusting the vapor trap. All measurements are performed at $T = 20$ °C. At each ϕ, we perform a small-strain oscillatory frequency sweep from $\omega = 20$ rad/s down to 0.02 rad/s at a small shear strain amplitude of $\gamma = 0.005$. The plateau storage modulus becomes noticeably frequency dependent for $\phi \leq 0.620$ at this $\gamma = 0.005$. We next conduct a strain sweep at each ϕ and $\omega = 1$ rad/s, yielding the linear and non-linear shear storage modulus, represented as $G'(\gamma)$. This frequency is within the range of time scales that correspond to the plateau associated with DWS MSD measurements. We probe down to shear strains as low as $\approx 1 \times 10^{-4}$, which is limited by the resolution of the RFS-II's motor. Under small strains, a dominant linear storage modulus can be detected down to $\phi = 0.610$. To obtain the small-strain $G'_{\mathrm{p,mech}}$ of the IA emulsion at each ϕ, we fit the measured $G'(\gamma)$ to a function that has a low-γ-plateau[115] (inset in Figure 3.6): $G'(\gamma) = G'_{\mathrm{p,mech}}/[(\gamma/\gamma_{\mathrm{y}})^{\kappa} + 1]$, where γ_{y} is the yield strain associated with the log slope change in $G'(\gamma)$, and κ is a power law exponent related to the non-linear response of $G'(\gamma)$ to larger strains. A two-step yielding strain-response, which has been reported previously in strain sweeps on a similar O/W emulsion system but which had a much stronger attractive strength ($|U_{\mathrm{d}}| \approx 21\ k_{\mathrm{B}}T$)[46], is not apparent in the measured strain sweeps of these IA emulsions.

3.3.4 Regularized fitting using the extended decorated core shell network model

In the prior DCSN model, developed for the SA emulsion, an effective probe-size factor $\alpha_{\mathrm{SA}} = 2.0$, corresponding to a local dense cluster that is approximately tetrahedral on average, has been introduced based on structural concepts for attractive gels of emulsion droplets. Consequently, for attractive colloidal systems, identifying the appropriate probe for interpreting a DWS correlation function as a MSD is complex. The prior study of SA emulsions showed that passive microrheology on these systems can be performed quantitatively via the GSER if the effective size of the DWS scattering probes is taken into account:

$G'_{\mathrm{p,GSER}} \propto 1/(\langle a_{\mathrm{pr}} \rangle \langle \Delta \boldsymbol{r}^2 \rangle_{\mathrm{p}}) = 1/(\alpha \langle a \rangle \langle \Delta \boldsymbol{r}^2 \rangle_{\mathrm{p}})$, where α is the dimensionless ratio between the effective average radius of the DWS scattering probes, $\langle a_{\mathrm{pr}} \rangle$, and the average hydrodynamic radius of an isolated droplet, $\langle a \rangle$. By contrast, the effective DWS probe-size is comparable to $\langle a \rangle$ in the MA system: $\alpha_{\mathrm{MA}} = 1.0$[59]. The IA system, studied herein, has an attractive potential depth that is in between the above-mentioned MA and SA regimes.

To set the magnitude of $\phi_{\mathrm{core,perc}}$ before introducing the fourth principal component of non-percolating droplets for the IA emulsion, we hypothesize an average droplet volume fraction $\phi_{\mathrm{net,core}} = 0.793$ within the percolating core regions, which is the maximum ϕ that we obtained experimentally with the emulsion having this droplet size distribution. We determine G'_{p} within the regions that only have percolating core droplets using the EEI model[37]: $G'_{\mathrm{p,EEI}}(\phi_{\mathrm{net,core}})$. The magnitude of $\phi_{\mathrm{core,perc}}(\phi)$ is determined based on the effective medium assumption: $\phi_{\mathrm{core,perc}}(\phi) = \phi_{\mathrm{net,core}}[G'_{\mathrm{p,GSER}}(\phi)/G'_{\mathrm{p,EEI}}(\phi_{\mathrm{net,core}})]$, where $G'_{\mathrm{p,GSER}}(\phi)$ is determined from the DWS plateau MSD measurements with the assumption of $\alpha = 2$ in the GSER: $G'_{\mathrm{p,GSER}}(\phi) = k_{\mathrm{B}}T/[\pi\alpha\langle a\rangle \langle \Delta \boldsymbol{r}^2(\phi) \rangle_{\mathrm{p}}]$.

Initially, we exclude non-percolating core droplets from consideration, and we minimize χ^2 of the nonlinear least-squares fit for $1/\ell^*_{\mathrm{IA}}(\phi)$ by varying the model's parameters [equation (3.1) with $\phi_{\mathrm{core,nonperc}}$ temporarily set to zero], in a manner similar to what has been previously done for the SA emulsion. This effectively ignores the notch initially but provides a comparable overall shape for the ϕ-dependent functional forms of SDD, shell, and percolating core components. Then, we take into account of $\phi_{\mathrm{core,nonperc}}$ by transferring weights from ϕ_{shell} at $\phi \leq 0.64$ and from ϕ_{SDD} within the lower end of notch region. This weight-transfer reflects the reorganization of outer droplets between different clusters as a consequence of the applied shear stress while diluting and mixing. We do so in a manner that preserves the smoothness of all four principal components, even as there are some rapid variations in the notch region itself as SDDs are converted to shell droplets, shell droplets into non-percolating core droplets, and shell and non-percolating core droplets into percolating core droplets. After iterations of minimizing χ^2 of the $1/\ell^*_{\mathrm{IA}}(\phi)$ fit over the entire ϕ range, having all key features considered, we obtain a regularized curve fit of $1/\ell^*_{\mathrm{IA}}(\phi)$ with smooth inter-conversions between all component droplet volume fractions.

3.3.5 Probability density functions of local coordination number

We assume that the distributions for all four principal components in the E-DSCN model are Gaussian; we have also assumed that the same standard deviation of $\sigma_N = 2.5$ is suitable for all of these distributions in order to provide total distributions that are smooth as a function of N for all ϕ considered. Enforcing this smoothness, thus, effectively amounts to a regularization assumption. The peaks of $p_{\mathrm{SDD}}(N)$, $p_{\mathrm{shell}}(N)$, $p_{\mathrm{core,nonperc}}(N)$, and $p_{\mathrm{core,perc}}(N)$ are located at $\langle N \rangle = 3$, 6, 9, and 12, respectively. We emphasize here that these plotted distributions have been inferred, not directly measured. Yet, these distributions show how increasing the osmotic pressure applied to an attractive emulsion can lead to very substantial changes in the local coordination number that are consistent with the measured trends in the optical transport properties of such emulsions over a wide range of ϕ.

Here, we note that $p_N(N \leq 2)$ has been folded to larger N, consistent with slippery diffusion-limited cluster aggregation in the dilute limit[58]. In our experimental system, $N = 2$ is theoretically possible, but highly unlikely. Droplets trapped in a mobile bridging configurations, for instance spanning between clusters, can have $N = 2$ in a very unusual situation when clusters are re-established following the cessation of loading and shear disruption. SDDs can also have $N = 2$ in a transient sense if a very strong Brownian excitation breaks one of the three bonds of the SDD and the droplet shifts into a new configuration with only two bonds still present. By contrast, $N \geq 3$ represents a relatively stable configuration that is only seldom destabilized by Brownian excitations in IA emulsions, resulting in transient droplet motion on the surface of a cluster rather than complete unbinding and liberation as an isolated droplet. Such transient bound droplet motion is one of the potential sources that could lead to excess DWS MSDs that become particularly noticeable toward lower ϕ.

3.4 Results and analysis

3.4.1 Diffusing wave spectroscopy

The measured ϕ-dependent inverse mean free path of optical transport, $1/\ell^*_{\mathrm{IA}}$, for the intermediately attractive emulsions (Figure 3.1, red diamonds) is asymmetric and has two knees, similar to $1/\ell^*_{\mathrm{SA}}$ for the strongly attractive emulsions (Figure 3.1, blue circles). Strikingly, $1/\ell^*_{\mathrm{IA}}(\phi)$ also exhibits a notch-like dip (Figure 3.1, bracket and arrow, $0.58 \leq \phi \leq 0.64$). By contrast, $1/\ell^*_{\mathrm{NH}}(\phi)$, measured for a very similar emulsion having nearly hard interactions at considerably lower [SDS] (Figure 3.1, gray squares), has a much simpler inverted parabolic

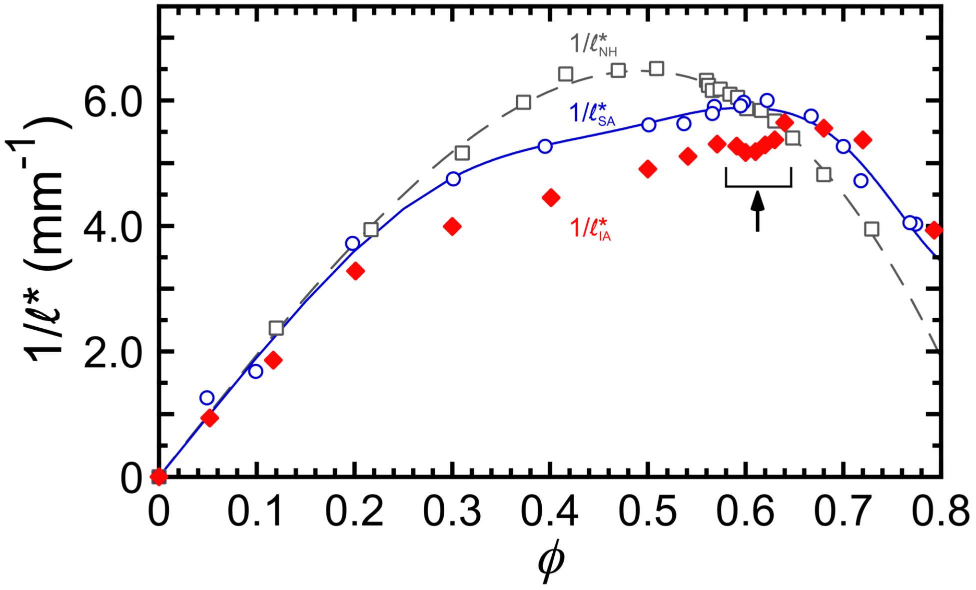

Figure 3.1. Measured inverse mean free path of optical transport, $1/\ell^*$, of fractionated silicone oil-in-water (O/W) emulsions as a function of droplet volume fraction, ϕ, for three different strengths of micellar depletion attraction (path-length L = 5.0 mm, light wavelength λ = 685 nm). Intermediately attractive (this study, [SDS] = 35 mM, $|U_{\mathrm{d}}| \approx 6\ k_{\mathrm{B}}T$, average droplet radius $\langle a\rangle$ = 484 nm): $1/\ell^*_{\mathrm{IA}}$ (red solid diamonds). Nearly hard interactions (Kim *et al.*[57], [SDS] = 10 mM, $|U_{\mathrm{d}}| < k_{\mathrm{B}}T$, similar $\langle a\rangle$ = 459 nm): $1/\ell^*_{\mathrm{NH}}$ (gray open squares); fit (gray dashed line) using equation (6) in Xu *et al.*[115]. Strongly attractive (Xu *et al.*[115], [SDS] = 80 mM, $|U_{\mathrm{d}}| \approx 15\ k_{\mathrm{B}}T$, $\langle a\rangle$ = 459 nm): $1/\ell^*_{\mathrm{SA}}$ (blue open circles); fit (blue solid line) from Xu *et al.*[115] using equation (2.5) with constraints imposed by equations (2.1)-(2.4).

shape that peaks at $\phi \approx 0.50$. For the IA emulsion, in the low ϕ regime, $0 < \phi \lesssim 0.20$, the magnitude and slope of $1/\ell^*_{\text{IA}}(\phi)$ are close to both $1/\ell^*_{\text{NH}}(\phi)$ and $1/\ell^*_{\text{SA}}(\phi)$. At larger ϕ, a first knee in $1/\ell^*_{\text{IA}}(\phi)$ is observed at $\phi \approx 0.2$, a slightly lower ϕ-value than the first knee in $1/\ell^*_{\text{SA}}(\phi)$. Above this first knee, $1/\ell^*_{\text{IA}}(\phi)$ grows approximately linearly but with a lower slope than in the dilute ϕ-regime; moreover, $1/\ell^*_{\text{IA}}$ has a smaller magnitude than both $1/\ell^*_{\text{NH}}$ and $1/\ell^*_{\text{SA}}$, indicating that dense microscale emulsions with intermediate attractions over $0.2 \lesssim \phi \lesssim 0.64$ scatter less than emulsions having nearly-hard interactions and also strong attractions. At the upper end of this ϕ-range, a dip-like notch is observed, and this notch region ends just before the second knee where the slope in $1/\ell^*_{\text{IA}}(\phi)$ becomes negative towards the highest ϕ shown. Within the notch, a local minimum is observed at $\phi \approx 0.60$. In the high-ϕ regime above the second knee, the magnitude of $1/\ell^*_{\text{IA}}$ and $1/\ell^*_{\text{SA}}$ are about the same, within experimental uncertainties in ϕ, and both are greater than $1/\ell^*_{\text{NH}}$. This implies that IA and SA emulsions scatter more in the strongly compressed high-ϕ limit than similar emulsions having NH interactions.

The optical transport results for the IA emulsion used in this present study can be directly compared with prior studies of nearly identical emulsions at other [SDS][57, 59, 115] because we have prepared a fractionated IA emulsion using the same materials and methods. The average hydrodynamic radius of the IA emulsion, $\langle a \rangle = 484$ nm, is within 5% of $\langle a \rangle = 459$ nm in the prior studies. Moreover, considering the Mie-scattering from an ideal isolated sphere, $1/\ell^*_{\text{ISA,Mie}}$, given by independent scattering approximation (ISA) in the highly dilute limit, the difference between the IA emulsion and the prior studies is less than 0.5%. Therefore, the substantial differences in $1/\ell^*(\phi)$, found between the present and prior studies as shown in Figure 3.1, arise from different droplet structures caused by the different attractive strengths $|U_{\text{d}}|$, not from the very small difference in $\langle a \rangle$.

Each of the measured DWS intensity autocorrelation functions, $g_2(t) - 1$, exhibits a primary decay at $t \approx 10^{-5}$ s, a primary plateau, and then a secondary decay at 10^{-1} s, considering both transmission and backscattering geometries, for the IA emulsion over a wide range of dense ϕ (Figure 3.2). From prior DWS experiments by Kim *et al.*[59] on dense MA emulsions at somewhat lower [SDS] = 20 mM, it has been hypothesized that secondary decays in DWS correlation functions can be attributed to a minor sub-population of droplets which are only marginally bound; this secondary decay gives rise to excess DWS MSDs at long times. While the details of the secondary decays are different for IA than MA emulsions, secondary decays observed in the present IA study also indicate the existence of excess MSDs. As with the MA emulsion, here for the IA emulsion, we seek to obtain primary plateau MSD values that can be gleaned from the measured DWS $g_2(t) - 1$ at intermediate times prior to the secondary

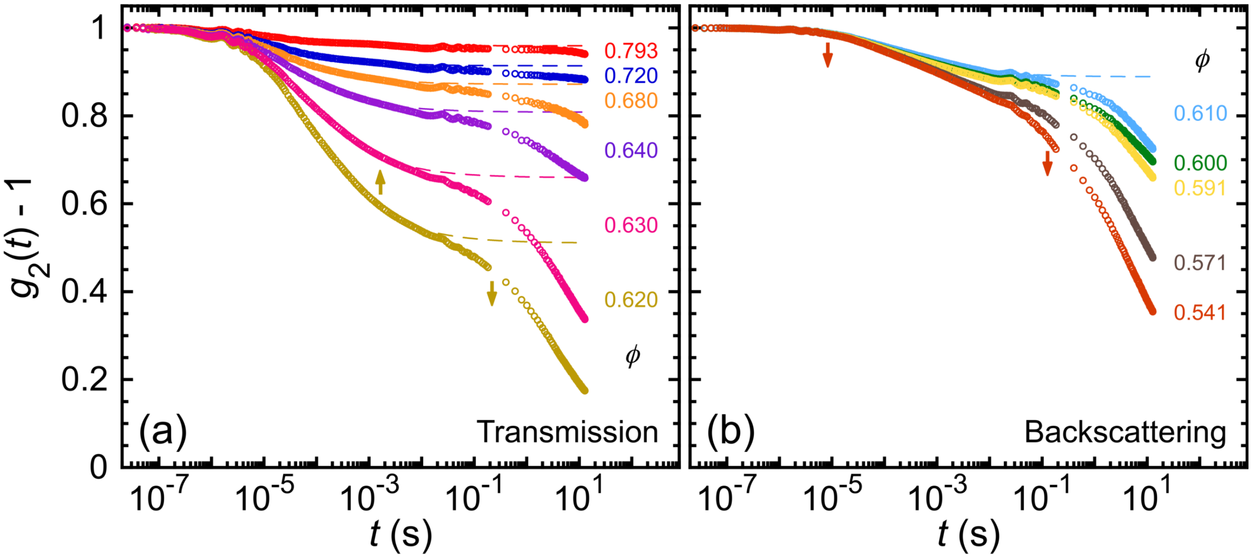

Figure 3.2. Measured time-dependent DWS intensity autocorrelation functions, $g_2(t) - 1$, of intermediately attractive O/W emulsions for dense droplet volume fractions ϕ (color-coded, see right), measured in (a) transmission and (b) backscattering geometries, respectively (pathlength $L = 5$ mm, light wavelength $\lambda = 685$ nm). DWS multi-tau correlation data extend from early times up to about 2×10^{-1} s; DWS echo data are shown at longer times. Arrows indicate the sign of concavity in the linear-log plot (up = +, down = -): [part (a)] for $\phi = 0.620$, $g_2(t) - 1$ is concave up at earlier times, then concave down at longer times; [part (b)] by contrast, at lower $\phi = 0.541$, no concave up region is observed (both arrows are down). Dashed lines correspond to the calculated primary decay-to-plateau $g_2(t) - 1$ using the fitting parameters obtained from the fits in Figure 3.3(a). Minor damped oscillatory noise signals, resulting from minute mechanical vibrations, are superimposed on the main $g_2(t) - 1$ signals, and visible for all ϕ at 3×10^{-7} s $\lesssim t \lesssim 10^{-5}$ s and 5×10^{-3} s $\lesssim t \lesssim 2 \times 10^{-1}$ s.

decays. We determine a plateau in the measured $g_2(t)-1$ by locating the transition between concave up and concave down features as shown in the linear-log format. This transition occurs at $t \approx 2 \times 10^{-2}$ s, as can be seen most easily at $\phi = 0.62$ in transmission [Figure 3.2(a)]. The secondary decay in $g_2(t)-1$ at longer time $t \gtrsim 2 \times 10^{-2}$ s can be attributed to the excess MSDs, which are not indicative of the average probe motion for microrheological purposes[59]. For $\phi \leq 0.60$, we cannot discern a transition from concave up to concave down; so, we refrain from identifying a plateau DWS MSD.

To obtain the primary plateau MSDs, $\langle \Delta \boldsymbol{r}^2 \rangle_\mathrm{p}$, for later use in the GSER of passive microrheology, we have extracted the probe MSDs $\langle \Delta \boldsymbol{r}^2(t) \rangle$ from measured $g_2(t)-1$; these MSDs are corrected for collective scattering using $1/\ell^*_\mathrm{IA}$ and the independent scattering approximation[57]. Each of the probe MSDs exhibits an early-time rise up to $t \approx 3 \times 10^{-5}$ s, a gradual bending to primary plateau, and then a secondary rise beyond $t \approx 2 \times 10^{-2}$ s [Figure 3.3(a)]. The primary plateau MSD values are obtained by utilizing the dense-emulsion MSD model[57] to fit the early-time rise-to-plateau of $\langle \Delta \boldsymbol{r}^2(t) \rangle$ for $\phi \geq 0.61$, while compensating slightly for the periodic vibrational noise (*i.e.* damped oscillatory signal superimposed on what would otherwise be a smooth MSD) that is mostly pronounced at 10^{-2} s $\leq t \leq 10^{-1}$ s. The early-time MSD fitting curves are displayed as solid lines in Figure 3.3(a), and the corresponding calculated primary decay-to-plateau $g_2(t)-1$ are represented by dashed lines in Figure 3.2.

We present the inverse primary-plateau probe MSDs , $1/\langle \Delta \boldsymbol{r}^2 \rangle_\mathrm{p}$, which are proportional to the shear elastic plateau moduli in the GSER, as a function of ϕ for the NH[57], IA, and SA[115] emulsion systems in Figure 3.3(b). All of these emulsion systems have very similar droplet radii and polydispersities; only the interactions between droplets are different. After correcting for collective scattering, $1/\langle \Delta \boldsymbol{r}^2 \rangle_\mathrm{p}$ of all the NH, IA, and SA systems, within the experimental uncertainties, are the same at higher $\phi \gtrsim 0.64$ [Figure 3.3(b)]. Interestingly, as ϕ decreasing from 0.64, the $1/\langle \Delta \boldsymbol{r}^2 \rangle_\mathrm{p}$ versus ϕ of these systems behave very differently. For the NH system, $1/\langle \Delta \boldsymbol{r}^2(\phi) \rangle_\mathrm{p,NH}$ follows the prediction of the entropic, electrostatic, and

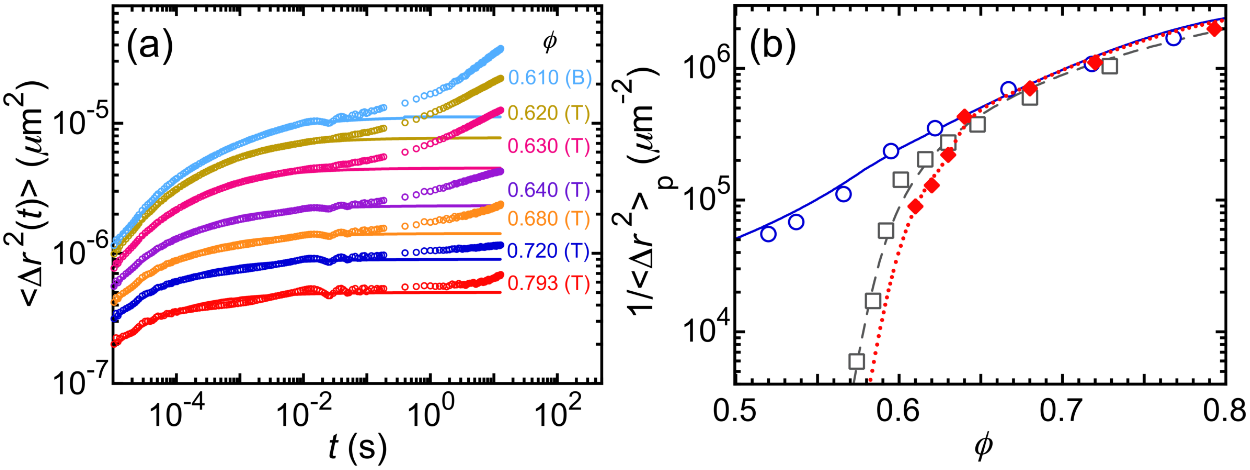

Figure 3.3. Time-dependent DWS mean square displacements (MSDs), $\langle\Delta \boldsymbol{r}^2(t)\rangle$, and inverse primary plateau MSDs, $1/\langle\Delta \boldsymbol{r}^2\rangle_{\mathrm{p}}$, as a function of $\boldsymbol{\phi}$. (**a**) Ensemble-averaged $\langle\Delta \boldsymbol{r}^2(t)\rangle$ for a series of different ϕ, extracted from $g_2(t)-1$ in Figure 3.2 and corrected for collective scattering using $1/\ell^*_{\mathrm{IA}}$ in Figure 3.1. Rises in the MSDs at long times are attributed to excess MSDs[59], which do not reflect average probe dynamics. DWS MSDs at early-to-intermediate times are fit to an emulsion model, developed for nearly hard droplet interactions by Kim *et al.*[57]. Fits (solid lines) provide plateau self-motion probe MSDs, $\langle\Delta \boldsymbol{r}^2\rangle_{\mathrm{p}}$. (T) and (B) indicate transmission and backscattering geometries, respectively. (**b**) $1/\langle\Delta \boldsymbol{r}^2(\phi)\rangle_{\mathrm{p}}$ for emulsion systems having different types of interactions between droplets. Intermediate attractions (this study): $1/\langle\Delta \boldsymbol{r}^2\rangle_{\mathrm{p,IA}}$ (red diamonds), obtained from long-time plateau values of the fits in part (a). Dotted line: prediction curve with a smooth transition between an analytical interpolation of measured $1/\langle\Delta \boldsymbol{r}^2\rangle_{\mathrm{p,IA}}$ for $\phi \geq 0.61$, and the rescaled calculation using the EEI model[37] and GSER for $\phi < 0.61$. Nearly hard interactions (Kim *et al.*[57]): $1/\langle\Delta \boldsymbol{r}^2\rangle_{\mathrm{p,NH}}$ (gray squares, dashed line: fit using the EEI model and GSER). Strong attractions (Xu *et al.*[115]): $1/\langle\Delta \boldsymbol{r}^2\rangle_{\mathrm{p,SA}}$ (blue circles, solid line: analytical interpolation).

interfacial (EEI) model[37] with a knee on the log-linear plot located near $\phi \approx 0.60$. Strikingly, $1/\langle\Delta \boldsymbol{r}^2(\phi)\rangle_{\mathrm{p,SA}}$ is substantially larger than inverse plateau MSDs of both the NH and IA systems over $0.52 \leq \phi \lesssim 0.64$, indicating highly restricted droplet motion in the SA system's gel network of droplets even for ϕ well below ϕ_{MRJ}. By contrast, $1/\langle\Delta \boldsymbol{r}^2(\phi)\rangle_{\mathrm{p,IA}}$ is somewhat smaller than $1/\langle\Delta \boldsymbol{r}^2(\phi)\rangle_{\mathrm{p,NH}}$ when $\phi \lesssim \phi_{\mathrm{MRJ}}$, and it exhibits a rapid drop just below ϕ_{MRJ} as ϕ decreasing to 0.61. For $\phi < 0.61$, the signal from excess MSDs is so strong that it interferes with our protocol to obtain primary plateau MSD values. Comparing to the NH system, the higher [SDS] in the IA system not only induces an intermediate strength of depletion attraction, but also leads to a smaller screening length that shifts the effective jamming point up in ϕ, resulting in a smaller $1/\langle\Delta\boldsymbol{r}^2(\phi)\rangle_{\mathrm{p}}$. The concave-up appearance of $1/\langle\Delta\boldsymbol{r}^2(\phi)\rangle_{\mathrm{p,IA}}$ in log-linear format is similar to the shape of the upper end of the notch in $1/\ell^*_{\mathrm{IA}}(\phi)$ over the same ϕ-range.

3.4.2 Model

We hypothesize that an extended decorated core-shell network (E-DCSN) model, which takes into account scattering contributions from droplets having different local coordination numbers, N[58], in different local regions, can describe the complicated shape of $1/\ell^*_{\mathrm{IA}}(\phi)$ for the disordered IA emulsion. Its predecessor, the DCSN model, had been introduced to describe and interpret the less complex shape of $1/\ell^*_{\mathrm{SA}}(\phi)$ of SA emulsions using only three principal components[115]. The lower attractive strength of $|U_{\mathrm{d}}| \approx 5.6\ k_{\mathrm{B}}T$ in the IA emulsion, as compared to $\approx 15\ k_{\mathrm{B}}T$ in the SA emulsion, leads to a greater population of compact dense clusters and less tenuous gel structures in the IA emulsion. Moreover, the notch-like feature in $1/\ell^*_{\mathrm{IA}}(\phi)$ cannot be captured using only three principal components. While retaining the three principal components of the DCSN model, the E-DCSN model introduces a fourth principal component (*i.e.* non-percolating core clusters having high $\langle N\rangle$), which enables the notch-like dip in $1/\ell^*_{\mathrm{IA}}(\phi)$ to be captured. By interpreting the principal components of the E-DCSN model, we are able to obtain further insight into the dynamical optical fluctuations and passive microrheological interpretation of the IA emulsion.

The four principal components in the E-DCSN model are: percolating core droplets, non-percolating core droplets, shell droplets, and surface decorating droplets (SDDs). We assume that only the percolating core droplets, which have high $\langle N\rangle \approx 12$, form a gel-like network, which can support macroscopic shear stresses elastically. In addition, there are non-percolating core droplets in the form of dense clusters, which have somewhat lower $\langle N\rangle \approx 9$ and do not participate in supporting macroscopic shear stresses elastically. Both types of core regions are typically surrounded by shell droplets, which have significantly smaller $\langle N \rangle \approx 6$. In turn, the shell regions are decorated with SDDs, which have $\langle N \rangle \approx 3$.

The scattering of the IA emulsion can be tied to the E-DSCN model through the relative scattering contributions of the four different principal components, each of which vary with ϕ. Droplets having lower $\langle N \rangle$ effectively scatter more than droplets having higher $\langle N \rangle$ because less crowding leads to a larger scattering cross section. We parameterize the principal components using component droplet volume fractions of the different species: ϕ_{SDD} for SDDs, ϕ_{shell} for shell droplets, $\phi_{\mathrm{core,nonperc}}$ for non-percolating core droplets, and $\phi_{\mathrm{core,perc}}$ for percolating core droplets. As ϕ is varied, each of these principal component droplet volume fractions can change, reflecting structural changes in the IA emulsion from the dilute regime to the concentrated regime. To ensure droplet volume conservation, the total droplet volume fraction is the sum of the four ϕ-dependent component droplet volume fractions: $\phi = \phi_{\mathrm{SDD}}(\phi) + \phi_{\mathrm{shell}}(\phi) + \phi_{\mathrm{core,nonperc}}(\phi) + \phi_{\mathrm{core,perc}}(\phi)$. At a given ϕ, we assume that scattering contributions from each of the four principal components are linear in their respective volume fractions in $1/\ell^*_{\mathrm{IA}}(\phi)$:

$$\begin{aligned} 1/\ell^*_{\mathrm{IA}} &= 1/\ell^*_{\mathrm{SDD}} + 1/\ell^*_{\mathrm{shell}} + 1/\ell^*_{\mathrm{core,nonperc}} + 1/\ell^*_{\mathrm{core,perc}} \\ &= (1/\ell^*_{\mathrm{SDD},0})(\phi_{\mathrm{SDD}} + r_{\mathrm{shell}}\phi_{\mathrm{shell}} + r_{\mathrm{core,nonperc}}\phi_{\mathrm{core,nonperc}} + r_{\mathrm{core,perc}}\phi_{\mathrm{core,perc}}), \end{aligned} \tag{3.1}$$

where $1/\ell^*_{\mathrm{SDD},0}$ is the slope of linear growth in scattering at dilute ϕ where SDDs dominate; r_{shell}, $r_{\mathrm{core,nonperc}}$ and $r_{\mathrm{core,perc}}$ are the dimensionless relative scattering intensity from a shell droplet, from a non-percolating core droplet, and from a percolating core droplet, respectively, compared to a SDD.

Ignoring the notch-like dip, the overall shape of $1/\ell^*_{\mathrm{IA}}(\phi)$ is determined initially without introducing the non-percolating core droplets in a manner similar to the DCSN model[115]. We assume a linear rise in ϕ_{SDD} as ϕ increasing from 0 to $\approx$0.2, followed by an exponential decrease toward $\phi \approx 0.6$. The initial rise in $\phi_{\mathrm{SDD}}(\phi)$ originates from the formation of small clusters through slippery diffusion-limited cluster aggregation[51, 58], whereas the later decrease in $\phi_{\mathrm{SDD}}(\phi)$ is attributed to the conversion of SDDs primarily to shell droplets. These features can be described using the formula: $\phi_{\mathrm{SDD}}(\phi) = \phi/\{1 + \exp[(\phi - \phi_{\mathrm{SDD,F}})/\Delta\phi_{\mathrm{SDD}}]\}$.

As for $\phi_{\mathrm{core}}(\phi)$ in the DCSN model of SA emulsions, here for IA emulsions, we deduce $\phi_{\mathrm{core,perc}}(\phi)$ from an interpolation of the measured DWS inverse plateau MSDs, $1/\langle\Delta\boldsymbol{r}^2(\phi)\rangle_{\mathrm{p}}$ [see the red dotted line in Figure 3.3(b)]. Again, based on the effective medium assumption inherent in the DCSN model, we assume that $\phi_{\mathrm{core,perc}}$ is proportional to $1/\langle\Delta\boldsymbol{r}^2\rangle_{\mathrm{p}}$ at a given ϕ, and we set the effective probe radius to be $2\langle a\rangle$ in the compressed regime at highest ϕ beyond the notch, where this is known to be the case when the DCSN model is applied to SA emulsions. Volume conservation of droplets, here continuing to exclude consideration of non-percolating core droplets, implies that $\phi_{\mathrm{shell}}(\phi)$ can be determined from $\phi_{\mathrm{shell}}(\phi) = \phi - [\phi_{\mathrm{SDD}}(\phi) + \phi_{\mathrm{core,perc}}(\phi)]$.

Having determined reasonable initial starting points for three of the four principal components, which broadly describe the overall shape of $1/\ell^*_{\mathrm{IA}}(\phi)$ without accounting for the notch, we then turn to the more complex aspect of modeling the notch of the IA emulsion. In particular, the existence of the notch can be interpreted as a consequence of a non-negligible population of non-percolating core droplets that lack adequate connectivity between constituent clusters, not the highly dense, well-interconnected cores of percolating gel-like networks of droplets. In effect, non-percolating core droplets reduce the scattering from the emulsion without contributing to its shear elasticity. We hypothesize that jamming of non-percolating dense clusters as ϕ is increased in the notch region leads to the creation of elastic shear-stress supporting networks that are less tenuous for the IA emulsion than for the SA emulsion. This cluster-jamming also is accompanied by a sharp reduction in SDDs towards the lower end of the notch, as clusters become closely proximate and SDDs are converted into shell and core droplets. Also, to account for the reduced magnitude of $1/\ell^*_{\mathrm{IA}}(\phi)$ over the wide range $\phi \leq 0.64$ as compared to the SA system in addition to the notch, we introduce the fourth component $\phi_{\mathrm{core,nonperc}}$, which we assume quadratically increases from very low ϕ, so as not to influence the low-ϕ slope in the scattering, and then exponentially decreases beyond $\phi \gtrsim 0.6$. Weights are transferred to non-percolating droplets from SDDs and shell droplets, while preserving ϕ conservation of all four components. This procedure

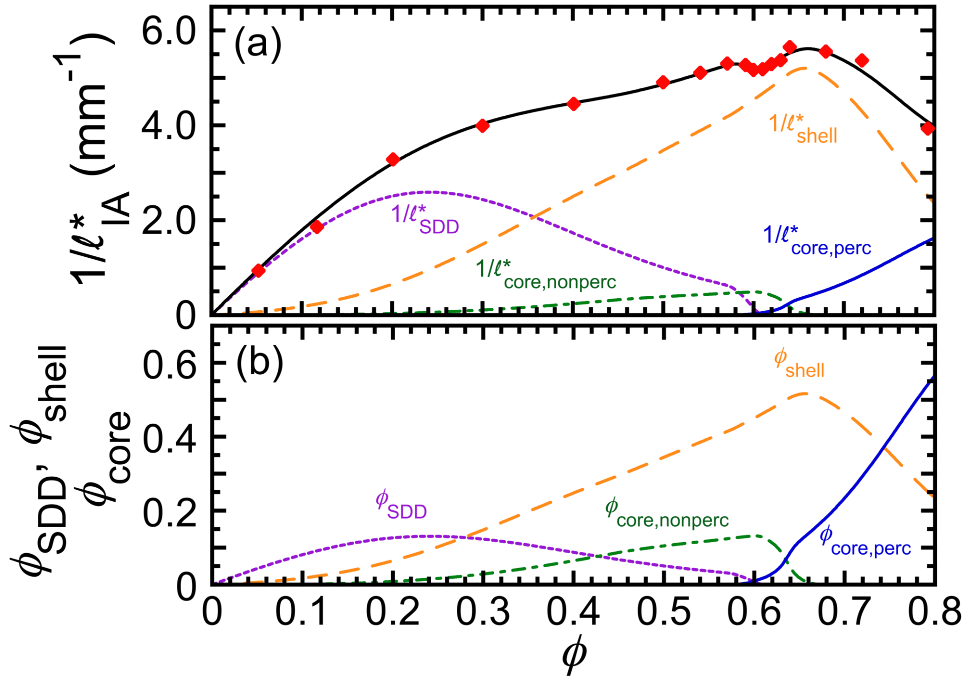

Figure 3.4. Principal component analysis of $1/\ell^*_{\mathrm{IA}}(\phi)$ using the extended decorated core-shell network (E-DCSN) model (see text). (**a**) Measured $1/\ell^*_{\mathrm{IA}}(\phi)$ (red diamonds) from Figure 3.1. Fit: equation (3.1) (black solid line). Inferred ϕ-dependent scattering contributions from: surface decorating droplets ($1/\ell^*_{\mathrm{SDD}}$, purple dotted line), shell droplets ($1/\ell^*_{\mathrm{shell}}$, orange dashed line), non-percolating core droplets ($1/\ell^*_{\mathrm{core,nonperc}}$, green dashed-dotted line), and percolating core droplets ($1/\ell^*_{\mathrm{core,perc}}$, blue solid line). (**b**) Component droplet volume fractions: ϕ_{SDD}, ϕ_{shell}, $\phi_{\mathrm{core,nonperc}}$, and $\phi_{\mathrm{core,perc}}$ [line colors and types as in part (a)].

results in a good match to the measured $1/\ell^*_{\mathrm{IA}}(\phi)$ and also provides plausible, smooth ϕ-dependences of the four principal components, as shown in Figure 3.4(a), recognizing that the solution to this problem is formally ill-posed given the available measurements. Although more principal components could be considered, even to the point of having separate components for each possible integer value of $\langle N \rangle$, the E-DCSN model with only four principal components describes all the key features of $1/\ell^*_{\mathrm{IA}}$ over all ϕ, including the notch, through the smooth conversion between the component volume fractions of different species (Figure 3.4). Given prior constraints on the relative scattering of different components, known from modeling SA emulsions, we set the optical transport parameters in equation (3.1) for this

IA emulsion to be the same as was found for the SA emulsion: $1/\ell^*_{\mathrm{SDD},0} = 19.8\ \mathrm{mm}^{-1}$ and $r_{\mathrm{shell}} = 0.509$. Starting from $r_{\mathrm{core}} = 0.150$ for the SA system, we determine $r_{\mathrm{core,\ nonperc}} = 0.187$ and $r_{\mathrm{core,\ perc}} = 0.145$ for the IA system by taking into account the relative surface-to-volume ratio of the non-percolating and percolating core droplets and minimizing χ^2 for the least-squares fit of $1/\ell^*_{\mathrm{IA}}(\phi)$. The optimized parameters for $\phi_{\mathrm{SDD}}(\phi)$ are determined to be $\phi_{\mathrm{SDD,F}} = 0.265$ and $\Delta\phi_{\mathrm{SDD}} = 0.105$ from the least-squares fitting of $1/\ell^*_{\mathrm{IA}}(\phi)$ at dilute ϕ where SDDs dominate. The detailed iterative procedure for obtaining smooth functions of the four principal components, while minimizing χ^2 for the least-squares fit of $1/\ell^*_{\mathrm{IA}}(\phi)$, is explained in the Methods (see chapter 3.3).

As a different way of parameterizing the relative proportions of the four principal components, we also calculate the component relative volume fractions: $f_{\mathrm{SDD}} = \phi_{\mathrm{SDD}}/\phi$, $f_{\mathrm{shell}} = \phi_{\mathrm{shell}}/\phi$, $f_{\mathrm{core,nonperc}} = \phi_{\mathrm{core,nonperc}}/\phi$, and $f_{\mathrm{core,perc}} = \phi_{\mathrm{core,perc}}/\phi$ [Figure 3.5(a)]. We hypothesize that the component relative volume fractions of non-percolating and percolating core

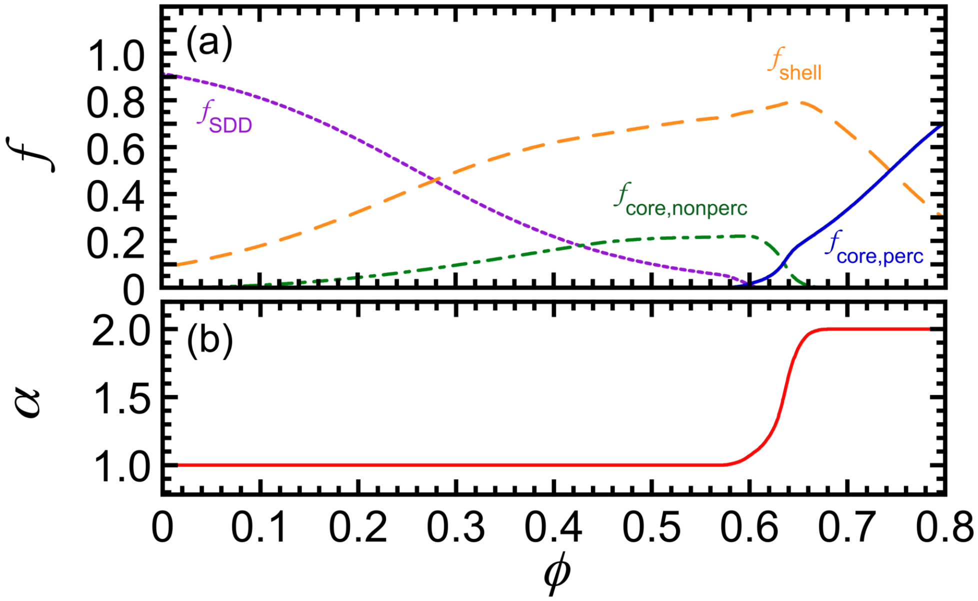

Figure 3.5. Droplet volume-fraction dependence of: (a) component relative volume-fractions, f, determined from Figure 3.4(a) using the E-DCSN model [line types and colors: same as Figure 3.4(a)], and (b) dimensionless effective DWS probe-size factor (see text), α, obtained from core components in part (a), which ranges from 1 (single-droplet probe) to 2 (LDC probe).

droplets can be used to determine the dimensionless ϕ-dependent effective DWS probe-size factor via: $\alpha(\phi) = \langle a_{\mathrm{pr}}(\phi)\rangle/\langle a\rangle = (f_{\mathrm{core,nonperc}} + 2f_{\mathrm{core,perc}})/(f_{\mathrm{core,nonperc}} + f_{\mathrm{core,perc}})$, where $\langle a_{\mathrm{pr}}(\phi)\rangle$ is the ϕ-dependent effective average radius of the DWS scattering probes. The resulting $\alpha(\phi)$, ranging from 2.0 in the high-ϕ limit to 1.0 in the low-ϕ limit, is shown in Figure 3.5(b). This hypothesis implies that the DWS scattering probes are effectively individual droplets at low ϕ, similar to the MA emulsions at lower depletion strength than the IA emulsions, and it implies that the DWS scattering probes are effectively LDCs at high ϕ well above jamming, similar to the SA emulsions at higher depletion strengths. In the notch region, the relative proportions of these change rapidly, and α effectively represents an average over populations of single droplets and LDCs.

3.4.3 Comparison of DWS microrheology with mechanical macrorheology

Based on the above hypothesis regarding the DWS probe-size factor, α, which is tied to the E-DCSN analysis of the measured optical transport properties, we use the GSER to calculate the low-frequency plateau elastic shear moduli, $G'_{\mathrm{p,GSER}}(\phi)$, of the IA emulsion:

$$G'_{\mathrm{p,GSER}}(\phi) = \frac{k_{\mathrm{B}}T}{\pi\langle a_{\mathrm{pr}}(\phi)\rangle \left\langle \Delta \boldsymbol{r}^2(\phi)\right\rangle_{\mathrm{p}}} = \frac{k_{\mathrm{B}}T}{\pi[\alpha(\phi)]\langle a\rangle \left\langle \Delta \boldsymbol{r}^2(\phi)\right\rangle_{\mathrm{p}}}. \tag{3.2}$$

We compare this result with mechanical rheometry measurements in Figure 3.6. We find good quantitative agreement between the mechanical $G'_{\mathrm{p,mech}}$ and microrheological $G'_{\mathrm{p,GSER}}$ over all ϕ probed. Use of ϕ-independent α of either 1 or 2 leads to small but systematic deviations that are apparent at either high or low ϕ, respectively. Of all emulsions that we have studied systematically thus far (*i.e.* NH, MA, IA, and SA), the IA emulsion is the most challenging to interpret, both in regards to optical transport properties and also to passive microrheology.

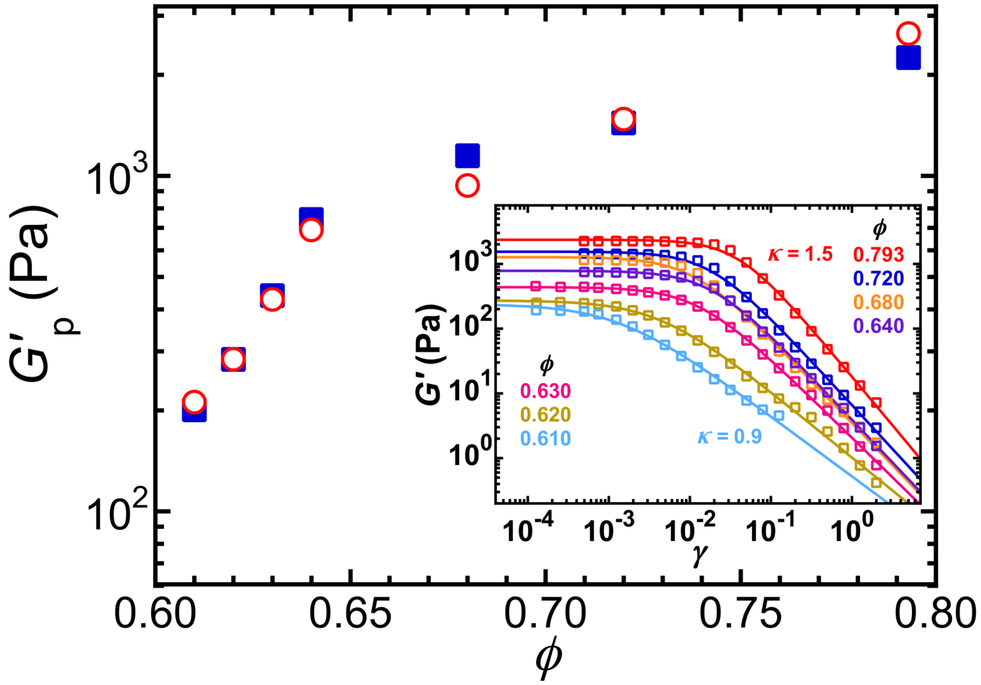

Figure 3.6. Comparison of DWS-GSER microrheological plateau elastic shear moduli, $G'_{\mathrm{p,GSER}}(\phi)$ (red open circles), obtained using plateau MSDs from Figure 3.3(a) and the E-DCSN model's $\alpha(\phi)$ from Figure 3.5(b), with plateau elastic shear moduli $G'_{\mathrm{p,mech}}(\phi)$ measured by mechanical rheometry (blue solid squares, from fits to strain-dependence in the inset). Inset: Mechanical shear oscillatory measurements of the storage modulus G' as a function of the applied peak strain amplitude γ for intermediately attractive dense emulsions at [SDS] = 35 mM and frequency $\omega = 1$ rad/s. Solid lines: fits using $G'(\gamma) = G'_{\mathrm{p,mech}}/\left[(\gamma/\gamma_{\mathrm{y}})^{\kappa} + 1\right]$, yielding the plateau shear modulus $G'_{\mathrm{p,mech}}$; yield strain γ_{y} indicates the position of the knee that defines yielding; and high-strain power law parameter κ describes the decrease in the non-linear G' well beyond yielding.

3.4.4 Probability distribution of local coordination number

At each ϕ, we infer discrete probability distributions, $p_N(N)$, using the results of the principal component analysis in the E-DCSN model. For each principal component (*i.e.* SDDs, shell droplets, non-percolating core droplets, and percolating core droplets), we assume Gaussian distributions as a function of N centered on $\langle N \rangle = 3$, 6, 9, and 12, respectively, each with a standard deviation $\sigma_N = 2.5$. The corresponding probability density functions are denoted as $p_{\mathrm{SDD}}(N)$, $p_{\mathrm{shell}}(N)$, $p_{\mathrm{core,nonperc}}(N)$, and $p_{\mathrm{core,perc}}(N)$. Here, $p_N(N \leq 2)$ has been folded toward larger N, corresponding to the known distribution of N for slippery diffusion-limited cluster aggregation (S-DLCA)[58]. At each ϕ, $p_N(N)$ is the sum of these probability density functions, each of which is weighted by its corresponding component volume fraction and normalized by the total ϕ:

$$\begin{aligned} p_N(N,\phi) = [&\phi_{\text{SDD}}(\phi)p_{\text{SDD}}(N) + \phi_{\text{shell}}(\phi)p_{\text{shell}}(N) \\ &+ \phi_{\text{core,nonperc}}(\phi)p_{\text{core,nonperc}}(N) + \phi_{\text{core,perc}}(\phi)p_{\text{core,perc}}(N)]/\phi. \end{aligned} \tag{3.3}$$

The results of these calculations are shown in Figure 3.7. The chosen $\sigma_N = 2.5$ yields smooth distributions at all ϕ shown; smaller σ_N leads to distributions that have local maxima and are less smooth. Here, the definition of N corresponds most closely to an effective coordination number (*i.e.* number of slippery attractive bonds corresponding to near-contact

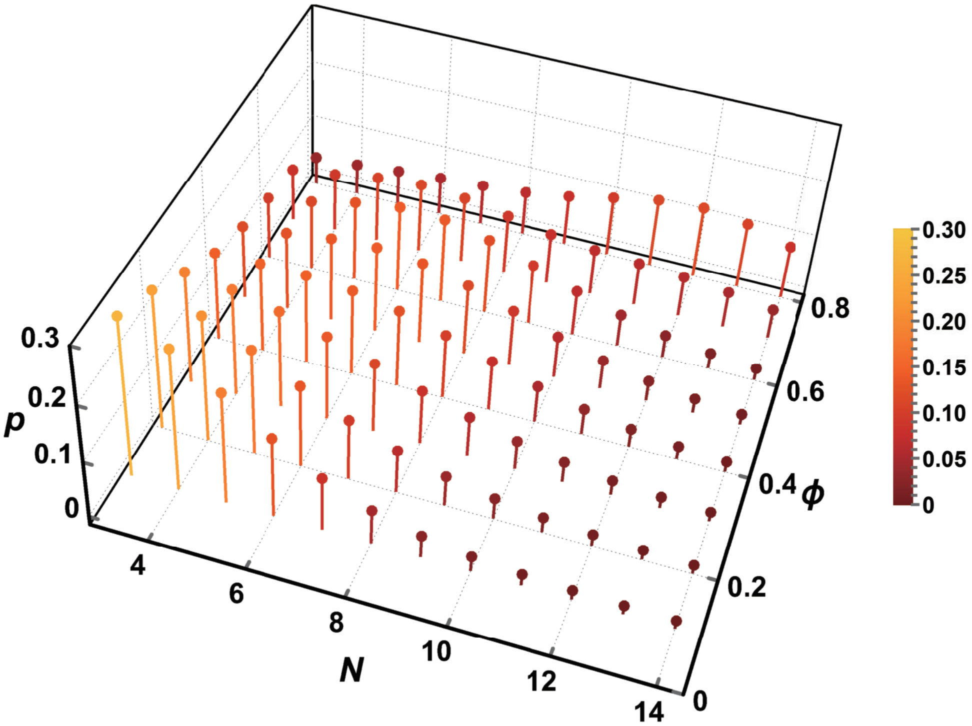

Figure 3.7. Normalized probability distributions of local coordination numbers, $p_N(N)$, for different volume fractions ϕ, inferred from the components of the E-DCSN model in Figure 3.4(b) (see text for details). For this intermediately attractive emulsion, $p_N(N)$ shifts from being low-N dominant at low ϕ, to mid-N dominant at $\phi \approx 0.5$, and then to high-N dominant at high ϕ.

between neighboring droplet interfaces), which is sometimes denoted z in other literature[107]. We emphasize that interdroplet bonding and near-contact configurations inherent in this definition of N are those that are most influential in determining optical transport properties (*i.e.* scattering) as well as in determining mechanical shear rigidity. Also, the substantial values in these distributions for $N > 12$ towards high ϕ are facilitated by droplet deformation, arising from at least one of short-range attraction and osmotic compression; yet, regions of near-contact are stabilized against coalescence by the screened electrostatic repulsion. The presented $p_N(N, \phi)$ are consistent with our particular experimental protocol for emulsion-preparation and observed optical transport properties; yet, these distributions are not necessarily universal for any method of preparing an attractive emulsion.

3.5 Discussion

Attractive colloidal systems are complex and rich, yet are also among the most challenging to explore experimentally. The precise structure of an attractive colloidal system can depend sensitively on the method of its preparation, and aging can sometimes occur and lead to slow structural evolution. Differences in preparation of short-range attractive colloidal systems can lead to non-unique structures and physical properties, even for monodisperse colloids at the same ϕ and same $|U_{\mathrm{d}}|$. Here, by developing and systematically applying a protocol for preparing dense attractive emulsion systems that have slippery short-range attractions, we have been able to reveal important new features in the optical transport properties and DWS MSDs that accompany intermediate attractions. Our results for IA emulsions differ substantially from either MA or SA emulsions; yet, some known aspects of MA and SA emulsions are useful in understanding IA emulsions: excess DWS MSDs at long time (MA emulsions), and a DWS probe-size factor of $\alpha \approx 2$ at high ϕ above ϕ_{MRJ} (SA emulsions). However, the ϕ-dependent optical scattering of the IA emulsion has a very interesting and striking notch near the random jamming point that has not be reported for either MA or

IA emulsions. This notch, as interpreted using the E-DSCN model, suggests that a cluster-jamming scenario likely occurs as ϕ is raised, rather than either a droplet-jamming scenario for NH emulsions or a gel-network forming scenario for SA emulsions. In addition, this notch provides an important clue that signals different proportions of local dense structures and different interconnectivity of those local dense structures for IA emulsions, as compared to both MA and SA emulsions. The overall lower scattering of the IA emulsion at ϕ below jamming indicates that loosely bound attractive clusters, which have a lower surface-to-volume ratio, exist in the IA emulsion, as compared to the more tenuous, gel-like network structures of the SA emulsion. Moreover, the measured low-frequency plateau shear rigidity of the IA emulsion does not extend for ϕ below the minimum in the notch, whereas at substantially stronger attractive strengths, such low-frequency shear rigidity of the SA emulsion does extend well below jamming. This is further confirmed microrheologically from the measured DWS MSDs of the IA emulsion, after accounting for the existence of long-time excess MSDs. Using emulsions, rather than solid particulates, has facilitated all of these advances in understanding, since emulsions can be concentrated and manipulated at very high ϕ without the problems with irreversible aggregation that can be present in solid particulate systems.

Our results for the IA emulsion imply a complex and non-monotonic behavior of the ϕ-dependent optical transport properties of concentrated emulsions as a function of $|U_{\mathrm{d}}|$. Very low strengths of depletion attractions relative to thermal energy in MA emulsions do not yield substantial changes in scattering compared to emulsions with nearly hard interactions. However, the limit of very high depletion strengths relative to thermal energy in SA emulsions does not yield the greatest possible reduction in scattering at intermediate $0.45 \leq \phi \leq 0.55$. Instead, among MA, IA, and SA emulsions, we find that the greatest reduction in scattering is actually present in this range of ϕ for IA emulsions. So, the full behavior of this non-monotonic trend deserves further consideration, including a more detailed set of measurements at other $|U_{\mathrm{d}}|$.

For IA emulsions, a ϕ-dependent DWS probe-size factor α, which varies from 1 in the notch region to 2 above the notch region, yields the best comparison with mechanical measurements. This probe-size factor reflects the relative proportions of scatterers that lead to the DWS signals which are interpreted as probe MSDs; the relative populations of scatterers in the cluster-jamming scenario of IA emulsions vary rapidly in the cluster-jamming regime corresponding to the notch in the optical transport. This DWS probe-size factor has been inferred from the measured optical transport and dynamic correlation functions by connecting these measurements to shear-rigidity percolation, which is linked to droplet coordination number through the principal component analysis and physical interpretation of the E-DCSN model. A full theoretical treatment of the DWS probe-size factor as a function of ϕ and $|U_\mathrm{d}|$ is needed in order to establish its fundamental origin as well as to further examine the hypothesis that it can be determined through a ratio related to the fraction of non-percolating and percolating core droplets.

Overall, our results point to a cluster-jamming scenario for the IA emulsion. At lower ϕ, clusters of droplets in the IA emulsion are compact and not strongly bonded together; the weak association of these clusters precludes the existence of a low-frequency plateau shear rigidity for the IA emulsion. However, as ϕ is raised, these clusters are forced to jam together, yielding plateau shear-rigidity, yet with a lower surface-to-volume ratio of the network structures as compared to the more tenuous networks of SA emulsions. Thus, it would be interesting to perform measurements over a broader range of $|U_\mathrm{d}|$ to see how the cluster-jamming scenario of the IA emulsion transitions into the gel-network scenario of the SA emulsion. Likewise, it would be useful to explore lower $|U_\mathrm{d}|$ to determine where the notch-like feature in $1/\ell^*(\phi)$ emerges.

As a consequence of our experimental protocol, dense IA emulsions have been formed by diluting the concentrated master emulsion sample and shear-agitating at constant $|U_\mathrm{d}|$ to form a system that is uniform in ϕ. The agitation does not rupture droplets but instead only alters the droplets' positional structure. This process of dilution and shear agitation at constant micellar concentration initially causes unjamming of attractive clusters that were originally jammed by osmotic compression through ultracentrifugation in the concentrated master emulsion. Subsequently, during the waiting time that we have designed into this protocol, attractive bonding between clusters can occur and gel-network formation is possible. For the SA system, to which the same experimental protocol has been applied, shear-rigid gel-like elastic networks form after disruption at ϕ well below ϕ_{MRJ} in the presence of strong $|U_{\mathrm{d}}| \approx 15\ k_{\mathrm{B}}T$. However, for the IA emulsion having $|U_{\mathrm{d}}| \approx 6\ k_{\mathrm{B}}T$, the weak association of clusters after disruption does not yield shear-rigidity percolation at the intermediate strength of attraction for ϕ extending well below ϕ_{MRJ}, as is evident in the measured $G'_{\mathrm{p}}(\phi)$ when compared to the SA emulsion. This interpretation is consistent with both macroscopic shear rheometry measurements as well as our passive microrheological DWS measurements.

Our results, analysis, and interpretation for IA emulsions point to many exciting future directions, both in simulations and experiments. For instance, simulations could be developed to treat slippery attractive colloidal systems formed by diluting osmotically compressed attractive emulsions, imposing shear disruption at constant $|U_{\mathrm{d}}|$, allowing subsequent cluster association and gel-network formation, and then exploring optical and mechanical responses with and without shear deformation. Such simulations would more closely align with our experimental protocols and observations than just quenching-in a secondary attraction in a homogeneous dispersion. In addition, the influence of minor populations of more mobile droplets on DWS signals could be identified and studied as a function of $|U_{\mathrm{d}}|$ and ϕ. Experimentally, one could potentially extend a reported confocal microscopy study that utilizes both refractive index-matched and density-matched, size-fractionated emulsions[85] by inducing a short-range attraction and varying ϕ at different fixed values of $|U_{\mathrm{d}}|$. In addition, further exploration of optical transport properties for values of $|U_{\mathrm{d}}|$ in between IA and MA and also in between IA and SA will reveal the range over which the notch feature in $1/\ell^*(\phi)$ can be observed.

In summary, our study provides a comprehensive set of experimental measurements of optical transport, rheological, and dynamic correlation functions for an intermediately attractive, dense system of fractionated, uniform emulsion droplets. Our experimental protocols have been refined to give reproducible results that enable direct quantitative microrheological comparisons of plateau elastic shear moduli that are not dominated by aging effects. We have found that discounting excess MSDs as well as utilizing a ϕ-dependent DWS probe-size factor are both needed to obtain the best possible match of the passive microrheological interpretation of all measurements, when compared to macroscopic shear rheological measurements. To explain the additional complexity in the measured optical scattering, it has been necessary to include a fourth principal component in the E-DCSN model. Taken together, both the data and the modeling point to highly complex IA system in which loosely connected dense clusters, not isolated droplets, jam as ϕ is raised. We anticipate that future work will reveal additional finer details in the transition between MA, IA, and SA regimes as $|U_{\mathrm{d}}|$ is varied and will provide insight into the fundamental origin of the DWS probe-size factor in short-range attractive colloidal systems.

Chapter 4 - Jamming and depletion in extremely bidisperse mixtures of microscale emulsions and nanoemulsions

This chapter has been written by Y. Xu and T. G. Mason, is currently copyrighted by Y. Xu and T. G. Mason in 2023, and has been accepted by *Science Advances* for publication (In Press). Since the contents of the chapter have not yet been published, written permission must be obtained by both authors to reproduce or transmit the contents of the herein Chapter 4, in whole or in part, prior to its publication in a scientific journal. Readers are encouraged to perform a search on the above authors and/or title using an internet search engine (e.g. Google Scholar or Web of Science) to determine if publication has occurred. If publication of the contents of this chapter has occurred in a scientific journal, then readers are directed to that journal's policies regarding permissions for potential use.

4.1 Abstract

While much attention has been given to jamming of granular and colloidal particles having monomodal size distributions, jamming of systems having more complex size distributions remains an interesting direction. Here, we create concentrated, disordered binary mixtures of size-fractionated nanoscale and microscale oil-in-water emulsions, which are stabilized by the same common ionic surfactant, and we measure the optical transport properties, microscale droplet dynamics, and mechanical shear rheological properties of these mixtures over a wide range of relative and total droplet volume fractions. Simple effective medium theories do not explain all of our observations. Instead, we show that our measurements are consistent

with more complex collective behavior in extremely bidisperse systems, involving an effective continuous phase that governs nanodroplet jamming, as well as depletion attractions between microscale droplets induced by nanoscale droplets.

4.2 Introduction

An interesting and challenging frontier in the science of colloidal systems is examining how the size-polydispersity of constituents affects the macroscopic physical properties of these systems[10]. Even for uniform, monodisperse colloidal systems of spheres, considerable complexity exists in making this connection. Despite this complexity, substantial progress has been made in revealing how physical properties, such as shear elasticity and scattering, are connected to the underlying colloidal sizes, positional structures, and interactions as a function of the volume fraction ϕ of the colloids[10, 116–119]. Recently, further insights have been made through passive microrheology studies of monodisperse microscale emulsions having nearly hard interactions[57] and also short-range attractions[59, 115, 120]. Even so, when broadly considered, different forms of size-polydispersity could introduce new levels of complexity in connecting these colloidal sizes, positional structures, and interactions to the system's macroscopic physical properties. One of the most compelling polydisperse size-distributions that deserves attention is the bidisperse size-distribution[121–123], also known as a bimodal size-distribution[124, 125], which can be made by mixing two different monodisperse systems of the same type of colloid, yet each having a different average size. In particular, examining the limit of extreme bidispersity, where the peaks in the colloidal size-distribution are separated by more than an order of magnitude, would provide a first view into emergent effects that are not explained by existing concepts and theories and that may also be found in very broadly polydisperse size-distributions.

Bidisperse colloidal systems, such as mixtures of larger and smaller rigid polymeric spheres[126–128] or mixtures of larger and smaller deformable emulsion droplets[50], have been used as idealized models for studying depletion attractions, an entropic interaction predicted theoretically by Asakura and Oosawa[44]. Depletion attractions can lead to phase separation[50, 79, 91] and even gelation[51, 115] of the larger colloids, if the strength of the depletion potential energy at contact, $|U_{\mathrm{d}}|$, is much larger than $k_{\mathrm{B}}T$, where k_{B} is Boltzmann's constant and T is the temperature. Prior studies of depletion attractions have typically been limited to volume fractions of the smaller colloids, which are sometimes referred to as depletion agents or depletants, that are below the jamming point of the smaller colloids. The rheological response of colloidal emulsions having monomodal size distributions in the presence of smaller surfactant micelles, which can act as depletion agents, has been investigated using macroscopic rheometry[46, 129, 130], as well as both macroscopic rheometry and diffusing wave microrheology[59, 115, 120]. These studies have revealed depletion-induced attractive gelation of emulsions that can lead to elastic responses for ϕ below the repulsive jamming point of the larger colloids, provided that the strength of the depletion attraction is much larger than $k_{\mathrm{B}}T$. Recent simulations, focused on steady shear viscosity, have been made on idealized bidisperse mixtures of spheres[131], but only at a relatively low size ratios of colloids, not in the limit of extreme bidispersity. These simulations do not address an essential rheological property related both to repulsive jamming and also to attractive gelation: the small-strain linear shear elasticity. Moreover, prior experiments and simulations have not addressed how optical transport properties (*i.e.* scattering), colloidal dynamics, and macroscopic shear elasticity vary with ϕ into the jamming limit for high concentrations of larger and smaller colloids of the same type. Thus, exploring key physical properties of stable colloidal emulsions in the limit of extreme bidispersity and at high droplet volume fractions of larger and smaller colloids, where both jamming and depletion can be present, represents an interesting direction.

Systematic experimental investigations of the plateau shear elastic modulus, G'_{p}, of uniform, size-fractionated, microscale, oil-in-water (O/W) emulsions[21, 28] over a wide range of droplet volume fractions ϕ[34] provided the key primary example of jamming of disordered soft colloidal spheres, prior to the introduction of and widespread use of jamming terminology. The abrupt onset of shear elasticity in these emulsions toward higher ϕ was initially connected broadly to the notion of disordered droplets coming into contact with each other and then deforming during a process of crowding. At that time, the best available quantitative measure of ϕ associated with monodisperse rigid spheres that had been crowded into a disordered structure and that could no longer be further compressed was known as random close packing (RCP), a concept introduced by J.D. Bernal and J. Mason[35]. The measured volume fraction of spheres associated with RCP was known to be $\phi_{\mathrm{RCP}} \approx 0.64$. Initial foundational simulations by Lacasse *et al.*[132] on highly crowded, disordered systems of monodisperse deformable droplets revealed that the loss of shear elasticity of these systems occurs at $\phi \approx 0.64$, consistent with the experiments after ϕ had been corrected for screened-charge electrostatic repulsions[133]. These experiments and simulations played a direct role in the subsequent introduction of jamming terminology[68]. Following these advances, the more precisely defined statistical concept of maximal random jamming (MRJ) of monodisperse hard spheres was developed through simulations and theory by S. Torquato *et al.*[36], who showed that jamming does not always occur at exactly the same volume fraction for different initial conditions of random sphere locations prior to compression, but instead in a distribution of volume fractions that is highly peaked around $\phi_{\mathrm{MRJ}} = 0.646$. Given the strong concordance in the experiments and simulations, the observation and interpretation of the rapid rise in $G'_{\mathrm{p}}(\phi)$ around a critical jamming volume fraction near 0.64 for disordered uniform emulsion systems has served as an archetype for the jamming elasticity of other disordered soft-matter systems composed of uniform colloids.

Going beyond microscale emulsions, high-throughput methods were subsequently developed for fabricating uniform O/W nanoemulsions, stabilized by an ionic surfactant, by combining high-pressure microfluidic homogenization with ultracentrifugal size-fractionation and concentration of nanoscale droplets[23,24]. Provided that the average droplet radius is far below the smallest wavelengths associated with the visible spectrum, highly controlled size-fractionated nanoemulsions appear translucent[134,135], exhibiting a dramatic reduction in optical scattering as compared to microscale emulsions, which instead typically have a white appearance as a consequence of strong multiple scattering by droplets that have radii closer to the range of visible wavelengths. In addition, surprisingly, it was shown that O/W nanoemulsions could have a very low effective jamming ϕ for compositions that were predominantly water, not oil[30]. Because the same electrostatic Debye screening length is a substantially larger fraction of the average droplet radius for nanoemulsions as compared to microscale emulsions, the effect of screened electrostatic repulsions on $G'_{\mathrm{p}}(\phi)$ of nanoemulsions is dramatic compared to microscale emulsions at the same surfactant concentration. Thus, short-range repulsive interactions in O/W nanoemulsions are known to create pronounced downward shifts in the effective ϕ associated with jamming, which occurs when Debye layers of neighboring nanodroplets begin to overlap strongly.

To explain a wide range of measurements of the linear shear elasticity of both microscale and nanoscale emulsions, an entropic-electrostatic-interfacial (EEI) model was developed[37]. Beyond including the essential concept of jamming of disordered uniform droplets at high ϕ, leading to droplet deformation through crowding, the interpretation of these classic measurements of the linear shear elasticity of concentrated emulsions also took into account other contributions to the free energy at high densities. These contributions include the influence of a short-range screened-charge repulsion provided by an ionic surfactant, which stabilizes the droplets against coalescence, and an entropic term[38]. This EEI model provides accurate predictions of $G'_{\mathrm{p}}(\phi)$ for microscale emulsions and nanoemulsions both above and below jamming. While size- and charge- polydispersities of the droplets do not explicitly enter into the EEI model, it reasonably describes the measured $G'_{\mathrm{p}}(\phi)$ of uniform size-fractionated colloidal O/W emulsions stabilized by an ionic surfactant over a wide range of average droplet radius. Since the EEI model has been specifically designed to describe repulsive jamming in disordered charge-stabilized emulsions without depletion attractions, it does not predict $G'_{\mathrm{p}}(\phi)$ for attractively gelled emulsion systems.

Here, we create and study experimentally a well-controlled model bidisperse colloidal system of size-fractionated microscale and nanoscale O/W emulsions that share the same ionic surfactant, sodium dodecyl sulfate (SDS) at high component droplet volume fractions ϕ_{NEM} and ϕ_{EM}, which are defined as the bare oil volume of the nanoscale and microscale droplets, respectively, relative to the total volume of the mixture: $\phi_{\mathrm{NEM}} = V_{\mathrm{o,NEM}}/V_{\mathrm{tot}}$ and $\phi_{\mathrm{EM}} = V_{\mathrm{o,EM}}/V_{\mathrm{tot}}$. The total volume of the binary mixture is $V_{\mathrm{tot}} = V_{\mathrm{o,NEM}} + V_{\mathrm{o,EM}} + V_{\mathrm{w}}$, and the volume of the aqueous continuous phase is V_{w}. The water in a given final mixture originates from: the continuous phase of the master emulsion, the continuous phase of the master nanoemulsion, and the SDS aqueous solution used to make the mixture (see chapter 4.3). Conservation of volume implies that the water volume fraction in the mixture is: $\phi_{\mathrm{w}} = V_{\mathrm{w}}/V_{\mathrm{tot}} = 1 - (\phi_{\mathrm{EM}} + \phi_{\mathrm{NEM}})$. The SDS concentration is adjusted to yield strong stability against droplet coalescence through screened-charge repulsions between droplets, yet is kept low enough so that the SDS micelles effectively do not play a role in depletion. In particular, we explore the interesting relative-size regime where the nanodroplets have an average radius, $\langle a_{\mathrm{NEM}} \rangle$, that is more than a decade smaller than the average radius of the microscale droplets, $\langle a_{\mathrm{EM}} \rangle$. In addition to probing how this extreme bimodal form of polydispersity (*i.e.* extreme bidispersity) in the droplet size distribution influences colloidal jamming for screened-charge repulsive systems, we also explore how *self-induced* entropic depletion attractions between microscale droplets, induced by sufficiently large volume fractions of nanoscale droplets, can play a role in the physical properties of broadly polydisperse emulsions.

Our experimental approach involves systematically making a combination of optical scattering and mechanical shear rheology measurements on two different sets of binary emulsion mixtures and comparing these measurements with similar reference measurements made on the individual component nanoscale and microscale emulsions. This combination of measurements provides several experimental results that can be used to test theories and simulations more stringently than limited measurements restricted to only one property. We measure the inverse mean free path of optical transport and also microscale droplet mean square displacements (MSDs) using diffusing wave spectroscopy (DWS)[55, 56, 108, 109]. Our mechanical measurements focus on the linear plateau shear elastic modulus G'_{p}. By analyzing these measurements, we show that a simple effective medium theory of G'_{p} based on the EEI model breaks down, and that a more sophisticated interpretation of jamming, involving an effective continuous phase of the nanoemulsion component, is necessary to explain the mechanical properties of extremely bidisperse colloidal emulsions. Moreover, our experimental results provide clear evidence that depletion attractions between microscale droplets, which arise as a consequence of the osmotic pressure exerted by the nanoscale droplets, can strongly influence these physical properties. Thus, we demonstrate that two different phenomena are responsible for these observed deviations from effective medium theory in this extremely bidisperse colloidal emulsion system: (1) an effective continuous phase associated with nanodroplet jamming and (2) self-induced depletion attractions between microscale droplets, caused when a substantial nanodroplet component exists in the overall size distribution.

4.3 Materials and Methods

4.3.1 Emulsion and nanoemulsion preparation and characterization

We prepare microscale emulsions (EM) using trimethylsiloxy terminated polydimethylsiloxane oil (PDMS, Gelest Inc; viscosity at 25°C: $\nu_{\mathrm{o,EM}} = 350$ cSt; refractive index: $n_{\mathrm{o,EM}} = 1.4031$; density: $\rho_{\mathrm{o,EM}} = 0.970$ g mL^{-1}), sodium dodecyl sulfate (SDS, Fisher Scientific; electrophoresis grade 99% purity), and deionized water (Millipore Milli-Q Academic; resistivity: 18.2 MΩ cm). Following the protocol of emulsification, microfluidic homogenization using a high flow rate microfluidic homogenizer (Microfluidics, M-110P; 75 μm Y-chamber) at a liquid pressure of about 70 MPa, and size-fractionation in Kim *et al.*[57], we obtain a 4× size-fractionated, concentrated master emulsion, stabilized at [SDS] = 10 mM. We dilute a small portion of this well-mixed, uniform master emulsion in a 10 mM aqueous SDS solution to $\phi \approx 10^{-4}$ and then characterize the radial size distribution of the diluted emulsion using dynamic and static light scattering. We characterize the droplet volume fraction of this master EM sample using a gravimetric evaporation method[80], $\phi_{\mathrm{m,EM}} = 0.778 \pm 0.007$. Emulsions having lower droplet volume fraction $\phi_{\mathrm{EM}} < \phi_{\mathrm{m,EM}}$ are prepared from diluting the master EM sample with 10 mM SDS solution.

In addition, we make nanoemulsions (NEMs) having much smaller, nanoscale droplets using lower viscosity PDMS oil (Gelest Inc; viscosity at 25°C: $\nu_{\mathrm{o,NEM}} = 10$ cSt; refractive index: $n_{\mathrm{o,NEM}} = 1.3990$; density: $\rho_{\mathrm{o,NEM}} = 0.935$ g mL^{-1}), SDS, and deionized water through high-flow rate emulsification. We prepare a crude premix emulsion having $\phi \approx 0.2$ in 50 mM aqueous SDS solution using a mixer (Fisher Scientific, PowerGen 125, speed 6) and allow any residual foam to disappear. We process the premix emulsion using the microfluidic homogenizer at a higher liquid pressure of about 210 MPa for 8 times before collecting and diluting the resulting nanoemulsion in 10 mM aqueous SDS solution to $\phi \approx 0.1$ after the final pass. We concentrate the diluted nanoemulsions to a higher ϕ via centrifugation (Beckman L8-55 ultracentrifuge, SW-28 swinging bucket, 18k rpm, 30 hours), yielding a set of concentrated, elastic, jammed nanoemulsion plugs at the tops of thick-wall polycarbonate centrifuge tubes. The effective gravitational forces acting on droplets, caused by this ultracentrifugation, are sufficiently small that nanodroplet coalescence is not observed. We then remove the SDS solution below these elastic concentrated nanoemulsion plugs, combine these plugs together, and dilute these combined plugs to $\phi \approx 0.1$ using 10 mM SDS solution. We repeat this process of centrifugation and dilution twice more to set the bulk SDS concentration in the continuous phase of the resulting NEM to 10 mM.

To decrease the droplet size polydispersity of this NEM, we perform a four-step size-fractionation as follows. After a first centrifugation for size-fractionation (18k rpm, 30 hours), we remove the concentrated elastic nanoemulsion plugs from the tops of the centrifuge tubes, cut them into two pieces using a spatula, and retain the bottom-half of all plugs, corresponding the to smaller droplets. We combine and dilute these bottom plug-pieces using 10 mM

SDS solution to set $\phi \approx 0.1$. We then perform a second centrifugation using the same conditions, cut the plugs, retain and combine the bottom-third of the plugs, and again dilute using 10 mM SDS solution to set $\phi \approx 0.1$. We repeat this process of centrifugation, cutting the plugs, combining and diluting plugs twice more and for each time, we retain and combine the bottom-half of the elastic nanoemulsion plugs. After the 4× centrifugation for size-fractionation, we obtain the concentrated master nanoemulsion that is a soft elastic solid at high ϕ. We mix this master nanoemulsion thoroughly using a spatula to exclude any size- and ϕ-gradient that could be induced by centrifugation. Using dynamic light scattering (Photocor, 90° scattering angle, $\lambda = 632.8$ nm), we measure the average droplet radius and polydispersity of this fractionated NEM. The droplet volume fraction of this master NEM sample is $\phi_{\mathrm{m,NEM}} = 0.403 \pm 0.003$, determined by gravimetric evaporation[80]. Nanoemulsions having lower droplet volume fraction $\phi_{\mathrm{NEM}} < \phi_{\mathrm{m,NEM}}$ are prepared by diluting the master NEM sample with 10 mM SDS solution.

Binary mixtures of nanoemulsion and microscale emulsion having various ϕ_{NEM} and ϕ_{EM} are made by diluting portions of the master NEM and EM samples with 10 mM SDS solution using an analytical balance (Denver Instruments APX-200, 0.1 mg precision). For a sample having desired final ϕ_{NEM} and ϕ_{EM} and a total mass ≈2 g, we calculate the masses of the needed master NEM, master EM and 10 mM SDS solution prior to the weighing and mixing procedure, ensuring that the total volume of aqueous continuous phase of the mixture is the aqueous continuous phase of the initial master NEM, of the initial master EM, and the 10 mM SDS solution added. We add these three components into a 3 mL vial and then determine the resulting ϕ_{NEM} and ϕ_{EM} of each sample from these measured masses using measured densities of the SDS solution and of the corresponding PDMS oil[80].

Each sample, either having lower ϕ than the master sample or that is an EM-NEM binary mixture having different relative volume fractions, has been stirred with a small spatula, imposing an estimated 50 s^{-1} average shear flow-rate, for approximately 10 minutes to ensure complete mixing before measurements made using DWS and mechanical rheometry. The overall appearance of the O/W emulsions and nanoemulsions is determined by their optical properties, which depend on how light waves interact with them through transmission, absorption, reflection, and scattering. The dimensions of NEM droplets are so small relative to the wavelength of visible light that NEM samples are clear and translucent with slightest bluish tint (Figure 4.3A, left). By contrast, the EM samples, which are composed of larger droplets, closer to the wavelength of visible light, scatter light strongly and are thus milky-white and opaque in appearance (Figure 4.3A, right). Before mixing via shear agitating, the EM-NEM mixture at a given ϕ_{NEM} and ϕ_{EM} initially appears cloudy and non-uniform after adding the 10 mM SDS solution, the master NEM, and the master EM into a glass vial. For each sample, the stirring process is continued for an additional 3 minutes after the sample appears homogeneous to ensure compositional uniformity (Figure 4.3A). For each well-mixed sample, we split it into two portions: approximately 0.5 mL for mechanical rheometry and 1.5 mL for DWS measurements. This procedure ensures that these two portions of a given binary EM-NEM mixture, used in these two different measurements, have exactly the same composition. For all subsequent measurements, both optical and mechanical, we wait 24 h after this initial stirring and splitting to ensure sample equilibration.

4.3.2 Mechanical shear rheometry

For each binary EM-NEM sample, having a given ϕ_{EM} and ϕ_{NEM}, we measure the plateau elastic shear moduli, $G'_{\mathrm{p,mech}}$, at small strains corresponding to the linear viscoelastic regime. To ensure that the samples are homogeneous after equilibration, to preclude undesirable gravitational effects, we stir the sample at ≈ 50 s^{-1} shear rate for 30 s by agitating with a spatula. We load each sample into a controlled-strain mechanical shear rheometer (Rheometrics RFS-II, 25-mm diameter stainless steel cone-and-plate geometry, equipped with a vapor trap). After lowering the cone to the appropriate pre-set gap with respect to the plate, we allow the sample to relax for 120 s. We then perform a small-strain frequency sweep from an angular frequency $\omega = 20$ rad s^{-1} down to 0.02 rad s^{-1} at a small shear strain amplitude of $\gamma = 0.005$. We next perform a strain sweep from $\gamma = 2 \times 10^{-4}$ up to 2 at $\omega = 1$ rad s^{-1} on exactly the same sample, yielding the linear and non-linear shear storage modulus, $G'(\gamma)$. We fit the measured $G'(\gamma)$ to a function, which has a low-γ-plateau[115]: $G'(\gamma) = G'_{\mathrm{p,mech}}/[(\gamma/\gamma_{\mathrm{y}})^{\kappa} + 1]$, to obtain the dominant linear storage modulus, $G'_{\mathrm{p,mech}}$, at small strains. Here γ_{y} is the yield strain associated with the log slope change in $G'(\gamma)$ and κ is a power law exponent associated with the non-linear response of $G'(\gamma)$ to larger strains. The yield strain of mixtures ranges from the smallest $\gamma_{\mathrm{y}} = 0.004$ for $(\phi_{\mathrm{EM}}, \phi_{\mathrm{NEM}}) = (0.5, 0.075)$ to the largest $\gamma_{\mathrm{y}} = 0.05$ for $(\phi_{\mathrm{EM}}, \phi_{\mathrm{NEM}}) = (0.04, 0.36)$. κ ranges from 1.4 to 1.6 for fixed $\phi_{\mathrm{tot}} = 0.4$ and from 1.0 to 1.4 for fixed $\phi_{\mathrm{EM}} = 0.5$. R^2 ranges from 0.957 to 0.995 over all fits for the binary mixtures. All measurements are made at $T = 20$ °C.

4.3.3 Optical transport and diffusing wave spectroscopy measurements

We perform DWS measurements using DWS Rheolab 3 (LS Instruments; equipped with backscattering option, wavelength $\lambda = 685$ nm) to obtain the optical transport mean free path ℓ^* and the intensity correlation functions for each of different compositional ϕ_{EM} and ϕ_{NEM}. Each sample has been loaded into a glass optical cuvette (pathlength $L = 5$ mm) following a loading protocol[115] to eliminate air bubbles while avoiding gradient in ϕ. After a 24-h waiting time that is also used for mechanical rheometry measurements, each loaded cuvette is then placed in the Rheolab 3 and allowed to equilibrate at $T = 20 \pm 0.1$ °C. Time-averaged backscattering and transmission intensities are used to determine ℓ^*, and fluctuating intensities in either the transmission and the backscattering detectors are used to determine $g_2(t) - 1$ for all ϕ_{EM} explored. For each sample at different ϕ_{EM}, a total of 11 trials, each containing 300 s of multi-tau duration and 60 s of echo duration, have been conducted and averaged. DWS echo signal has been measured beyond 2×10^{-1} s for EM-NEM mixtures having $\phi_{\mathrm{NEM}} \geq 0.148$ (*i.e.* $\phi_{\mathrm{EM}} \leq 0.252$) at fixed $\phi_{\mathrm{tot}} = 0.4$ and for EM-NEM mixtures having $\phi_{\mathrm{NEM}} \geq 0.075$ at fixed $\phi_{\mathrm{EM}} = 0.5$.

We correct the inverse optical transport mean free path, $1/\ell^*$, by accounting for the contributions from NEM and EM oil droplets to the effective refractive index of the continuous phase. Given that the DWS scattering probes are essentially the microscale emulsion droplets, we calculate the effective refractive index difference between the bulk oil used to create the emulsions and the continuous phase: $\Delta n_{\mathrm{eff}} = n_{\mathrm{o,EM}} - n_{\mathrm{cont}}$, where we take into account the influence of aqueous surfactant solution, nanodroplets, and surrounding microdroplets to the continuous phase refractive index, n_{cont}, of a given microscale droplet, and infer n_{cont} using the effective medium theory: $n_{\mathrm{cont}} = n_{\mathrm{w}}\phi_{\mathrm{w}} + n_{\mathrm{o,NEM}}\phi_{\mathrm{NEM}} + n_{\mathrm{o,EM}}\phi_{\mathrm{EM}}$, in which $n_{\mathrm{w}} = 1.3320$.

For the system having fixed total droplet fraction, the inverse ℓ^* normalized by effective refractive index, $(1/\ell^*)/\Delta n_{\mathrm{eff}}$, as a function of ϕ_{EM} has been fit to a semi-empirical function having a smooth linear-to-quadratic crossover as more nanodroplets are introduced in the EM-NEM mixtures:

$$\frac{1/\ell^*}{\Delta n_{\mathrm{eff}}} = \left(\frac{1/\ell^*}{\Delta n_{\mathrm{eff}}}\right)_0 + \left(\frac{1/\ell^*}{\Delta n_{\mathrm{eff}}}\right)_{\mathrm{ref}} \left\{\frac{\phi_{\mathrm{EM}}}{1+\exp\left[\frac{-(\phi_{\mathrm{EM}}-\phi_{\mathrm{F}})}{\Delta\phi_{\mathrm{EM}}}\right]} + \frac{A\phi_{\mathrm{EM}}^2}{1+\exp\left[\frac{\phi_{\mathrm{EM}}-\phi_{\mathrm{F}}}{\Delta\phi_{\mathrm{EM}}}\right]}\right\} \tag{4.1}$$

where the slope of the linear regime, $[(1/\ell^*)/\Delta n_{\mathrm{eff}}]_{\mathrm{ref}} = 292 \pm 8\ \mathrm{mm}^{-1}$, is comparable to the slope of the linearly ϕ_{EM}-dependent $(1/\ell^*_{\mathrm{ref}})/\Delta n_{\mathrm{eff,ref}}$ (black reference line in Figure 4.3D), which is $307 \pm 2\ \mathrm{mm}^{-1}$; the fit parameter $\phi_{\mathrm{F}} = 0.31 \pm 0.03$ captures the transition ϕ between linear and quadratic dependence; the prefactor $A = 2.6 \pm 0.6$ of the quadratic term and the denominator within both the exponential term $\Delta\phi_{\mathrm{EM}} = 0.03 \pm 0.02$ create the smooth transition between the linear and quadratic regime of ϕ_{EM}-dependent $[(1/\ell^*)/\Delta n_{\mathrm{eff}}]$. The offset parameter $[(1/\ell^*)/\Delta n_{\mathrm{eff}}]_0 = 3.5 \pm 2.9\ \mathrm{mm}^{-1}$ extracts the normalized inverse optical transport mean free path for a concentrated nanoscale-only emulsion, which corresponds to $1/\ell^*_0 = 0.16\ \mathrm{mm}^{-1}$ for $\phi_{\mathrm{NEM}} = 0.4$ when ϕ_{EM} is zero ($\mathrm{R}^2 = 0.995$).

For the series of binary EM-NEM mixtures having fixed ϕ_{EM}, we fit the measured $(1/\ell^*)/\Delta n_{\mathrm{eff}}$ as a function of ϕ_{NEM} to the semi-empirical functional form ($\mathrm{R}^2 = 0.910$, see Figure 4.6C):

$$\frac{1/\ell^*}{\Delta n_{\mathrm{eff}}} = \left(\frac{1/\ell^*}{\Delta n_{\mathrm{eff}}}\right)_{\mathrm{ref}} \left\{1 - \frac{B}{1+\exp[-(|U_{\mathrm{d}}| - |U_{\mathrm{d,F}}|)/\Delta U_{\mathrm{d}}]}\right\}. \tag{4.2}$$

Here, $[(1/\ell^*)/\Delta n_{\mathrm{eff}}]_{\mathrm{ref}} = 146.55\ \mathrm{mm}^{-1}$ is the normalized inverse optical transport mean free path of only the microscale emulsion at $\phi_{\mathrm{EM}} = 0.5$. The depletion strength at which the changes in the optical properties are no longer described by effective medium theory is identified as: $|U_{\mathrm{d,F}}|/(k_{\mathrm{B}}T) = 8.3 \pm 1.5$. The dimensionless strength of the depletion-induced departures from simple effective medium theory is given by: $B = 0.38 \pm 0.05$. The range of depletion potential, around $|U_{\mathrm{d,F}}|$, over which the transition in the normalized inverse scattering length occurs is: $\Delta U_{\mathrm{d}}/(k_{\mathrm{B}}T) = 3.3 \pm 1.4$. For each $\phi_{\mathrm{NEM}} \neq 0$, the dimensionless $|U_{\mathrm{d}}|/(k_{\mathrm{B}}T)$ is calculated using the osmotic pressure $\Pi(\phi_{\mathrm{NEM}})$ according to the EEI model[37]. The osmotic pressure Π arises from the screened-charge repulsions and is linearly proportional to the deformation volume fraction, which is minimized to satisfy the near-equilibrium condition of free energy minimization[37]. Then, $|U_{\mathrm{d}}|/(k_{\mathrm{B}}T)$ as a function of $\phi_{\mathrm{NEM}} \leq 0.15$ is fit to an exponential form: $|U_{\mathrm{d}}|/(k_{\mathrm{B}}T) = \epsilon \exp(\phi_{\mathrm{NEM}}/\phi^*_{\mathrm{NEM}})$, yielding $\epsilon = 1.26 \pm 0.06$ and $\phi^*_{\mathrm{NEM}} = 0.0391 \pm 0.0006$ ($R^2 = 0.9995$).

Using the measured $g_2(t) - 1$ and ℓ^*, we extract the apparent mean square displacements, $\langle \Delta \boldsymbol{r}_{\mathrm{a}}^2(t) \rangle$, by solving the classic transcendental equation of DWS[57,82,83]. These apparent MSDs need to be corrected for collective scattering effects of the DWS probes using a structural factor $\langle S(q) \rangle = \ell^*_{\mathrm{ISA}}/\ell^*$, where ℓ^*_{ISA} is the optical transport mean free path of the scattering probe in the absence of collective scattering, also known as the independent scattering approximation (ISA)[57]. For the extremely bidisperse emulsion mixtures, the scattering probes, even in the ISA, cannot be hypothesized as single microscale droplets as in prior studies[57,59,115,120], because the nanoscale droplets, either individually or collectively, may also contribute to optical scattering events. Therefore, we take the following steps to determine the effective DWS-probe radius and the medium refractive index, both of which are required for determining the ℓ^*_{ISA} using the Mie scattering calculation.

We deduce the fraction of inverse optical transport mean free path that is given rise by the microscale component in the mixture via $f = [(1/\ell^*)/\Delta n_{\mathrm{eff}}]/[(1/\ell^*_{\mathrm{ref}})/\Delta n_{\mathrm{eff,ref}}]$, which is the ratio between the normalized scattering of the mixtures [*i.e.* $(1/\ell^*)/\Delta n_{\mathrm{eff}}$] and the normalized scattering of the microscale-only emulsions [*i.e.* $(1/\ell^*_{\mathrm{ref}})/\Delta n_{\mathrm{eff,ref}}$] at each given ϕ_{NEM}, having the effective refractive index difference taken into account (see Figure 4.4A and 4.7A). We then calculate the effective DWS-probe radius, $a_{\mathrm{eff}} = (f\phi_{\mathrm{EM}}\langle a_{\mathrm{EM}}\rangle + \phi_{\mathrm{NEM}}\langle a_{\mathrm{NEM}}\rangle)/(f\phi_{\mathrm{EM}} + \phi_{\mathrm{NEM}})$, using this fraction f in combination with the volume-weighted average of the measured mean droplet radius of the EM and NEM (see Figure 4.4B and 4.7B). The medium refractive index used in the Mie scattering calculation is determined using the effective medium theory, $(n_{\mathrm{w}}\phi_{\mathrm{w}} + n_{\mathrm{o,NEM}}\phi_{\mathrm{NEM}})/(\phi_{\mathrm{w}} + \phi_{\mathrm{NEM}})$, which involves the nanodroplets and the SDS solution in the continuous phase. In the ISA, the microscale droplet component is not included in the medium refractive index due to the absence of collective scattering, which is distinct from the previous definition of n_{cont} that leads to Δn_{eff}. From Mie scattering calculation, we obtain $1/\ell^*_{\mathrm{ISA}}$ at each ϕ_{EM} and ϕ_{NEM} (see Figure 4.4C and 4.7C).

We correct the apparent MSDs, using the measured ℓ^* and the ISA in the dilute ϕ_{EM} limit, to obtain the time-dependent DWS-probe's MSDs at each ϕ: $\langle\Delta\boldsymbol{r}^2(t)\rangle = (\ell^*_{\mathrm{ISA}}/\ell^*)\langle\Delta\boldsymbol{r}_{\mathrm{a}}^2(t)\rangle$. We determine the primary plateau MSDs, $\langle\Delta\boldsymbol{r}^2\rangle_{\mathrm{p}}$, by using the dense-emulsion MSD model[57] to fit the early-time rise-to-plateau of $\langle\Delta\boldsymbol{r}^2(t)\rangle$ for the mixtures having $\phi_{\mathrm{NEM}} \geq 0.148$ and $\phi_{\mathrm{tot}} = 0.4$, and for mixtures having $\phi_{\mathrm{NEM}} \geq 0.075$ and $\phi_{\mathrm{EM}} = 0.5$. The resulting $\langle\Delta\boldsymbol{r}^2\rangle_{\mathrm{p}}$ are used to deduce the linear plateau shear elastic moduli, $G'_{\mathrm{p,GSER}}$, using the GSER of passive microrheology:

$$G'_{\mathrm{p,GSER}} = \frac{k_{\mathrm{B}}T}{\pi a_{\mathrm{eff}}\langle\Delta\boldsymbol{r}^2\rangle_{\mathrm{p}}}. \tag{4.3}$$

For all ϕ explored, we show the time-dependent $a_{\mathrm{eff}}\langle\Delta\boldsymbol{r}^2(t)\rangle$ in Figure 4.4E and 4.7E. For higher ϕ_{NEM} where the primary plateau MSDs can be extracted, the primary plateau values, $a_{\mathrm{eff}}\langle\Delta\boldsymbol{r}^2\rangle_{\mathrm{p}}$, are inversely proportional to $G'_{\mathrm{p,GSER}}$.

4.4 Results

We present the results of two sets of experimental studies made on mixtures of size-fractionated microscale and nanoscale emulsions. Each of these studies has been designed to reveal the potential impact that a substantial portion of nanoscale droplets in the droplet size

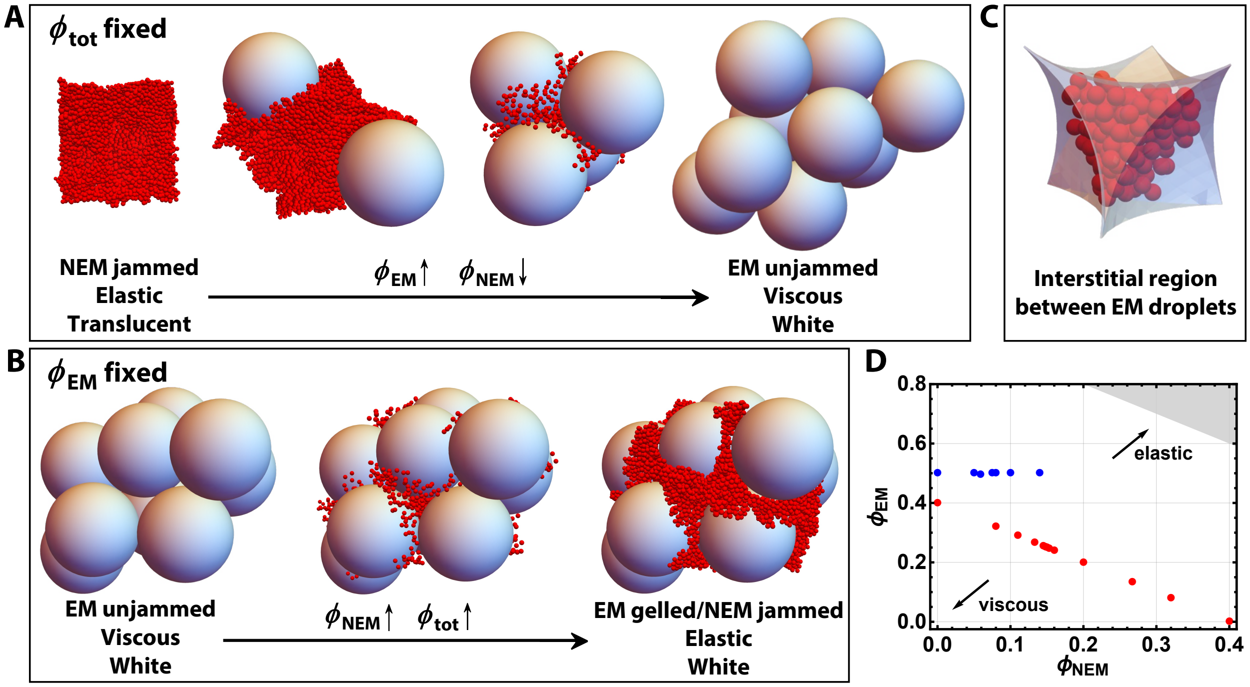

Figure 4.1. Schematic diagram of extremely bidisperse oil-in-water emulsions obtained by mixing microscale and nanoscale emulsions. The ionic surfactant concentration C and Debye screening length λ_D are fixed. (**A**) Fixed total droplet volume fraction $\phi_{\text{tot}} = \phi_{\text{EM}} + \phi_{\text{NEM}} = 0.4$ in the concentrated regime but well below the jamming limit of hard spheres. From left to right: repulsively jammed screened-charge nanoemulsion having average radius $\langle a_{\text{NEM}} \rangle = 28$ nm (small red spheres); Elastic bidisperse mixture at a low volume fraction of microscale droplets having radius $\langle a_{\text{EM}} \rangle = 605$ nm (large white spheres), where microscale droplets are subject to strong depletion attractive interaction induced by nanodroplets while nanodroplets are jammed in the effective continuous phase; Viscoelastic bidisperse mixture at higher ϕ_{EM} yet far below jamming of microscale droplets and at lower ϕ_{NEM}, where clusters of microscale droplets can form due to weak depletion attraction; Viscous emulsion having ϕ_{EM} far below jamming in absence of nanodroplets. (**B**) Bidisperse mixtures at fixed oil volume fraction of EM droplets. From left to right: Viscous emulsion having ϕ_{EM} near but below jamming in absence of nanodroplets; Microscale droplets aggregation under depletion attraction induced by nanodroplets; Gelled microscale emulsion in presence of close-packed nanodroplets. (**C**) Close-up of an interstitial region between a tetrahedron of microscale droplets, containing approximately 140 jammed nanodroplets. (**D**) Composition of the two sets of bidisperse EM-NEM mixtures having fixed $\phi_{\text{tot}} = 0.4$ (red circles) and fixed $\phi_{\text{EM}} = 0.5$ (blue circles), respectively, in terms of nanoscale oil volume fraction ϕ_{NEM}, and microscale oil volume fraction ϕ_{EM}.

distribution of the mixture could have on the physical properties of a colloidal emulsion, yet via different mechanisms. In the first study, we vary the relative component oil volume fractions of the EM and NEM droplets in a given mixture, ϕ_{EM} and ϕ_{NEM}, respectively, while fixing the total oil-droplet volume fraction at $\phi_{\mathrm{tot}} = \phi_{\mathrm{EM}} + \phi_{\mathrm{NEM}} = 0.4$ (see Figure 4.1A and red circles in Figure 4.1D). In the limit when this mixed emulsion is only a microscale emulsion at $\phi_{\mathrm{EM}} = 0.4$, no evidence of droplet jamming is predicted; however, in the limit when this mixed emulsion is only a nanoemulsion at $\phi_{\mathrm{NEM}} = 0.4$, a strong jamming shear elasticity is predicted by the EEI model. In the second study, we fix the microscale oil droplet volume fraction at $\phi_{\mathrm{EM}} = 0.5$, near but below the jamming point of the microscale emulsion, and we vary the volume fraction of the nanoscale droplets up to $\phi_{\mathrm{NEM}} = 0.14$ (see Figure 4.1B and blue circles in Figure 4.1D). This second study has been designed to explore the role that attractive depletion forces between microscale droplets, induced by the presence of the nanoscale droplets, could potentially have on the optical and mechanical properties of the mixed emulsion system. As a consequence of the extreme difference in droplet sizes, approximately 140 nanoscale droplets, when jammed, fit in an interstitial region between a close-packed tetrahedron of microscale droplets (Figure 4.1C).

4.4.1 Size distributions of fractionated nanoscale and microscale emulsions

To characterize the droplet size distributions of the nanoscale and microscale emulsions, we have performed separate dynamic light scattering of highly diluted dispersions of each. The average hydrodynamic droplet radius of the depletion-fractionated EM is $\langle a_{\mathrm{EM}} \rangle = 605 \pm 32$ nm, and its polydispersity is $\delta a_{\mathrm{EM}} / \langle a_{\mathrm{EM}} \rangle \simeq 0.23$, where δa_{EM} is the standard deviation of the droplet radial size distribution. The average droplet radius of the ultracentrifugally fractionated NEM is measured to be $\langle a_{\mathrm{NEM}} \rangle = 28 \pm 5$ nm, and its polydispersity is $\delta a_{\mathrm{NEM}} / \langle a_{\mathrm{NEM}} \rangle \simeq 0.18$.

We model the size distribution of the binary mixture by assuming that shifted log-normal functions can be used to represent the radial droplet size-distributions of the component NEM and EM, respectively. The normalized log-normal functions[136] for these are:

$$g_{\mathrm{NEM}}(a) = \frac{\exp(-\{\ln[(a - a_{\mathrm{m,NEM}})/b_{\mathrm{NEM}}]\}^2/(2c_{\mathrm{NEM}}^2))}{\sqrt{2\pi}c_{\mathrm{NEM}}(a - a_{\mathrm{m,NEM}})} \quad \text{for } \ a > a_{\mathrm{m,NEM}} \tag{4.4}$$

$$g_{\mathrm{EM}}(a) = \frac{\exp(-\{\ln[(a - a_{\mathrm{m,EM}})/b_{\mathrm{EM}}]\}^2/(2c_{\mathrm{EM}}^2))}{\sqrt{2\pi}c_{\mathrm{EM}}(a - a_{\mathrm{m,EM}})} \quad \text{for } \ a > a_{\mathrm{m,EM}}, \tag{4.5}$$

and zero for smaller a than the expressed limits. Here, $a_{\mathrm{m,NEM}}$ and $a_{\mathrm{m,EM}}$ represent the droplet radii at and below which $g_{\mathrm{NEM}}(a)$ and $g_{\mathrm{EM}}(a)$, respectively, are zero. The half-width of each log-normal function is calculated from the measured polydispersity using the corresponding standard deviation from DLS measurements: $W_{\mathrm{NEM}} = 2\delta a_{\mathrm{NEM}}$ and $W_{\mathrm{EM}} = 2\delta a_{\mathrm{EM}}$. Since the measured information from DLS does not include skewness, s, for both the NEM and EM, we assume a skewness $s = 1.3$, which is the average of a range measured for a uniform nanoemulsion using passivated gel-electrophoresis[137]. This effectively means that the distance in a from the upper limit of the half-width is 1.3 times the distance in a from the peak to the lower limit of the half-width in each of the $g(a)$ curves[136]. The parameters c_{NEM} and c_{EM} are related only to this skewness: $c_{\mathrm{NEM}} = c_{\mathrm{EM}} = \ln(s)/\sqrt{2\ln 2}$. The b-parameters are determined by the half-width and skewness of each distribution for NEM and EM, respectively: $b_{\mathrm{NEM}} = W_{\mathrm{NEM}}[s/(s^2 - 1)]\exp(c_{\mathrm{NEM}}^2)$ and $b_{\mathrm{EM}} = W_{\mathrm{EM}}[s/(s^2 - 1)]\exp(c_{\mathrm{EM}}^2)$. Using $a_{\mathrm{p,NEM}} = \langle a_{\mathrm{NEM}} \rangle$ and $a_{\mathrm{p,EM}} = \langle a_{\mathrm{EM}} \rangle$, which represent the peak locations of $g_{\mathrm{NEM}}(a)$ and $g_{\mathrm{EM}}(a)$, respectively, we calculate $a_{\mathrm{m,NEM}} = a_{\mathrm{p,NEM}} - W_{\mathrm{NEM}} s/(s^2 - 1)$ and $a_{\mathrm{m,EM}} = a_{\mathrm{p,EM}} - W_{\mathrm{EM}} s/(s^2 - 1)$. There exist alternative equivalent expressions for log-normal functions that are parameterized differently[136]. Here, we have chosen a log-normal form that explicitly depends upon the lower cut-off radius a_{m}, the radius associated with the peak a_{p}, and the half-width W; certain other equivalent log-normal forms are not parameterized using a_{m} explicitly.

The overall ϕ-weighted droplet radial size distribution of the EM-NEM mixture, shown in Figure 4.2, is calculated through:

$$p_\phi(a) = p_{\phi,\mathrm{NEM}}(a) + p_{\phi,\mathrm{EM}}(a) = \phi_{\mathrm{NEM}} g_{\mathrm{NEM}}(a) + \phi_{\mathrm{EM}} g_{\mathrm{EM}}(a) \tag{4.6}$$

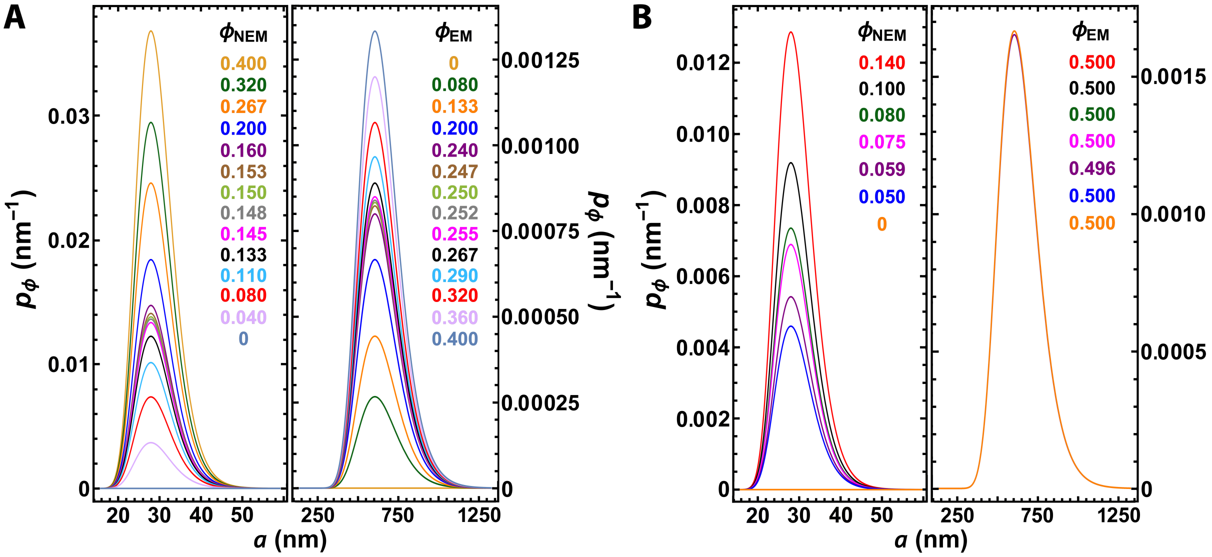

Figure 4.2. Shifted log-normal models of ϕ-weighted droplet radial size distributions, $p_\phi(a)$, of binary EM-NEM mixtures based on dynamic light scattering data [see text, equations (4.4)-(4.6)]: (**A**) fixed total droplet volume fraction $\phi_{\mathrm{tot}} = \phi_{\mathrm{NEM}} + \phi_{\mathrm{EM}} = 0.4$; (**B**) fixed volume fraction of microscale droplets $\phi_{\mathrm{EM}} = 0.5$ for different added ϕ_{NEM}.

The integral of $p_\phi(a)$ with respect to a between a_1 and a_2 corresponds to the volume fraction of oil droplets having radii between a_1 and a_2 (*i.e.* the integral of $p_\phi(a)$ over the range of a corresponding just to the NEM region yields ϕ_{NEM} and the integral of $p_\phi(a)$ over the range of a corresponding just to the EM region yields ϕ_{EM}). The integral of $p_\phi(a)$ over the entire range of a, covering both NEM and EM regions, yields ϕ_{tot}.

4.4.2 Binary EM-NEM mixtures at fixed total oil volume fraction

4.4.2.1 Optical transport: inverse scattering mean free path

The concentrated size-fractionated microscale emulsion, which has droplets comparable in size to the wavelength range of visible light, exhibits strong multiple scattering and appears milky white (see Figure 4.3A, right). To provide a quantitative reference, we have measured the inverse scattering mean free path $1/\ell^*_{\mathrm{ref}}$ of only the microscale emulsion as a function of ϕ_{EM} in SDS solution at 10 mM (see Figure 4.3B, black squares), in which the interaction

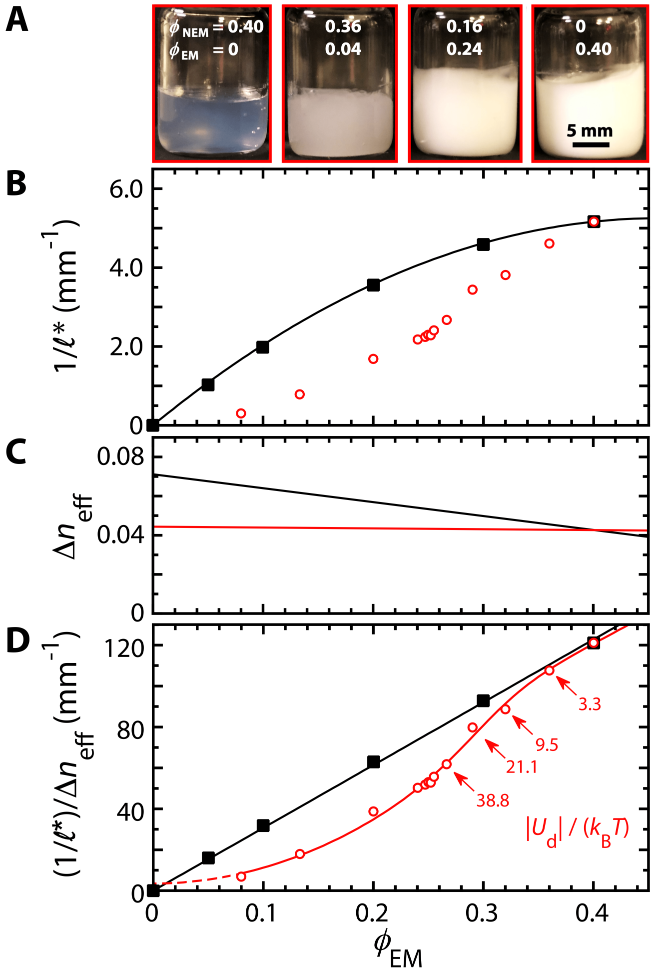

Figure 4.3. Visual appearance, inverse mean free path of optical transport, $1/\ell^*$, and effective refractive index difference, Δn_{eff} for bidisperse EM-NEM mixtures at fixed total droplet volume fraction $\phi_{\mathrm{tot}} = \phi_{\mathrm{NEM}} + \phi_{\mathrm{EM}} = 0.4$. (**A**) Photographic images of the extremely bidisperse emulsions. Increasing ϕ_{EM} and decreasing ϕ_{NEM} from left to right: translucent concentrated NEM with slight bluish tint; translucent mixture that appears hazy; well-mixed mixture that appears closer to an opaque emulsion; microscale-only opaque, milky-white emulsion. (**B**) Measured $1/\ell^*$ as a function of ϕ_{EM} for the bidisperse EM-NEM mixture (red circles). For comparison: measured $1/\ell^*_{\mathrm{ref}}(\phi_{\mathrm{EM}})$ of only the microscale emulsion by itself (at fixed $\phi_{\mathrm{NEM}} = 0$, black squares). (**C**) Calculated Δn_{eff} as a function of ϕ_{EM} (red line). For comparison: calculated $\Delta n_{\mathrm{eff,ref}}$ for the emulsion alone ($\phi_{\mathrm{NEM}} = 0$, black line). (**D**) Inverse optical scattering length from microscale droplets in the binary emulsion system normalized by the refractive index difference with the effective continuous phase containing nanodroplets, $(1/\ell^*)/\Delta n_{\mathrm{eff}}$, as a function of ϕ_{EM} (red circles). Fit using equation (4.1) shows a smooth crossover from quadratic to linear behavior as ϕ_{EM} is raised (red line, square of correlation coefficient, $R^2 = 0.995$). For comparison: measured ϕ_{EM}-dependent $(1/\ell^*_{\mathrm{ref}})/\Delta n_{\mathrm{eff,ref}}$ of only the microscale emulsion with $\phi_{\mathrm{NEM}} = 0$ (black squares) and a linear fit (black line).

between the droplets is known to be nearly hard[57]. The inverted parabolic shape of $1/\ell^*(\phi_{\mathrm{EM}})$ for $\phi_{\mathrm{NEM}} = 0$ is similar to what has been previously observed for other microscale emulsions at the same SDS concentration[57]. By contrast, the concentrated size-fractionated nanoemulsion, which has droplets much smaller in size than the wavelength range of visible light, does not scatter light as strongly and appears translucent (see Figure 4.3A, left). The relative differences in optical transport arise from droplet size, since the PDMS silicone oils in the microscale emulsion and nanoemulsion have nearly the same refractive index within 0.3% of one another. So, in the mixed system, both microdroplets and nanodroplets contribute in different proportions to optical transport.

Measurements made on the binary EM-NEM mixture at fixed $\phi_{\mathrm{tot}} = 0.4$ reveal that $1/\ell^*$ decreases linearly as ϕ_{EM} is reduced from 0.4 and gradually turns into a parabolic decrease towards lower ϕ_{EM} and higher ϕ_{NEM} (see Figure 4.3B, red circles). To analyze this result, we develop and apply an optical effective medium theory for the effective refractive index difference, $\Delta n_{\mathrm{eff}}(\phi_{\mathrm{EM}})$, between a microscale droplet and a medium outside it (see Figure 4.3C). This homogeneous effective medium has an effective refractive index, n_{eff}, that is defined to be a volume-weighted average of the refractive indexes of the SDS solution, nanoscale droplets, and other microscale droplets outside this given microscale droplet of interest (see chapter 4.3). In the reference microscale emulsion-only system, an increasing density of EM droplets results in a decreasing $\Delta n_{\mathrm{eff,ref}}(\phi_{\mathrm{EM}})$ (Figure 4.3C, black line). In the mixture, $\Delta n_{\mathrm{eff}}(\phi_{\mathrm{EM}})$ is approximately constant because PDMS oils of the EM and NEM have nearly the same refractive indexes and because ϕ_{tot} is fixed (Figure 4.3C, red line).

Assuming that the scattering (*i.e.* $1/\ell^*$) depends linearly on Δn_{eff}, we normalize the measurements in Figure 4.3B by the corresponding calculated values in Figure 4.3C; these results are shown in Figure 4.3D. For the microscale-only emulsion, this normalization leads to a linear dependence, and the slope of this line, $[(1/\ell^*)/\Delta n_{\mathrm{eff}}]_{\mathrm{ref}} = 307 \pm 2\ \mathrm{mm}^{-1}$, corresponds to the effective $1/\ell^*$ of an isolated droplet in the SDS solution (Figure 4.3D, black squares and linear fit). By contrast, for the EM-NEM mixture, this normalization does not substantially change the shape of the measured scattering; yet, it is still useful for comparison with the normalized emulsion-only system. We fit the normalized scattering of the mixture to a semi-empirical functional form that is essentially quadratic at low ϕ_{EM} and transitions smoothly to linear at high ϕ_{EM} [see equation (4.1) in chapter 4.3, Figure 4.3D, red line]. The fit parameter corresponding to the line at high ϕ_{EM} matches the slope of the black reference line: $[(1/\ell^*)/\Delta n_{\mathrm{eff}}]_{\mathrm{ref}} = 292 \pm 8\ \mathrm{mm}^{-1}$. The transition ϕ between linear and quadratic dependence is captured by the fit parameter $\phi_{\mathrm{F}} = 0.31 \pm 0.03$, which coincides with the onset of depletion attractions substantially stronger than $k_{\mathrm{B}}T$ between microscale droplets in the EM-NEM mixture. To estimate the depth of the depletion potential $|U_{\mathrm{d}}|$ between microscale droplets at contact, induced by nanodroplets, we employ Asakura-Oosawa theory[44]. We calculate the non-linear osmotic pressure Π of the nanoemulsion as a function of ϕ_{NEM} using the EEI model[37]. The values of $|U_{\mathrm{d}}|/(k_{\mathrm{B}}T)$ around the transition regime are shown in Figure 4.3D. The transition ϕ_{EM} at 0.31 corresponds to a strong depletion attractive strength of $|U_{\mathrm{d}}| \approx 9.5\ k_{\mathrm{B}}T$, near which a reduction in $1/\ell^*$ caused by depletion attraction as compared to nearly hard interaction has been observed in prior studies[115].

4.4.2.2 Effective scattering probe dynamics by DWS

Both the microscale and nanoscale droplets in a given binary EM-NEM mixture give rise to the optical scattering by different amounts, leading to an effective DWS-probe radius that could not be naively interpreted as the radius of a single microscale or nanoscale droplet. From the ratio between the normalized scattering of the mixture (Figure 4.3D, red circles and curve) and that of the microscale-only emulsion (Figure 4.3D, black squares and line), we deduce the fraction of the inverse optical transport mean free path that is attributed to the microscale component in the mixture via $f = [(1/\ell^*)/\Delta n_{\mathrm{eff}}]/[(1/\ell^*_{\mathrm{ref}})/\Delta n_{\mathrm{eff,ref}}]$. This optical transport fraction, f, for the EM-NEM mixtures having a fixed $\phi_{\mathrm{tot}} = 0.4$ is equal to 1.0 when $\phi_{\mathrm{EM}} = 0.4$ and $\phi_{\mathrm{NEM}} = 0$, and gradually decreases as ϕ_{EM} is reduced towards 0 (Figure 4.4A). For $\phi_{\mathrm{NEM}} \leq 0.1$ (*i.e.* $\phi_{\mathrm{EM}} \geq 0.3$), the dominant origin of optical scattering

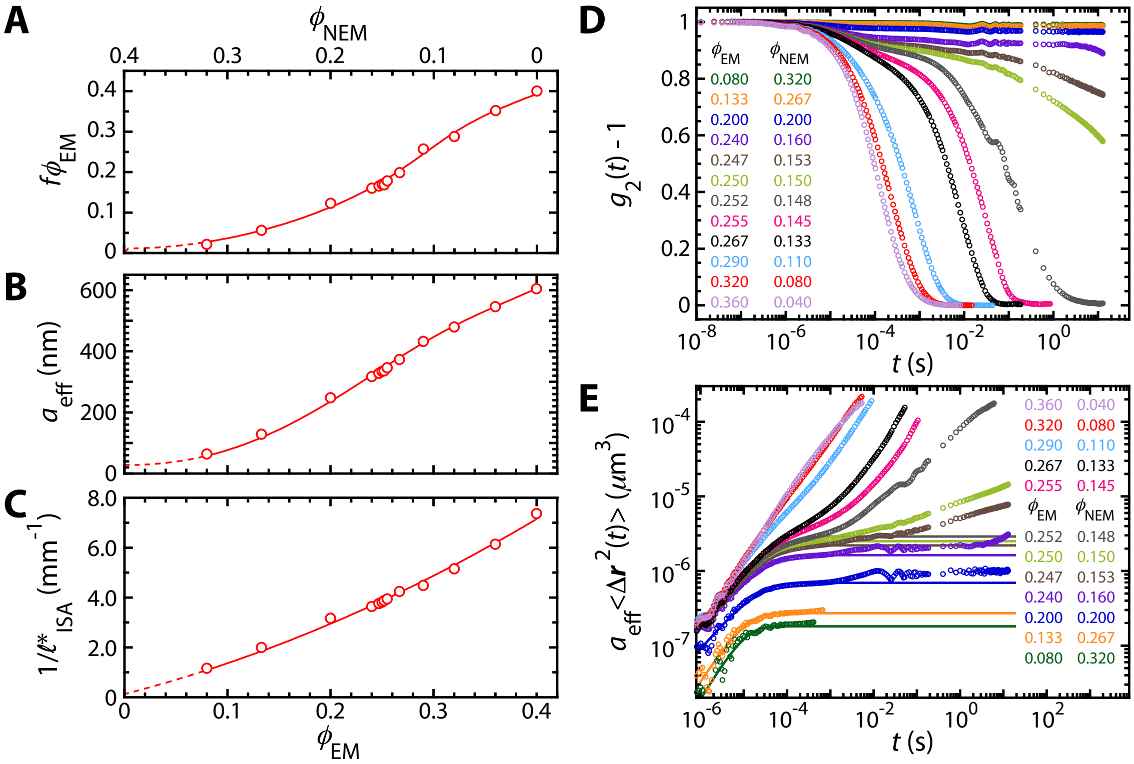

Figure 4.4. Inverse optical transport fraction, f, attributed to the EM component multiplied by ϕ_{EM}; Effective DWS-probe radius, a_{eff}; and $1/\ell^*_{\mathrm{ISA}}$ in the absence of collective scattering, as functions of ϕ_{EM}. Time-dependent DWS intensity autocorrelation functions, $g_2(t) - 1$, and mean square displacements (MSDs) multiplied by probe radius, $a_{\mathrm{eff}}\,\langle \Delta \boldsymbol{r}^2(t)\rangle$, for EM-NEM mixtures at fixed $\phi_{\mathrm{tot}} = 0.4$. (**A**) Fraction f is the ratio between $(1/\ell^*)/\Delta n_{\mathrm{eff}}$ for EM-NEM mixture (red in Figure 4.3D) and $(1/\ell^*_{\mathrm{ref}})/\Delta n_{\mathrm{eff,ref}}$ for EM-only reference (black in Figure 4.3D). $f\phi_{\mathrm{EM}}$ is the weight for the EM component in calculating a_{eff}. (**B**) DWS-probe radius deduced from measured $\langle a_{\mathrm{EM}}\rangle$ and $\langle a_{\mathrm{NEM}}\rangle$, weighted by $f\phi_{\mathrm{EM}}$ and ϕ_{NEM}, respectively. (**C**) Calculated $1/\ell^*_{\mathrm{ISA}}$ using a_{eff} and medium refractive index containing NEM droplets. Red line guides the eye. (**D**) Measured $g_2(t) - 1$ for various ϕ_{EM} and ϕ_{NEM} (color-coded, see left). DWS multi-tau correlation data span early times up to $\approx 2 \times 10^{-1}$ s, with echo data shown for $\phi_{\mathrm{EM}} \leq 0.252$; DWS multi-tau correlation functions decay fully, precluding echo data for $\phi_{\mathrm{EM}} \geq 0.255$. Lower-frequency damped oscillatory noises from DWS apparatus vibrations are superimposed on $g_2(t) - 1$, and visible starting near $t \approx 10^{-2}$ s for $\phi_{\mathrm{EM}} \leq 0.252$. (**E**) Ensemble-averaged $\langle \Delta \boldsymbol{r}^2(t)\rangle$, extracted from $g_2(t) - 1$ in part (D) and corrected for collective scattering using $1/\ell^*$ in Figure 4.3B and $1/\ell^*_{\mathrm{ISA}}$ in part (C), multiplied by a_{eff} (color-coded, see right). Fits (solid lines) at early-to-intermediate times up to $\approx 2 \times 10^{-4}$ s, which reflect average probe dynamics, provide the primary plateau MSDs, $\langle \Delta \boldsymbol{r}^2\rangle_{\mathrm{p}}$[57]. Rises in MSDs at longer times are attributed to excess MSDs[59,120] and excluded from these fits.

is the microscale droplets, given that $f \geq 0.9$ in this regime. As ϕ_{NEM} increases beyond 0.1, there is an almost linear reduction in the proportion of optical transport attributable to EM droplets, indicating that an increasing number of NEM droplets are involved in the scattering events.

As the optical scattering transitions from EM-dominated to NEM-dominated, the interpretation of DWS $g_2(t) - 1$ is quite complex. Given the absence of any directly applicable theory, here, we hypothesize that an effective probe radius can be used to interpret the resulting MSDs obtained for binary mixtures. In considering DWS dynamics, we propose that the extracted DWS MSD can be ascribed to an effective probe-radius, denoted by a_{eff}, which we define to be the volume-weighted average of the measured mean droplet radii of the EM and NEM, after taking into account their relative contribution to optical scattering, as determined by the fraction f. Specifically, we calculate $a_{\mathrm{eff}} = (f\phi_{\mathrm{EM}} \langle a_{\mathrm{EM}} \rangle + \phi_{\mathrm{NEM}} \langle a_{\mathrm{NEM}} \rangle)/(f\phi_{\mathrm{EM}} + \phi_{\mathrm{NEM}})$. When ϕ_{NEM} is zero, DWS-probes represent single EM droplets in microscale-only emulsions, and a_{eff} is equivalent to the mean EM droplet radius, $\langle a_{\mathrm{EM}} \rangle$. As ϕ_{NEM} increases and ϕ_{EM} decreases, a_{eff} decreases and approaches the mean NEM droplet radius, $\langle a_{\mathrm{NEM}} \rangle$ (see Figure 4.4B). To account for the collective scattering of the effective DWS-probes, we use this effective probe size and a medium refractive index that is determined using the effective medium theory, $(n_{\mathrm{w}}\phi_{\mathrm{w}} + n_{\mathrm{o,NEM}}\phi_{\mathrm{NEM}})/(\phi_{\mathrm{w}} + \phi_{\mathrm{NEM}})$, in the Mie scattering calculation to obtain the ϕ-dependent $1/\ell^{*}_{\mathrm{ISA}}$ in the limit of independent scattering approximation (ISA) (see Figure 4.4C). It should be noted that the medium refractive index used in the ISA calculation takes into account only the refractive index of nanoscale droplets and the SDS solution that surrounds a single microscale droplet. This is in contrast to the calculation of Δn_{eff} related to Figure 4.3C-D, where the refractive index of other microscale droplets is also included in the definition of the refractive index of the continuous phase, n_{cont} (see chapter 4.3).

Each of the measured DWS intensity autocorrelation functions, $g_2(t) - 1$, exhibits a primary decay at $t \approx 10^{-5}$ s for the EM-NEM mixture (see chapter 4.3, Figure 4.4D). For

$\phi_{\mathrm{EM}} \geq 0.255$, each $g_2(t) - 1$ fully decays to baseline in the multi-tau correlation range. By contrast, for $\phi_{\mathrm{EM}} \leq 0.252$ (*i.e.* $\phi_{\mathrm{NEM}} \geq 0.148$), $g_2(t) - 1$ exhibits a primary decay-to-plateau followed by a secondary decay at long times in the echo range. The probe MSDs $\langle \Delta \boldsymbol{r}^2(t) \rangle$ are extracted from DWS correlation functions and have been corrected for collective scattering using the ϕ-dependent structure factor, $\langle S(q) \rangle = \ell^*_{\mathrm{ISA}}/\ell^*$ (see chapter 4.3). The product of a_{eff} and $\langle \Delta \boldsymbol{r}^2(t) \rangle$ for all ϕ values studied within the restricted ϕ_{tot} is shown in Figure 4.4E. To enhance clarity, we exclude the long-time $a_{\mathrm{eff}} \langle \Delta \boldsymbol{r}^2(t) \rangle$ data, associated with the mechanical vibration-induced damped oscillatory noise, from displaying for the two samples having the lowest $\phi_{\mathrm{EM}} \leq 0.133$, as they do not affect the magnitude of the extracted primary plateau MSDs. Each probe MSD exhibits an early-time rise up to $t \approx 2 \times 10^{-5}$ s, a primary plateau indicating confinement, and then a secondary rise beyond $t \approx 5 \times 10^{-4}$ s. This secondary rise at long times resembles a feature known as an excess MSD that has been previously seen in emulsions subjected to micellar depletion attractions[59, 120]. Using a model that captures the primary rise-to-plateau features in MSDs for dense microscale emulsions[57], we fit $\langle \Delta \boldsymbol{r}^2(t) \rangle$ for the mixtures having $\phi_{\mathrm{EM}} \leq 0.252$ (see solid lines in Figure 4.4E), yielding primary plateau MSDs, $\langle \Delta \boldsymbol{r}^2 \rangle_{\mathrm{p}}$.

4.4.2.3 Plateau shear elastic modulus

For the binary EM-NEM mixtures at fixed $\phi_{\mathrm{tot}} = 0.4$, the measured $G'_{\mathrm{p,mech}}(\phi_{\mathrm{NEM}})$ increases rapidly around $\phi_{\mathrm{NEM}} \approx 0.15$, far below ϕ_{MRJ} (see red squares in Figure 4.5A). For comparison, we have performed control measurements of only the nanoemulsion, not the mixture, for $0.2 \leq \phi_{\mathrm{NEM}} \leq 0.4$ (see black diamonds in Figure 4.5A); the rapid increase in $G'_{\mathrm{p,mech}}$ of the nanoemulsion by itself occurs at higher $\phi_{\mathrm{NEM}} \approx 0.20$. Because these onset values are close but not the same, these measurements indicate that nanoemulsion jamming is likely to be playing a major role in the onset of elasticity in $G'_{\mathrm{p,mech}}$ of the binary mixture.

To determine if nanoemulsion jamming is dominating the shear rheological response of the binary mixture, we make and test the following hypothesis. For this restricted range of lower ϕ_{NEM} and ϕ_{EM}, we hypothesize that the water in the mixture can be considered to be associated primarily with the nanodroplets and that the microscale emulsion droplets, which remain well below the emulsion jamming point, do not participate substantially in the shear rheological response of the mixture. Based on this, we define a volume fraction of nanoemulsion in what amounts to an effective continuous phase, $\phi_{\mathrm{NEM,ecp}}$, in which the entire water volume is associated with the nanodroplets: $\phi_{\mathrm{NEM,ecp}} = V_{\mathrm{o,NEM}}/(V_{\mathrm{o,NEM}}+V_{\mathrm{w}}) = \phi_{\mathrm{NEM}}/(1-\phi_{\mathrm{EM}})$. This definition essentially treats the microscale emulsion droplets as elastic inclusions, which

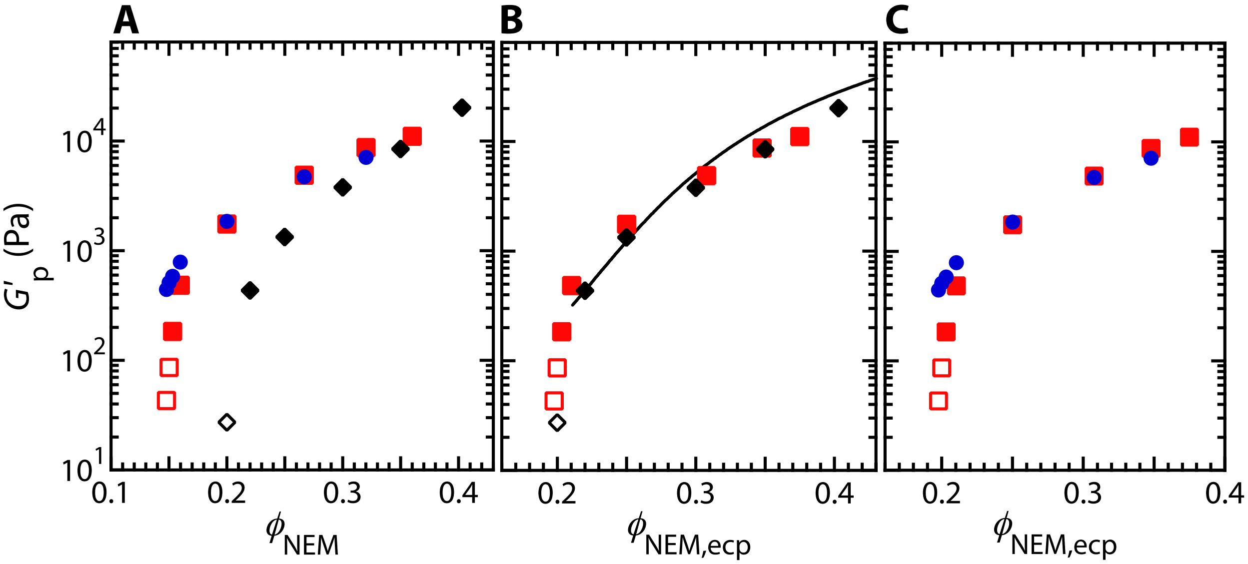

Figure 4.5. Measured plateau elastic shear moduli, G'_{p}, as a function of droplet volume fraction of nanoemulsions, ϕ_{NEM}, and droplet volume fraction of nanoemulsions in the effective continuous phase, $\phi_{\mathrm{NEM,ecp}}$, for the binary EM-NEM mixture at fixed $\phi_{\mathrm{tot}} = 0.4$. (**A**) Comparison of plateau elastic shear moduli, $G'_{\mathrm{p,mech}}(\phi_{\mathrm{NEM}})$, obtained using mechanical rheometry, for the binary mixtures (red squares); DWS-GSER microrheological plateau elastic shear moduli, $G'_{\mathrm{p,GSER}}(\phi_{\mathrm{NEM}})$ (blue circles), obtained using primary plateau MSDs that have accounted for collective scattering from Figure 4.4E; and bare nanoemulsions ($\phi_{\mathrm{EM}} = 0$, black diamonds). (**B**) Comparison of plateau elastic shear moduli $G'_{\mathrm{p,mech}}(\phi_{\mathrm{NEM,ecp}})$ measured by mechanical rheometry (red squares) with measured $G'_{\mathrm{p,mech}}(\phi_{\mathrm{NEM,ecp}})$ for bare nanoemulsions ($\phi_{\mathrm{EM}} = 0$, black diamonds), and fit using the EEI model[37] (black line). (**C**) Comparison of $G'_{\mathrm{p,GSER}}(\phi_{\mathrm{NEM,ecp}})$ (blue circles) with $G'_{\mathrm{p,mech}}(\phi_{\mathrm{NEM,ecp}})$ (red squares). Open symbols represent that G' of these emulsions exhibit strong frequency dependence; the small-strain plateau $G'_{\mathrm{p,mech}}$ are extracted from fits of $G'(\gamma)$ at a frequency of 1 rad s^{-1}, where γ represents the applied peak strain amplitude in the strain sweep measurements.

do not weaken the entire system substantially, within a dominant elastic matrix that results from nanodroplet jamming. Here, ϕ_{NEM} and ϕ_{EM} refer to volume fractions of the respective components in the binary mixture *after mixing*, not to initial volume fractions of the separate microscale and nanoscale emulsions prior to mixing.

This hypothesis of the effective continuous phase associated with the nanoemulsion causes the binary mixture's $G'_{\mathrm{p,mech}}(\phi_{\mathrm{NEM,ecp}})$ to overlap the pure NEM's $G'_{\mathrm{p,mech}}(\phi_{\mathrm{NEM}})$ and also the EEI model fit within a factor of 2 (see Figure 4.5B). Thus, we infer from this overlap that the jamming of the nanoemulsion component in the binary mixture, excluding consideration of the microscale component, largely explains the macroscopic measurement of small-strain shear elasticity of the mixture over this restricted range of ϕ_{EM} and ϕ_{NEM}. In this set of mixtures at $\phi_{\mathrm{tot}} = 0.4$, the oil volume fraction of EM droplets remains well below the jamming ϕ of the microscale emulsion.

In addition, we calculated the plateau elastic shear moduli, $G'_{\mathrm{p,GSER}}$ from the primary plateau MSDs, $\langle \Delta \boldsymbol{r}^2 \rangle_{\mathrm{p}}$, after accounting for the collective scattering of the effective DWS probes, using the generalized Stokes-Einstein relation (GSER) of passive microrheology[11] [see chapter 4.3, equation (4.3)]. This optically deduced $G'_{\mathrm{p,GSER}}$ exhibits good agreement with the mechanically measured $G'_{\mathrm{p,mech}}$, in consideration of the orthogonal distance between them that takes into account the observational errors on both ϕ and G'_{p} (see Figure 4.5A and 4.5C). While we find evidence of substantial depletion attractions between microscale droplets in the measured optical transport ℓ^* and in DWS excess MSDs, the bulk linear shear elastic response of the mixture for $\phi_{\mathrm{tot}} = 0.4$ can be explained by nanoemulsion jamming using the concept of the effective continuous phase.

Prior studies of microscale-only emulsions subjected to micellar depletion attraction have shown that in the modified GSER, there is a ϕ_{EM}-independent effective probe size factor $\alpha = 2.0$ for strongly attractive emulsions[115], and a ϕ_{EM}-dependent α ranging from 1.0 to 2.0 for intermediately depletion attractive emulsions[120], to account for the effective size of scattering probes. These probes can be local dense clusters of the microscale droplets rather than single microscale droplets in presence of micellar depletion agents. However, these studies do not incorporate the nanodroplet jamming scenario; the nanodroplets are also the depletion agents for the microscale droplets. Due to the limited structural information available, we refrain from applying the α-factor correction which accounts for the effective probe size induced by depletion, and which would be necessary to determine whether the microscale droplets are randomly distributed in the elastic matrix of the nanoemulsion or form aggregated gel structures. If we were to apply this correction, which assumes the effective probes are twice as large as the currently used probe size due to depletion, we would obtain better agreement between the calculated $G'_{\mathrm{p,GSER}}$ and the mechanically measured $G'_{\mathrm{p,mech}}$ at the onset of elasticity near $\phi_{\mathrm{NEM,ecp}} \approx 0.2$ using the same data.

4.4.3 Binary EM-NEM mixtures at fixed oil volume fraction of EM droplets

4.4.3.1 Optical transport: inverse scattering mean free path

The measured ϕ_{NEM}-dependent $1/\ell^*$ of the binary EM-NEM mixture at fixed $\phi_{\mathrm{EM}} = 0.5$ decreases as ϕ_{NEM} is raised from 0 to 0.14 (Figure 4.6A). The calculated effective refractive index difference $\Delta n_{\mathrm{eff}}(\phi_{\mathrm{NEM}})$ decreases linearly as ϕ_{NEM} is increased since a greater percentage of the medium outside any given microscale droplet is oil, leading to a smaller refractive index difference (Figure 4.6B, red line). After normalizing $1/\ell^*$ by Δn_{eff}, we fit the ϕ_{NEM}-dependent $(1/\ell^*)/\Delta n_{\mathrm{eff}}$ to a semi-empirical Fermi-like function [equation (4.2), see chapter 4.3], which captures the reduction to a plateau in the strongly attractive limit at high ϕ_{NEM} (Figure 4.6C). This additional decrease is associated with attractive depletion potentials beyond about 4 $k_{\mathrm{B}}T$ (see chapter 4.3).

4.4.3.2 Effective scattering probe dynamics by DWS

As the fraction of nanodroplets in the binary EM-NEM mixture increases while holding ϕ_{EM} constant at 0.5, the fraction of the inverse optical transport mean free path attributed to

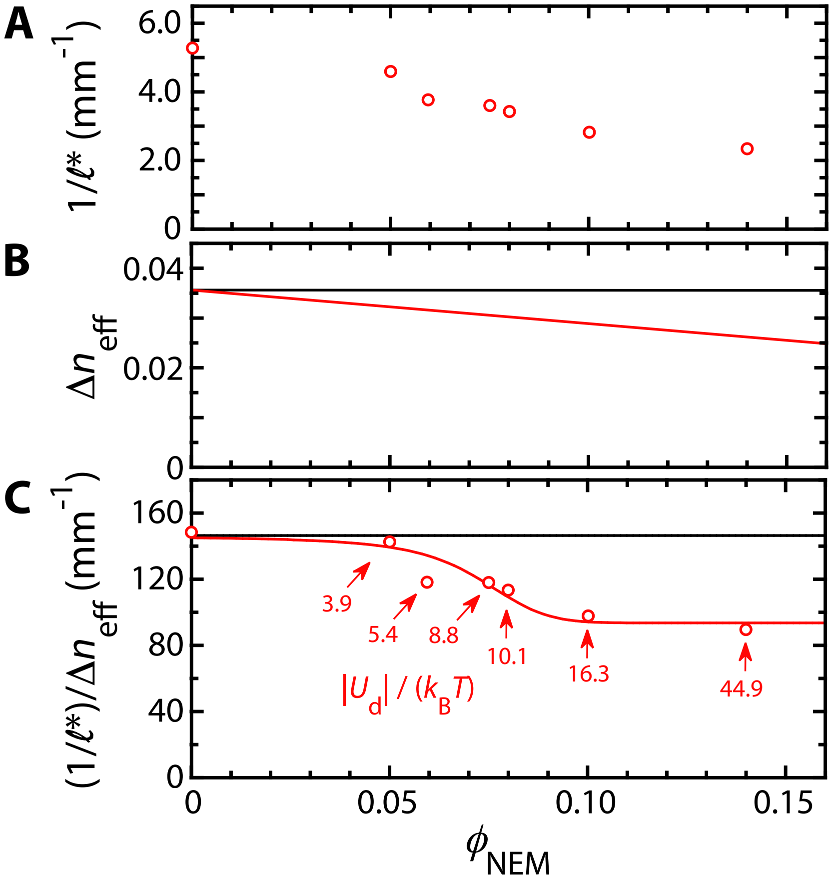

Figure 4.6. Inverse mean free path of optical transport, $1/\ell^*$, and effective refractive index difference, Δn_{eff} for the binary EM-NEM mixture at fixed oil volume fraction of EM droplets $\phi_{\text{EM}} = 0.5$. (**A**) Measured $1/\ell^*$ as a function of nanoscale emulsion droplet volume fraction ϕ_{NEM} (red circles). (**B**) Calculated Δn_{eff} as a function of ϕ_{NEM} (red line). For comparison: calculated $\Delta n_{\text{eff,ref}}$ for the emulsions alone ($\phi_{\text{NEM}} = 0$, black line). (**C**) Scattering strength normalized by the corresponding effective refractive index difference, $(1/\ell^*)/\Delta n_{\text{eff}}$, as ϕ_{NEM} is varied while keeping $\phi_{\text{EM}} = 0.5$. Fit using equation (4.2) shows a Fermi-like decay as $|U_{\text{d}}|$ increases, while $|U_{\text{d}}|$ increases exponentially as ϕ_{NEM} is raised (red line, $\text{R}^2 = 0.910$). For comparison: $(1/\ell^*_{\text{ref}})/\Delta n_{\text{eff,ref}}$ at $\phi_{\text{EM}} = 0.5$ and $\phi_{\text{NEM}} = 0$ (black line).

the microscale component decreases from 1.0 to around 0.6 when ϕ_{NEM} is increased from 0 to 0.14; therefore, $f\phi_{\text{EM}}$ decreases from 0.5 to ≈ 0.3, as shown in Figure 4.7A. The effective DWS-probe radius, a_{eff}, of the mixture decreases from 605 nm when ϕ_{NEM} is zero to 424 nm when ϕ_{NEM} is 0.14 (see Figure 4.7B). The ϕ-dependent $1/\ell^*_{\text{ISA}}$, calculated using a_{eff} from Figure 4.7B and a refractive index of medium containing NEM and SDS solution (see chapter

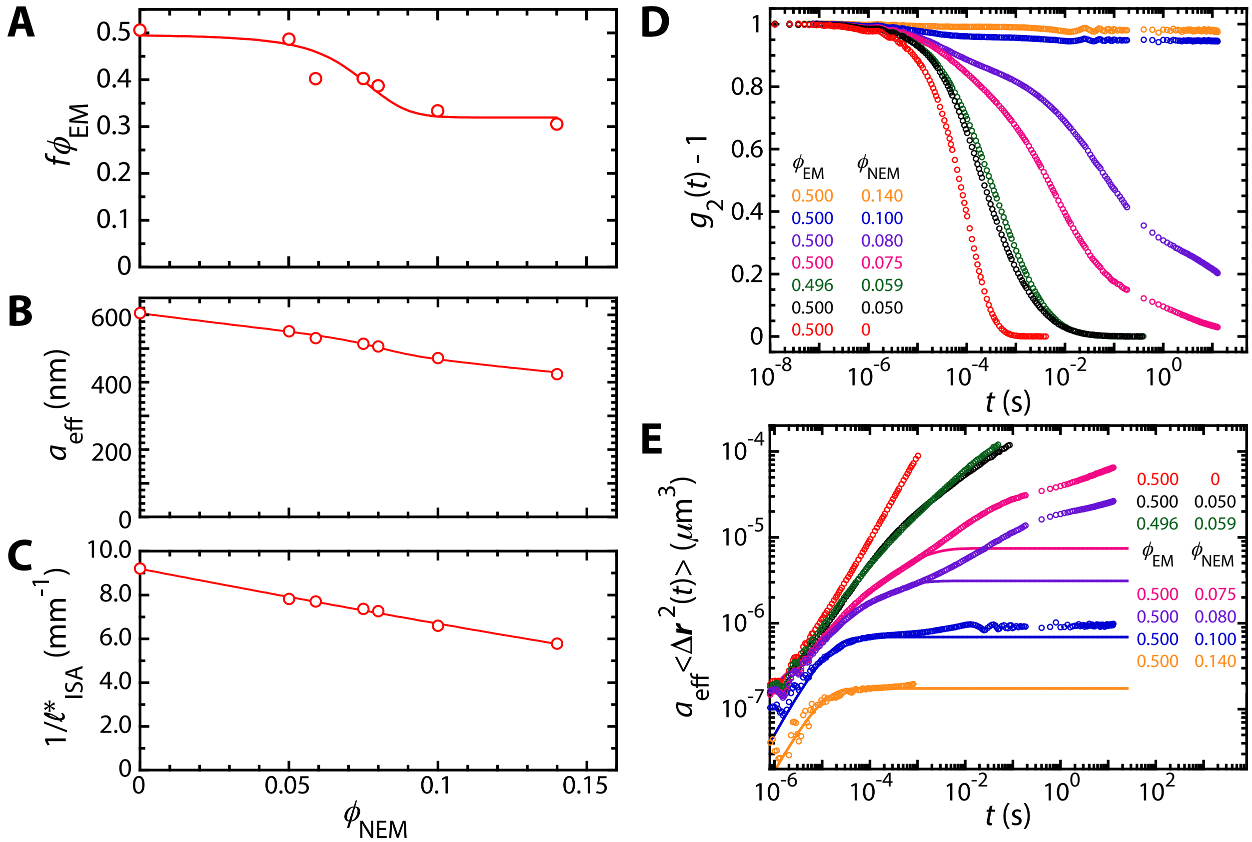

Figure 4.7. Inverse optical transport fraction, f, attributed to the EM component multiplied by ϕ_{EM}; Effective DWS-probe radius, a_{eff}; and $1/\ell^*_{\mathrm{ISA}}$, as functions of ϕ_{NEM}. Time-dependent DWS intensity autocorrelation functions, $g_2(t) - 1$, and mean square displacements (MSDs) multiplied by probe radius, $a_{\mathrm{eff}}\,\langle \Delta \boldsymbol{r}^2(t)\rangle$, of the binary EM-NEM mixture at fixed $\phi_{\mathrm{EM}} = 0.5$. (**A**) Fraction f is given by the ratio between $(1/\ell^*)/\Delta n_{\mathrm{eff}}$ for EM-NEM mixture (red in Figure 4.6C) and $(1/\ell^*_{\mathrm{ref}})/\Delta n_{\mathrm{eff,ref}}$ for EM-only reference (black in Figure 4.6C). $f\phi_{\mathrm{EM}}$ is the weight applied on the EM component in calculating a_{eff}. (**B**) DWS-probe radius deduced from measured $\langle a_{\mathrm{EM}}\rangle$ and $\langle a_{\mathrm{NEM}}\rangle$, weighted by $f\phi_{\mathrm{EM}}$ and ϕ_{NEM}, respectively. (**C**) Calculated $1/\ell^*_{\mathrm{ISA}}$ using a_{eff} and medium refractive index containing NEM droplets. Red line guides the eye. (**D**) Measured $g_2(t) - 1$ for various ϕ_{NEM} (color-coded, see left). DWS multi-tau correlation data extend from early times up to $\approx 2 \times 10^{-1}$ s and DWS echo data are shown at longer times for $\phi_{\mathrm{NEM}} \geq 0.075$; DWS multi-tau correlation functions fully decay to baseline with no echo signal measured for $\phi_{\mathrm{NEM}} \leq 0.059$. Damped oscillatory noise signals, resulting from mechanical vibrations, are superimposed on the main $g_2(t) - 1$ signals, and visible for all $\phi_{\mathrm{NEM}} \geq 0.100$. (**E**) Ensemble-averaged $\langle \Delta \boldsymbol{r}^2(t)\rangle$, which are extracted from $g_2(t) - 1$ in part (D) and corrected for collective scattering using $1/\ell^*$ in Figure 4.6A and $1/\ell^*_{\mathrm{ISA}}$ in part (C), multiplied by a_{eff} (color-coded, see right). Fits (solid lines) of DWS MSDs at early-to-intermediate, which reflect average probe dynamics, provide the primary plateau MSDs, $\langle \Delta \boldsymbol{r}^2\rangle_{\mathrm{p}}$ (see ref.[57]). Rises in MSDs at longer times are attributed to excess MSDs[59,120], and so are excluded from these fits.

4.3), decreases in a nearly linear manner with increasing ϕ_{NEM} (see Figure 4.7C).

At fixed $\phi_{\mathrm{EM}} = 0.5$, the measured $g_2(t) - 1$ for EM-NEM mixtures having $\phi_{\mathrm{NEM}} < 0.06$ fully decay to baseline. By contrast, at the highest $\phi_{\mathrm{NEM}} \geq 0.100$, $g_2(t) - 1$ exhibits a primary decay-to-plateau followed by a secondary decay-to-plateau (see Figure 4.7D). In between these ranges, we find a primary decay-to-plateau and then a secondary decay that is incomplete and non-exponential over the measurement window. We extract the probe MSDs $\langle \Delta \boldsymbol{r}^2(t) \rangle$ from measured $g_2(t) - 1$ for $\phi_{\mathrm{NEM}} \geq 0.075$; these MSDs have been corrected by the structure factor $\langle S(q) \rangle$ (see chapter 4.3) to account for collective scattering using $1/\ell^*(\phi_{\mathrm{NEM}})$ in Figure 4.6A and the $1/\ell^*_{\mathrm{ISA}}(\phi_{\mathrm{NEM}})$ in Figure 4.7C. For each of the ϕ_{NEM} explored, the product of a_{eff} and time-dependent $\langle \Delta \boldsymbol{r}^2(t) \rangle$ is shown in Figure 4.7E. Each of the probe MSDs exhibits an early-time rise up to $t \approx 2 \times 10^{-5}$ s, a gradual bending to the primary plateau, and then a secondary rise. The onset lag time of the secondary rise slightly decreases as ϕ_{NEM} increases, from $t \approx 5 \times 10^{-3}$ s when ϕ_{NEM} is 0.05 to $t \approx 5 \times 10^{-4}$ s when ϕ_{NEM} is 0.14. For each $\phi_{\mathrm{NEM}} \geq 0.075$, the primary rise-to-plateau $\langle \Delta \boldsymbol{r}^2(t) \rangle$ has been fit to the dense-emulsion MSD model (see solid lines in Figure 4.7E), yielding the primary plateau MSD, which is inversely proportional to the plateau shear elastic modulus as per the GSER of passive microrheology. For the mixture sample having the highest $\phi_{\mathrm{NEM}} = 0.14$, the long-time $a_{\mathrm{eff}} \langle \Delta \boldsymbol{r}^2(t) \rangle$ data, superimposed by the mechanical vibration-induced damped oscillatory noise, do not influence the magnitude of the extracted primary plateau MSDs and are excluded from displaying for clarity. At lower $\phi_{\mathrm{NEM}} < 0.6$, there is no distinct change in the curvature of $a_{\mathrm{eff}} \langle \Delta \boldsymbol{r}^2(t) \rangle$ in the log-log scales that can be used to extract the primary plateau MSDs with high confidence.

4.4.3.3 Plateau shear elastic modulus

The emulsion system having $\phi_{\mathrm{EM}} = 0.5$ is dominantly viscous and has no measurable $G'_{\mathrm{p,mech}}$ for $\phi_{\mathrm{NEM}} = 0$. As ϕ_{NEM} is raised in the binary EM-NEM mixture, the measured $G'_{\mathrm{p,mech}}(\phi_{\mathrm{NEM}})$ increases most rapidly around $\phi_{\mathrm{NEM}} \approx 0.08$, which is well below the jamming

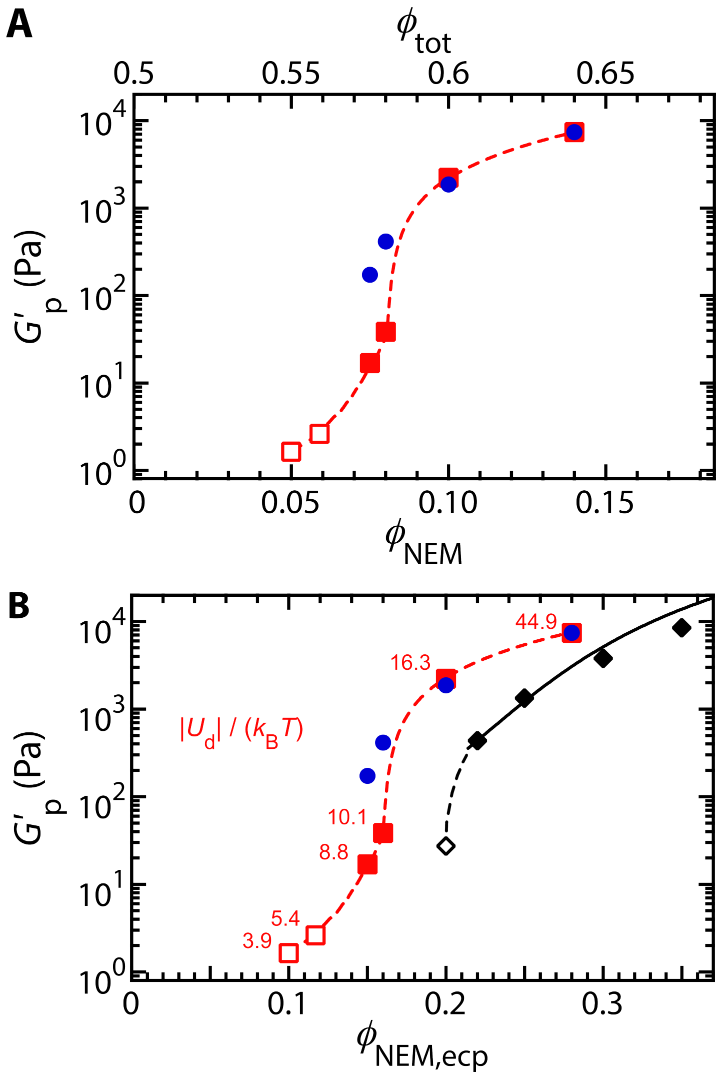

Figure 4.8. Measured plateau elastic shear moduli, G'_p, as a function of droplet volume fraction of nanoemulsions, ϕ_{NEM}, and droplet volume fraction of nanoemulsions in the effective continuous phase, $\phi_{NEM,ecp}$ for the binary EM-NEM mixture at fixed $\phi_{EM} = 0.5$. (**A**) Comparison of DWS-GSER microrheological $G'_{p,GSER}(\phi_{NEM})$ (blue circles), obtained using primary plateau MSDs that have accounted for collective scattering from Figure 4.7E, with $G'_{p,mech}(\phi_{NEM})$ measured by mechanical rheometry (red squares). Red dashed line: interpolation curve guides the eye. (**B**) Measured $G'_{p,GSER}(\phi_{NEM,ecp})$ (blue circles) and $G'_{p,mech}(\phi_{NEM,ecp})$ of the binary mixtures (red squares); red dashed line: interpolation curve guides the eye. For comparison: $G'_{p,mech}$ of bare nanoemulsions ($\phi_{EM} = 0$, black diamonds); black solid line: fit of $G'_{p,mech}(\phi_{NEM,ecp})$ using the EEI model[37] for nanoemulsions. Open symbols represent small-strain plateau $G'_{p,mech}$ extracted from fits of $G'(\gamma)$ at 1 rad s^{-1} for emulsions having frequency-dependent G'.

point of nanodroplets; yet, ϕ_{tot} is still far lower than ϕ_{MRJ} (Figure 4.8A, red squares). For $\phi_{\mathrm{NEM}} \geq 0.075$, the microrheological $G'_{\mathrm{p,GSER}}(\phi_{\mathrm{NEM}})$, calculated from the primary plateau MSDs in Figure 4.7E that have been corrected for collective scattering, using the GSER [see chapter 4.3, equation (4.3)], are shown as blue circles in Figure 4.8A. The passive microrheological $G'_{\mathrm{p,GSER}}$, obtained from optical transport and DWS dynamics measurements, and the bulk mechanical $G'_{\mathrm{p,mech}}$, obtained from shear rheometry, present an adequate agreement within the experimental and fitting error range, considering the orthogonal distance (*i.e.* total least squares) between $G'_{\mathrm{p,GSER}}(\phi_{\mathrm{NEM}})$ and $G'_{\mathrm{p,mech}}(\phi_{\mathrm{NEM}})$. If taking into account the depletion attraction that enlarges the effective DWS-probes by a factor of ≈ 2[115,120], the differences between $G'_{\mathrm{p,GSER}}$ and $G'_{\mathrm{p,mech}}$ at $\phi_{\mathrm{NEM}} = 0.075$ and 0.08 would be further reduced and the level of the agreement would be improved.

To take into account the jamming effects of nanodroplets in the EM-NEM mixture, we compare the measured $G'_{\mathrm{p,mech}}$ of these mixtures with the $G'_{\mathrm{p,mech}}$ of the reference NEM-only system as a function of $\phi_{\mathrm{NEM,ecp}}$ using the concept of the nanoemulsion's effective continuous phase (see Figure 4.8B). The rapid rise in $G'_{\mathrm{p,mech}}$ appears around $\phi_{\mathrm{NEM,ecp}} = 0.16$, which is lower than the jamming point of NEM near 0.2. At this $\phi_{\mathrm{NEM,ecp}}$ value, nanodroplets induce a strong attractive depletion potential $\approx 10\ k_{\mathrm{B}}T$ between the microscale droplets. Therefore, in addition to jamming of NEM, the depletion attractions between microscale droplets begin to play an important role in supporting bulk shear elasticity, and the use of $\phi_{\mathrm{NEM,ecp}}$ is not sufficient to cause a collapse of the measurements of the mixtures at large fixed ϕ_{EM} onto the NEM-only measurements. As $\phi_{\mathrm{NEM,ecp}}$ decreases, $G'_{\mathrm{p.mech}}$ of the mixture remains greater than the reference NEM-only $G'_{\mathrm{p,mech}}$. Just below $\phi_{\mathrm{NEM,ecp}} = 0.2$ corresponding to jamming of the NEM, $G'_{\mathrm{p,mech}}$ falls by two orders of magnitude, indicating the formation of percolating structures of EM droplets over macroscopic length scales. However, while much lower $G'_{\mathrm{p,mech}}$ is still substantial over the range where repulsive NEM-jamming is absent. For $\phi_{\mathrm{NEM,ecp}} < 0.2$, the nanodroplets are not repulsively jammed; so, the mechanical shear rigidity can be attributed to percolating gels of microdroplets subjected to strong depletion attractions.

4.5 Discussion

We have shown that extreme bidispersity in a droplet size distribution of a concentrated colloidal emulsion can be a source of striking emergent effects in that emulsion's optical transport properties, droplet dynamics, and bulk linear mechanical response to shear. These effects can arise from additional complexity in the jamming scenario, when taking into account screened-charge electrostatic repulsions between droplet interfaces, and alternatively from entropic depletion attractions between microscale droplets, caused by nanoscale droplets that act as a depletion agent. Thus, for colloidal emulsions having extreme bidispersity or other forms of extreme polydispersity, which typically extends over one order of magnitude or more in droplet radius, such emergent effects can exist and thereby preclude naïve interpretations that would be based only upon simple relative volume-fraction-weighted effective medium theories.

Our measurements of optical transport properties in extremely bidisperse colloidal emulsions, summarized in Figure 4.9, provide a sensitive indicator of the existence of depletion attractions at sufficiently high ϕ_{NEM}; these attractions are strong enough to cause microscale droplets to have a larger average coordination number. Such depletion attractions reduce the scattering strength and therefore lower $1/\ell^*$ below values that would otherwise be expected using simple effective medium theory for the effective refractive index outside a given microscale droplet. So, there is a range of higher ϕ_{NEM} that can cause strong enough depletion attractions between microscale droplets, relative to $k_{\mathrm{B}}T$, yet below the nanoemulsion jamming limit, allowing microdroplets to form aggregates or gels by exploring different configurations and approaching each other. Our measurements of optical transport properties provide key local-structural evidence for the existence of strong depletion attractions between microscale droplets in our studies, both at fixed $\phi_{\mathrm{tot}} = 0.4$ and at fixed $\phi_{\mathrm{EM}} = 0.5$, for large ϕ_{NEM}. Thus, we have demonstrated that self-induced depletion attractions can exist in an extremely bidisperse colloidal O/W emulsion, stabilized by an ionic surfactant; yet, the nanoemulsion droplets, not surfactant micelles, act as the depletion agent that can cause

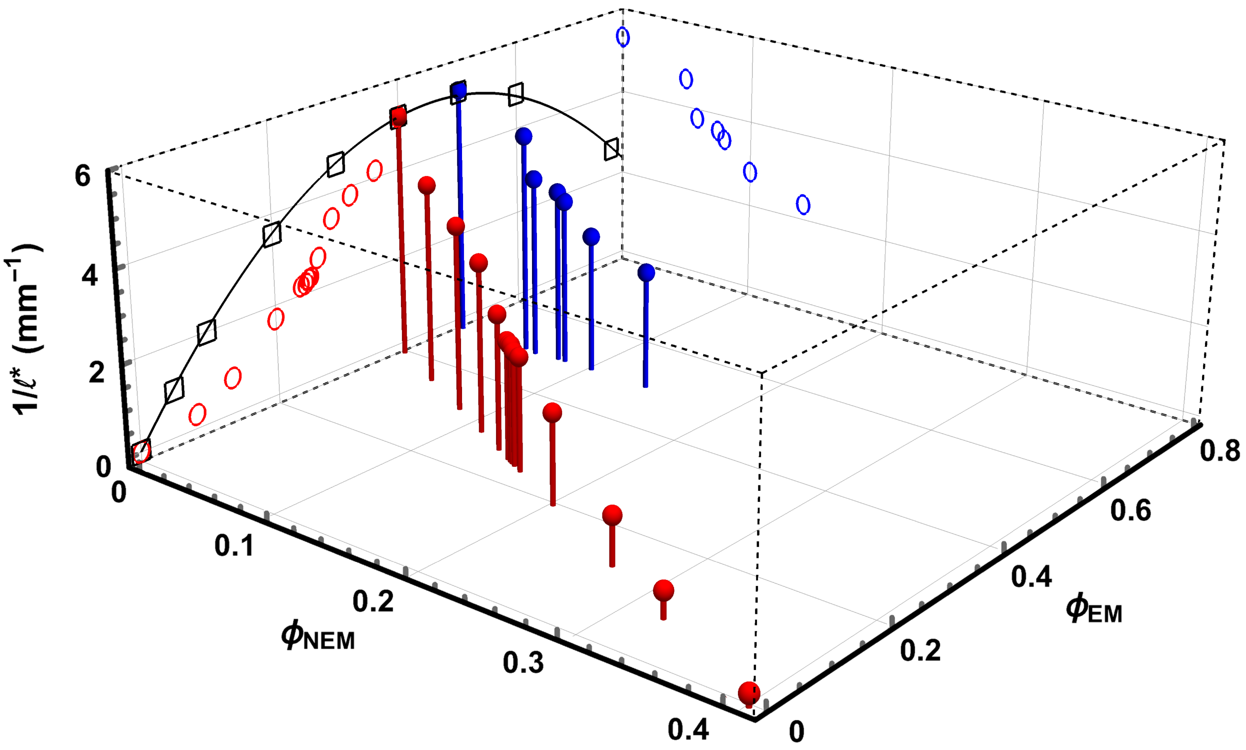

Figure 4.9. Inverse mean free path of optical transport, $1/\ell^*(\phi_{\mathrm{EM}}, \phi_{\mathrm{NEM}})$, for binary mixtures of fractionated oil-in-water emulsions and nanoemulsions having total droplet volume fraction $\phi_{\mathrm{tot}} = 0.4$ (red pins) and fixed $\phi_{\mathrm{EM}} = 0.5$ (blue pins). Open circles are projections of the two sets of $1/\ell^*(\phi_{\mathrm{EM}}, \phi_{\mathrm{NEM}})$ to planes at $\phi_{\mathrm{NEM}} = 0$ and $\phi_{\mathrm{EM}} = 0.8$, respectively. For comparison: measured $1/\ell^*(\phi_{\mathrm{EM}})$ for bare microscale emulsions (black squares) and fit to an inverse parabola (black line): $1/\ell^* = (1/\ell^*_{\mathrm{ISA}})\phi_{\mathrm{EM}}(1-\phi_{\mathrm{EM}}/\phi_{\mathrm{EM,trans}})$, where $1/\ell^*_{\mathrm{ISA}} = (22.9 \pm 0.1)\ \mathrm{mm}^{-1}$, $\phi_{\mathrm{EM,trans}} = 0.918 \pm 0.003$ ($\mathrm{R}^2 = 0.994$).

aggregation and gelation of the microscale droplets. Therefore, the observed decrease in scattering and turbidity of this extremely bidisperse emulsion, as indicated by the reduction in $1/\ell^*$ beyond what simple effective medium theory would describe, can be linked to an increase in the average local coordination number of microscale droplets in close proximity in such depletion-induced aggregates or gels.

Our measurements likewise show that DWS, when properly interpreted at high volume fractions of probe droplets, can provide MSDs of microscale droplets in this extreme bidisperse emulsion that are useful for quantitative passive microrheological interpretation through the GSER. Our study shows that an effective probe radius a_{eff} can be used to interpret DWS MSDs in the GSER; this a_{eff} is a volume-weighted average of radii for microscale droplets and nanoscale droplets after accounting for their relative scattering contributions through the factor f, which is defined from the measured $1/\ell^*$. In addition, this is true both when the jamming of the nanoemulsion is the dominant source of the shear elasticity and also when attractive gels of microscale droplets are formed through strong slippery depletion attractions. Considering a wider range of possible bidisperse colloidal droplet size distributions than those we have studied, we anticipate that performing quantitative microrheology will be much more challenging in the limit where scattering cannot be associated only with size-fractionated microscale emulsion droplets having a well-defined $\langle a_{\mathrm{EM}} \rangle$. Thus, it is likely that the interpretation of DWS for broadly polydisperse colloidal emulsions in terms of a single meaningful probe MSD and the passive microrheological interpretation, will be considerably more challenging than for this extremely bidisperse colloidal emulsion that we have investigated. Our observation of excess MSDs at long times, rather than simple plateau behavior, when $|U_{\mathrm{d}}|$ is substantially larger than $k_{\mathrm{B}}T$, also supports the interpretation that depletion attractions are playing a role in the microscale droplet dynamics; such excess MSDs have also been observed for microscale emulsions subjected to micellar depletion attractions caused by excess surfactant far above the critical micelle concentration. Thus, the presence of self-induced depletion attractions in this extremely bidisperse emulsion can be detected using the long-time behavior of measured DWS correlation functions and MSDs, not just through the optical transport properties.

The bulk linear shear elasticity of this extremely bidisperse colloidal emulsion, while systematic as a function of ϕ_{NEM} and ϕ_{EM}, cannot be described by simple effective medium theory, as shown in Figure 4.10. Instead, in cases where ϕ_{EM} is well below the jamming limit for the microscale droplets, this elasticity can be explained by the jamming of the nanoemulsion droplets in an effective continuous phase that apportions all of the water volume in the system only to the nanodroplets. In this limit of lower ϕ_{EM}, corresponding to the study at fixed $\phi_{\mathrm{tot}} = 0.4$, the microscale emulsion droplets act only as inclusions that

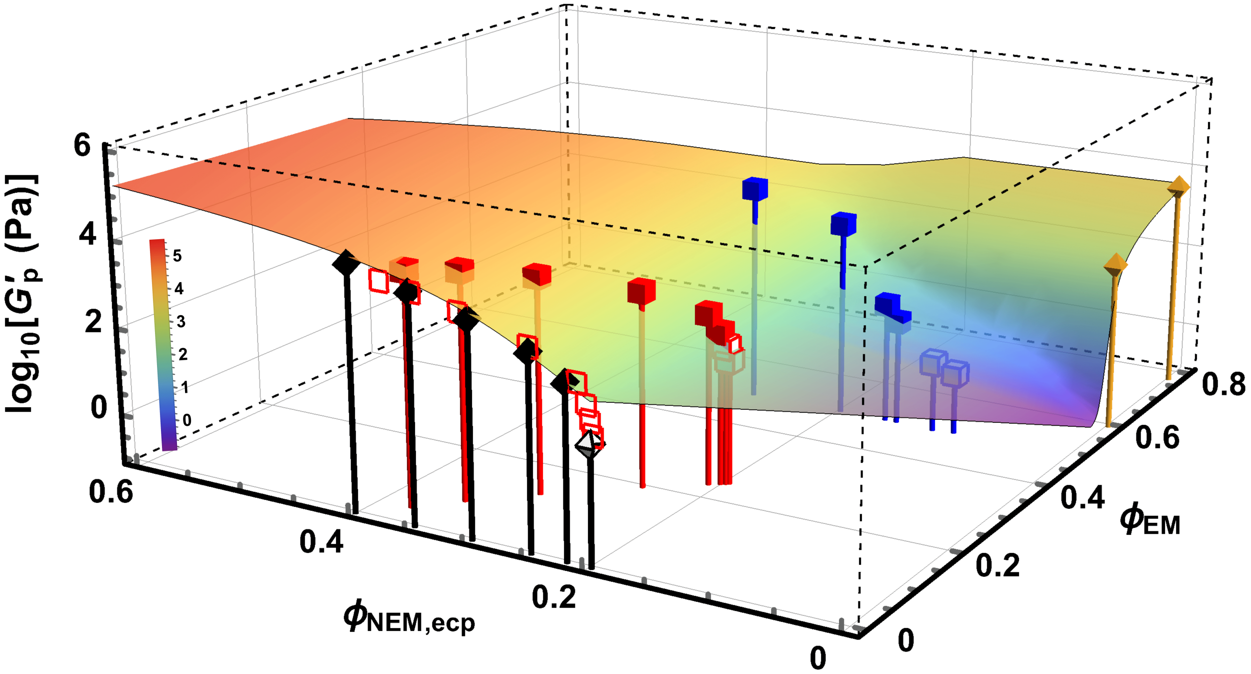

Figure 4.10. Measured plateau elastic shear moduli, $G'_p(\phi_{EM}, \phi_{NEM,ecp})$, using mechanical rheometry for binary EM-NEM mixtures at fixed total droplet volume fraction $\phi_{tot} = 0.4$ (red cubes from Figure 4.3B) and fixed $\phi_{EM} = 0.5$ (blue cubes from Figure 4.6B). For comparison: measured $G'_p(\phi_{NEM,ecp})$ for bare nanoemulsions (black diamonds) and $G'_p(\phi_{EM})$ for bare emulsion (tan diamonds). Rainbow-colored surface: plateau elastic shear moduli calculated from the $G'_{p,EEI}$ predicted via the Entropic, electrostatic, and interfacial (EEI) model[37] using simple effective medium theory (EMT): $G'_{p,EMT,EEI}(\phi_{EM}, \phi_{NEM,ecp}) = [G'_{p,EEI,EM}(\phi_{EM})\phi_{EM} + G'_{p,EEI,NEM}(\phi_{NEM,ecp})\phi_{NEM,ecp}]/(\phi_{EM} + \phi_{NEM,ecp})$. Open red squares are projections of $G'_{p,EMT,EEI}$ for fixed $\phi_{tot} = 0.4$ to the plane at $\phi_{EM} = 0$.

do not substantially impact the value of $G'_{p,mech}$; so, $G'_{p,mech}(\phi_{NEM,ecp})$ of the extreme bidisperse emulsion matches the jamming curve $G'_{p,mech}(\phi_{NEM})$ of the nanoemulsion-only control study. By contrast for ϕ_{EM} near but below jamming, corresponding to the study at fixed $\phi_{EM} = 0.5$, for progressively higher ϕ_{NEM}, we find that the measured increase in $G'_p(\phi_{NEM})$ cannot be explained merely using the effective continuous phase of nanoemulsion jamming. Instead, depletion-induced attractive gel formation of the microscale droplets, which have ϕ_{EM} near but below the microscale jamming point, is the source of the rise in G'_p as the concentration of nanoemulsion depletion agent causes $|U_d|$ to become large compared to

$k_\mathrm{B}T$. This interpretation of both optical transport and linear mechanical shear response for extremely bidisperse emulsions in our study at fixed $\phi_\mathrm{EM} = 0.5$ is also consistent with prior experiments on micelle-induced depletion attractions between microscale droplets that causes slippery cluster aggregation and gelation[115], where ϕ_EM is near but below the hard-sphere jamming point.

In addition to self-induced depletion effects, we have also shown that elastic jamming of the depletion agent can occur as $\phi_\mathrm{NEM,ecp}$ is raised above the nanoemulsion's jamming point, thereby precluding rearrangement of the microscale droplets and inhibiting long-time cluster-cluster aggregation and gel formation. So, we have shown that the jamming of a depletion agent into an elastic solid can occur in certain scenarios of colloidal aggregation and gelation when the concentration of the depletion agent becomes very large. This jamming of the depletion agent effectively limits the applied osmotic pressure that can be used in depletion-driven assembly scenarios, since motion of the larger structures into different relative configurations is precluded by the elasticity of the jammed depletion agent. Here, the use of nanoemulsions over other depletion agents, such as surfactant micelles, polymer micelles, and polymers, is advantageous because each nanodroplet has a well-defined incompressible volume; whereas, the shapes, sizes, and effective aggregation number of many micellar and polymer structures are known to change in the high concentration limit. Likewise, for certain relative compositions of nanoscale and microscale droplets, we infer that long-time aging effect could occur for some regions of ϕ_NEM and ϕ_EM; here, our two main studies have utilized a protocol that has been designed to provide systematic optical, dynamic, and mechanical responses after loading transients have died out but before long-term aging could play an important role. This protocol has been successfully applied previously to microscale emulsions in the presence of a micellar depletion agent.

Our study of bidisperse colloidal emulsions extends into high ϕ_EM and ϕ_NEM; this regime is basically inaccessible to bidisperse systems of charge-stabilized solid colloidal spheres because solid colloidal spheres typically undergo irreversible solid-solid aggregation when strongly concentrated toward the jamming limit. Such irreversible aggregation is undesirable, since it precludes controlling the volume fractions through subsequent mixing and dilution. By contrast, the deformability of the droplets in emulsions provides reversibility in mixing and dilution by avoiding this solid-solid aggregation, and droplet deformability thereby enables us to make, control, and study stable binary mixtures of emulsions and nanoemulsions that remain soft solids over a much broader range of ϕ_{EM} and ϕ_{NEM}. Thus, considering dispersed colloidal systems broadly, emulsions prove to be a more flexible colloidal system for probing jamming and depletion effects over a greater range than colloidal systems composed of solid spheres.

In summary, our comprehensive set of measurements on extreme bidisperse colloidal emulsion provides a key benchmark for future theories of broadly polydisperse colloidal systems; such theories can be compared to this comprehensive set, which relates to local structure and dynamics of the microscale droplets, through $1/\ell^*$ and DWS MSDs, as well as the bulk linear shear elastic response through G'_{p}. We have shown that self-induced depletion attractions can lead to changes in both optical transport through and shear elasticity of colloidal emulsions having extreme bidispersity, and we anticipate that these emergent effects could also be seen in certain broadly polydisperse colloidal emulsions, too. Moreover, because charge-stabilized O/W nanoemulsions have a lower jamming point than charge-stabilized O/W microscale emulsions, when considered at the same ionic surfactant concentration and Debye screening length, typically the jamming of the nanoemulsion dominates the rheological response of the extremely bidisperse emulsion when ϕ_{EM} is well below the microscale emulsion's jamming point. If non-ionic surfactants might be used instead, different findings and interpretations could result.

Our findings for extremely bidisperse colloidal O/W emulsions stabilized by a simple ionic surfactant contrast with prior findings of extremely bidisperse colloidal polymer solutions. When a small percentage of a high molecular-weight non-electrolyte polymer is added to a viscous polymer solution, composed of low molecular-weight (MW) polymer of the same type in a good solvent, the added high MW polymer can lead to a dominant low-frequency shear-elastic response. This elastic response is a consequence of the much larger radius of gyration and, consequently, much lower overlap concentration of the high MW polymer. By contrast, in our extremely bidisperse ionic O/W emulsions, a small volume fraction of much larger microscale droplets added to a nanoemulsion does not lead to the same consequence; instead, such larger droplets merely serve as large-scale defect structures within the nanoemulsion without substantially influencing the jamming of the nanodroplets. Moreover, the formation of strong, shear-rigid gels of microscale droplets by slippery aggregation is not observed at ϕ_{EM} well below the jamming limit of the microscale droplets. Thus, the nanoemulsion component of the size distribution in extremely bidisperse colloidal emulsions will typically dominate the emulsion's mechanical response through nanodroplet jamming mediated by the screened-charge interfacial repulsion. In addition, nanodroplet-induced depletion attractions between microscale droplets can lead to gelation and elasticity for ϕ_{EM} near but below the jamming point of the microscale emulsion. Because droplets have fully two-dimensional surfaces, whereas simple polymers in a good or theta solvent are quasi-one-dimensional coil-like objects, depletion attractions far in excess of $k_{\mathrm{B}}T$ can be created over a greater range of bidisperse compositions in emulsion systems, again leading to large increases in G'_{p}. Such increases are not captured in a simple effective medium theory, which does not include entropic depletion that can be present in extremely bidisperse colloidal systems.

We anticipate that our studies will motivate additional work, both experimental and theoretical, that will further explore and clarify the role that colloidal size-polydispersity can have in influencing macroscopic physical properties of complex colloidal systems. Although we have discussed our results primarily using jamming and depletion concepts, which are centrally important, the glass transition could also have an impact in the rheology and long-time DWS correlation functions at a more detailed level. For example, the colloidal hard-sphere glass transition, which marks the ergodic-nonergodic transition for ideally monodisperse spheres, is known to occur at a glass transition volume fraction $\phi_{\mathrm{g}} \approx 0.56$ to 0.58[96–98], somewhat below the jamming point $\phi_{\mathrm{MRJ}} = 0.646$. So, uniform colloidal emulsions, which effectively have hard interdroplet interactions, could exhibit a weak zero-frequency entropic shear elasticity for $\phi < \phi_{\mathrm{MRJ}}$ before the onset of droplet jamming[135]. Additional theoretical work is needed to clarify how the glass transition and long-time relaxations are modified in broadly polydisperse colloidal systems, including systems having extreme bidispersity. Moreover, determining if there are meaningful interpretations of DWS in terms of MSDs, perhaps based on the notion of an average probe-sphere radius, for highly concentrated polydisperse colloidal systems, including emulsions, remains to be explored. Theoretical calculations of $1/\ell^*$ and a_{eff}, made over a wide range of size-ratios and droplet volume fractions of colloidal binary emulsion systems, are needed to compare directly with our measurements. Likewise, it remains to be seen if DWS-based forms of passive microrheology can be used to determine mechanical shear elasticities of broadly polydisperse emulsions that match with bulk shear rheometry measurements made on the same emulsions. In addition, more sophisticated theoretical models, which go beyond the EEI model, are needed for predicting macroscopic optical transport and rheological properties of polydisperse colloidal emulsions having complex size-distributions. Our studies here indicate that such models would need to include the notion of an effective continuous phase volume fraction for the nanoscale components of the size distribution that can also serve as depletion agents for the microscale components of the size distribution. To develop a general model, including a depletion attraction, derived solely from the droplet size distribution, as a term in the interdroplet interaction potential would be necessary. In addition, accounting for the different heterogeneous structure of attractively gelled emulsions, compared to repulsively jammed emulsions, would also be necessary. A term describing a depletion attraction has been explicitly included in a recent model of the total pair-interaction potential energy between droplets[138]; while noteworthy and in the right direction, this model does not account for entropic and interfacial contributions at high ϕ near and beyond the jamming point. It might be possible to include a depletion attraction in the EEI model; yet, even such a modification would not necessarily capture structural differences between repulsively jammed and attractively gelled emulsions. Given these many exciting challenges, there is a rich future ahead for advances in the science of broadly polydisperse colloidal systems.

Chapter 5 - Signatures of nanoemulsion jamming and unjamming in stimulated-echo NMR

Reproduced with permission from Xu, Y., Nelson, M. L., Seymour, J. D., and Mason, T. G., “Signatures of nanoemulsion jamming and unjamming in stimulated-echo NMR.” *Phys. Rev. E* 107(2), pages 024605 (2023).

5.1 Abstract

The unjamming of elastic concentrated nanoemulsions into viscous dilute nanoemulsions, through dilution with the continuous phase, offers interesting opportunities for a pulsed-field gradient (PFG) NMR, particularly if the nanoemulsion is designed to take advantage of the nuclear specificity offered by NMR. Here, we make and study size-fractionated oil-in-water nanoemulsions using a perfluorinated co-polymer silicone oil that is highly insoluble in the aqueous continuous phase. By studying these nanoemulsions using ^{19}F stimulated-echo (StE) PFG-NMR, we avoid any contribution from the aqueous continuous phase, which contains a non-fluorinated ionic surfactant. We find a dramatic change in the ^{19}F PFG-NMR decays at high field-gradient strengths as the droplet volume fraction, ϕ, is lowered through dilution. At high ϕ, observed decays as a function of field-gradient strength exhibit decay-to-plateau behavior, indicating jamming of nanodroplets, which contain ^{19}F probe molecules, in an elastic material reminiscent of a nanoporous solid. In contrast, at lower ϕ, only a simple decay is observed, indicating that the nanodroplets have unjammed and can diffuse over much larger distances. Through a comparison with bulk mechanical rheometry, we show that this dramatic change coincides with the loss of low-frequency shear elasticity

of the nanoemulsion.

5.2 Introduction

Nuclear magnetic resonance (NMR) is a powerful and sensitive experimental technique that can reveal structure and dynamics within both simple homogeneous and complex heterogeneous forms of condensed matter. Pulsed-field gradient (PFG) NMR provides access to the dynamics of molecules which contain specific nuclei of interest[139]. In one particular application of PFG-NMR, investigations of the dynamics of liquid molecules in nanoporous solids have revealed the very substantial impact of molecular confinement within nanopores[140]. Because the nanopores are sufficiently small, the high degree of spatial confinement of the liquid molecules, as these experience quiescent Brownian excitations, can be readily detected at high field-gradient strengths. Instead of exhibiting a simple exponential decay, as in a bulk liquid, the PFG-NMR signal does not fully decay when a liquid is so highly confined within nanopores. The substantial impact of nanoporous confinement on molecular diffusion has been observed using ^{1}H PFG-NMR and reported for poly-dimethylsiloxane silicone oil in open-pore polymeric host matrices[141], water in single-walled carbon nanotubes[142], hexadecane in core-shell latex particles[143], hexane in nanoporous zeolite crystallites[144], and eicosane in electrochemically etched silicon nanochannels[145]. In particular, the simple exponential decay associated with molecular diffusion in the bulk liquid can transition to a decay-to-plateau behavior[146] for the same liquid that is highly confined within a nanoporous solid[140].

Investigating the molecular dynamics of polymers subjected to shear or flow has opened up an application of PFG-NMR equipped with rheometer components, known as Rheo-NMR[147,148]. Probe molecules can either be attractively bound to or repulsively confined by other neighboring molecules; examples include a solid phase of bulk polymers[147,149] and a glassy state of concentrated polymer solutions[150]. Different techniques, such as NMR spectroscopy, relaxometry, diffusivity and velocity imaging, have been applied to study the microscopic response to shear- and flow-induced anisotropy in bulk materials[149–152]. While these prior Rheo-NMR experiments have combined certain aspects of rheology and NMR, so far these approaches have not been based on the notions of passive microrheology[11], even as such a possibility has been suggested previously[12].

Nanoemulsions are dispersions of liquid droplets having sub-100 nm radii in an immiscible continuous solution phase that are stabilized against subsequent coalescence by a surfactant[23, 24, 153]. Customized nanoemulsions are continuously being developed and applied in many different areas, including pharmaceuticals and industrial products[154]. Although the nanoemulsion is composed entirely of liquids, if the volume fraction of droplets, ϕ, is raised beyond the jamming point, a well-stabilized nanoemulsion becomes a soft elastic solid as a consequence of a combination of interfacial tension and interfacial repulsion between the jammed nanodroplets in close proximity[10]. These jammed nanodroplets are confined by neighboring nanodroplets, and the positional structure of the solid nanoemulsion resembles that of a disordered glass in the absence of strong interdroplet attractions[24]. Concentrated nanoemulsions can mimic disordered closed-pore nanoporous solids when ϕ is above the jamming point. Interestingly, this nanoporous solid can effectively be melted through dilution with sufficient continuous-phase solution, thereby lowering ϕ below the jamming point. Thus, nanoemulsions could provide a route for studying what happens to molecular dynamics when an elastic closed-pore nanoporous material is melted as the pores (*i.e.* nanodroplets) effectively transition from being confined to unconfined as ϕ is reduced. If the nanoemulsion could be customized appropriately, in principle, PFG-NMR could then be used to probe the dynamics of only the dispersed-phase oil molecules within the nanodroplets, and thus could potentially provide a sensitive means of exploring droplet unjamming as the closed-pore nanoporous solid melts, since the molecular dynamics are inherently coupled to the nanodroplets' dynamics.

While ^{1}H PFG-NMR has many different important uses, its potential application for studying confined molecular diffusion in simple oil-in-water nanoemulsions would likely be difficult to interpret because hydrogen is extensively present both in the water of the continuous phase as well as in the most common hydrocarbon and silicone oils in the dispersed droplet phase[155]. Consequently, it would be desirable to consider ^{19}F PFG-NMR as an alternative, since this can create comparably strong signals as ^{1}H PFG-NMR. Silicone oils having perfluorinated side groups offer a potential route for developing a stable oil-in-water nanoemulsion, in which ^{19}F-laden silicone oil molecules are present only within the interior of the constituent nanodroplets. While prior experiments demonstrated that stable perfluorinated silicone oil-in-water nanoemulsions could be produced, these experiments relied upon a perfluorinated surfactant soluble only in the aqueous continuous phase[156]. Such use of a perfluorinated surfactant in combination with a perfluorinated oil would be less desirable, since ^{19}F PFG-NMR would yield a convolution of signals from surfactant molecules experiencing unconfined diffusion in the continuous phase, adsorbed surfactant molecules diffusing on the interfaces of nanodroplets, and also oil molecules experiencing confined diffusion within the nanodroplets.

Consequently, in order to study only the dynamics of the oil molecules within nanodroplets, it would be desirable to formulate a special customized perfluorinated oil-in-water nanoemulsion that is extremely stable even when concentrated to high ϕ above jamming, yet does not rely upon perfluorinated surfactant for stability. In addition, it would be desirable for this nanoemulsion to have a narrow droplet size distribution, and also for the perfluorinated silicone oil to be very highly insoluble in the aqueous continuous phase so that interdiffusion of oil molecules between different nanodroplets, which can lead to Ostwald ripening, is avoided. For such a highly customized nanoemulsion, in principle, the total average molecular motion of ^{19}F-laden oil molecules would depend in part on the degree of nanodroplet motion and hence ϕ relative to the nanodroplet jamming point. Detecting nanodroplet unjamming by reducing ϕ in such a customized perfluorinated nanoemulsion would be an important first step towards finding a way to use PFG-NMR for quantitative passive microrheology based on inferred motion of colloidal structures (*i.e.* nanodroplets), as has been previously suggested more broadly.

This overall approach is different than prior investigations involving PFG-NMR on other emulsion systems. Several of these investigations have focused on extracting distributions of droplet (*i.e.* cavity) sizes by fitting the signal attenuation, typically assuming a log-normal distribution[157–160]. Moreover, for emulsions in which the dispersed phase has a reasonably high solubility in the continuous phase, complex transport of molecules can be observed as these molecules hop intermittently from one droplet to another through the continuous phase[161,162], akin to transport of liquid molecules in solid open-pore porous media having larger cavities and narrow constrictions[163]. While some PFG-NMR studies of emulsions have been made previously, examining how droplet jamming and unjamming in highly concentrated monodisperse nanoemulsions affects PFG-NMR attenuation still remains largely unexplored.

Here, we have created a customized, size-fractionated, highly stable ^{19}F-oil-in-water nanoemulsion system, having screened-charge repulsive droplet interactions, that provides a useful model system, and we show using ^{19}F StE PFG-NMR that droplet jamming can lead to a strong sub-diffusive signal in the effective molecular-probe MSDs. We obtain high-quality functional fits of the effective MSDs, showing a smooth rise-to-plateau transition at each higher ϕ above the droplet jamming point. Through comparison with macroscopic rheological measurements, we associate the changes in these effective MSDs with the rheological transition between viscous unjammed nanoemulsions at lower ϕ and elastic jammed nanoemulsions at higher ϕ. Furthermore, by interpreting the mechanical measurements using the theoretical framework of passive microrheology, we extract plateau MSDs of nanodroplets in elastic nanoemulsions at high ϕ. By combining both NMR measurements with the passive microrheological interpretation of these mechanical measurements, we show that the nanoemulsion's unjamming transition is consistent with a Lindemann melting criterion of 0.3 known for a wide range of materials[164].

5.3 Experimental

5.3.1 Emulsion preparation and characterization

We have designed and prepared an oil-in-water fluorinated nanoemulsion (O/W FNEM) composed of 48%:52% poly-(3,3,3-trifluoropropyl-methylsiloxane):poly-(dimethylsiloxane) block copolymer (FMS oil, Gelest Inc.; mass density: $\rho_\mathrm{o} = 1.16$ g mL^{-1}; average molecular weight: MW$_\mathrm{o}$ = 1800 g mol^{-1}; kinematic viscosity: $\nu_\mathrm{o} = 124$ cSt), sodium dodecyl sulfate (SDS, Fisher Scientific; electrophoresis grade 99% purity), and deionized water (Millipore Milli-Q Academic; resistivity: 18.2 MΩ cm). After conducting a series of emulsification and stability screening tests using a variety of ^{19}F-containing oils, we have selected block-copolymer FMS because it: is highly perfluorinated to provide strong NMR signal-to-noise, has a low enough viscosity to facilitate fabrication of an nanoemulsion using only high flow-rate emulsification processing without evaporative ripening[23, 24, 165], has a high enough molecular weight to preclude Ostwald ripening, and remains stable against coalescence when using only a standard non-perfluorinated ionic surfactant, SDS. Because FMS is highly insoluble in the continuous aqueous phase, as revealed by the absence of Ostwald ripening, the ^{19}F-laden oil molecules do not migrate appreciably through the continuous phase from one droplet to another. Also, our use of a non-fluorinated SDS surfactant, which is atypical in most formulations of stable fluorinated O/W emulsions, ensures that all NMR signals arise from the fluorinated oil inside nanoemulsion droplets without any contribution from the surfactant.

We initially prepare 500 mL of a crude microscale premix emulsion at a droplet volume fraction $\phi = 0.15$ of FMS oil in 50 mM aqueous SDS solution using a mixer (Fisher Scientific, PowerGen 1000 S1, speed 3). After allowing any residual foam to disappear, we process this premix emulsion using a high flow rate microfluidic homogenizer (Microfluidics Inc., model M-110P; 75 µm Y-chamber) at a liquid pressure of approximately 200 MPa. We recover and re-process the resulting nanoemulsion through this homogenizer 7 additional times before collecting and diluting the resulting nanoemulsion in 10 mM aqueous SDS solution. We centrifuge this diluted nanoemulsion to obtain a much higher droplet volume fraction (Beckman L8-55 ultracentrifuge, SW-28 swinging bucket, 18,000 rpm, 4 hours), yielding a set of concentrated, elastic, jammed nanoemulsion plugs at the bottoms of thick-wall polycarbonate centrifuge tubes. The effective gravitational forces acting on droplets, caused by this ultracentrifugation, are still small enough that nanodroplet coalescence is not observed. We next remove the SDS solution above these elastic concentrated nanoemulsion plugs, combine these plugs together, and then dilute these combined plugs to $\phi \approx 0.1$ using an aqueous solution at [SDS] = 10 mM. This process of centrifugation and dilution is repeated twice more to set the SDS concentration in the continuous phase of the resulting FNEM to 10 mM.

To decrease the droplet size polydispersity of this FNEM, we perform a four-step size-fractionation at fixed [SDS] = 10 mM as follows. After a first centrifugation for size-fractionation (conditions also 18,000 rpm, 4 hours), we remove the concentrated elastic nanoemulsion plugs from the bottoms of the centrifuge tubes, cut them into two pieces using a spatula, and retain the bottom three-quarters of all plugs, corresponding to larger droplets. We combine and dilute these bottom plug-pieces using 10 mM SDS solution to set $\phi \approx 0.1$. We then perform a second centrifugation using the same conditions, cut the plugs, retain and combine the top three-quarters of the plugs, and again dilute using 10 mM SDS solution to set $\phi \approx 0.1$. We then perform a third centrifugation using the same conditions and procedure, as above, and the top-half of the plugs are combined and diluted to $\phi \approx 0.1$ in 10 mM SDS solution. Finally, we perform a fourth centrifugation using the same conditions and procedure, retain and combine the bottom three-quarters of the plugs, yielding $\approx$ 20 g of concentrated, fractionated master nanoemulsion, which is a soft elastic solid, at high ϕ. We next mix this master nanoemulsion thoroughly using a spatula to exclude any size-separation that potentially could be induced by centrifugation. The oil droplet volume fraction of the master nanoemulsion sample is measured to be $\phi_{\mathrm{m}} = 0.751 \pm 0.008$ using a gravimetric evaporation method[80]. Using dynamic light scattering (Photocor, 90° scattering angle, $\lambda = 632.8$ nm), the average droplet radius of this fractionated FNEM is measured to be $\langle a \rangle = 63 \pm 2$ nm, and its radial size polydispersity is $\delta a / \langle a \rangle = 0.16$, where δa is the standard deviation of the emulsion's radial size distribution. FNEM samples at lower ϕ are obtained by diluting a portion of the master nanoemulsion with an aqueous 10 mM SDS solution using an analytical balance (Denver Instruments APX-200, 0.1 mg precision). Based on prior experiments on similarly fabricated, stabilized, and fractionated O/W nanoemulsions, the droplet structure in the fractionated O/W FNEMs is disordered at all ϕ we explore. Moreover, the pair interaction between two FNEM nanodroplets can be described by a screened electrostatic repulsion having a Debye screening length $\lambda_{\mathrm{D}} \approx 3$ nm.

Each FNEM sample is loaded into a clean glass NMR tube, having an inner diameter of 8 mm, to a height of at least 25 mm from the bottom of the tube, as follows. For $0.248 \leq \phi \leq 0.420$, we load these viscous FNEM samples by pouring against the walls of tubes very slowly in order to avoid creating any air bubbles. For soft elastic FNEM samples at higher $0.480 \leq \phi \leq 0.751$, we load each into a NMR tube with a spatula and perform a low-speed centrifugation for a short duration to remove air bubbles without generating gradients in ϕ. The maximum centrifugal speed does not exceed 1500 rpm. The total duration, including acceleration and deceleration, varies from 60 s to 1200 s; this duration is increased to 1200 s as ϕ is raised toward 0.751. After loading, we cap the NMR tubes with plastic caps and apply Parafilm to seal them, thereby precluding evaporation, which could otherwise lead to undesirable changes in ϕ and ultimately droplet coalescence.

5.3.2 Stimulated-echo ^{19}F-NMR

The samples in 8mm glass NMR tubes are stored upright at room temperature until measurements. We perform all diffusion measurements using a Bruker 250 MHz super conducting magnet with a Micro5 probe base and 8 mm rf coil (Bruker Biospin, Karlsruhe) for ^{19}F nuclei excitation and detection, integrated with a Diff30 gradient coil providing 17.81 T/m pulsed magnetic field gradients at 60 A in the z-direction of the applied magnetic field. We hold the temperature stable at 20°C through the Bruker BTU system with N_2 gas flow and active feedback control. For the diffusion measurements, we utilize a standard pulsed-field gradient stimulated echo (PFG-StE) pulse sequence[160]. In these experiments, we implement a constant gradient duration δ and diffusion displacement time Δ between gradient pulses and increasing gradient strength g to step through the displacement reciprocal wave length $q = (2\pi)^{-1}\gamma\delta g$ space, where γ is the gyromagnetic ratio of the ^{19}F nuclei. This standard implementation of the PFG-StE sequence allows the mean square displacement (MSD) to be calculated from the normalized echo voltage signal as $E(q) = S(q)/S(q = 0) = \exp[-4\pi^2 q^2 D(\Delta - \delta/3)] = \exp(-2\pi^2 q^2 \langle z^2 \rangle)$, where $\langle z^2 \rangle = 2D(\Delta - \delta/3)$ is the 1-dimensional (1D) MSD and D is the molecular diffusion coefficient[160]. This equation is also often written in terms of the effective diffusion using the nomenclature $E(b) = S(b)/S(b = 0) = \exp(-bD_{\text{eff}})$, where an effective gradient and displacement time parameter $b = 4\pi^2 q^2(\Delta - \delta/3) = (\gamma\delta g)^2(\Delta - \delta/3)$ is used to reflect the displacement time dependence inherent in D_{eff}[160].

Additionally, we vary the gradient duration δ and displacement time Δ to optimize the measurements for probing the MSD of the nanoemulsion droplets. The molecular diffusion coefficient of the FMS oil is measured to be 4.19×10^{-12} m^2/s. The value of $\Delta = 700$ ms ($\gg \langle a \rangle^2 / D_0 = 9.47 \times 10^{-3}$ ms) provides the long time asymptotic MSD of the droplets by allowing the fluorinated polymer to fully sample the interior of the nanoemulsion droplets and the droplets to diffuse within the emulsion structure[161,166]. To provide additional data on the emulsion structure in terms of a porous media, we examine a range of δ values from 2 ms to 5 ms, for which $\delta \gg \langle a \rangle^2 / D_0$, to observe the signal dependence on the varying gradient durations[161,163,166]. For all experiments reported here, we use a gradient duration $\delta = 2$ ms, which for the particle motion scale results in $l_{\text{D}} = \sqrt{2D_{\text{SE}}\delta} = 1.67 \times 10^{-7}$ m, equivalent to $1.85\langle a \rangle$ which generates a small additional signal attenuation in the dilute system, accounted for by the $\delta/3$ in the definition of b, which results in no relaxation weighting of the diffusion data based on the measurement of a single T_2 relaxation time of 291 ms observed using a Carr-Purcell Meiboom-Gill[167] experiment. We report measurements over a wide range of ϕ from 0.751 down to 0.1. Having a single relaxation time larger than the δ indicates the signal does not decay significantly during the gradient duration, corresponding to no relaxation weighting of the diffusion data. We increment gradients from 0.89 T/m up to 17.81 T/m with 32 linearly spaced steps. For each gradient step, we perform ensemble averaging of a 16-step phase cycle eight times.

5.3.3 Mechanical shear rheometry

We first ensure proper calibration of our strain-controlled shear rheometer (Rheometrics RFS-II), both in magnitude of the complex shear modulus and crossover frequency, using a polymeric viscoelastic reference standard. Following calibration, for samples having $0.359 \leq \phi \leq 0.751$, we load each FNEM into a 25-mm diameter stainless steel cone-and-plate geometry enclosed by a vapor trap. At a shear strain $\gamma = 0.01$, we perform a frequency sweep from frequency $\omega = 10$ rad/s down to 0.02 rad/s. We then perform a strain sweep at $\omega = 1$ rad/s from $\gamma = 0.002$ to 2 to verify that the strain of 0.01 selected for the frequency sweep is below the yield strain, ensuring that reported G'_{p} values for $0.373 \leq \phi \leq 0.751$ correspond to the linear stress-strain response-regime. For $\phi = 0.365$, the low-strain storage shear modulus $G'(\gamma)$ is effectively identical to the loss shear modulus $G''(\gamma)$ at $\gamma \leq 0.02$. For more highly diluted samples having $\phi \leq 0.360$, $G''(\gamma)$ dominates $G'(\gamma)$ even at small shear strains. We determine the dynamic viscosity of the FMS bulk oil, using steady shear rate sweep measurements, to be $\eta_{\mathrm{o}} = 143$ mPa s. The measured shear stress τ varies linearly with the shear strain rate $\dot{\gamma}$ from 1000 s^{-1} to 0.2 s^{-1}. Using the mass density of the FMS oil, we then convert to the kinematic viscosity: $\nu_{\mathrm{o}} = 124$ cSt.

5.4 Results

5.4.1 NMR magnetization decay and MSD analysis

Using a fitting procedure, we normalize the StE PFG-NMR magnetization attenuation, $E(b) = S(b)/S(b = 0)$, determined by varying g at fixed $\Delta = 700$ ms, so that it decays exponentially from unity in the low-b (*i.e.* low-q^2) limit. This ensures that dimensionless $-\ln[E(b)]$, which is proportional to the ensemble- and time-average MSD of the probes, rises linearly with b in a double logarithmic scale at low b for all ϕ [open circles in Figure 5.1(a)]. For all ϕ, we have also subtracted the small baseline noise signal of $E(b)$ before normalizing; this baseline is determined by the measured noise plateau in $E(b)$ beyond the decay at high b only at low ϕ where the samples are purely viscous and simple diffusion of ^{19}F-laden FMS oil molecules is observed. This baseline noise subtraction makes no more than a 5% adjustment in the values of $E(b)$ over all ϕ measured.

We fit the measured dimensionless MSDs to a simple diffusion model for lower ϕ and to a bound diffusion model (called the single exponential model in Magin *et al.*[146]) for higher ϕ:

$$-\ln[E(b)] = \begin{cases} bD_0 & \phi \leq \phi_\mathrm{c} \\ (D_0/D_1)[1 - \exp(-bD_1)] & \phi > \phi_\mathrm{c} \end{cases}, \tag{5.1}$$

where D_0 is the low-b diffusion coefficient, ϕ_c is a critical nanodroplet volume fraction associated with droplet jamming and the onset of sub-diffusive behavior in the decay at high b, and D_0/D_1 indicates the relative amount of decay, corresponding to the plateau of the MSD in the high-b limit [solid lines in Figure 5.1(a)]. This high-b plateau is also reminiscent of harmonically bound Brownian behavior[56]. From our measurements, recognizing that the limited upper range of b of our measurement window could have some impact on the exact value, we find $\phi_\mathrm{c} \approx 0.32$ is an empirical volume fraction threshold below which the attenuation signal can be described as a simple exponential decay corresponding to a diffusive random walk. Using the determined fit parameters, we also plot the normalized $E(b)$ data

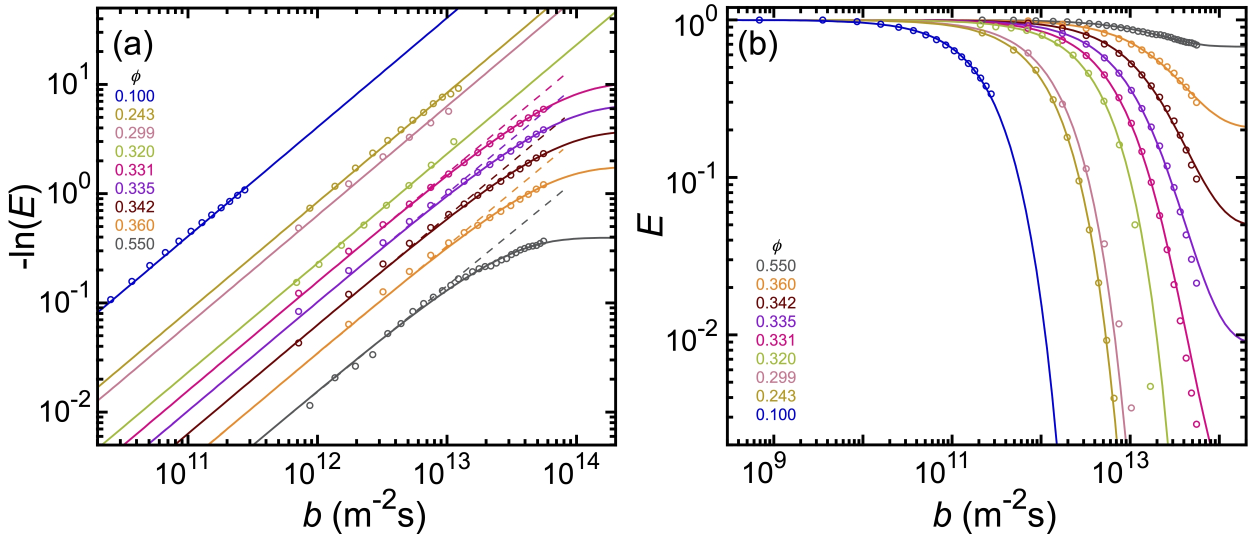

Figure 5.1. (a) **Effective mean square displacements (MSDs) of the ^{19}F-laden oil molecules of the O/W nanoemulsions having average droplet radius $a = 63$ nm for different droplet volume fraction ϕ (color-encoded, see left), represented by negative natural logarithm of the corrected StE PFG-NMR diffusion signal attenuation, $-\ln[E(b)]$, measured at diffusion time between refocused pulses $\Delta =$ 700 ms and gradient pulse duration $\delta = 2$ ms.** Solid lines are functional fits to equation (5.1). For $\phi \geq 0.331$, the departure from low-b diffusive $-\ln[E(b)]$ behavior (dashed lines show the extension toward high-b) occurs at $b \approx 5 \times 10^{12}$ m^{-2}s. The largest b at the maximum experimentally explored gradient strength is $b_{\max} = 5.6 \times 10^{13}$ m^{-2}s. (**b**)**Effective correlation functions of the FNEM, represented by baseline-subtracted and normalized attenuation, $E(b)$.** The lines represent calculations using equation (5.2) and parameters from the corresponding functional fits in part (a). The order of ϕ goes from top to bottom in the caption of part (a) and from left to right in part (b).

with lines that correspond to the exponential of equation (5.1):

$$E(b) = \begin{cases} \exp(-bD_0) & \phi \leq \phi_c \\ \exp\{-(D_0/D_1)[1-\exp(-bD_1)]\} & \phi > \phi_c \end{cases}, \tag{5.2}$$

as shown in Figure 5.1(b). The trend toward non-zero positive values of a plateau in $E(b)$ at high b is clearly seen; this is associated with sub-diffusive measured log-slopes of -ln$[E(b)]$ at high b.

Nanodroplet unjamming behavior, as ϕ is reduced and the FNEM transitions rheologically from elastic solid to a viscous liquid, is clearly seen through the large changes in the observed NMR $E(b)$. To understand and describe this, we assume that the total MSD of ^{19}F-probe-molecules arises from a combination of confined internal molecular diffusion of the FMS oil within nanodroplets and also the diffusion of nanodroplets in the aqueous continuous phase– yet modified by interactions with neighboring nanodroplets which can lead to nanodroplet confinement through jamming at high ϕ. The viscosity of the bulk fluorinated oil is 143 mPa s, determined by mechanical shear rheometry. The NMR measurements determine the translational diffusion coefficient of the bulk oil to be 4.19×10^{-12} m^2 s^{-1}, yielding a viscosity of 128 mPa s according to Stokes-Einstein relation, using the macromolecular radius of gyration of 0.4 nm. The difference between these two measurements is within 11%. The diffusion time between two adjacent refocused pulses and the duration of gradient pulses are fixed at $\Delta = 700$ ms and $\delta = 2$ ms, respectively, in all reported NMR measurements. For a higher ϕ above the unjamming, the NMR magnetization decays at a lower rate and exhibits less amount of attenuation at high b, reflecting the confinement from droplet jamming [Figure 5.1(b)]. The decay signal in the high ϕ regime can be fit to the bound diffusion model, showing a concave-up bending towards a plateau as b increases [equation (5.2) for $\phi > \phi_{\rm c}$]. In the high ϕ regime, the droplet motion is geometrically restricted in the cage formed by adjacent droplets so that droplet diffusion contributes less in the combined apparent probe diffusion. When the emulsion is diluted to lower ϕ, viscous response is obtained and the magnetization attenuation can be fit to a single exponential model [Figure 5.1(b) and equation (5.2) for low $\phi \leq \phi_{\rm c}$]. In the low ϕ regime, the mobility of a droplet in the emulsion, having a high-frequency viscosity close to water's 1 mPa s, is much higher with respect to the mobility of a confined ^{19}F probe molecule in the droplet whose viscosity is more than a hundred-folds higher. Therefore, the droplet diffusion predominates the confined probe molecular diffusion and effectively results in the apparent diffusive behavior of the probe that can be detected by NMR.

The transition in NMR magnetization decay features above and below the droplet unjamming can be more readily seen in the -ln$E(b)$ functions, where -ln$E$ is proportional to the mean square displacements of the probe [equation (5.2) and Figure 5.1(a)]. Linear correlation between -ln$E$ and b over the entire explored b range is observed for an unjammed emulsion having low $\phi \leq 0.320$. By contrast, dense emulsions having high $\phi \geq 0.325$ presents a linear rise at low b, followed by a bending knee as b is varied from low to high. Independent to ϕ, the divergence from the linearity occurs at $b \approx 5 \times 10^{12}$ m^{-2}s.

The influence of droplet confinement on NMR magnetization decay is revealed distinctly in the -ln$E(b)$ log-slope plot as a function of ϕ [Figure 5.2(a)]. At a given ϕ, the log-slope (*i.e.* the MSD scaling exponent, represented by the slope of the log-log plot of the effective MSD[168]) is calculated from the first derivative of the fitting function equation (5.1) and evaluated at the maximum measured b_{max}. A gradual increase in the b_{max}-log-slope is observed from high ϕ down to $\phi \approx 0.34$, followed by an abrupt increase until ϕ approaches 0.32; and by definition, the log-slope is strictly equal to unity for $\phi \leq 0.32$. The ratio of D_0/D_1, obtained from the fits using equation (5.1) for $\phi > \phi_{\mathrm{c}}$, is associated with the amount of magnetization decay observed at high b. As ϕ is decreased, D_0/D_1 increases slowly in the high-ϕ regime, bends up more rapidly near $\phi \approx 0.4$, and diverges at $\phi \approx 0.33$ [Figure 5.2(b)]. The diffusion coefficient D_0, representing the low-b diffusibility, is fit to a four-parameter function having a cubic decrease multiplied by a Fermi-like function [see the caption to Figure 5.2(c)]. In the high-ϕ regime where droplets are jammed, the droplet is highly confined by the cage of its nearest neighboring droplets, and the internal double-bound molecular probe exhibits low diffusibility, reflected by the low magnitude of $D_0 \approx 2 \times 10^{-14}$ m^{2}s^{-1} for $\phi \geq 0.38$. As ϕ is reduced, a rapid exponential rise of D_0 is observed, attributed to a weaker cage effect, reflecting the droplet unjamming in the range $0.38 \geq \phi \geq 0.30$. As further diluted to lower ϕ, the measured D_0 gradually increases towards the diffusion coefficient of an isolated droplet in water near 3.4 $\times 10^{-12}$ m^{2}s^{-1}, calculated by Stokes-Einstein relation, which declares that the droplet diffusion confinement disappears. The uncertainty of the fitting parameter $D_{0,\mathrm{d}} \approx 5.5 \times 10^{-12}$ m^{2}s^{-1} is comparable to its value due to the limit amount of data in the very dilute ϕ regime. The critical volume fraction ϕ_{c} for droplet unjamming,

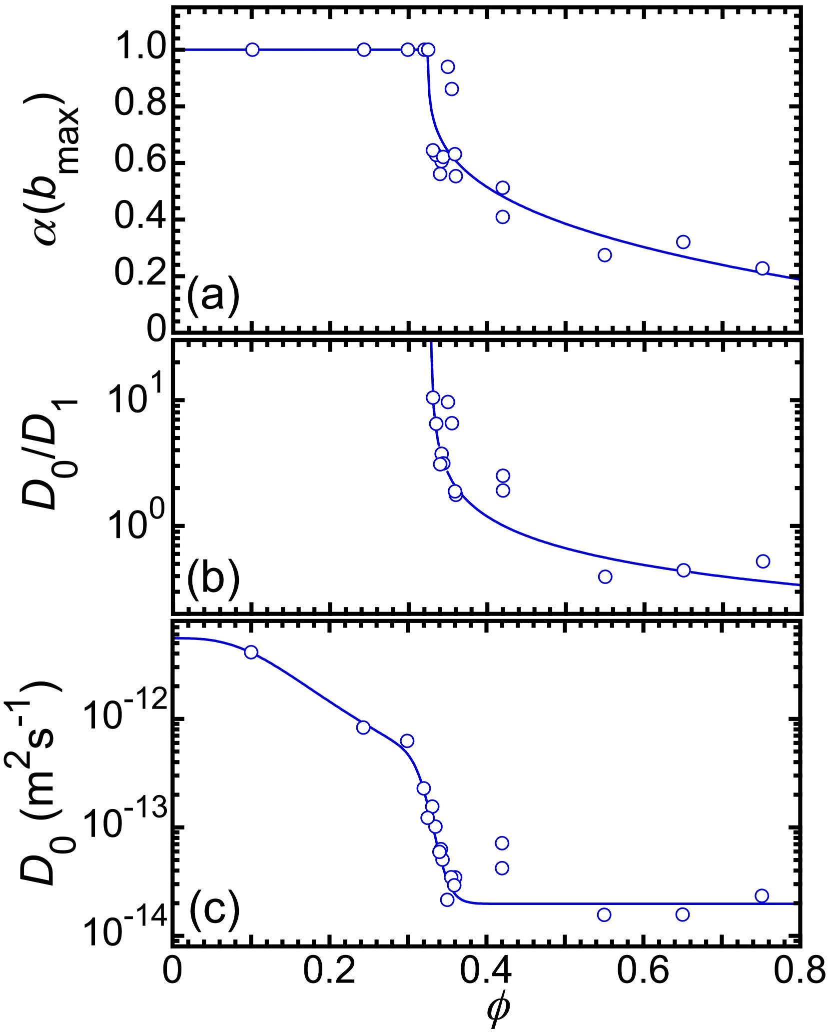

Figure 5.2. High-b log-slope and fitting parameters of the effective MSDs, $-\ln[E(b)]$, as functions of ϕ. (**a**) Log-slope of $-\ln[E(b)]$ approaching the maximum measured b, $\alpha(b_{\text{max}}) = d\ln[-\ln(E)]/d\ln(b)$ evaluated at b_{max}, calculated from the $-\ln[E(b)]$ fits [solid lines in Figure 5.1(a)] and fit to: 1 for $\phi \leq \phi_{\text{c}}$; and $1-(\phi-\phi_{\text{c}})^n$ for $\phi > \phi_{\text{c}}$, where $\phi_{\text{c}} = 0.325 \pm 0.011$, and $n = 0.28 \pm 0.04$ (square of the correlation coefficient: $\text{R}^2 = 0.835$). (**b**) The ratio D_0/D_1, representing the amount of attenuation at high-b, obtained from fits using equation (5.1) for each given $\phi \geq 0.325$ and fit to $D_0/D_1(\phi) = [\phi_{\text{m}}/(\phi-\phi_{\text{c}})]^{\nu}$, where $\phi_{\text{c}} = 0.328 \pm 0.007$, $\phi_{\text{m}} = 0.09 \pm 0.05$, and $\nu = 0.67 \pm 0.30$ ($\text{R}^2 = 0.751$). (**c**) The low-b diffusion coefficient D_0 for all measured ϕ obtained from equation (5.1) and fit to $D_0(\phi) = \{D_{0,\text{d}}/[1+(\phi/\phi_{\text{v}})^3]\}/\{1+\exp[(\phi-\phi_{\text{c}})/\phi_{\text{m}}]\}+D_{0,\text{conf}}$, where $\phi_{\text{c}} = 0.32 \pm 0.02$, $\phi_{\text{v}} = 0.14 \pm 0.10$, $\phi_{\text{m}} = 0.0098 \pm 0.0068$, $D_{0,\text{d}} \approx 5.5 \times 10^{-12}$ m^2/s, and $D_{0,\text{conf}} = (1.9 \pm 0.9) \times 10^{-14}$ m^2/s (R^2 = 0.778).

associated with the occurrence of the sub-diffusive molecular motion, have been obtained from the fits of the b_{max}-log-slope of effective MSDs, the D_0/D_1 ratio and the low-b diffusion coefficient D_0, respectively, as functions of ϕ. The ϕ_{c} values inferred from all three of these approaches are highly consistent within the error range, having a standard deviation less than 2% of the average value (see caption of Figure 5.2 for fitting functions, parameters, and regression coefficients).

5.4.2 Mechanical shear rheometry

Mechanical shear oscillatory measurements are performed in both strain sweep and frequency sweep modes. The measured strain sweep data, $G'(\gamma)$, at a fixed frequency $\omega = 1$ rad/s, are fit to $G'(\gamma) = G'_{\mathrm{p}}/\left[(\gamma/\gamma_{\mathrm{y}})^{\kappa} + 1\right]$, yielding: the plateau shear modulus G'_{p}, the yield strain γ_{y}, and the high-strain power-law parameter κ that describes the decrease in the non-linear G' beyond yielding [Figure 5.3(a)]. For all ϕ in the range from 0.751 to 0.359, the elastic shear modulus G'_{p} at $\gamma = 0.01$ is in the low-strain plateau region. In the frequency sweeps, conducted at a peak shear strain $\gamma = 0.01$, the measured G' is frequency-independent over the range of ω from 10 to 0.02 rad/s for dense emulsion having $\phi \geq 0.380$ [Figure 5.3(b)]. At such high ϕ, the measured plateau values of storage shear modulus G'_{p} are almost equal to the magnitude of the complex shear modulus $G^{*}(\omega)$ at $\omega = 1$ rad/s over the frequency range explored. However, for $\phi \leq 0.373$, the frequency-dependence of G' at $\gamma = 0.01$ renders inaccuracy of determining G'_{p} from mechanical measurements using the $G'(\gamma)$ fits as in Figure 5.3(a). For $\phi \geq 0.380$, the plateau shear elastic moduli G'_{p} are fit to the entropic, electrostatic, interfacial (EEI) model[37] using the following parameters: droplet radius $a = 63$ nm, critical volume fraction for random close packing $\phi_{\mathrm{rcp}} = 0.646$, Debye-screening length $\lambda_{\mathrm{D}} = 4$ nm, surface tension $\sigma = 0.0098$ N/m and surface potential $|\psi_0| = 52$ mV [Figure 5.3(c)]. The loss of macroscopic elastic shear rigidity occurs very rapidly as ϕ is reduced in the range from 0.38 to 0.34.

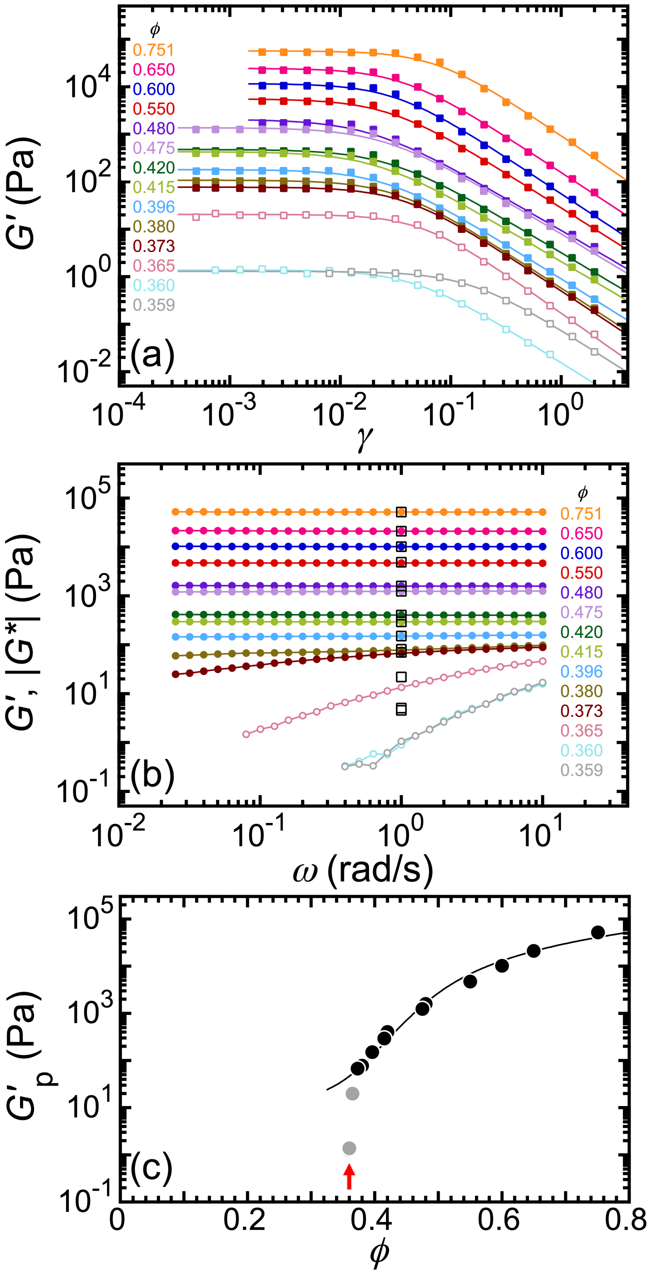

Figure 5.3. Mechanical shear oscillatory measurements of elastic shear moduli. (**a**) Measured $G'(\gamma)$ at frequency $\omega = 1$ rad/s with fitting curves (see text) for ϕ from 0.751 to 0.359 (top to bottom, color-code on left). (**b**) Measured $G'(\omega)$ at a fixed peak shear strain of $\gamma = 0.01$ for different ϕ and complex shear modulus $|G^*|(\omega)$ (open squares at $\omega = 1$ rad/s). (**c**) Plateau elastic shear modulus G'_p, obtained from strain sweeps in part (a), as a function of ϕ with the EEI model[37] prediction (solid line). Low-frequency relaxation of the system is evident at the frequency (*i.e.* 1 rad/s) associated with the strain sweeps at lower $\phi \leq 0.365$ (grayed markers). Red arrow highlights the lowest ϕ where G'_p can be measured using mechanical rheometry.

5.4.3 Droplet MSDs from NMR and rheometry

The plateau MSDs associated with caged nanodroplet motion in the high-ϕ regime can be inferred from the mechanical rheometry measurements using the generalized Stokes-Einstein relation (GSER) of passive microrheology. We first deduce the 3-dimensional (3D) droplet plateau MSDs, $\langle \Delta \boldsymbol{r}_{\mathrm{d}}^2 \rangle_{\mathrm{p}}$, from the measured G'_{p} at each ϕ by applying the GSER[11]: $\langle \Delta \boldsymbol{r}_{\mathrm{d}}^2 \rangle_{\mathrm{p}} = k_{\mathrm{B}}T/(\pi a G'_{\mathrm{p}})$, where k_{B} is Boltzmann's constant, T is the temperature, and a is the average droplet radius. We then convert these 3D droplet plateau MSDs to 1D droplet plateau MSDs, $\langle \Delta z_{\mathrm{d}}^2 \rangle_{\mathrm{p}}$, by dividing by 3 since the disordered nanoemulsion is spatially isotropic. By contrast, in the lower ϕ regime, near and below unjamming, we determine 1D total molecular MSDs assuming $\langle \Delta z^2 \rangle \approx 2D_0\Delta$ using the low-b diffusion coefficients from Figure 5.2(c) for fixed $\Delta = 700$ ms. We hypothesize that these NMR-detected total molecular MSDs $\langle \Delta z^2 \rangle$ are associated with a superposition of the Brownian center-of-mass (COM) motion of the nanodroplets $\langle \Delta z_{\mathrm{d}}^2 \rangle$, which varies with ϕ, and the confined molecular motion within the nanodroplets $\langle \Delta z_{\mathrm{c}}^2 \rangle$, which is independent of ϕ. Assuming that the distributions for nanodroplet displacements and confined molecular motion in stationary nanodroplets are both Gaussian, we extract the 1D droplet MSDs $\langle \Delta z_{\mathrm{d}}^2 \rangle$ for $\phi < 0.37$ through subtraction: $\langle \Delta z_{\mathrm{d}}^2 \rangle = \langle \Delta z^2 \rangle$ - $\langle \Delta z_{\mathrm{c}}^2 \rangle$. To obtain a smooth match of the NMR-inferred droplet MSDs to the microrheologically-inferred droplet MSDs, yielding smooth overlap at unjamming, we deduce a value of $\langle \Delta z_{\mathrm{c}}^2 \rangle = 3.9 \times 10^{-14}$ m^2. This matching process yields a systematic 1D droplet MSD as a function of ϕ over the entire range of all measurements. This $\langle \Delta z_{\mathrm{c}}^2 \rangle$ corresponds to a confined molecular diffusion coefficient of $D_{0,\mathrm{conf}} = 2.8 \times 10^{-14}$ m^2 s^{-1}, which is slightly greater than but in reasonable accord (within one standard deviation) with the value, $D_{0,\mathrm{conf}} = (1.9 \pm 0.9) \times 10^{-14}$ m^2 s^{-1}, obtained from the fit of $D_0(\phi)$ at high ϕ in Figure 5.2(c). If this alternative fit-parameter value were to be used instead, the agreement would still be quite reasonable overall, but the matching would not be quite as smooth near the droplet unjamming point. The droplet root mean square displacement, $\langle \Delta z_{\mathrm{d}}^2 \rangle^{1/2}$, normalized by the effective interdroplet center-to-center spacing (*i.e.*, which is

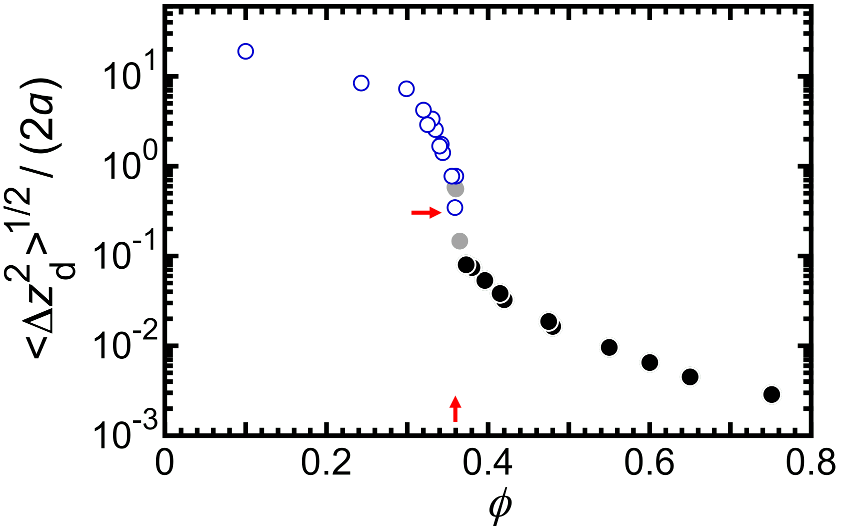

Figure 5.4. Droplet root mean square displacement, $\left\langle \Delta z_{\rm d}^2 \right\rangle^{1/2}$, normalized by the droplet diameter $2a$, as a function of ϕ. Solid black circles: plateau $\langle \Delta z_{\rm d}^2 \rangle^{1/2} / (2a)$ deduced from the measured $G'_{\rm p}$ from Figure 5.3(c) using the GSER; 3D MSDs from the GSER have been converted to 1D MSDs. Solid gray circles: the used small-strain $G'_{\rm p}$ in the GSER are extracted from fits of $G'(\gamma)$ for viscoelastic samples having small yield strain. Open blue circles: droplet $\langle \Delta z_{\rm d}^2 \rangle^{1/2} / (2a)$ calculated for $\Delta = 700$ ms using NMR low-b diffusion coefficients D_0 for $\phi < 0.37$ from Figure 5.2(c), where the total molecular probe 1D MSDs are: $\langle \Delta z^2 \rangle = 2D_0\Delta$. To match droplet MSDs inferred from both sets of measurements at the unjamming point, we deduce that the confined molecular MSD $\langle \Delta z_{\rm c}^2 \rangle$ is 3.9×10^{-14} m^2 and subtract this value from $\langle \Delta z^2 \rangle$, yielding the droplet MSDs $\langle \Delta z_{\rm d}^2 \rangle$. Horizontal red arrow indicates a Lindemann melting criterion of $\langle \Delta z_{\rm d}^2 \rangle^{1/2} / (2a) = 0.3$, corresponding to a droplet unjamming (melting) point of $\phi_{\rm c} \approx 0.36$.

approximately given by the droplet diameter $2a$), is reminiscent of the Lindemann ratio that has been used to quantify disorder-induced amorphization and to predict the melting point of crystalline materials[164, 169] (see Figure 5.4). In this presented disordered nanoemulsion system, we find that the droplet unjamming point, determined via a Lindemann melting criterion of $\langle \Delta z_{\rm d}^2 \rangle^{1/2} / (2a) = 0.3$, coincides with the value of $\phi_{\rm c} \approx 0.36$ associated with the loss of zero-frequency plateau shear elasticity, determined using mechanical rheometry [see arrows in Figures 5.3(c) and 5.4]. Using alternative values for the Lindemann criterion, which are in the range 0.15 to 0.30 for most materials, does not substantially change this unjamming point.

5.5 Discussion and conclusion

These ^{19}F StE PFG-NMR measurements of concentrated nanoemulsions show that the attenuation, resulting from the total motion of ^{19}F-laden molecular probes diffusing within nanodroplets, changes dramatically when the nanodroplets unjam as ϕ is reduced and the low-frequency shear rigidity of the nanoemulsion vanishes. Thus, the total molecular motion reflects a superposition of center-of-mass motion of the nanodroplets as well as confined molecular diffusion of the ^{19}F-labeled silicone oil within the nanodroplets. At high ϕ, droplets are strongly jammed, and the nanoemulsion is a soft yet rigid solid; in this strongly jammed limit, the NMR attenuation decays resemble decays of liquids in other kinds of nanoporous solids. This indicates that the strongly jammed nanoemulsion can be considered as a closed-pore nanoporous solid having sufficiently large rigidity that only the highly confined molecular motion contributes substantially to the observed decay-to-plateau behavior. By contrast, the superposition of the nanodroplet motion in combination with the confined molecular motion becomes evident through rapid changes in the NMR attenuation near and below the nanodroplet jamming point, where the nanoemulsion loses shear-rigidity as ϕ is reduced. Moreover, the evidence of decay-to-plateau behavior at high-b disappears, and the decays become simple-exponential instead. In the dilute-ϕ limit, for the particular nanoemulsion that we have created and investigated, the NMR attenuation at low b is dominated by nanodroplet diffusion in the aqueous continuous phase, not by confined molecular motion of the oil within the nanodroplets. These new measurements and insights have been made possible through the fabrication of a custom-formulated size-fractionated O/W nanoemulsion that is composed of a perfluorinated co-polymer silicone oil and a non-fluorinated surfactant.

By combining both NMR measurements with a passive microrheological interpretation of macroscopic mechanical rheometry measurements, we have obtained a master curve of droplet root-MSDs, normalized by the average diameter of the nanodroplets, as a function of ϕ both above and below the unjamming droplet volume fraction. This master curve enables us to show how droplet unjamming can be related to the classic idea of melting in terms of Lindemann's ratio. Using a Lindemann criterion of 0.3, known from other types of materials, we have shown that the ϕ associated with Lindemann melting coincides with ϕ_c associated with nanodroplet unjamming and the loss of low-frequency mechanical shear rigidity. The average diameter-normalized droplet MSDs as a function of ϕ for an emulsion system stabilized by screened electrostatic repulsion, in which the droplets are twice as large in radius as the droplets in our NMR study, have been reported in[135], showing the same ϕ-dependent trend as in Figure 5.4 but with a higher droplet unjamming volume fraction due to the difference in droplet size. While we use the term "unjamming," we recognize that the screened-charge-stabilized system of nanodroplets may also be considered as a glassy colloidal system, below the electrostatic droplet-jamming point, that effectively undergoes a non-ergodic to ergodic transition as ϕ is reduced; so, taken more broadly, the dramatic change we show also relates to the melting of disordered glassy systems, not just unjamming.

The model perfluorinated O/W nanoemulsion that we have designed, created, and studied using ^{19}F StE PFG-NMR is highly size-fractionated, has a disordered droplet structure, has short-range screened-charge repulsive interactions between the droplets, and effectively precludes interdroplet diffusion of perfluorinated oil molecules through the aqueous continuous phase. Therefore, the NMR attenuation in our measurements is not influenced by diffusion of probe molecules between nanodroplets. This enables us to interpret our NMR measurements more readily, as compared to prior studies in which oil molecules diffuse between droplets[163, 170, 171]. In addition, the high degree of size-fractionation of the nanodroplets enables us to fit the low-ϕ decays well using only a single exponential form.

Our investigations have revealed several key signatures in the PFG-NMR attenuation that are associated with unjamming and melting of a model soft colloidal solid; yet, many exciting directions still remain. For example, a higher magnetic field gradient could be used to explore the high-b regime to even larger b, potentially providing a direct measurement of the effective plateau of the NMR attenuation in the highly concentrated ϕ-regime. For instance, if more accurate and precise measurements can be made at higher b, it may be possible to deduce G'_{p} directly from the high-b plateau MSDs that can potentially be obtained. Fabricating and studying nanoemulsions that have a smaller average droplet radius would potentially be worthwhile, since this could further increase the sensitivity to nanodroplet motion in the jammed ϕ-regime relative to confined molecular motion. Thus, it would be interesting to perform similar studies on nanoemulsions having a range of different nanodroplet sizes. Moreover, varying the viscosity of the oil within the nanodroplets, through the molar mass of the oil, could also potentially enhance the NMR attenuation arising from nanodroplet motion relative to the confined molecular diffusion. Furthermore, our experiments broadly indicate that theories and simulations of the total motion of probe molecules within dense colloidal droplet probes would be interesting to explore through the glass and jamming transitions.

Chapter 6 - Double-bound Brownian motion of molecular probes in concentrated emulsions and nanoemulsions

This chapter has been written by Y. Xu and T. G. Mason, is currently copyrighted by Y. Xu and T. G. Mason in 2023, and has been submitted to *Physical Review E* for consideration. Since the contents of the chapter have not yet been published, written permission must be obtained by both authors to reproduce or transmit the contents of the herein Chapter 6, in whole or in part, prior to its publication in a scientific journal. Readers are encouraged to perform a search on the above authors and/or title using an internet search engine (e.g. Google Scholar or Web of Science) to determine if publication has occurred. If publication of the contents of this chapter has occurred in a scientific journal, then readers are directed to that journal's policies regarding permissions for potential use.

6.1 Abstract

We present a two-dimensional trajectory-based simulation study of the bound diffusion of molecular probes within droplets that also undergo bound diffusion in dense, elastic emulsions and nanoemulsions, yielding an interesting, physically realizable form of double-bound Brownian motion. Probe trajectories are obtained by coupling the stochastic Brownian dynamics of probe-molecules diffusing within colloidal droplets to harmonically bound Brownian motion of those droplets in the soft elastic material. We show that the ensemble-averaged center-of-mass mean square displacement (MSD) of droplets can be extracted by subtracting a reference MSD obtained from probe-molecules diffusing in stationary droplets from the to-

tal probe-molecule MSD. From this colloidal droplet MSD, we then deduce the elastic plateau shear storage modulus, G'_{p}, at each droplet volume fraction, ϕ, considered. Our simulations demonstrate that smaller droplet radii and higher internal phase viscosities can increase the sensitivity and broaden the range of detection for the probe MSD-subtraction approach, potentially making pulse-field gradient nuclear magnetic resonance techniques feasible for passive microrheology of specifically formulated dense nanoemulsions.

6.2 Introduction

Passive microrheology of soft materials has been applied using a wide variety of techniques, predominantly optical, ranging from scattering, primarily through diffusing wave spectroscopy (DWS)[11,172,173], to real-space particle tracking methods[12,53,54]. These techniques directly measure motion of colloidal probes, from which rheological properties are extracted. Extending passive microrheology to other experimental techniques that have been optimized around molecular probes, rather than colloidal probes, represents an interesting frontier. While directly using molecular probe motion could be possible in principle for certain materials, problematic issues could also arise if the generalized Stokes-Einstein relation (GSER)[11] would be applied when the probe size is substantially smaller than the scale of structures that provide the elastic component of the viscoelastic response; such an attempted application would violate the fundamental assumptions inherent in the GSER. Consequently, there is a non-trivial challenge in using molecular probes for performing passive microrheology, and therefore also opportunities for novel approaches to solve this challenge.

Recent nuclear magnetic resonance (NMR) experiments have revealed droplet unjamming in ^{19}F-laden oil-in-water (O/W) nanoemulsions through stimulated-echo pulse-field-gradient NMR (StE PFG-NMR)[174]. While revealing the droplet unjamming using molecular probes is a promising development, obtaining confined mean square displacements (MSDs) of nanodroplets in highly concentrated nanoemulsions, for the purposes of extracting the plateau elastic shear storage modulus, G'_{p}, through the droplet GSER, was beyond the limits of that particular NMR experiment applied to that particular nanoemulsion. In order to better optimize the nanoemulsions for future PFG-NMR experiments, it would be useful to model the molecular motion of oil probe-molecules within nanoemulsion droplets into the jammed droplet limit. For nanoemulsions having different droplet radii, a, and droplet volume fractions, ϕ, such modeling could help determine the proportion of the MSDs of oil probe-molecules resulting from droplet motion compared to the total MSDs of the oil probe-molecules, which includes both droplet motion combined with confined diffusion of the oil probe-molecules within droplets. While such an exploration would be potentially useful for future NMR experiments, this idea also opens up an interesting general question related to double-bound Brownian motion, in which probe motion is influenced by two different types of confinement. Thus, developing a general framework for simulating double-bound Brownian motion would be beneficial not only for answering specific questions about optimizing nanoemulsion compositions and physical properties for future NMR experiments, but also for understanding the behavior of probe-molecule motion resulting from different types of confinement at different length scales that are coupled.

In the harmonically bound Brownian particle (HBBP) model, the motion of a particle is governed by the interplay between its Brownian motion and the confining harmonic potential[56,175]. The Brownian component stems from the random, diffusive motion caused by the thermal agitation of the surrounding medium, while the harmonic potential symbolizes the restoring forces that act on the particle, binding it to a specific region. Importantly, the HBBP model introduces a characteristic relaxation time, which arises due to the potential, providing a temporal scale for the system. This relaxation time reflects the time taken by the particle to return to equilibrium after a disturbance, and it directly links the particle's MSD and velocity autocorrelation to the effective spring constant of the potential and temperature of the system. The HBBP model thus offers a powerful tool for understanding systems where thermal fluctuations and spatial constraints significantly influence particle dynamics. In our study, we effectively utilize the HBBP to model the Brownian motion of oil droplets in the emulsion system.

Investigating molecular diffusion within porous media, such as in NMR studies, provides important insights into the complex motions of probe molecules. For example, ^{19}F StE PFG-NMR has been used to study the diffusion of probe molecules, specifically ^{19}F-tagged molecules, within confined spaces like nanodroplets in concentrated nanoemulsions[174]. This study reveals that the diffusion behavior is influenced by both the nanodroplets' center-of-mass motion and the confined molecular diffusion within the nanodroplets themselves, offering an intriguing superposition of effects. When droplets are strongly jammed, the nanoemulsion behaves as a rigid yet soft solid, with the NMR attenuation decays resembling those of liquids in other nanoporous solids. By contrast, in the dilute regime below the jamming point, both the nanodroplet motion and the confined molecular motion contribute to swift changes in the NMR attenuation as the nanoemulsion loses its shear rigidity. In a broader context, the concept of probe-molecule confinement becomes crucial. This is the phenomenon where the diffusion of probe molecules is constrained within a physical boundary, akin to what is observed within these nanodroplets. Reflective boundary conditions and trial rejection are among the ways this confinement can be modeled. In our study, we employ reflective boundary conditions, an approach that models situations where the molecules are reflected back upon reaching a boundary. On the other hand, trial rejection, which we do not use here, discards impractical paths during the simulation, effectively replicating the physical restrictions inherent in real-world diffusion.

Here, we investigate the double-bound Brownian motion of diffusing molecular probes confined within droplets in jammed, soft-elastic emulsions and nanoemulsions. We simulate the free diffusion of a probe-molecule within a droplet and the Brownian motion of the droplet, which is harmonically bound within the cage formed by its neighboring droplets. We illustrate that a subtraction analysis of the MSDs for the detectable probe molecular motion can be used to deduce the droplet self-motion MSDs, which are essential for microrheology.

We explore a wide range of material parameters, including droplet size, relative viscosity between the dispersed phase and the continuous phase, the plateau shear elastic modulus, and volume fraction, and determine the threshold for doing microrheology based on these different material properties and the detection limit of the equipment.

6.3 Model and simulation

6.3.1 Two-dimensional trajectories

We simulate the two-dimensional (2D) trajectories of a probe in a harmonically bound Brownian diffusing droplet, thereby elucidating the process of inferring the self-motion of droplets within a soft viscoelastic material. This is accomplished by detecting the total combined probe motion and employing the confined probe motion in a stationary droplet as the reference signal, which can be ascertained in the high droplet volume fraction limit. To better illustrate this process, we present the partial trajectory of a probe in a central droplet at a short elapsed time when the trajectory has not yet entirely filled the droplet area (Figure 6.1).

At ϕ near or lower than the entropic near-glass regime, which is ergodic [Figure 6.1(a)], the central droplet is weakly confined by the transient cage of nearest neighbors, providing more free space for the droplet motion compared to higher ϕ. This weak and transient geometrical restriction results in larger droplet center-of-mass (COM) displacements for a given time lag τ. As ϕ is raised to the electrostatic jamming point [Figure 6.1(b)], at which the screened electrostatic repulsive forces dominate as the droplets are jammed and Debye screening layers of the droplets begin to significantly overlap, the droplet motion is highly restricted by the cage effect so that the root-MSD of the droplet is typically small relative to its radius. The model emulsion enters the interfacially jammed region as ϕ is further increased [Figure 6.1(c)], in which droplets are weakly deformed and the jamming is dominated by interfacial tension. Droplets undergo strongly bound HBBP motion when interfacially

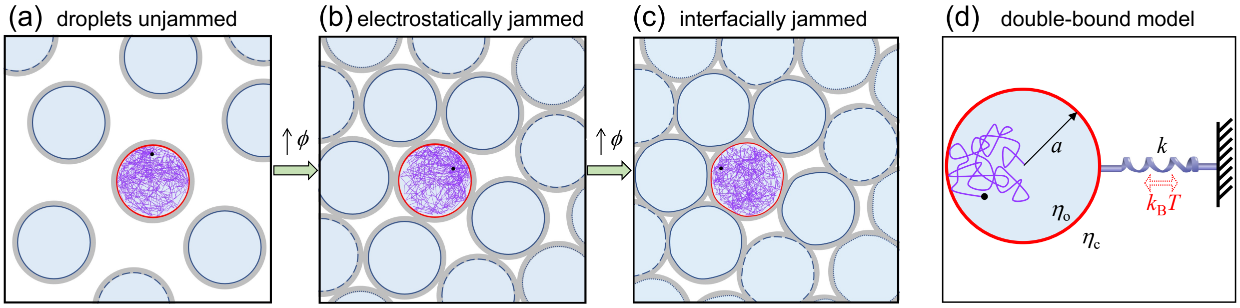

Figure 6.1. Schematic diagram depicting the elements of the probe-trajectory model for double-bound Brownian motion: the partial trajectory of a probe confined within a slowly diffusing harmonically bound Brownian colloidal droplet. Oil droplets (blue) are dispersed in the continuous phase (white) in presence of ionic surfactant molecules that lead to a Debye-screening length λ_{D} (grey coronas). A Brownian probe trajectory (black filled circle and purple line), confined in a central droplet (red outline) surrounded by its nearest neighbors (cobalt outline) and second nearest neighbors (dashed outline), in emulsions having droplet volume fractions ϕ: (**a**) below, (**b**) near, and (**c**) above the electrostatic jamming point. (**d**) Illustration of simulating the harmonically bound Brownian motion of the droplet, having a radius of a and a spring force constant, $k = 6\pi a G'_{\mathrm{p}}$, for the harmonic potential, where G'_{p} is the plateau elastic shear modulus. Dynamic viscosities of the oil and the continuous phase are η_{o} and η_{c}, respectively. The droplet experiences a restoring spring force towards an effective anchor, and Brownian excitations cause droplet motion.

jammed. In our model, we ignore any small deformation of droplets from perfect circles that would accompany a very high degree of interfacial jamming. For the purpose of inferring the droplet self-motion by analyzing the total and droplet-confined probe motion, a higher ratio of droplet MSD relative to total probe MSD is obtained from a larger droplet mean displacement in relation to the droplet size, which is the Gaussian distribution width of large-τ displacements of the confined probe motion. Therefore, our approach is mainly associated with colloidal suspension systems having relatively small colloids (*i.e.* small a) and high colloid volume fraction (*i.e.* high ϕ). A simplified illustration depicts the partial trajectory of a confined probe in a droplet of interest, having a radius of a and internal oil viscosity η_{o} [Figure 6.1(d)]. The droplet of interest is anchored to the origin by a spring with force constant k, which is determined by the soft elasticity of the jammed emulsion system. While this diagram demonstrates in 1D that the droplet having harmonic energy of $|U| = \frac{1}{2}kr^2$ at a radial position r from the origin moves along one axis as the spring vibrates, our simulation has been performed in 2D by solving the Langevin equation.

In the simulation, we first produce a strictly confined probe trajectory that has uniformly distributed radial positions within the droplet region. The confined probe is in a deep square potential well whose boundary is exactly at the droplet radius. To model the confined thermally excited probes in a perfectly stationary droplet, we generate a set of Gaussian-distributed random numbers, containing N elements, where N is the number of steps in the trajectory, as the initial step lengths Δr for a given time step Δt, using *Mathematica*. The scalar Δr has a mean of $2\sqrt{D_{\mathrm{p}}\Delta t}$, where $D_{\mathrm{p}} = k_{\mathrm{B}}T/(6\pi\eta_{\mathrm{o}}a_{\mathrm{p}})$ is the associated diffusion coefficient of the probe, k_{B} is Boltzmann's constant, T is the temperature, η_{o} is the dynamic viscosity of the oil within the droplet, and a_{p} represents the radius of the probe, while the standard deviation (SD) of the Δr distribution is $2\sqrt{(2/\pi)D_{\mathrm{p}}\Delta t}$. A separate set of uniformly distributed random numbers, ranging from 0 to 2π, is generated to represent the angle associated with the vector displacement for each step. The elapsed time and position of the jth step are $t_j = \Sigma_{i=1}^{j}\Delta t_i$ and $\boldsymbol{r}_j = \Sigma_{i=1}^{j}\Delta\boldsymbol{r}_i$, where i and j are integer indices, $\Delta\boldsymbol{r}_i$ is the ith step vector. If the oil probe-molecule encounters the boundary at the droplet radius (*i.e.* $r_j > a$, where $r_j = |\boldsymbol{r}_j|$ is the radial distance of jth position from the origin), then the jth step is split into two segments, and the probe-molecule is reflected from the droplet's curved boundary back inside the droplet. The $\boldsymbol{r}_j$ is updated and this operation is repeated for all N steps of the trajectory, yielding a time series of vector positions of the probe-molecule, which is the probe-molecule trajectory in the droplet's reference frame, $\boldsymbol{r}_{\mathrm{pr,conf},i}$, where i ranges from 1 to N.

We then create a trajectory for a harmonically bound Brownian droplet, whose radial positions are Gaussian-distributed in a central force field. The droplet motion can be described by the HBBP model. Ignoring inertial effects, the Langevin equation for the forces along the $x-$direction acting on the droplet is given by

$$0 = F_r(t) - kx - 6\pi a\eta_{\mathrm{c}}\frac{dx}{dt}, \tag{6.1}$$

where $F_r(t)$ is the Brownian random force having a white-noise frequency spectrum[176]: $\langle F_r(t)\rangle = 0$ and $\langle F_r(t)F_r'(t)\rangle = 12\pi a\eta_\mathrm{c}k_\mathrm{B}T\delta(t-t')$; the elastic restoring force constant $k = 6\pi aG_\mathrm{p}'$ is related to the plateau elastic modulus G_p' of the viscoelastic material, assuming stick boundary conditions; a is the droplet radius and η_c is the dynamic viscosity of the continuous phase. Note that the viscous Stokes drag, as formulated in equation 6.1, acts on a three-dimensional spherical droplet with stick boundary conditions. However, we only simulate trajectories in 2D, which is typical of what is often observed in optical microscopy measurements as in[176]. We make the assumption that η_c is a frequency-independent Newtonian viscosity, which however does not reflect the viscosity of the emulsion. To investigate realistic material parameters for viscoelastic emulsion model having nearly hard interactions between droplets, we calculate the plateau elastic shear moduli $G_\mathrm{p,EEI}'$ using the entropic,

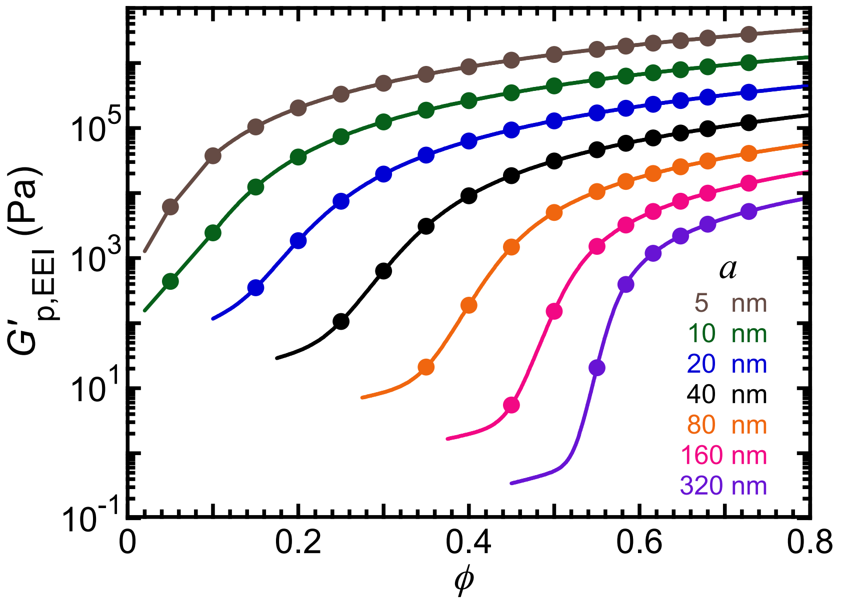

Figure 6.2. Simulation parameters used in the double-bound Brownian model. Plateau elastic shear moduli G_p' as a function of droplet volume fraction ϕ for monodispersed nanoscale and microscale 350 cSt trimethyl terminated polydimethylsiloxane (PDMS) oil-in-water emulsions stabilized by 10 mM sodium dodecyl sulfate (SDS); lines and points are predictions, based on mechanical rheological measurements, using the entropic, electrostatic, interfacial (EEI) model[37], for different droplet radii a. The oil density is 0.97 g cm^{-3} and oil viscosity $\eta_\mathrm{o} = 339.5$ mPa s. G_p' defines the elastic force constant k in the HBBP model for the droplet motion.

electrostatic, interfacial (EEI) model[37] for various droplet radii (Figure 6.2).

Solving the Langevin equation [equation (6.1)], we obtain the Green's function, $G(x_i, x_{i-1}; \Delta t)$, that provides the probability of finding a droplet at position x_i after a time interval Δt for the initial condition at x_{i-1}[176–178]:

$$G(x_i, x_{i-1}; \Delta t) = [2\pi B(\Delta t)]^{1/2} \exp\{-\frac{[x_i - A(\Delta t)]^2}{2B(\Delta t)}\}, \tag{6.2}$$

$$A(\Delta t) = x_{i-1} \exp(-\Delta t/\tau_{\mathrm{B}}), \tag{6.3}$$

$$B(\Delta t) = \frac{k_{\mathrm{B}}T}{k}[1 - \exp(-2\Delta t/\tau_{\mathrm{B}})], \tag{6.4}$$

where $\tau_{\mathrm{B}} = 6\pi a \eta_{\mathrm{c}}/k = \eta_{\mathrm{c}}/G'_{\mathrm{p}}$ represents the crossover time between dominantly viscous and elastic responses. The Green's function [equation (6.2)] is a Gaussian-distributed positional function, having mean $A(\Delta t)$ [equation (6.3)] and variance $B(\Delta t)$ [equation (6.4)].

To simulate the droplet trajectories in 2D, we generate two sets of N-element Gaussian-distributed random numbers, R_x and R_y, corresponding to the $x-$ and $y-$direction, respectively. The mean of each set is zero and the SD is unity. The motion of the center-of-mass (COM) of the droplet is simulated in the reference frame of the harmonic well according to the HBBP model. Defined by the Green's function [equation (6.2)], the positional time series of the droplet COM are constructed by modifying each element of R_x and R_y at a given Δt: $x_{\mathrm{drop},i} = R_{x,i}\sqrt{B_i} + A_{x,i}$, $y_{\mathrm{drop},i} = R_{y,i}\sqrt{B_i} + A_{y,i}$, and the corresponding vector $\boldsymbol{r}_{\mathrm{drop},i} = (x_{\mathrm{drop},i},\ y_{\mathrm{drop},i})$, where integer i ranges from 1 to N.

Combining the trajectory of confined probe motion in a stationary droplet and the COM trajectory of the harmonically bound Brownian droplet, we obtain the apparent total trajectory of the probe motion: $\boldsymbol{r}_{\mathrm{pr,tot},i} = \boldsymbol{r}_{\mathrm{pr,conf},i} + \boldsymbol{r}_{\mathrm{drop},i}$, for each time step t_i through t_1 to t_N. The resulting total probe trajectory presents a smeared boundary near and just above the droplet radius.

6.3.2 Mean square displacements

For a given time interval Δt, we calculate the time-averaged mean square displacement (MSD) from each trajectory by $\langle \Delta \boldsymbol{r}^2(\tau_j) \rangle = [1/(N-j+1)]\Sigma_{i=0}^{N-j} |\boldsymbol{r}_{i+j} - \boldsymbol{r}_i|^2$, where the lag time $\tau_j = j\Delta t$ and the integer index j ranges from 1 to N. Since the shorter-time trajectory coordinates are involved in a more averaging process than longer-time coordinates for calculating MSDs, to reduce the computational duration and increase the data density for good statistics, we perform trajectory calculations using a set of different time intervals: $\Delta t = 10^{-8}$ s, 10^{-7} s, 10^{-6} s, 10^{-5} s, 10^{-4} s, and 10^{-3} s; and total $N = 5 \times 10^4$ steps for each Δt when droplet radius $a \geq 60$ nm. The first two decades of the calculated $\langle \Delta \boldsymbol{r}^2(\tau) \rangle$ for each Δt are retained for any subsequent calculations. These values are averaged (5 to 4.99) $\times 10^4$ times, from the first to the 100th discrete τ.

The maximum $\Delta t_{\max} = 10^{-4}$ s is used for $a \approx 40$ nm, and 10^{-5} s for $a \leq 20$ nm, to avoid the issue of over-weighting the confined probe trajectory in the center than at the boundary of the droplet, which is originated from the reflection procedure when using a very large Δt in a small droplet. By setting a relatively short $\Delta t_{\max}$ while increasing the number of total steps to $N = 10^5$ for small droplets $a \leq 40$ nm, we confirm that the confined probe trajectories fill the entire droplet, including the area near the boundary where reflection events occur.

We define M bins in τ that are logarithmically spaced, where M is the number of desired data points in the τ-dependent MSD plot. All the $\langle \Delta \boldsymbol{r}^2(\tau_j) \rangle$ values that belong to the mth bin, satisfying $\tau_{\mathrm{s},m} < \tau_j < \tau_{\mathrm{e},m}$, where $\tau_{\mathrm{s},m}$ and $\tau_{\mathrm{e},m}$ are the starting and ending times of the mth bin, are averaged, yielding $\langle \Delta \boldsymbol{r}^2(\tau_m) \rangle$ in the final MSD plot, where τ_m is the bin's geometric mean time, $\tau_m = (\tau_{\mathrm{s},m}\tau_{\mathrm{e},m})^{1/2}$. Applying the MSD calculation, stitching, and re-binning process to the positional time series of confined probe diffusion, $\boldsymbol{r}_{\mathrm{pr,conf}}(t)$, harmonically bound Brownian droplet motion, $\boldsymbol{r}_{\mathrm{drop}}(t)$, and total combined probe motion, $\boldsymbol{r}_{\mathrm{pr,tot}}(t)$, respectively, we obtain the corresponding MSDs as functions of the lag time τ.

6.3.3 Extracting droplet MSDs from total molecular probe MSDs

According to the HBBP model, the step sizes of the bound droplet motion in the lab frame, $\Delta r_{\mathrm{drop}}(\tau_j) = |\boldsymbol{r}_{\mathrm{drop},i+j} - \boldsymbol{r}_{\mathrm{drop},i}|$, where $\tau_j = j\Delta t$, i and j can take any integer from 0 to N, is Gaussian-distributed. We certify that the step sizes of the confined probe motion in the droplet frame, $\Delta x_{\mathrm{pr,conf}}(\tau_j)$ and $\Delta y_{\mathrm{pr,conf}}(\tau_j)$, calculated from the corresponding trajectory, can also be fit to zero-mean Gaussian distributions with regression coefficient $R^2 \geq 0.9985$ for all τ from 10^{-8} s to $\Delta t_{\max}$ for the given droplet radius. Thus, for a given τ, both Δr_{drop} for the droplet COM's trajectory and $\Delta r_{\mathrm{pr,conf}} = (\Delta x^2_{\mathrm{pr,conf}} + \Delta y^2_{\mathrm{pr,conf}})^{1/2}$ for the confined molecular probe's trajectory are proven to be Gaussian-distributed. Therefore, the vector superposition of these trajectories will also have a Gaussian displacement distribution with a total molecular probe MSD that is the sum of the MSDs of these two components (*i.e.* droplet and confined molecular probe): $\left\langle \Delta \boldsymbol{r}^2_{\mathrm{pr,tot}}(\tau) \right\rangle = \left\langle \Delta \boldsymbol{r}^2_{\mathrm{drop}}(\tau) \right\rangle + \left\langle \Delta \boldsymbol{r}^2_{\mathrm{pr,conf}}(\tau) \right\rangle$.

To extract the droplet self-motion MSD from the probe motion MSDs, we take the confined probe motion MSD as the reference signal and subtract it from the total probe motion MSD: $\left\langle \Delta \boldsymbol{r}^2_{\mathrm{drop}}(\tau) \right\rangle = \left\langle \Delta \boldsymbol{r}^2_{\mathrm{pr,tot}}(\tau) \right\rangle - \left\langle \Delta \boldsymbol{r}^2_{\mathrm{pr,conf}}(\tau) \right\rangle$. The extracted droplet self-motion MSDs from the subtraction analysis are compared to the known droplet self-motion MSDs, which are directly calculated from the droplet trajectory, to show the capability of inferring droplet self-motion by solely detecting the droplet-confined probe motion in a viscoelastic, soft material.

We produce trajectories using different material parameters, including the ratio between viscosities of the dispersed oil phase and the continuous phase $\eta_{\mathrm{o}}/\eta_{\mathrm{c}}$, droplet radius a, and plateau elastic modulus G'_{p}, to examine how these parameters influence the performance of the MSD subtraction analysis for extracting the droplet self-motion from the probe motion. Realistic microrheological parameters are determined using the EEI model that is originally designed for emulsions having nearly hard interactions between droplets, and used in the simulations to testify whether the extracted droplet plateau MSDs can be related to the shear elastic moduli through the GSER.

6.4 Results

6.4.1 Probe and droplet positional statistics

We calculate the radial positional distribution by binning r in the polar coordinates ($r = \sqrt{x^2 + y^2}$) for each set of trajectories into equal-area annuli. For the confined probe diffusion in a perfectly stationary droplet, the probability density function (PDF), $p_{\text{pr,conf}}(r)$, shows a uniform distribution at $0 < r < a$, followed by an instant cutoff to zero at the droplet radius $r = a$ [Figure 6.3(a)]. The $p_{\text{drop}}(r)$ for the trajectory of the HBBP droplet motion is Gaussian-distributed [Figure 6.3(b)], and for the total combined probe trajectory, the radial positional distribution resembles that for the confined probe trajectory at small r but gradually decays to zero as r approaching a, manifesting a smeared boundary compared to the confined case [Figure 6.3(c)]. The $p_{\text{pr,tot}}(r)$ for total probe motion is fit to a Fermi-like function $p_{\text{pr,tot}}(r) \propto r/\{1 + \exp[(r - a)/\sigma]\}$, where σ is related to how rapidly $p_{\text{pr,tot}}(r)$ decreases, with $\mathrm{R}^2 \geq 0.996$.

To more intuitively present the positional distribution probabilities, we normalize and make dimensionless the heights of each bar in the statistic histogram, denoted by $p(r)/r$. The uniform $p_{\text{pr,conf}}(r)/(2r/a^2)$ at $r \leq a$ depicts the approximately equal probability of finding the center of the probe molecule in each annulus, having boundaries at r and $r + \mathrm{d}r$, with the same area [Figure 6.3(d)]. The $p_{\text{drop}}(r)/r$ is normalized by σ^2, where σ is the standard deviation obtained from the fit to $p_{\text{drop}}(r)$ in Figure 6.3(b). The resulting $p_{\text{drop}}(r)/(r/\sigma^2)$ is proportional to $(1/\sigma)\exp[-r^2/(2\sigma^2)]$, showing that the center of the droplet is highly confined around the origin in a Gaussian manner with a zero mean and small σ relative to a [Figure 6.3(e)]. The probability of locating the droplet vanishes at about 3 nm with respect to its starting position; whereas the probe molecule can freely diffuse within the entire circle having a radius of 60 nm. For the total combined probe motion, the profile of $p_{\text{pr,tot}}(r)/[2r/(a^2+2\sigma^2)]$ reflects a uniform distribution up to ≈57 nm and a narrow Gaussian-like distribution near the edge of the droplet, vanishing at about 63 nm [Figure 6.3(f)]. This

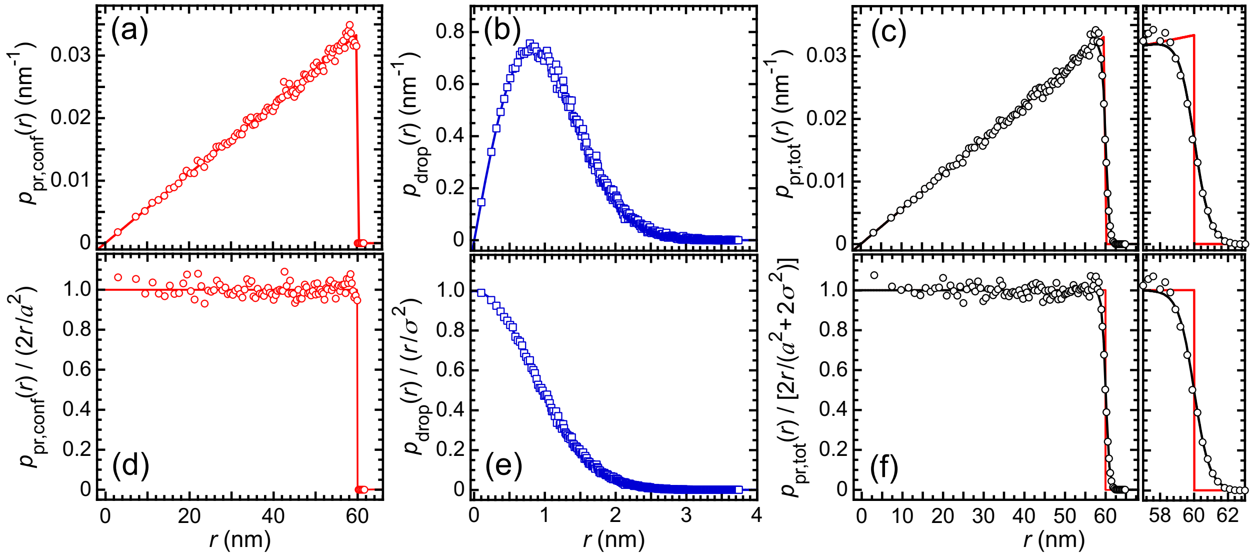

Figure 6.3. Normalized radial positional probability density functions (PDFs), $p(r)$, obtained from the component and total probe-molecule trajectories. (**a**) PDF $p_{\rm pr,conf}(r)$ (red circles) of the confined probe-molecule positions in a perfectly stationary droplet rises linearly out to the edge of the disk at $a = 60$ nm (red line: linear fit, $\rm R^2 = 0.993$). (**b**) PDF of the HBBP droplet trajectory (blue circles) follows a Gaussian distribution: $p_{\rm drop}(r) = (1/\sigma^2)\exp[-r^2/(2\sigma^2)]r$, where $\sigma = 0.823 \pm 0.001$ nm (blue line: fit, $\rm R^2 = 0.998$). (**c**) PDF of the total combined probe trajectory in the lab frame, $p_{\rm pr,tot}(r)$, (black circles) shows a smeared boundary near r approaching a (zoomed in the right frame having a narrow range of r near a). Fit of $p_{\rm pr,tot}(r)$: black line (see text for linear-Fermi functional form, $\rm R^2 \geq 0.996$). (**d**) - (**f**) 2D PDFs in (a)-(c), converted through division by r, each having unity value at $r = 0$: $p_{\rm pr,conf}(r)/(2r/a^2)$, $p_{\rm drop}(r)/(r/\sigma^2)$, and $p_{\rm pr,tot}(r)/[2r/(a^2+2\sigma^2)]$, reflect the probability density of locating either the center of the molecular probe or the center of the droplet in the corresponding trajectory at a radius between r and $r + \mathrm{d}r$, binned by equal annular area. The smeared boundary of $p_{\rm pr,tot}(r)/[2r/(a^2+2\sigma^2)]$ near $r = a$ (black), in contrast with the step change of $p_{\rm pr,conf}(r)/(2r/a^2)$ (red), is highlighted in the right section of part (f). The presented results are for an emulsion having volume fraction $\phi = 0.45$, droplet radius $a = 60$ nm, and probe size $a_{\rm p} = 1.5$ nm. Other simulation parameters: dynamic oil viscosity $\eta_{\rm o} = 339.5$ mPa s (kinematic viscosity $\nu_{\rm o} = 350$ cSt, density $\rho_{\rm o} = 0.97$ g cm^{-3}), viscosity of continuous phase $\eta_{\rm c} = 1$ mPa s; and the plateau elastic modulus $G'_{\rm p} = 5247.5$ Pa is predicted using the EEI model[37].

smeared boundary in close proximity to $r = a$ is distinctive from the step change as seen in the circumstance of a confined probe in a stationary droplet.

6.4.2 Droplet self-motion MSD extraction

The extracted droplet self-motion MSDs, determined by subtracting the pure confined probe MSDs from the corresponding total combined probe MSDs, present a great agreement with the calculated droplet self-motion MSDs from the droplet trajectory, which can be readily seen through the match of the blue data points and the calculation curve in Figure 6.4(a). The good performance of the presented instance is promised by a large ratio between the droplet mean displacement and the droplet radius; and consequentially, a large ratio of $\left\langle \Delta \boldsymbol{r}^2_{\text{drop}}(\tau) \right\rangle / \left\langle \Delta \boldsymbol{r}^2_{\text{pr,tot}}(\tau) \right\rangle$ for the entire span of τ.

After exploring a wide range of different combinations of material parameters, we find that the ratio $\left\langle \Delta \boldsymbol{r}^2_{\text{drop}} \right\rangle / \left\langle \Delta \boldsymbol{r}^2_{\text{pr,tot}} \right\rangle$ needs to be greater than 0.2% for the probe MSD-subtraction analysis to be effectively sensitive for droplet MSD extraction, while the minimum detectable long-τ plateau droplet MSD, $\left\langle \Delta \boldsymbol{r}^2_{\text{drop}} \right\rangle_{\text{p,min}}$, reaches 8×10^{-20} m^2, and the MSDs need to be resolvable for at least τ shorter than 10^{-4} s. Commensurately, from the perspective of experiments, if one wants to successfully extract the self-motion MSD of a droplet, the equipment used to measure the probe motion is required to be accurate for a displacement of at least a few angstroms within sub-milliseconds. Exceeding these threshold values, the extracted $\left\langle \Delta \boldsymbol{r}^2_{\text{drop}} \right\rangle$ is capable of capturing the feature at short $\tau \leq 10^{-4}$ s but is prone to scattering around the expected magnitude and then fail as τ extends to a larger value. In addition to an explicit numerical calculation, the ratio $\left\langle \Delta \boldsymbol{r}^2_{\text{drop}} \right\rangle / \left\langle \Delta \boldsymbol{r}^2_{\text{pr,tot}} \right\rangle$ can be visually and qualitatively evaluated by comparing the effective radius of the droplet trajectory (blue) and the total probe trajectory (black) in Figure 6.4(b). Alternatively, it can be evaluated by the thickness of the black corona relative to the effective radius of the confined probe trajectory (red) that equals the droplet radius a. In principle, a good resolution of the $\left\langle \Delta \boldsymbol{r}^2_{\text{drop}} \right\rangle$ extraction is guaranteed by a thick corona around a small droplet, seen in such overlay of probe trajectories. Albeit that the long-τ plateau MSDs of the probe motion, before and after applying the superposition of droplet motion, are nearly identical when plotted on a logarithmic scale [red and black in Figure 6.4(a)], the systematic difference that

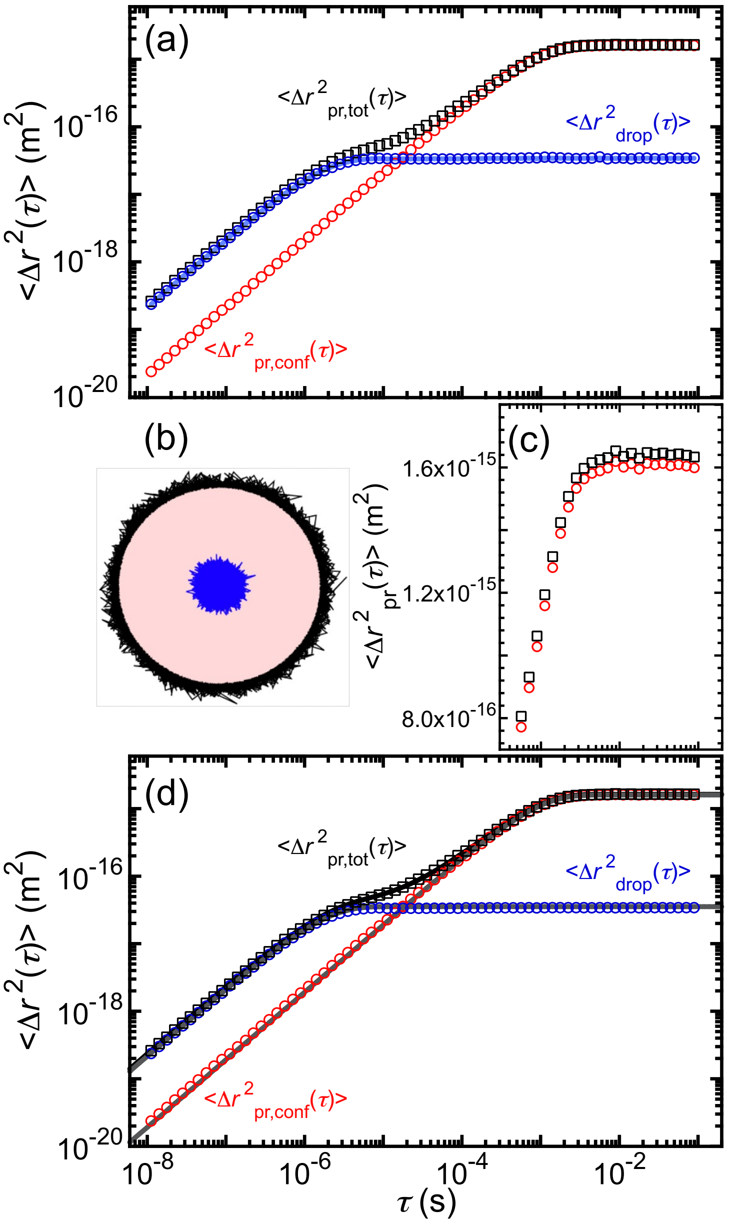

Figure 6.4. Mean square displacement analysis for inferring droplet self-motion from the total droplet-confined probe motion. (**a**) The harmonically bound Brownian droplet motion MSD (blue circles), $\langle \Delta \boldsymbol{r}^2_{\mathrm{drop}}(\tau) \rangle$, is extracted by subtracting the confined probe MSD (red circles), $\langle \Delta \boldsymbol{r}^2_{\mathrm{pr,conf}}(\tau) \rangle$, from the apparent total probe MSD (black squares), $\langle \Delta \boldsymbol{r}^2_{\mathrm{pr,tot}}(\tau) \rangle$. The later two probe MSDs are determined from the corresponding probe trajectories. The extracted $\langle \Delta \boldsymbol{r}^2_{\mathrm{drop}}(\tau) \rangle$ is compared to the known droplet self-motion MSD (light blue line), determined directly from the droplet COM trajectory. (Caption continued on next page.)

Figure 6.4. (Caption continued.) (**b**) Overlay of trajectories: the droplet trajectory (blue) is overlaid on the probe-molecule trajectory in the droplet frame (light red) and that is overlaid on the total probe-molecule trajectory (black), all sharing a common origin. The total probe-molecule trajectory is largely obscured except for the boundary region, corresponding to the zoom-in of part (c). Any area beneath the occlusion by other trajectories in the red and black region is fully filled by itself. An inconspicuous fuzzy edge is observed in the red region in comparison to a perfect circle. (**c**) A zoom-in view of probe MSDs from $\tau \approx 5 \times 10^{-4}$ s to 10^{-1} s using the linear scale in the vertical axis, showing the systematic difference between $\left\langle \Delta \boldsymbol{r}^2_{\mathrm{pr,conf}}(\tau) \right\rangle$ and $\left\langle \Delta \boldsymbol{r}^2_{\mathrm{pr,tot}}(\tau) \right\rangle$ when $\left\langle \Delta \boldsymbol{r}^2_{\mathrm{drop}}(\tau) \right\rangle$ is in the plateau regime. (**d**) Extracting the two HBBP components, $\left\langle \Delta \boldsymbol{r}^2_{\mathrm{pr,conf}}(\tau) \right\rangle$ and $\left\langle \Delta \boldsymbol{r}^2_{\mathrm{drop}}(\tau) \right\rangle$ (gray lines), by fitting $\left\langle \Delta \boldsymbol{r}^2_{\mathrm{pr,tot}}(\tau) \right\rangle$ to a double-bound Brownian model [equation (6.5), black line]. Material parameters used in the presented results are $a = 40$ nm, $a_{\mathrm{p}} = 1.5$ nm, $\eta_{\mathrm{o}} = 339.5$ mPa s, $\eta_{\mathrm{c}} = 1$ mPa s, and $G'_{\mathrm{p}} = 634.35$ Pa that corresponds to $\phi = 0.3$ according to the EEI model[37].

corresponds to the plateau droplet MSD has been readily observed on a linear scale [Figure 6.4(c)].

Given the well-defined dual rise-to-plateau feature of the apparent total probe MSDs, the two-component self-motion MSDs have been extracted by fitting $\left\langle \Delta \boldsymbol{r}^2_{\mathrm{pr,tot}}(\tau) \right\rangle$ to a double-bound Brownian model having two HBBP components, associated with $\left\langle \Delta \boldsymbol{r}^2_{\mathrm{drop}}(\tau) \right\rangle$ and $\left\langle \Delta \boldsymbol{r}^2_{\mathrm{pr,conf}}(\tau) \right\rangle$, respectively:

$$\left\langle \Delta \boldsymbol{r}^2_{\mathrm{pr,tot}}(\tau) \right\rangle = \left\langle \Delta \boldsymbol{r}^2_{\mathrm{pr,conf}} \right\rangle_{\mathrm{p}} [1 - \exp(-\tau/\tau_{\mathrm{pr}})] + \left\langle \Delta \boldsymbol{r}^2_{\mathrm{drop}} \right\rangle_{\mathrm{p}} [1 - \exp(-\tau/\tau_{\mathrm{drop}})], \qquad (6.5)$$

where $\left\langle \Delta \boldsymbol{r}^2_{\mathrm{pr,conf}} \right\rangle_{\mathrm{p}}$ and $\left\langle \Delta \boldsymbol{r}^2_{\mathrm{drop}} \right\rangle_{\mathrm{p}}$ are the corresponding low-frequency plateau MSDs; τ_{pr} and τ_{drop} are the characteristic time scales associated with the two bending knees [see Figure 6.4(d)]. We have shown that the confined probe step sizes for a variety of τ are Gaussian-distributed (see chapter 6.3.3), which verifies the feasibility of fitting the confined probe motion MSD with an HBBP function. The decoupling is allowed because, in our model, the self-motion modes of the probe and the droplet are independent of each other. The yielding fitting parameters represent the characteristic time scales and the low-frequency plateau MSDs for both component motions. Naturally, the rise-to-plateau with the shorter characteristic time scale and lower plateau MSD magnitude is associated with the droplet motion, and the other is associated with the confined probe motion.

6.4.3 Viscosity and droplet size

A higher ratio of droplet MSD relative to total probe MSD, $\xi = \left\langle \Delta \boldsymbol{r}^2_{\text{drop}} \right\rangle_{\text{p}} / \left\langle \Delta \boldsymbol{r}^2_{\text{pr,tot}} \right\rangle_{\text{p}}$, for a given droplet radius and plateau shear elasticity can be achieved by enhancing the contrast of viscosity between the oil phase and the continuous phase. For each decade in the range of $\eta_{\text{o}}/\eta_{\text{c}}$ from 10^0 to 10^6, we show representative behaviors of the total combined and the purely confined probe motion MSDs, using other fixed parameters of $a = 60$ nm, $G'_{\text{p}} = 100$ Pa and $\eta_{\text{c}} = 1$ mPa s, in Figure 6.5. The dual rise-to-plateau feature of $\left\langle \Delta \boldsymbol{r}^2_{\text{pr,tot}}(\tau) \right\rangle$ cannot be readily seen when $\eta_{\text{o}}/\eta_{\text{c}} \leq 10^2$, whereas it becomes increasingly pronounced for an emulsion having higher-viscosity in the dispersed phase. Varying $\eta_{\text{o}}/\eta_{\text{c}}$ while keeping η_{c} constant, the characteristic time scale τ_{drop} and the plateau droplet motion MSD $\left\langle \Delta \boldsymbol{r}^2_{\text{drop}} \right\rangle_{\text{p}}$ remain unchanged, which defines the location and magnitude of the droplet motion MSD's

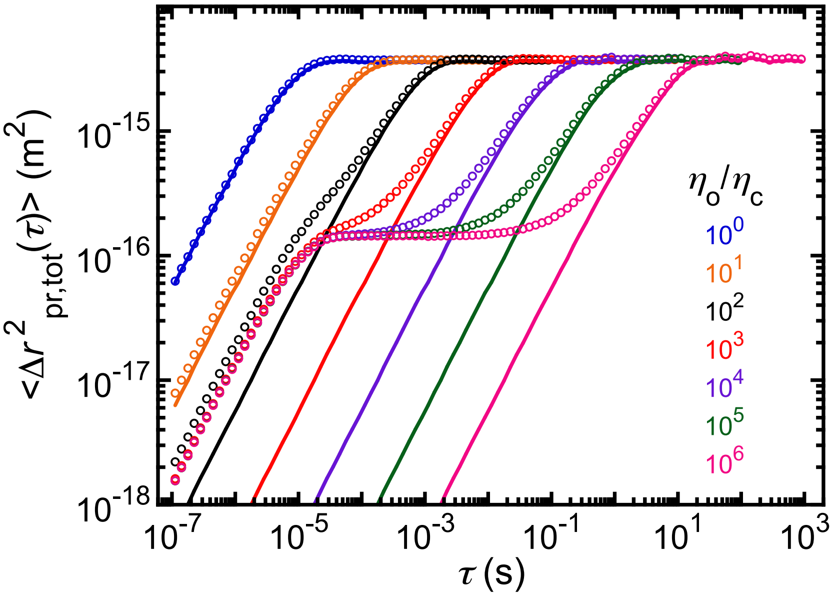

Figure 6.5. Time-averaged mean square displacements of the double-bound total probe motions, $\left\langle \boldsymbol{\Delta r^2_{\text{pr,tot}}(\tau)} \right\rangle$, in a harmonically bound droplet having $a = 60$ nm, at different viscosity ratio of the oil (dispersed phase) and the continuous phase, $\eta_{\text{o}}/\eta_{\text{c}}$. The solid lines are for reference the confined molecular probe MSDs for perfectly stationary droplets. The plateau elastic modulus of the emulsion is $G'_{\text{p}} = 100$ Pa, and η_{c} is fixed at 1 mPa s.

bending knee, respectively, corresponding to the first rise-to-plateau of $\left\langle\Delta\boldsymbol{r}^2_{\mathrm{pr,tot}}(\tau)\right\rangle$. The well-defined dual rise-to-plateau of $\left\langle\Delta\boldsymbol{r}^2_{\mathrm{pr,tot}}(\tau)\right\rangle$ for $\eta_{\mathrm{o}}/\eta_{\mathrm{c}} \geq 10^3$ offers the opportunity to extract the droplet COM MSDs from fitting $\left\langle\Delta\boldsymbol{r}^2_{\mathrm{pr,tot}}(\tau)\right\rangle$ to the double-bound Brownian model, defined in equation 6.5. The total probe motion MSDs for $\eta_{\mathrm{o}}/\eta_{\mathrm{c}} \geq 10^3$ effectively overlap with one another at short time lag $\tau < \tau_{\mathrm{drop}}$. However, a higher viscosity in the oil phase decelerates the self-motion of the internal probe in the droplet, yielding smaller reference signal $\left\langle\Delta\boldsymbol{r}^2_{\mathrm{pr,conf}}(\tau)\right\rangle$ for $\tau < \tau_{\mathrm{pr}}$, where τ_{pr} defines the bending knee of the confined probe MSD in a stationary droplet. Therefore, prior to entering the second plateau of $\left\langle\Delta\boldsymbol{r}^2_{\mathrm{pr,tot}}(\tau)\right\rangle$, the difference between the signal and the reference increases with an increased $\eta_{\mathrm{o}}/\eta_{\mathrm{c}}$.

Moreover, by contrast to the previously defined Newtonian η_{c} of the continuous phase, the dynamic viscosity of the emulsion is ϕ- and frequency-dependent, which reflects the hydrodynamic effective viscosity acting on the droplets. Thus, we extract the high-frequency viscosities, $\eta_{\mathrm{e},\infty}(\phi)$, of the viscoelastic emulsion having $\langle a\rangle = 459$ nm for $\phi \geq 0.5$ from the DWS measurements in[57]. We recognize that at higher ϕ, the emulsion's viscosity $\eta_{\mathrm{e},\infty}$ is needed for simulating the droplet COM motion, not the Newtonian viscosity of the continuous phase, for emulsions that are near and above the jamming limit.

In a different scenario of fixing the viscosity contrast and shear elasticity, the smaller the droplet size is the higher accuracy of extracted droplet self-motion MSD at long τ (see Figure 6.6). By fixing the other parameters at $\eta_{\mathrm{o}} = 100$ mPa s, $\eta_{\mathrm{c}} = 1$ mPa s, and $G'_{\mathrm{p}} = 100$ Pa, the droplet COM MSD is the dominant portion of the total double-bound molecular probe MSD, spanning the entire range of τ explored, for $a \leq 40$ nm [Figure 6.6(a)], leading to an excellent agreement between the extracted droplet self-motion MSD and its theoretical value for $a \leq 40$ nm [Figure 6.6(b)]. As the droplet radius is increased to 40 nm $\leq a \leq 80$ nm, the dual rise-to-plateau feature of $\left\langle\Delta\boldsymbol{r}^2_{\mathrm{pr,tot}}(\tau)\right\rangle$ has been observed [Figure 6.6(a)], indicating the feasibility of extracting the droplet MSDs by fitting $\left\langle\Delta\boldsymbol{r}^2_{\mathrm{pr,tot}}(\tau)\right\rangle$ to the double-bound Brownian model (equation 6.5). For larger droplet radii $a > 80$ nm, the

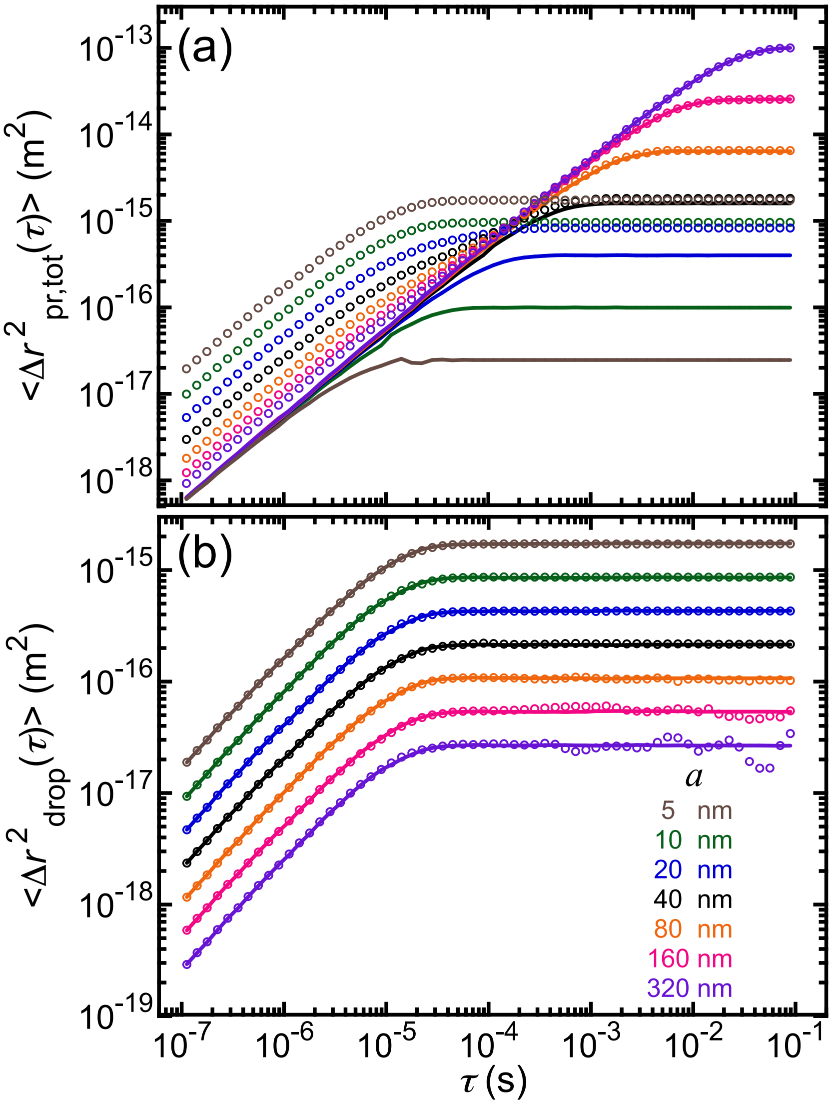

Figure 6.6. Time-averaged mean square displacements of the total double-bound probe motion, $\left\langle \boldsymbol{\Delta r^2_{\mathrm{pr,tot}}(\tau)} \right\rangle$, and the harmonically bound droplet motion, $\left\langle \boldsymbol{\Delta r^2_{\mathrm{drop}}(\tau)} \right\rangle$, at different droplet radii. (**a**) $\langle \Delta \boldsymbol{r}^2_{\mathrm{pr,tot}}(\tau) \rangle$ determined from trajectories of the double-bound molecular probe motions for a wide range of a [open circles; color-coded, see legend in part (b)]. Solid lines represent $\langle \Delta \boldsymbol{r}^2_{\mathrm{pr,conf}}(\tau) \rangle$ of confined molecular probe MSDs in stationary droplets for reference. (**b**) $\langle \Delta \boldsymbol{r}^2_{\mathrm{drop}}(\tau) \rangle$ (open circles) extracted from the probe MSDs: $\langle \Delta \boldsymbol{r}^2_{\mathrm{drop}}(\tau) \rangle = \langle \Delta \boldsymbol{r}^2_{\mathrm{pr,tot}}(\tau) \rangle - \langle \Delta \boldsymbol{r}^2_{\mathrm{pr,conf}}(\tau) \rangle$. Solid lines represent the droplet self-motion MSD calculated directly from the COM trajectory of the droplet. The viscosity of the oil is $\eta_{\mathrm{o}} = 100$ mPa s and that of the continuous phase is $\eta_{\mathrm{c}} = 1$ mPa s. The plateau elastic modulus of the emulsion is $G'_{\mathrm{p}} = 100$ Pa.

percentage of $\left\langle \Delta \boldsymbol{r}^2_{\mathrm{pr,tot}}(\tau) \right\rangle$ that arises from the droplet HBBP motion is strongly reduced, yielding the very subtle difference between $\left\langle \Delta \boldsymbol{r}^2_{\mathrm{pr,tot}}(\tau) \right\rangle$ and $\left\langle \Delta \boldsymbol{r}^2_{\mathrm{pr,conf}}(\tau) \right\rangle$. Thus, slight fluctuation around the theoretical magnitude of $\left\langle \Delta \boldsymbol{r}^2_{\mathrm{drop}} \right\rangle$ has been observed for $a = 80$ nm at $\tau \geq 5 \times 10^{-4}$ s, and the fluctuation becomes more obvious for larger droplet radii $a = 160$ nm and 320 nm [Figure 6.6(b)]. As stated in chapter 6.4.2, a higher $\left\langle \Delta \boldsymbol{r}^2_{\mathrm{drop}} \right\rangle / \left\langle \Delta \boldsymbol{r}^2_{\mathrm{pr,tot}} \right\rangle$ and equivalently, a lower $\left\langle \Delta \boldsymbol{r}^2_{\mathrm{pr,conf}} \right\rangle / \left\langle \Delta \boldsymbol{r}^2_{\mathrm{drop}} \right\rangle$ is desired to achieve higher accuracy of the extracted $\left\langle \Delta \boldsymbol{r}^2_{\mathrm{drop}} \right\rangle$. Because the droplet radius a is the Gaussian distribution semi-width of the step sizes $\Delta r_{\mathrm{pr,conf}}$ in the long-τ limit, using a smaller droplet size when other material parameters are invariable will potentially enhance the accuracy of the extracted droplet self-motion MSDs.

6.4.4 Double-bound Brownian MSDs of emulsions: varying droplet size and volume fraction

For the purpose of broadening the ϕ range of an emulsion whose droplet self-motion MSDs are extractable from probe motion detection, using small droplets is advantageous. For example, droplet self-motion MSDs of a nanoemulsion system having $a = 10$ nm can be extracted over a wide range of ϕ from 0.728 down to 0.100 [Figure 6.7(a-b)]; while for an emulsion system having $a = 320$ nm, it can only be extracted for $\phi \geq 0.500$ [Figure 6.7(c-d)]. This is because rather than ϕ, it is G'_{p}, connected to the force constant by $k = 6\pi a G'_{\mathrm{p}}$, that is the parameter directly involved in the Langevin equation [equation (6.1)]. However, according to the EEI model, G'_{p} at a given ϕ radically decreases as droplet size increases, and the difference in G'_{p} for a set of two droplet radii is even enlarged as ϕ decreases. For instance, the G'_{p} for $a =$ 320 nm at the highest $\phi = 0.728$ is of the same magnitude of the G'_{p} for $a = 5$ nm at $\phi =$ 0.05 (see Figure 6.2).

For a viscoelastic emulsion having a fixed droplet radius, the more dilute the emulsion is, the higher resolution of droplet MSD extraction one can obtain over a wide range of τ. The dual rise-to-plateau feature of $\left\langle \Delta \boldsymbol{r}^2_{\mathrm{pr,tot}}(\tau) \right\rangle$ is observed at low $\phi \leq 0.3$ for $a = 10$ nm when

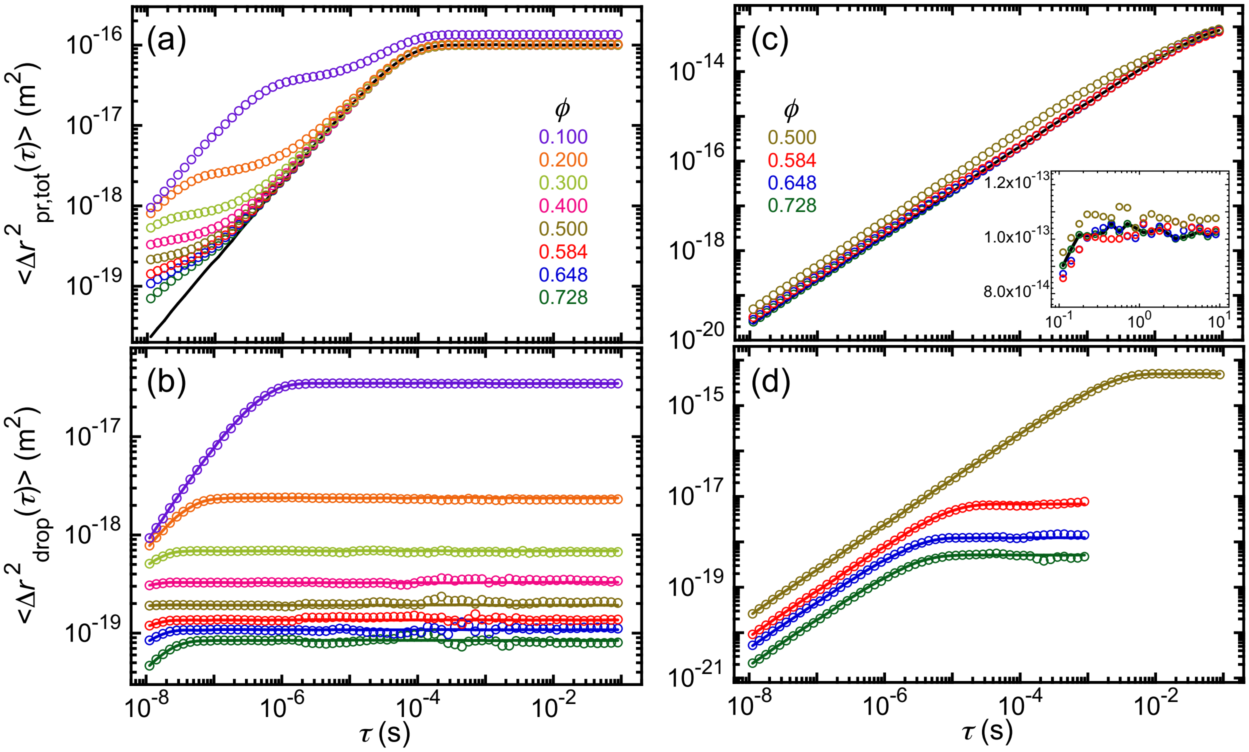

Figure 6.7. Mean square displacements of the total double-bound probe motion, $\left\langle \Delta \boldsymbol{r}^2_{\mathrm{pr,tot}} \right\rangle$, and the droplet motion, $\left\langle \Delta \boldsymbol{r}^2_{\mathrm{drop}} \right\rangle$, as functions of the lag time τ at different droplet volume fractions ϕ, for viscoelastic emulsion models having droplet radii of 10 nm [parts (a) and (b)] and 320 nm [parts (c) and (d)]. In parts (**a**) and (**c**), the black solid lines represent the confined probe motion MSDs in a stationary droplet, $\left\langle \Delta \boldsymbol{r}^2_{\mathrm{pr,conf}}(\tau) \right\rangle$, while the color-coded open circles represent the total droplet-confined probe MSDs as the droplet is in the harmonic potential well, $\left\langle \Delta \boldsymbol{r}^2_{\mathrm{pr,tot}}(\tau) \right\rangle$, associated with different ϕ. The inset of part (c) displays the probe MSDs at long $\tau \geq 0.1$ s for a droplet having $a = 320$ nm, showing $\left\langle \Delta \boldsymbol{r}^2_{\mathrm{pr,tot}}(\tau) \right\rangle$ is hardly resolved from $\left\langle \Delta \boldsymbol{r}^2_{\mathrm{pr,conf}}(\tau) \right\rangle$ in this long-τ region when ratio $1/(aG'_{\mathrm{p}})$ of the emulsion model is sufficiently small. In parts (**b**) and (**d**), the open circles are droplet motion MSDs, extracted by subtracting $\left\langle \Delta \boldsymbol{r}^2_{\mathrm{pr,conf}}(\tau) \right\rangle$ from $\left\langle \Delta \boldsymbol{r}^2_{\mathrm{pr,tot}}(\tau) \right\rangle$, and are compared with the known droplet self-motion MSDs (color-coded lines) calculated from the droplet COM trajectories. In part (**d**), $\left\langle \Delta \boldsymbol{r}^2_{\mathrm{drop}}(\tau) \right\rangle$ at higher $\phi \geq 0.584$ is truncated at 10^{-3} s due to noisy data resulting from closely aligned values of $\left\langle \Delta \boldsymbol{r}^2_{\mathrm{pr,tot}}(\tau) \right\rangle$ and $\left\langle \Delta \boldsymbol{r}^2_{\mathrm{pr,conf}}(\tau) \right\rangle$ at longer τ for $a = 320$ nm. Material parameters have been determined as in Figure 6.2: G'_{p} calculated using the EEI model[37]; high-frequency viscosities $\eta_{\mathrm{e},\infty}(\phi)$ inferred from[57], and $\eta_{\mathrm{o}} = 339.5$ mPa s.

the minimum τ is set at 10^{-8} s [Figure 6.7(a)]. For the given $a = 10$ nm, the position of the first bending knee, associated with τ_{drop}, decreases in the highly elastic regime as ϕ is lowered down to $\phi = 0.5$. This can be attributed to the decrease in the high-frequency viscosity of the emulsion, $\eta_{\mathrm{e},\infty}$, for reduced ϕ^{57}. At $\phi = 0.5$, τ_{drop} is near but below 10^{-8} s so $\left\langle \Delta\boldsymbol{r}^2_{\mathrm{drop}}(\tau) \right\rangle$ is in the plateau region for entire $\tau \geq 10^{-8}$ s. As the nanoemulsion is further diluted down to $\phi = 0.1$, τ_{drop} increases to as high as 10^{-6} s. However, the dual rise-to-plateau feature cannot be readily seen for $a = 320$ nm over all the ϕ explored and the signal can hardly be resolved from the reference even in linear scale at $\tau > 0.1$ s [Figure 6.7(c) and inset]. Fluctuation of the extracted $\left\langle \Delta\boldsymbol{r}^2_{\mathrm{drop}}(\tau) \right\rangle$ around the theoretical value, yet within the range of permissible error, is observed when $\phi \geq 0.4$ for $a = 10$ nm [Figure 6.7(b)]. By contrast, in the case of $a = 320$ nm, longer $\tau > 10^{-5}$ s results for $\phi \geq 0.584$ are excluded from accurate inference [Figure 6.7(d)].

We then study the influence of radial droplet size on the MSD subtraction analysis of the superposition of probe MSDs for viscoelastic emulsions at fixed ϕ. We choose the value $\phi = 0.3$ since it is sufficiently high to include a relatively wide range of a from 80 nm down to 10 nm, and also low enough to have a good sensitivity for the smaller droplets. We present the probe motion MSDs for the subtraction analysis and the resulting droplet self-motion MSDs in Figure 6.8. For all the explored a, the dual rise-to-plateau feature of $\left\langle \Delta\boldsymbol{r}^2_{\mathrm{pr,tot}}(\tau) \right\rangle$ is observed. The characteristic time scales, τ_{drop} and τ_{pr}, and the magnitude of the plateau MSDs, $\left\langle \Delta\boldsymbol{r}^2_{\mathrm{drop}} \right\rangle_{\mathrm{p}}$ and $\left\langle \Delta\boldsymbol{r}^2_{\mathrm{pr,conf}} \right\rangle_{\mathrm{p}}$, exhibit a systematic increase as a is raised [Figure 6.8(a)]. For each of the presented droplet sizes, we show a good agreement between the extracted and theoretical $\left\langle \Delta\boldsymbol{r}^2_{\mathrm{drop}}(\tau) \right\rangle$ [Figure 6.8(b)].

The long-τ plateau droplet MSD $\left\langle \Delta\boldsymbol{r}^2_{\mathrm{drop}} \right\rangle_{\mathrm{p}}$ of a given colloidal soft material catches the most attention in performing passive microrheology using GSER. Accurately extracting $\left\langle \Delta\boldsymbol{r}^2_{\mathrm{drop}} \right\rangle_{\mathrm{p}}$ from the droplet-confined probe MSD-subtraction analysis requires a high dimensionless ratio of $\xi = \left\langle \Delta\boldsymbol{r}^2_{\mathrm{drop}} \right\rangle_{\mathrm{p}} / \left\langle \Delta\boldsymbol{r}^2_{\mathrm{pr,tot}} \right\rangle_{\mathrm{p}}$. In Figure 6.9, we show this ξ ratio calculated at long τ, where both the droplet MSD and probe MSD are in the plateau region, for a broad range of radial droplet sizes using parameters from the EEI model, covering the range of ϕ in which the model emulsion having a given droplet radius is shear elastic. Consider-

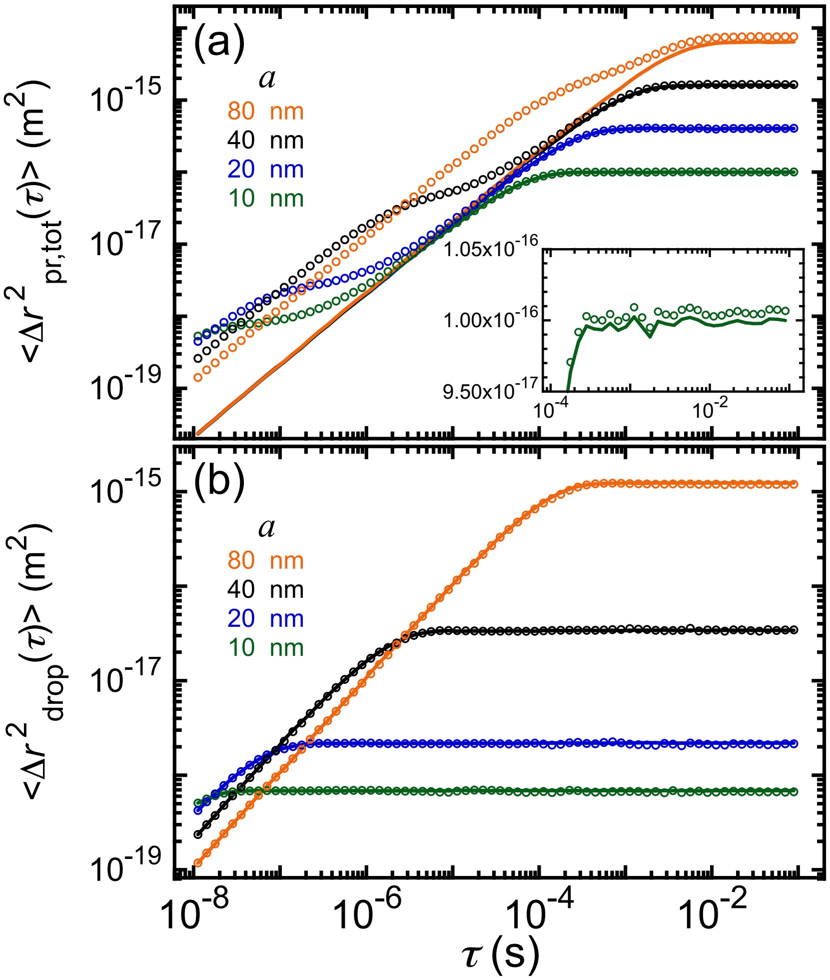

Figure 6.8. Mean square displacements of (a) the droplet-confined probe motion and (b) the harmonically bound droplet motion for emulsions having different droplet radii at a fixed volume fraction $\phi = 0.30$ using microrheological parameters as in Figure 6.2: G'_{p} determined by the EEI model^{37} and $\eta_{\mathrm{c}} = 1$ mPa s. (**a**) The total combined probe MSDs are shown in open circles and the purely confined probe MSDs as reference signals are presented in solid lines. (**b**) The extracted droplet MSDs (open circles), obtained from the probe MSDs, show good agreement with the known droplet MSDs (solid lines) from the droplet trajectory.

ing a sensitivity of 10^{-3} that is commonly seen in experimental apparatuses, for example, NMR, using a droplet radius $a \leq 10$ nm allows measurements above the threshold of ξ to be significantly above the jamming ϕ of the nanoemulsion, reaching $\phi \approx 0.7$. Meanwhile, the measurable range enters the jammed regime up to $\phi \approx 0.45$ for a droplet radius of 20 nm.

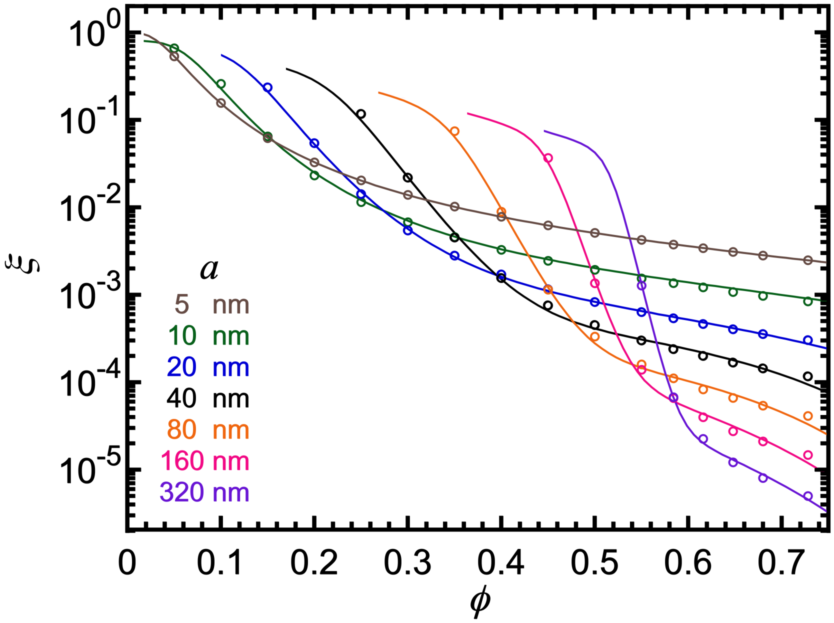

Figure 6.9. Dimensionless ratio of long-$\boldsymbol{\tau}$ plateau droplet mean square displacement and total probe mean square displacement, $\boldsymbol{\xi = \left\langle \Delta r^2_{\mathrm{drop}} \right\rangle_{\mathrm{p}} / \left\langle \Delta r^2_{\mathrm{pr,tot}} \right\rangle_{\mathrm{p}}}$, for emulsions having different droplet radii. Material parameters have been determined as in Figure 6.2: G'_{p} calculated using the EEI model[37]; and high-frequency viscosities $\eta_{\mathrm{e},\infty}(\phi)$ inferred from[57]. Fitting curves guide the eye.

However, for emulsions having droplet radius $a \geq 40$ nm, only the unjamming behavior and the diffusion coefficient at low droplet density can be resolved through the MSD subtraction analysis from NMR experiments[174]. Therefore, using nanoscale colloids down to $a \leq 10$ nm is beneficial to perform passive microrheology on elastically jammed probe molecule-laden colloidal systems via probe MSD detection.

6.5 Discussion and conclusion

In this trajectory-based simulation study, we demonstrate how to perform passive microrheology by analyzing the MSDs of a Brownian probe molecule confined within a droplet that undergoes harmonically bound Brownian motion. The motion of probe molecules within droplets has been modeled as simple diffusion confined within a disk representing the HBBP droplet. By subtracting the MSDs of the confined motion of probe molecule from the MSDs of the total molecular probe motion, we obtain the self-motion MSDs of the droplet's COM, which can be used to calculate the elastic plateau shear storage modulus at each packing fraction using the GSER.

To obtain higher values of ξ in future experiments, which would therefore be easier to analyze for passive microrheology, it would helpful to have a high viscosity in the dispersed phase and to have smaller nanoscale droplet sizes, particularly those less than 10 nm in radius; this indicates that restricting confined molecular probe motion is desirable if one primarily seeks to obtain droplet motion. This could enable future NMR experiments to determine droplet MSDs for ϕ well into the elastically jammed regime of the droplets, thereby facilitating passive microrheological interpretations.

Our simulation is akin to using a local molecular probe, which allows for particle-tracking methods of microrheology[179–181]. These techniques are not limited to ensemble averages and can potentially be used to characterize heterogeneous systems. With a clear grasp of the mechanics and relevant material parameters, we anticipate the potential use of techniques, such as NMR[140, 141, 146] and electron paramagnetic resonance (EPR) spectroscopy[182, 183], which inherently capture the fine details of molecular dynamics, to extract colloidal dynamics, and thereby perform passive microrheology.

Chapter 7 - Fingerprinting short-range attractions in dense emulsions using optical scattering

7.1 Motivation

In Chapters 2 and 3, we have elucidated the richness and complexity of the optical transport properties of dense, attractive colloidal emulsions, namely strongly attractive (SA) and intermediately attractive (IA), respectively, having certain specific short-range depletion attractions between droplets relative to $k_{\mathrm{B}}T$. By contrast with the inverted parabola-like $1/\ell^*(\phi)$ for emulsions having nearly hard interactions, we have observed the asymmetric $1/\ell^*(\phi)$ with two knees for SA emulsions (14.5 $k_{\mathrm{B}}T$, [SDS] = 80 mM) and also for IA emulsions (5.6 $k_{\mathrm{B}}T$, [SDS] = 35 mM). In addition, for the IA emulsions, there is a dip-like notch feature in $1/\ell^*(\phi)$ between the hard-sphere glass transition, ϕ_{g}, and maximal random jamming, ϕ_{MRJ}. We have developed the DCSN model and E-DCSN model for the SA and IA emulsions, respectively, as ways of performing regularized fitting of $1/\ell^*(\phi)$ using the minimum principal scattering-mechanical components for each system. These models have enabled us to infer the effective DWS probe radii, leading to quantitative passive microrheological interpretation of both sets of DWS measurements. From the DCSN model for the SA emulsions, we have determined that the MSDs cannot be assigned to individual droplets, instead they are associated with small clusters having effective size about twice the droplet over a wide range of ϕ. From the E-DCSN model, we have inferred that for the IA emulsions, the effective DWS probes are individual droplets at lower ϕ and are small clusters at higher ϕ; the ϕ-dependent effective DWS probe radius exhibits a smooth yet rapid transition between the droplet and cluster limits within the notch regime. Further theoretical work is necessary to refine these ideas and come up with predictions of DWS correlation functions based on first-principles, rather than a principal component model.

Knowing the optical transport properties over the full range of ϕ is essential for performing DWS passive microrheology of dense attractive emulsions. Without this $1/\ell^*(\phi)$ information, it would not be possible to either do the fitting in the (E-)DCSN model and determine the effective probe radius or to account for the collective scattering effects properly. Since the signatures of $1/\ell^*(\phi)$ for the SA and IA emulsions are distinctive, there is an opportunity for mapping the optical transport captured in $1/\ell^*(\phi)$ at other attractive strengths than those corresponding to NH, MA, IA, and SA already presented herein. By measuring additional $1/\ell^*(\phi)$ in between MA and IA as well as between IA and SA, we can further experimentally determine a complete set of fingerprints of $1/\ell^*(\phi)$ that can be linked to individual interaction strength.

Here, we present measurements of $1/\ell^*(\phi)$ at $|U_\mathrm{d}| \approx 3.3\ k_\mathrm{B}T$ between MA and IA (labelled MA-IA) and also measurements of $1/\ell^*(\phi)$ at $|U_\mathrm{d}| \approx 7.3\ k_\mathrm{B}T$ between IA and SA (labelled IA-SA). Thus, we show a comprehensive $1/\ell^*(\phi)$ plot for dense emulsions having depletion attractions over a wide range of attractive strengths from NH to SA. The non-monotonic behavior of the scattering with respect to strength of short-range attraction is very interesting, and presently there are no theoretical predictions of this set of measurements based on first-principles, even as we have fit some using regularized principal component analyses based on the DCSN and E-DCSN models.

7.2 Materials and methods

7.2.1 Size-fractionated attractive emulsions

We prepare a uniform silicone oil-in-water (O/W) microscale emulsion (polydimethyl siloxane oil, Gelest Inc.; viscosity: $\nu_\mathrm{o} = 350$ cSt), SDS (Fisher Scientific; electrophoresis grade 99% purity), and deionized water (Millipore Milli-Q Academic; resistivity: 18.2 MΩ cm), following the protocol of emulsification, homogenization, and size-fractionation in the similar manner as in chapters 2.3.1 and 3.3.1, but here fix [SDS] = 25 mM and thereby obtain a 4× size-fractionated, concentrated master emulsion. We store this master emulsion sample in a temperature-controlled chamber at 20°C to avoid water vapor evaporation-condensation that could alter ϕ. The droplet volume fraction of this master emulsion is $\phi_{\mathrm{m}} = 0.782 \pm 0.004$, characterized via a gravimetric evaporation method. A very small portion of the master emulsion is also diluted in 10 mM SDS solution down to $\phi \sim 10^{-4}$ and then characterized using dynamic and static light, yielding primary characteristics of the droplet radial size distribution: average hydrodynamic radius $\langle a \rangle = 456 \pm 15$ nm and polydispersity $\delta a / \langle a \rangle \simeq 0.18$, where δa is the standard deviation of this distribution.

We prepare samples of emulsions at different ϕ values, which are less than ϕ_{m}, by diluting the master emulsion sample with a 25 mM SDS solution using a Denver Instruments APX-200 analytical balance with 0.1 mg precision. The resulting ϕ of each sample can then be calculated from these measured masses using the known densities of the SDS solution and PDMS. Each emulsion with $\phi < \phi_{\mathrm{m}}$ is approximately 1.5 mL in total volume and is stirred for 3 minutes, imposing an estimated 50 s^{-1} average shear flow-rate, to ensure complete mixing before measurements using Rheolab 3.

After the entire set of DWS measurements of emulsions at 25 mM SDS concentration have been completed, we collect and combine the emulsions at different ϕ, re-disperse the droplets in 45 mM SDS solutions to $\phi \approx 0.1$, and then concentrate the emulsions to a higher ϕ through ultracentrifugation (Beckman L8-55 ultracentrifuge, SW-28 swinging bucket rotor, 10,000 rpm, 1.25 hours). This re-dispersion and concentration cycle has been repeated three more times at fixed [SDS] = 45 mM to set the bulk SDS concentration. Followed by the final concentration step, the droplet volume fraction of the resulting new master emulsion is $\phi_{\mathrm{m}} = 0.789 \pm 0.005$. We use the same protocol as described above for dilution and storage of the emulsions, yet with 45 mM SDS solutions, for the studies of IA-SA emulsions.

7.2.2 Optical transport measurements

We perform optical transport measurements using Rheolab 3 light scattering instrument (equipped with backscattering option, wavelength $\lambda = 685$ nm; LS Instruments, Fribourg CH) for MA-IA emulsions and IA-SA emulsions, respectively, at different ϕ. Each emulsion is loaded into a glass optical cuvette having a pathlength of $L = 5$ mm; a ϕ-dependent loading protocol is used to eliminate air bubbles while avoiding gradients in ϕ (refer to chapter 3.3.2). Each loaded cuvette is then placed in the Rheolab 3 and allowed to equilibrate at a set temperature $T = 20 \pm 0.1$ °C. The waiting time is 24 hours for $\phi \geq 0.4$ and 1,200 s for $\phi < 0.4$. Time-averaged backscattering and transmission intensities are used to determine ℓ^*. For each emulsion sample at a given [SDS] and ϕ, a total of 11 trials have been performed and averaged.

7.3 Results and conclusions

We present the comprehensive $1/\ell^*(\phi)$ features over the full range of ϕ for emulsions having nearly hard interactions (NH, [SDS] = 10 mM), moderate to intermediate attractions (MA-IA, [SDS] = 25 mM), intermediate attractions (IA, [SDS] = 35 mM), intermediate to strong attractions (IA-SA, [SDS] = 45 mM), and strong attractions (SA, [SDS] = 80 mM), measured using the Rheolab 3 (see Figure 7.1). The results of optical transport obtained for the MA-IA and IA-SA emulsions can be directly compared with previous studies on similar emulsions with varying SDS concentrations, as we have prepared the fractionated MA-IA and IA-SA emulsions utilizing the same materials and protocols. The average hydrodynamic radius of the MA-IA and IA-SA emulsions, denoted by $\langle a \rangle$, equals 456 nm, which is within 1% of $\langle a \rangle = 459$ nm reported for the NH[57] and SA emulsions[115], and it is within 6% of $\langle a \rangle = 484$ nm for the IA emulsions[120]. Furthermore, when taking into account Mie-scattering from a hypothetical isolated sphere, symbolized as $1/\ell^*_{\mathrm{ISA,Mie}}$ and derived from the independent scattering approximation (ISA) in the extremely dilute limit, the variation between these

MA-IA and IA-SA emulsions and previous studies is below 0.5%. Consequently, the significant differences noted in $1/\ell^*(\phi)$, as depicted in Figure 7.1, between these present studies, stem from differing droplet structures due to different attractive strengths, denoted as $|U_\mathrm{d}|$, rather than the minuscule disparity in $\langle a \rangle$.

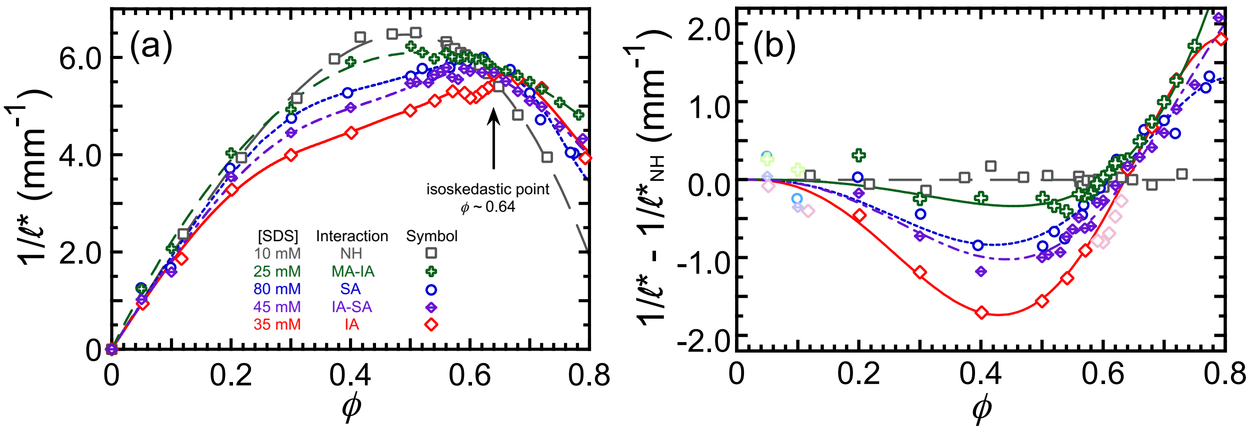

Figure 7.1. Measured inverse mean free path of optical transport, $1/\ell^*$, of fractionated silicone oil-in-water (O/W) emulsions as a function of droplet volume fraction, ϕ, for a repulsive nearly hard interaction and also for four different strengths of micellar depletion attraction, and their difference between $1/\ell^*_\mathrm{NH}$ (pathlength $L = 5.0$ mm, light wavelength $\lambda = 685$ nm). (a) Nearly hard interactions (Kim *et al.*[57], [SDS] = 10 mM, $|U_\mathrm{d}| < k_\mathrm{B}T$, average droplet radius $\langle a \rangle = 459$ nm): $1/\ell^*_\mathrm{NH}$ (gray squares); fit (gray long dashed line) using equation (6) in Xu *et al.*[115]. Moderately-to-intermediately attractive ([SDS] = 25 mM, $|U_\mathrm{d}| \approx 3\ k_\mathrm{B}T$, $\langle a \rangle = 456$ nm): $1/\ell^*_\text{MA-IA}$ (green crosses); fit (green short dashed line) to a zeroaxial cubic polynomial equation. Intermediately attractive ([SDS] = 35 mM, $|U_\mathrm{d}| \approx 6\ k_\mathrm{B}T$, similar $\langle a \rangle = 484$ nm): $1/\ell^*_\mathrm{IA}$ (red diamonds). Intermediately-to-strongly attractive ([SDS] = 45 mM, $|U_\mathrm{d}| \approx 7\ k_\mathrm{B}T$, $\langle a \rangle = 456$ nm): $1/\ell^*_\text{IA-SA}$ (violet lined diamonds); fit (violet dash-dotted line) to the DCSN model. Strongly attractive (Xu *et al.*[115], [SDS] = 80 mM, $|U_\mathrm{d}| \approx 15\ k_\mathrm{B}T$, $\langle a \rangle = 459$ nm): $1/\ell^*_\mathrm{SA}$ (blue circles); fit (blue solid line) from Xu *et al.*[115] using equation (2.5) with constraints imposed by equations (2.1)-(2.4). Legends are organized to highlight the non-monotonic behavior of the scattering as $|U_\mathrm{d}|$ is increased, most readily seen in the intermediate ϕ range between 0.4 and 0.5. **(b)** Difference in $1/\ell^*$ for each attractive emulsion from $1/\ell^*_\mathrm{NH}$, fit to a function proportional to a semi-empirical form: $\phi^3(\phi - \phi_\mathrm{iso})(\phi_\mathrm{u} - \phi)$, where the fit parameter $\phi_\mathrm{u} \approx 1$ represents optical transparency of the dense emulsion at $\lambda = 685$ nm for ϕ near unity where $1/\ell^*$ vanishes; ϕ_iso indicates the crossover with the NH curve. Similarity of values of crossovers at a particular ϕ indicates an isoskedastic point. Data in the dilute regime of $\phi < 0.2$ for MA-IA, IA, IA-SA, and SA emulsions, as well as $1/\ell^*_\mathrm{IA} - 1/\ell^*_\mathrm{NH}$ within the notch regime for the IA emulsions, have been excluded from fitting (symbols in light shade).

A prior study has shown very little difference in $1/\ell^*(\phi)$ for the same emulsion (*i.e.* droplet size distribution) having moderate attractions at [SDS] = 20 mM when compared to nearly hard interactions at [SDS] = 10 mM; yet only a narrow range of ϕ between 0.57 and 0.65 has been reported[59]. By slightly increasing [SDS] to 25 mM, we observe that $1/\ell^*(\phi)$ of MA-IA emulsions is still not appreciably distinct from the NH values over this $0.57 \leq \phi \leq 0.65$ and the overall $1/\ell^*_{\mathrm{MA-IA}}(\phi)$ exhibits an inverted parabola-like shape [see the green crosses and short dashed line in Figure 7.1(a)], which is similar to the NH scenario and is radically different from the asymmetric shape with two knees and a notch in the IA scenario. In the intermediate ϕ range between 0.3 and 0.56, the light scattering intensity is reduced in MA-IA emulsions as compared to NH emulsions, depicted by $1/\ell^*_{\mathrm{MA-IA}} < 1/\ell^*_{\mathrm{NH}}$ in this regime, implying the formation of clusters caused by depletion attractions between droplets. For higher ϕ beyond 0.65, the scattering intensity for MA-IA emulsions is significantly enhanced, yielding the highest $1/\ell^*_{\mathrm{MA-IA}}$ values among the various interactive strengths in the dense regime, due to the heterogeneity in the droplet structures caused by depletion attractions.

To investigate the transition between the SA emulsions at [SDS] = 80 mM and the IA emulsions at [SDS] = 35 mM, which have been thoroughly studied in Chapters 2 and 3, we have measured and presented $1/\ell^*(\phi)$ for the IA-SA emulsions at [SDS] = 45 mM [see the violet lined diamonds in Figure 7.1(a)]. With a very high data density, particularly in the ϕ regime that corresponds to the notch feature of $1/\ell^*_{\mathrm{IA}}(\phi)$, we have shown that the overall $1/\ell^*_{\mathrm{IA-SA}}(\phi)$ curve falls in between $1/\ell^*_{\mathrm{IA}}$ and $1/\ell^*_{\mathrm{SA}}$. The measured $1/\ell^*_{\mathrm{IA-SA}}(\phi)$ is in the absence of the notch feature and has been fit using the DCSN model [violet dash-dotted line in Figure 7.1(a)]. In the dense limit beyond $\phi = 0.65$, the $1/\ell^*$ values for the IA, IA-SA, and SA emulsions at a given ϕ are effectively of the same magnitude, implying the similar dense, heterogeneous droplet structures beyond jamming, formed through cluster aggregation.

The master $1/\ell^*(\phi)$ diagram [Figure 7.1(a)] indicates that inducing intermediate attractions at 35 mM SDS yields the strongest reduction in the magnitude of $1/\ell^*_{\mathrm{IA}}(\phi)$ for $\phi \leq$

0.65 among all the different attractive strengths measured. In addition, the notch feature just below hard-sphere repulsive jamming ϕ_{MRJ} and above glass transition ϕ_{g} has been only observed in the IA emulsions. In the range of $0.2 \leq \phi \leq 0.5$, it is evident that increasing the SDS concentration (*i.e.* enhancing the attractive strength) up to 35 mM SDS results in a progressive decrease in $1/\ell^*$. This reduction is correlated with the formation of denser struts or constituent droplet clusters in the gel network, characterized by a smaller surface-to-volume ratio and reduced scattering contribution per droplet. However, the addition of more SDS creates stronger attractions that partially mitigate local inhomogeneity, yielding more tenuous gel networks with a marginally higher (but still notably small) surface-to-volume ratio compared to individual droplets. Consequently, this leads to an increasing value of $1/\ell^*$ as the emulsion transitions from IA to SA states. Interestingly, we have observed an "isoskedastic" point at $\phi \approx 0.64$, where the optical scattering intensity (*i.e.* $1/\ell^*$) remains constant at a specific value, irrespective of the interaction strength, within the confines of our investigative framework [refer to the arrow in Figure 7.1(a)].

While complex, these optical transport measurements indicate that it is possible to effectively determine the strength of short-range attractions relative to $k_{\mathrm{B}}T$ in a dense uniform emulsion having unknown strength through fingerprinting: comparing the magnitude and shape of measurements of $1/\ell^*(\phi)$ of that unknown emulsion with the set we have determined. We have measured a non-monotonic progression in $1/\ell^*$ near $\phi = 0.5$, where oil and water each takes up half volume of the emulsion, as the attractive strength is raised [highlighted by legends to Figure 7.1(a)]. At a given ϕ between 0.4 and 0.5, where $1/\ell^*$ values are distinctive from one other for all the explored emulsion systems having various attractive strengths, the measured $1/\ell^*$ for NH with an [SDS] of 10 mM is at the highest level. Then it proceeds downwards to MA-IA and SA, corresponding to [SDS] values of 25 mM and 80 mM, respectively. Finally, it transitions to IA-SA at an [SDS] of 45 mM, and concludes with IA at an [SDS] of 35 mM at the bottom-most level. The reduction in scattering at $\phi \approx 0.5$, caused by attractions, is the greatest for the IA emulsions, in which long-lived dense clusters are present to a substantial degree. In the higher ϕ regime beyond the isoskedastic point, compared to nearly hard interactions, all of the attractive systems exhibit a substantial increase in scattering. However, it is difficult to distinguish among different attractive strengths using only $1/\ell^*$ in this jammed, elastic regime near $\phi \approx 0.7$. Therefore, if the goal is to utilize $1/\ell^*(\phi)$ as a tool to differentiate the strength of attractions in a given emulsion system, the most insightful data can be obtained by performing measurements when ϕ lies between ≈0.4 and ≈0.5. These ϕ values are below the isoskedastic point far enough that variations in $1/\ell^*$ with $|U_\mathrm{d}|/(k_\mathrm{B}T)$ are maximized. This range of ϕ also sidesteps the complexity associated with the notch feature present in IA emulsions and ensures aging effects are minimal, too.

To more distinctly highlight how short-range attractions influence $1/\ell^*$ as a consequence of depletion attractions, compared to the baseline case of NH interactions, we subtract $1/\ell^*_\mathrm{NH}(\phi)$ from the measured $1/\ell^*(\phi)$ for all the dense emulsions, taking the NH emulsions as the reference. Then, we fit the ϕ-dependent difference $1/\ell^* - 1/\ell^*_\mathrm{NH}$ to the equation $\Delta(1/\ell^*)_0\phi^3(\phi - \phi_\mathrm{iso})(\phi_\mathrm{u} - \phi)$ [see Figure 7.1(b)]. Here, the similarity of fit parameters ϕ_iso reflects the *isoskedastic* point, at which $1/\ell^*$ values for NH, MA-IA, IA, IA-SA, and SA emul-

Table 7.1. Parameters used in fitting ϕ-dependent $1/\ell^* - 1/\ell^*_\mathrm{NH}$ for moderately-to-intermediately attractive (MA-IA), intermediately attractive (IA), intermediately-to-strongly attractive (IA-SA), and strongly attractive (SA) emulsions compared to nearly hard (NH) emulsions.

Interaction	MA-IA	IA	IA-SA	SA
[SDS] (mM)	25	35	45	80
$\lvert U_\mathrm{d}\rvert$ ($k_\mathrm{B}T$)	3.3	5.6	7.3	14.5
$\Delta(1/\ell^*)_0$ (mm^{-1})	92 ± 8	229 ± 7	103 ± 14	116 ± 22
ϕ_iso	0.588 ± 0.008	0.636 ± 0.002	0.637 ± 0.004	0.615 ± 0.008
ϕ_u	1.002 ± 0.006	0.894 ± 0.006	1.03 ± 0.04	0.92 ± 0.04
R^2	0.906	0.998	0.980	0.948

sions coincide; ϕ_{u} indicates optical transparency at a ϕ near unity; the parameter $\Delta(1/\ell^*)_0$ represents the amplitude of the polynomial formula. Fit parameters for all these attractive emulsions are presented in Table 7.1.

In future studies, employing more meticulous experimentation with narrower SDS concentration intervals, along with comparisons to mechanical rheometry, theoretical analysis, and simulations, as well as the development of comprehensive opto-microrheological models, can further facilitate the quantitative mapping of optical transport, dynamics, and rheological properties for short-range attractive emulsions (and perhaps also some other attractive systems) to the strengths of their attractive potential energy relative to thermal energy.

Chapter 8 - Surface-bound molecular probe diffusion for microrheology

8.1 Motivation

Given the results in Chapter 6, it is clear that a higher degree of confinement of molecular probe motion within droplets would be beneficial, if one wishes to extract a droplet MSD from a total molecular probe MSD accurately. This could enable a broad extension of passive microrheology using molecular probes, since droplet dynamics, which are coupled to total molecular probe motion, could then be extracted. Since this approach uses confined molecular probe motion to extract droplet motion, we have defined a dimensionless ratio of droplet MSD relative to total probe MSD, $\xi = \left\langle \Delta \boldsymbol{r}^2_{\mathrm{drop}} \right\rangle_{\mathrm{p}} / \left\langle \Delta \boldsymbol{r}^2_{\mathrm{pr,tot}} \right\rangle_{\mathrm{p}}$.

In the scenario of droplet-confined probe diffusion, as discussed in Chapter 6, we have shown that ξ decreases by orders of magnitude as ϕ is raised over a broad range, and it drops rapidly in the jamming regime below the detection limit of $\sim 10^{-3}$ for average droplet radii greater than 40 nm. Although it is still possible to use remarkably small droplet radii, preferably under 10 nm, for passive microrheology of nanoemulsions using ^{19}F-NMR, this involves difficulties in nanoemulsion preparation and limits the application of molecular probe microrheology to the broader range of materials. Thus, we consider simulations based on a different type of molecular probe, namely a probe bound as a surfactant that has been irreversibly adsorbed onto droplet surfaces[184]. In particular ^{19}F-labeled surfactant molecules would still take advantages of the isotopic specificity of NMR, and in dense nanoemulsions, adsorbed surfactant can still be a large enough percentage of the total composition to make ^{19}F PFG-NMR experiments feasible.

Here, we present the trajectory-based simulations of an irreversibly adsorbed probe surfactant molecule at high densities on the surface of a HBBP droplet. At a high surfactant surface densities, we assume that the motion of an irreversibly adsorbed probe molecule undergoes HBBP confinements caused by the neighboring molecules, providing a higher percentage of droplet center-of-mass MSD in the total molecular probe MSD over a wide range of times, particularly long times. Unrestricted diffusion of irreversibly adsorbed surfactant at low surface densities on the droplet interfaces provides an intermediate result; if the tails of these surfactants are in a very viscous oil, thereby restricting surface diffusion rates, then even this unrestricted surface diffusion scenario could be similar to the HBBP surface confinement. Given that the level of confinement applied to the probe molecules on droplet surfaces (which we assume to be comparable to the intermolecular distance of adsorbed surfactant molecules) is much higher than that applied to the labeled oil molecules inside the droplets (comparable to the droplet diameter), this approach using surface-bound probes leads to distinctly higher ξ as compared to the scenario of Chapter 6 which considered diffusion of oil probe-molecules confined within droplets.

8.2 Methods

A 2D trajectory of a surface-bound molecular probe is generated by mapping a one-dimensional HBBP motion onto a two-dimensional ring, which represents the droplet surface in 2D. In brief, we solve the Langevin equation, having the same functional form as equation (6.1), for the forces along the x-direction acting on the molecular probe. The resulting Green's function, $G(x_{\mathrm{pr},j}, x_{\mathrm{pr},j-1}; \Delta t)$ [equation (8.1)] provides the probability of finding a probe molecule at position $x_{\mathrm{pr},j}$ after a time interval Δt for the initial condition at ${x_{\mathrm{pr},j-1}}^{176–178}$:

$$G(x_{\mathrm{pr},j}, x_{\mathrm{pr},j-1}; \Delta t) = [2\pi B_{\mathrm{pr}}(\Delta t)]^{1/2} \exp\{-\frac{[x_{\mathrm{pr},j} - A_{\mathrm{pr}}(\Delta t)]^2}{2B\mathrm{pr}(\Delta t)}\}, \tag{8.1}$$

where j is the integer index ranging from 1 to N, the total number of steps in simulating the trajectory of a molecular probe. The mean $A_{\mathrm{pr}}(\Delta t)$ and variance $B_{\mathrm{pr}}(\Delta t)$ of the Gaussian-distributed Green's positional function are shown in equations (8.2) and (8.3), respectively.

$$A_{\mathrm{pr}}(\Delta t) = x_{\mathrm{pr},j-1}\mathrm{exp}(-\Delta t/\tau_{\mathrm{B,pr}}), \tag{8.2}$$

$$B_{\mathrm{pr}}(\Delta t) = \frac{k_{\mathrm{B}}T}{k_{\mathrm{pr}}}[1 - \mathrm{exp}(-2\Delta t/\tau_{\mathrm{B,pr}})], \tag{8.3}$$

where $\tau_{\mathrm{B,pr}} = 6\pi a_{\mathrm{p}}\eta_{\mathrm{o}}/k_{\mathrm{pr}}$ represents the time that the probe molecule takes to reach equilibrium in the harmonic potential well; a_{p} is the radius of the probe molecule and η_{o} is the dynamic viscosity of the oil phase. The force constant k_{pr} associated with the molecular HBBP motion is determined by the resulting long-time surface-confined molecular MSDs, whose magnitude is obtained by using a surfactant density $C_{\mathrm{s}} = 2.3$ molecules/nm^2 measured in[185], in association with a Lindemann melting criterion of 0.3.

To simulate the molecular probe trajectories, we generate a set of N-element Gaussian-distributed random numbers, $R_{x,\mathrm{pr}}$, corresponding to the $x-$direction, having the mean of zero and the SD of unity. We first calculate the 1D trajectory of the probe molecule in the reference frame of the harmonic well according to the HBBP model. Defined by the Green's function [equation (8.1)], the positional time series of the probe molecule are constructed by modifying each element of $R_{x,\mathrm{pr}}$ at a given Δt: $x_{\mathrm{pr},j} = R_{x,\mathrm{pr},j}\sqrt{B_{\mathrm{pr},j}} + A_{\mathrm{pr},x,j}$, where integer j ranges from 1 to N. Here, we set the starting position of the probe molecule is at a Cartesian coordinate $(0, a)$ relative to the droplet COM at $(0, 0)$ for ease of explanation. We map the 1D HBBP trajectory onto a 2D ring by calculating the polar angle at each step $\theta_{\mathrm{j}} = x_{\mathrm{pr},j}/a + \pi/2$ and updating the jth position in the complex plane: $z_{\mathrm{pr},j} = a\mathrm{exp}(i\theta_{\mathrm{j}})$, where i is the imaginary unit, corresponding to the point $(\mathrm{Re}(z_{\mathrm{pr},j}), \mathrm{Im}(z_{\mathrm{pr},j}))$ in the Cartesian plane.

Given that the surface bound probe motion is highly spatially restricted, individual trajectories can be anisotropic; whereas the NMR tends to provide 1D MSDs along the direction relative to field gradient z. Since we anticipate applications involving NMR, we have calculated the 1D MSDs along the z-direction of the simulated molecular probe trajectories, located at different positions on the droplet's perimeter, not only at $(0, a)$ as demonstrated above. The average of 1D MSDs probed at various molecular positions yield the same result, confirming that if the surfactant molecules are uniformly or nearly uniformly distributed on the droplet surface, the anisotropy of individual molecular trajectories does not impact the overall ensemble-averaged 1D MSDs.

The simulation methods for generating droplet trajectories and total molecular trajectories, as well as the MSD subtraction analysis for extracting droplet MSDs, are identical to the methods described in Chapter 6 (see chapter 6.3 for details).

8.3 Results and conclusions

We have obtained highly quantitative agreement between the droplet MSDs, extracted through the MSD subtraction analysis: $\left\langle \Delta \boldsymbol{r}^2_{\mathrm{drop}}(\tau)\right\rangle = \left\langle \Delta \boldsymbol{r}^2_{\mathrm{pr,tot}}(\tau)\right\rangle - \left\langle \Delta \boldsymbol{r}^2_{\mathrm{pr,conf}}(\tau)\right\rangle$, and the known droplet MSDs calculated directly from trajectories of the droplet COM, over the entire lag time range 10^{-10} s $\leq \tau \leq 10^{0}$ s for all the droplet radii that we have explored from 5 nm to 320 nm (Figure 8.1). In the context of investigating the influence of droplet radii, we fix all the other parameters at $\eta_{\mathrm{o}} = 100$ mPa s, $\eta_{\mathrm{c}} = 1$ mPa s, and $G'_{\mathrm{p}} = 100$ Pa, same as the values used to yield the results in Figure 6.6 for parallel comparison. For all droplet radii ranging from 5 nm to 320 nm, the droplet's center-of-mass MSD is the predominant component in the total surface-bound molecular probe MSD across the entire τ range [Figure 8.1(a)]. This is because the droplet COM MSD exceeds the purely confined probe MSD (that is, the reference signal) by more than three orders of magnitude. The value of $\left\langle \Delta \boldsymbol{r}^2_{\mathrm{pr,conf}}(\tau)\right\rangle$ is so minute when compared to $\left\langle \Delta \boldsymbol{r}^2_{\mathrm{drop}}(\tau)\right\rangle$ that the initial rise-to-plateau of $\left\langle \Delta \boldsymbol{r}^2_{\mathrm{pr,tot}}(\tau)\right\rangle$, which has a smaller τ_{pr} than τ_{drop}, is nearly imperceptible. Only a barely noticeable trace of the $\left\langle \Delta \boldsymbol{r}^2_{\mathrm{pr,conf}}(\tau)\right\rangle$ within the $\left\langle \Delta \boldsymbol{r}^2_{\mathrm{pr,tot}}(\tau)\right\rangle$ can be spotted at early lag times $\tau < 10^{-7}$ s when $a \geq 160$ nm. In contrast with the droplet-confined oil-molecule diffusion approach shown in Figure 6.6(b), where obvious fluctuations of the extracted droplet MSDs around their theoretical magnitudes have been observed for larger droplet radii $a \geq 80$ nm at $\tau \geq 5 \times 10^{-4}$ s, this surface-confined approach offers excellent agreement in the absence

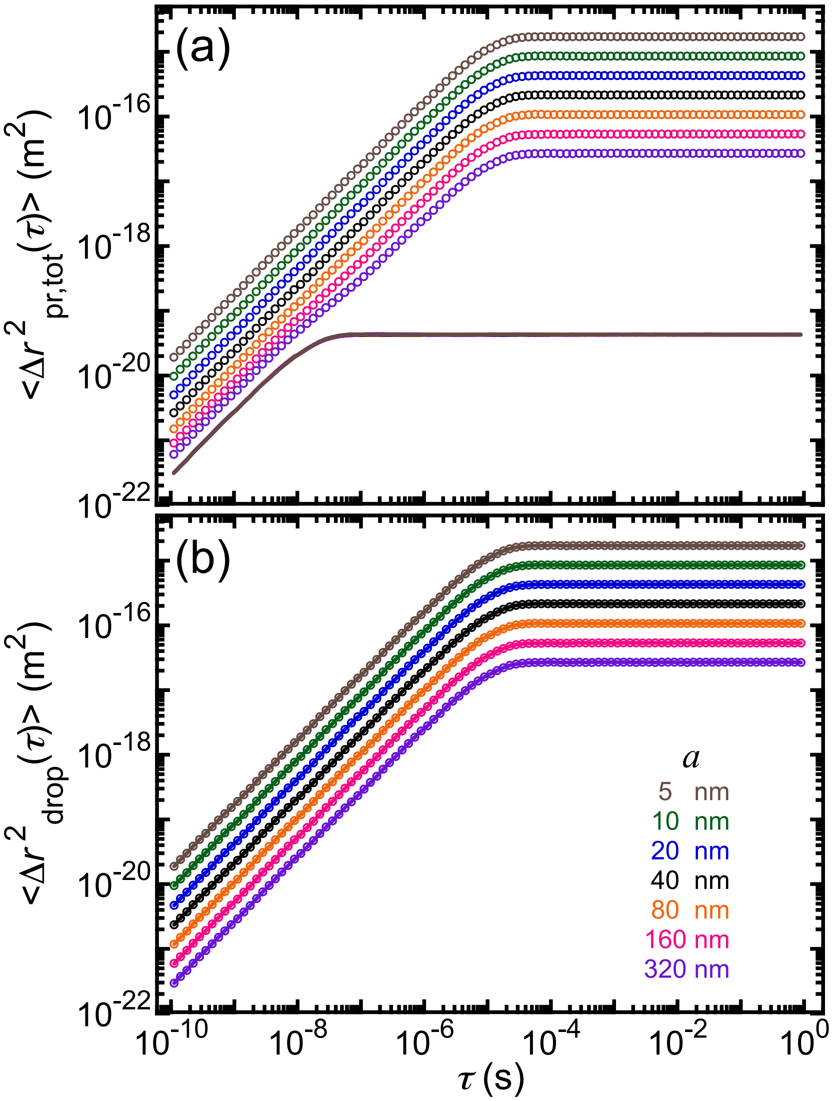

Figure 8.1. Time-averaged mean square displacements of the total surface-bound probe motion, $\left\langle \Delta \boldsymbol{r}^2_{\mathbf{pr,tot}}(\boldsymbol{\tau}) \right\rangle$, and the harmonically bound droplet motion, $\left\langle \Delta \boldsymbol{r}^2_{\mathbf{drop}}(\boldsymbol{\tau}) \right\rangle$, at different droplet radii. (**a**) $\left\langle \Delta \boldsymbol{r}^2_{\mathrm{pr,tot}}(\tau) \right\rangle$ determined from trajectories of the surface-bound molecular probe motions for a wide range of a [open circles; color-coded, see legend in part (b)]. Solid lines represent $\left\langle \Delta \boldsymbol{r}^2_{\mathrm{pr,conf}}(\tau) \right\rangle$ of confined molecular probe MSDs in stationary droplets for reference. (**b**) $\left\langle \Delta \boldsymbol{r}^2_{\mathrm{drop}}(\tau) \right\rangle$ (open circles) extracted from the probe MSDs: $\left\langle \Delta \boldsymbol{r}^2_{\mathrm{drop}}(\tau) \right\rangle = \left\langle \Delta \boldsymbol{r}^2_{\mathrm{pr,tot}}(\tau) \right\rangle - \left\langle \Delta \boldsymbol{r}^2_{\mathrm{pr,conf}}(\tau) \right\rangle$. Solid lines represent the droplet self-motion MSD calculated directly from the COM trajectory of the droplet. The viscosity of the oil is $\eta_{\mathrm{o}} = 100$ mPa s and that of the continuous phase is $\eta_{\mathrm{c}} = 1$ mPa s. The plateau elastic modulus of the emulsion is $G'_{\mathrm{p}} = 100$ Pa.

of fluctuations throughout the full range of both τ and a [Figure 8.1(b)].

Similarly, we investigate how the use of this surface-bound molecular probe method might be influenced by realistic material parameters for viscoelastic emulsions, particularly when the interactions between droplets are nearly hard. We calculate the plateau elastic shear moduli $G'_{\mathrm{p,EEI}}$ as functions of droplet volume fraction ϕ using the EEI model[37] for various droplet radii (see Figure 6.2), and extract the high-frequency viscosities for different ϕ

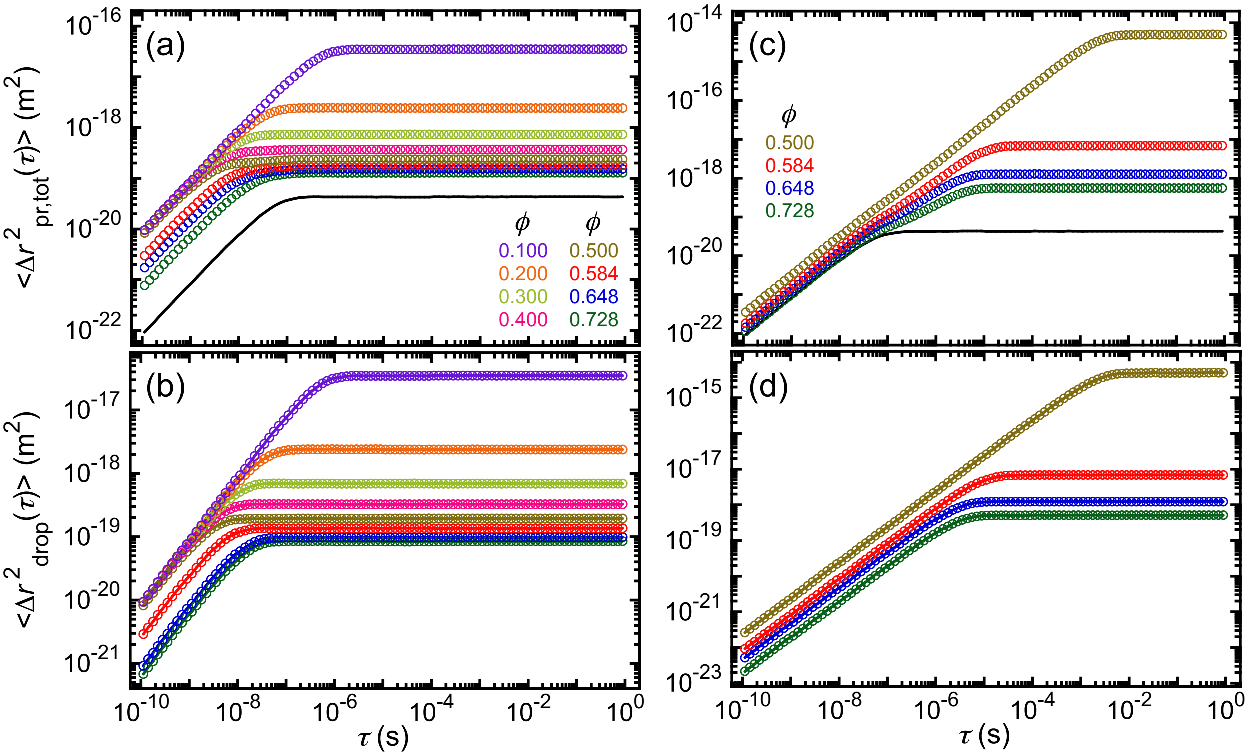

Figure 8.2. Mean square displacements of the total surface-bound probe motion, $\left\langle \Delta \boldsymbol{r}^2_{\mathbf{pr,tot}} \right\rangle$, and the droplet motion, $\left\langle \Delta \boldsymbol{r}^2_{\mathbf{drop}} \right\rangle$, as functions of the lag time $\boldsymbol{\tau}$ at different droplet volume fractions $\boldsymbol{\phi}$, for viscoelastic emulsion models having droplet radii of 10 nm [parts (a) and (b)] and 320 nm [parts (c) and (d)]. In parts (**a**) and (**c**), the black solid lines represent the confined probe motion MSDs on the surface of a stationary droplet, $\langle \Delta \boldsymbol{r}^2_{\mathrm{pr,conf}}(\tau) \rangle$, while the color-coded open circles represent the total surface-confined probe MSDs as the droplet is in the harmonic potential well, $\langle \Delta \boldsymbol{r}^2_{\mathrm{pr,tot}}(\tau) \rangle$, associated with different ϕ. In parts (**b**) and (**d**), the open circles are droplet motion MSDs, extracted by subtracting $\langle \Delta \boldsymbol{r}^2_{\mathrm{pr,conf}}(\tau) \rangle$ from $\langle \Delta \boldsymbol{r}^2_{\mathrm{pr,tot}}(\tau) \rangle$, and are compared with the known droplet self-motion MSDs (color-coded lines) calculated from the droplet COM trajectories.

from[57]. For both $a = 10$ nm and 320 nm, the long-time plateaus of total molecular probe MSDs are well-defined, and their magnitudes are far above the surface-confined probe MSDs (*i.e.* the baseline) at all ϕ values [Figure 8.2(a) and (c)]. This results in the agreement between the extracted droplet COM MSDs and their theoretical values [Figure 8.2(b) and (d)]. In the droplet-confined oil-molecule diffusion scenario, the dual rise-to-plateau feature of $\left\langle \Delta \boldsymbol{r}^2_{\mathrm{pr,tot}}(\tau) \right\rangle$ could only be readily seen for very small droplet radii near and below $a = 10$ nm [Figure 6.7(a)]. However, at a larger droplet radius at $a = 320$ nm, the secondary rise-to-plateaus that arise from the confined molecular motion could not be observed appreciably [Figure 6.7(c)]. By contrast, here, for the surface-confined scenario, the dual rise-to-plateau feature is more noticeable at $a = 320$ nm [Figure 8.2(c)] since the dominant portion of the total molecular MSDs arises from the droplet center-of-mass motion. Moreover, the characteristic time scales for droplet MSDs, τ_{drop}, are longer than the characteristic time scales for probe MSDs, τ_{pr}, leading to the well-defined secondary plateau of $\left\langle \Delta \boldsymbol{r}^2_{\mathrm{pr,tot}}(\tau) \right\rangle$, from which the droplet MSDs can be readily extracted.

The radial droplet size does not appreciably influence the performance the MSD subtraction analysis of the superposition of probe MSDs for viscoelastic emulsions at fixed ϕ. We choose the value $\phi = 0.4$ to include a relatively wide range of a from 80 nm down to 5 nm. We present the probe motion MSDs for the subtraction analysis and the resulting droplet self-motion MSDs in Figure 8.3. Because the surface-confined probe MSDs are determined by the given surface density of surfactants and the Lindemann criterion, no difference in $\left\langle \Delta \boldsymbol{r}^2_{\mathrm{pr,conf}} \right\rangle (\tau)$ has been predicted or observed among different a. A minuscule secondary rise-to-plateau has been observed only for $a = 5$ nm, associated with the characteristic time scale τ_{pr} near 10^{-7} s. For droplet COM MSDs, the characteristic time scales, τ_{drop}, and the magnitude of the plateau MSDs, $\left\langle \Delta \boldsymbol{r}^2_{\mathrm{drop}} \right\rangle_{\mathrm{p}}$, exhibit a systematic increase as a is raised [Figure 8.3(b)]. For each of the presented droplet sizes, we show an excellent agreement between the extracted and theoretical $\left\langle \Delta \boldsymbol{r}^2_{\mathrm{drop}}(\tau) \right\rangle$ [Figure 8.3(b)].

To provide a more intuitive comparison between the two distinct strategies of using

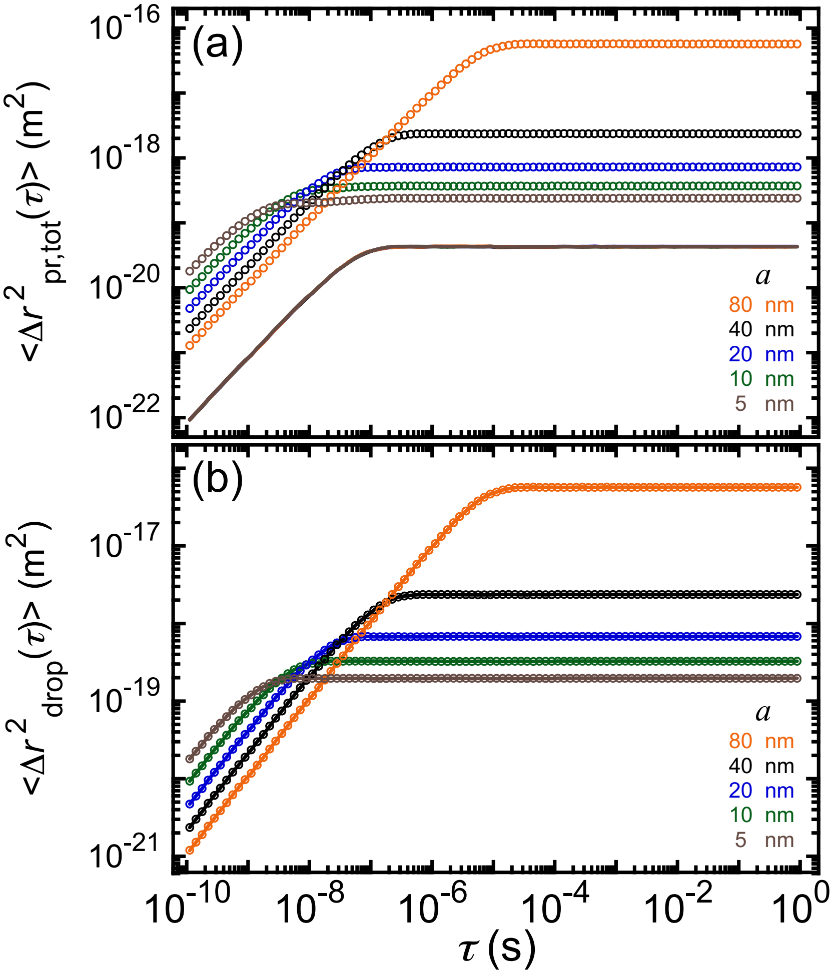

Figure 8.3. Mean square displacements of (a) the surface-confined probe motion and (b) the harmonically bound droplet motion for emulsions having different droplet radii at a fixed volume fraction $\phi = 0.40$ using microrheological parameters as in Figure 6.2: G'_{p} determined by the EEI model[37] and $\eta_{\mathrm{c}} = 1$ mPa s. (**a**) The purely confined probe MSDs as reference signals are presented in solid lines and the total combined probe MSDs are shown in open circles. (**b**) The extracted droplet MSDs (open circles), obtained from the probe MSDs, show good agreement with the known droplet MSDs (solid lines) from the droplet trajectory.

droplet surface-confined probe molecules and of using droplet-confined free diffusive probe molecules, we present the MSD analyses for the two systems, respectively, using a common set of material parameters, including $a = 20$ nm and $\phi = 0.4$ (Figure 8.4). In the case of HBBP confined molecular motion bound to the droplet surface, the droplet COM

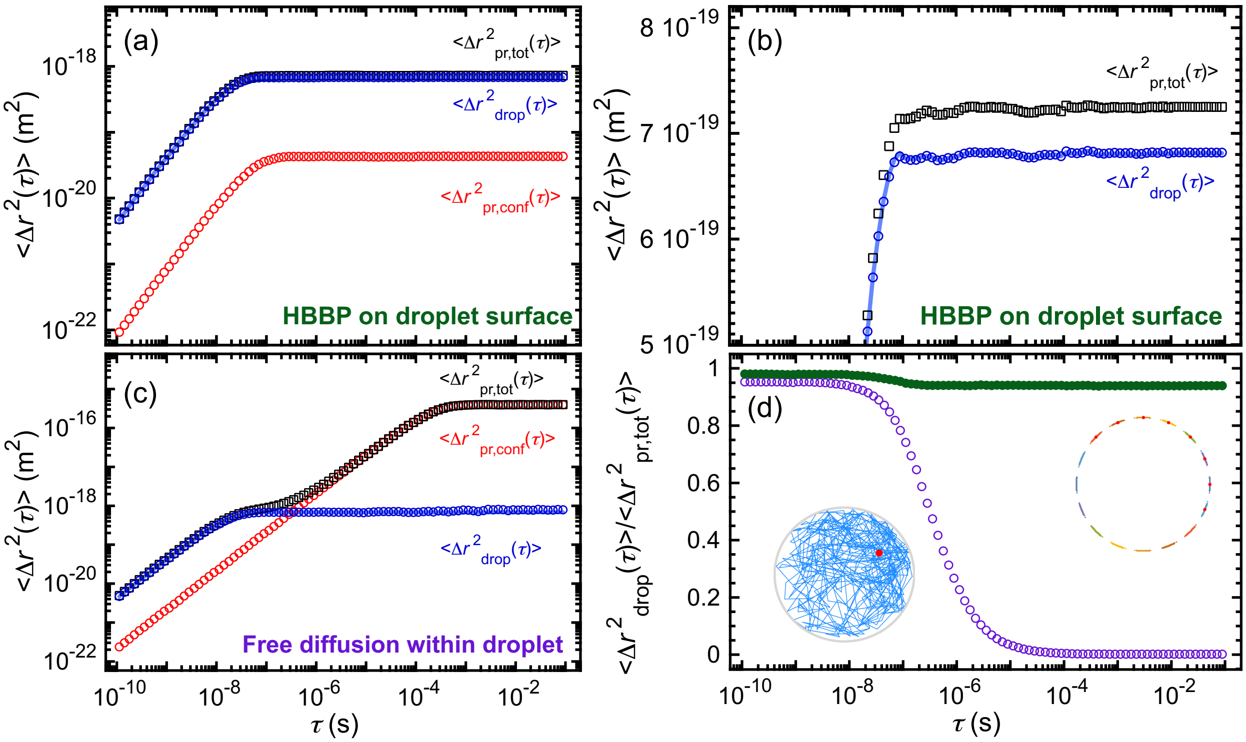

Figure 8.4. Comparison of mean square displacement analyses for inferring droplet self-motion from the total probe motion between using surface-bound molecular probe diffusion on the droplet surface and using free probe diffusion within a droplet. (**a**) The harmonically bound Brownian droplet motion MSD (blue circles), $\langle \Delta \boldsymbol{r}^2_{\mathrm{drop}}(\tau) \rangle$, is extracted by subtracting the surface-confined probe MSD (red circles), $\langle \Delta \boldsymbol{r}^2_{\mathrm{pr,conf}}(\tau) \rangle$, from the apparent total probe MSD (black squares), $\langle \Delta \boldsymbol{r}^2_{\mathrm{pr,tot}}(\tau) \rangle$. The later two probe MSDs are determined from the corresponding probe trajectories. The extracted $\langle \Delta \boldsymbol{r}^2_{\mathrm{drop}}(\tau) \rangle$ is compared to the known droplet self-motion MSD (light blue line), determined directly from the droplet COM trajectory. Molecular surface density $C_{\mathrm{s}} = 2.3$ molecules/nm^2 as measured in[185], and Lindemann constant is 0.3. (**b**) A zoom-in of the long-time regime from part (a), displayed in linear scale for the vertical axis, showing the systematic difference between $\langle \Delta \boldsymbol{r}^2_{\mathrm{pr,tot}}(\tau) \rangle$ and $\langle \Delta \boldsymbol{r}^2_{\mathrm{drop}}(\tau) \rangle$. (**c**) The MSD analysis in the same manner as in part (a) yet for a molecular probe diffusion strictly confined within a droplet, which is undergoing harmonically bound Brownian motion. (**d**) The dimensionless ratio of droplet MSD relative to total probe MSD, $\langle \Delta \boldsymbol{r}^2_{\mathrm{drop}}(\tau) \rangle / \langle \Delta \boldsymbol{r}^2_{\mathrm{pr,tot}}(\tau) \rangle$, for the droplet surface-bound probe diffusion and free probe diffusion within a droplet, respectively. Insets show partial trajectories of the droplet-confined (left) and surface-confined (right) molecules, respectively. Other material parameters used in the presented results are $a = 20$ nm, $a_{\mathrm{p}} = 1.5$ nm, $\eta_{\mathrm{o}} = 339.5$ mPa s, $\eta_{\mathrm{c}} = 1$ mPa s, and $G'_{\mathrm{p}} = 63$ kPa, which corresponds to $\phi = 0.4$ according to the EEI model[37].

MSDs predominate the total molecular probe MSDs and the dual rise-to-plateau feature in $\left\langle \Delta \boldsymbol{r}^2_{\mathrm{pr,tot}} \right\rangle(\tau)$ is not noticeable due to the fact that the confined molecular MSDs are smaller than the droplet MSDs by more than an order of magnitude [Figure 8.4(a-b)]. In comparison, in terms of the free molecular probe diffusion confined within a droplet, the total molecular probe MSDs are predominated by the droplet COM MSDs at short times, while these are predominated by the confined molecular MSDs at long times [Figure 8.4(c)]. There is a crossover of these two component MSDs at $\tau \approx 3 \times 10^{-7}$ s, leading to the intriguing dual rise-to-plateau feature in $\left\langle \Delta \boldsymbol{r}^2_{\mathrm{pr,tot}} \right\rangle(\tau)$. The dimensionless ratio $\left\langle \Delta \boldsymbol{r}^2_{\mathrm{drop}}(\tau) \right\rangle / \left\langle \Delta \boldsymbol{r}^2_{\mathrm{pr,tot}}(\tau) \right\rangle$ at long times (*i.e.* ξ) is as high as 0.94 for the case of surface-confined probe; whereas the long-time ξ decays to 0.002 for the case of droplet-confined oil-molecule diffusion, which can

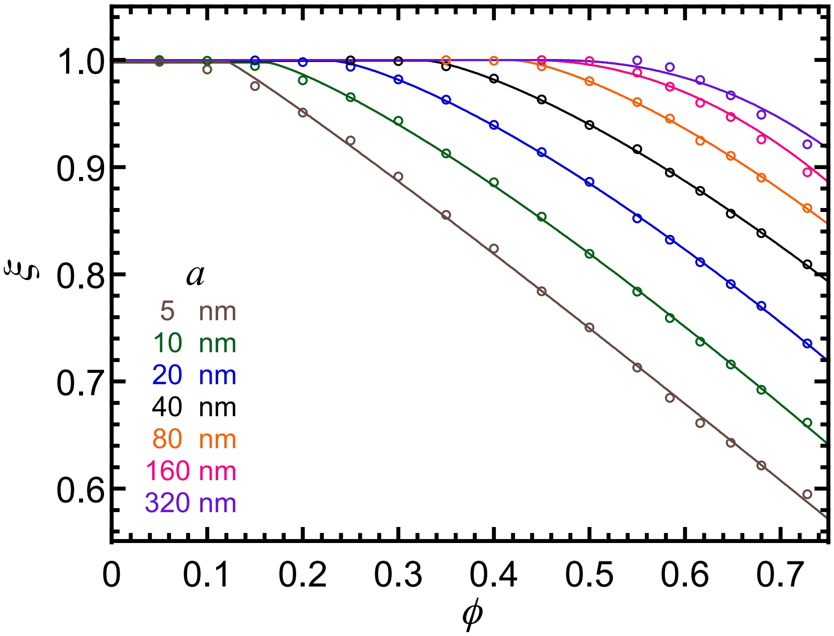

Figure 8.5. Dimensionless ratio of long-$\boldsymbol{\tau}$ plateau droplet mean square displacement and total droplet surface-confined probe mean square displacement, $\boldsymbol{\xi} = \left\langle \Delta \boldsymbol{r}^2_{\mathbf{drop}} \right\rangle_{\mathbf{p}} / \left\langle \Delta \boldsymbol{r}^2_{\mathbf{pr,tot}} \right\rangle_{\mathbf{p}}$, for emulsions having different droplet radii. Microrheological parameters have been determined as in Figure 6.2: G'_{p} calculated using the EEI model[37] and η_{c} inferred from[57]. Molecular surface density $C_{\mathrm{s}} = 2.3$ molecules/nm^2 as measured in[185], and Lindemann melting criterion of 0.3, known for a wide range of materials[164]. Fitting curves guide the eye.

be hardly captured using linear scale for vertical axis [Figure 8.4(d)].

We demonstrate here that confining the probe molecules on the surfaces of droplets leads to greater ξ, much closer to unity (see Figure 8.5 in comparison to Figure 6.9). This surface-confined molecular detection approach remarkably enhances ξ by up to five orders of magnitude at higher $\phi > 0.7$, as compared with the droplet-confined bulk molecular diffusion detection approach developed in Chapter 6. However, it requires accurate detection of the molecular motion at a significantly smaller length scale, which likely would require the development of more sensitive molecular detection techniques and the enhancement of higher field gradients in NMR. Advanced optical molecular probe-tracking methods could also potentially measure probe motion of irreversibly adsorbed surfactant on droplets in order to extract droplet COM motion. Herein, we have also assumed that droplet surface waves, which can be induced by Brownian excitations, are small compared to the bound surfactant molecule motion. If the surface tension at oil-water interfaces is sufficiently reduced, such surface waves could become an important contribution to the overall molecular probe MSDs, further complicating the extraction of droplet COM MSDs.

Chapter 9 - Conclusions and future directions

In this dissertation, we have covered a broad range of topics related to the rheological and optical properties of dense colloidal emulsions. We have made significant progress in understanding the impact of entropic depletion attractions between droplets over a wide range of strengths, and the influence of extremely bimodal droplet size distribution on these properties. We have advanced the quantitative description and diffusing wave microrheological measurements of these dense colloidal emulsions crossing the regimes of repulsive glasses and attractive gels. By extending the DWS analysis to depletion-induced attractive emulsions, we have quantitatively identified DWS characteristics that are associated with such attractive emulsions, including signatures in ϕ-dependent inverse optical transport mean free path $1/\ell^*(\phi)$, additional ϕ-dependent features in the decays of the correlation functions $g_2(t)-1$, and in the extracted mean square displacements $\langle \Delta \boldsymbol{r}^2(t) \rangle$. Our improved DWS analysis yields an effective DWS scattering probe size derived from these optical measurements, resulting in quantitative agreement between the optical microrheological measurements and the mechanical shear rheological measurements. Additionally, we have made the primary exploration towards passive microrheology by using molecular probes through the application of an NMR experimental approach and trajectory-based simulations, showcasing its promising potential for future advances.

In Chapter 2, we have extensively studied the rheology and optical properties of dense colloidal emulsions, focusing on the strong attractive (SA) limit at 14.5 $k_{\mathrm{B}}T$ induced by SDS micelles at a high SDS concentration of 80 mM. Our findings indicate that measuring an asymmetrically shaped $1/\ell^*(\phi)$ for disordered systems of uniform dielectric colloidal spheres can serve as a useful indicator of the presence of strong attractions relative to thermal energy. This qualitative identification significantly influences how to perform passive microrheology quantitatively using DWS. We have developed the decorated core-shell network (DCSN) model, providing a simplified way of representing and coupling optical and mechanical properties of the dense heterogeneous system of droplets that interact through strong slippery attractions. Using the DCSN model, we have established a method for extracting the effective scattering probe size associated with the time-dependent MSDs. Strikingly, we demonstrate that the radius of effective DWS scattering probes is approximately twice the radius of individual droplets, independent of ϕ.

In Chapter 3, we have explored intermediate attractive (IA) emulsions with attractive interaction potential of 5.6 $k_{\mathrm{B}}T$ induced by 35 mM SDS, comparing their optical transport properties, rheological behavior, and dynamic correlation functions to those of nearly hard (NH), moderately attractive (MA) and strongly attractive (SA) emulsions. We have developed a protocol for preparing dense IA emulsions and revealed a non-monotonic behavior in the ϕ-dependent optical transport properties, which significantly differs from both MA and SA emulsions and has a characteristic notch feature just below the repulsive jamming ϕ. A ϕ-dependent DWS probe-size factor is used to provide the best comparison with mechanical measurements, while the extended decorated core-shell network (E-DCSN) model is expanded to include a fourth principal component to explain the additional complexity in the measured optical scattering. The results suggest a cluster-jamming scenario for IA emulsions, with loosely connected dense clusters jamming when ϕ is increased. This study lays the groundwork for further exploration of the transitions between MA, IA, and SA regimes and the fundamental origin of the DWS probe-size factor in short-range attractive colloidal systems.

In Chapter 4, we have investigated the impact of extreme bidispersity in droplet size distribution on the optical transport properties, droplet dynamics, and bulk linear mechanical response to shear in concentrated colloidal emulsions. We have demonstrated that additional complexity arises from screened-charge electrostatic repulsions between droplet interfaces and entropic depletion attractions between microscale droplets, induced by nanoscale droplets acting as depletion agents. We have observed these emergent effects in extremely bidisperse colloidal emulsions; such effects preclude interpretations based on simple effective medium theories. Optical transport properties in extremely bidisperse colloidal emulsions can serve as sensitive indicators of depletion attractions. Moreover, DWS of bidisperse colloidal emulsions, when properly interpreted, can provide useful information for quantitative passive microrheological interpretation through the generalized Stokes-Einstein relation. This study has revealed the importance of considering droplet size polydispersity in understanding the macroscopic properties of complex colloidal systems.

In Chapter 5, we have explored the unjamming of a model soft colloidal solid using ^{19}F StE PFG-NMR measurements on concentrated nanoemulsions. We find that the total molecular motion, consisting of center-of-mass motion of nanodroplets and confined molecular diffusion of ^{19}F-labeled silicone oil within the nanodroplets, exhibits dramatic changes as the nanodroplets unjam upon reducing ϕ. Our custom-formulated size-fractionated O/W nanoemulsion allow for a more straightforward interpretation of NMR measurements, as interdroplet diffusion of perfluorinated oil molecules is effectively precluded. By combining NMR measurements with a passive microrheological interpretation of macroscopic mechanical rheometry measurements, we derive a master curve of droplet root-MSDs, normalized by the average diameter of the nanodroplets, as a function of ϕ. This enabled us to relate droplet unjamming to Lindemann's ratio, showing that the ϕ associated with Lindemann melting coincides with ϕ_{c} associated with nanodroplet unjamming and the loss of low-frequency mechanical shear rigidity.

There remain many exciting directions for future research, including the use of higher magnetic field gradients to explore larger b values, the investigation of nanoemulsions with different droplet sizes and oil viscosities, and the development of theories and simulations for the total motion of probe molecules within dense colloidal droplet systems during glass and jamming transitions. Higher magnetic field gradients could provide a direct measurement of the effective plateau of the NMR attenuation in the highly concentrated ϕ-regime and may allow for the deduction of G'_p directly from the high-b plateau MSDs. Investigating nanoemulsions with varying droplet sizes and oil viscosities may further increase sensitivity to nanodroplet motion in the jammed ϕ-regime and provide insights into the relative contributions of confined molecular diffusion and nanodroplet motion. Overall, our work in Chapter 5 has contributed to a deeper understanding of the unjamming and melting of soft colloidal solids and has paved the way for future studies in this area.

In Chapter 6, we have presented a trajectory-based simulation study that demonstrates passive microrheology by analyzing the MSDs of a Brownian probe molecule confined within a droplet undergoing harmonically bound Brownian motion. The motion of probe molecules within droplets has been modeled as simple diffusion confined within a disk representing the HBBP droplet. By subtracting the MSDs of the confined motion of probe molecule from the MSDs of the total molecular probe motion, we obtain the self-motion MSDs of the droplet's center of mass, which allow us to calculate the elastic plateau shear storage modulus at each packing fraction using the GSER for droplets. Thus, we propose that, for a limited range of soft materials and for certain experimental techniques, colloidal droplet motion can be extracted from total molecular probe motion, and, herein, we have used only the extracted droplet MSDs in determining G'_p through the framework of passive microrheology. Our simulation of dispersed phase-confined molecular diffusion emphasizes the importance of high contrast between the viscosity of the dispersed and continuous phases for accurate results, as it increases the relative proportion of contributing droplet MSD in the total probe MSD. Using smaller nanoscopic droplet sizes could extend the range of PFG-NMR experiments from extremely dilute to the elastically jammed regime of droplets, potentially enabling direct NMR measurements of G'_p above the jamming limit. The simulation approach we present could potentially be used in a wide range of experiments, including single-molecular probe super-resolution optical tracking experiments, to enable passive methods of microrheology in heterogeneous soft colloidal systems.

In Chapter 7, we have shown the map of optical transport fingerprints of dense emulsions having short-range attractions. We have presented the inverted parabola-like $1/\ell^*(\phi)$ behavior for moderately to intermediately attractive (MA-IA) emulsions at 3.3 $k_\mathrm{B}T$ micellar depletion attractive strength, as well as the asymmetric $1/\ell^*(\phi)$, which can be described using the DCSN model, for intermediately to strongly attractive (IA-SA) emulsions at 7.3 $k_\mathrm{B}T$. Intriguingly, we have observed an *isoskedastic* point, corresponding to the crossover of $1/\ell^*(\phi)$ for all the explored attractive emulsions and the emulsions having nearly hard interactions.

In Chapter 8, through 2D trajectory-based simulations, we have elucidated that a surface bound molecular probe technique has the potential to significantly enhance the dimensionless ratio, $\xi = \left\langle \Delta \boldsymbol{r}_\mathrm{drop}^2 \right\rangle_\mathrm{p} / \left\langle \Delta \boldsymbol{r}_\mathrm{pr,tot}^2 \right\rangle_\mathrm{p}$, of extracting colloidal dynamics from probed molecular dynamics. Accordingly, we have depicted an experimental design for future ^{19}F-NMR, which is to use fluorinated surfactant molecules that have been irreversibly adsorbed at high density onto nanodroplet interfaces in O/W nanoemulsions, while using non-fluorinated oil inside the nanodroplets. This approach offers a higher level of confined molecular diffusion compared to the approach using labeled molecular probes that diffuse inside droplets, as studied in Chapter 5 (experimentally) and 6 (numerically). Surface confinement of probe molecules leads to an effectively higher relative contribution of droplet MSDs to the total molecular probe MSDs by orders of magnitude at high ϕ. Therefore, the surface-bound molecular probe strategy could potentially extend passive microrheology of nanoemulsions using ^{19}F-NMR to the strongly elastic regime. While this approach could be sufficient with existing NMR techniques, having higher field gradients in ^{19}F-NMR and also more sensitive coils would also be helpful.

Numerous possible directions for future research can be pursued to expand upon the knowledge gained in this dissertation. One potential avenue involves the microrheological DWS investigation of uniform O/W emulsions with different droplet radii, distinct from the approximate 500 nm radius analyzed in this study, which corresponds to the wavelength of visible light. This will allow the broadening of the conclusions drawn from this research.

However, there are challenges in DWS when the scattering becomes greatly reduced as the droplet sizes go far below the laser's wavelength. Thus, this could be challenging to do well at a highly quantitative level.

Moreover, the study of how varying degrees of polydispersity and droplet size ratios could affect the light scattering and rheological characteristics of dense emulsions is a captivating topic. Our research has indicated that, when there is an extremely large droplet size ratio (*e.g.* exceeding 20), the smaller droplets have the tendency to jam and can also induce depletion attractions among the larger droplets within binary mixtures of emulsions and nanoemulsions. In the scenario of a considerably reduced droplet size ratio, taking into account the Debye-screening length, when only a single droplet can fit within the interstices of other larger jammed droplets, it may be plausible to push towards a higher total volume fraction, beyond 0.64, without the occurrence of jamming, even among the smaller droplets. We are intrigued to understand how the effective continuous phase defined for the extremely bidisperse emulsions might function in the case of bidisperse emulsions with a significantly reduced droplet size ratio of around 5. Furthermore, it is probable that such minimal droplet size difference might not result in self-induced depletion attractions. Consequently, exploring jamming and depletion in emulsion systems with different droplet size distributions will require further experimental investigations.

It is also prospective to explore the passive microrheological interpretation of DWS to various kinds of emulsions, such as water-in-oil (W/O) emulsions[186,187]. This exploration could enhance our understanding of the behavior and stability of dense colloidal emulsions and provide insights into the design of emulsions with tailored properties for specific applications. While engaging, interpreting the scattering from DWS of multicompartment emulsions[156,188] or multiple emulsions[189] would be extraordinarily challenging when compared to single emulsions. Therefore, the path to passive microrheological interpretations may not be straightforward in these cases.

Future investigation could emphasize the potential of employing the methodologies devised in this dissertation to a broader range of dense colloidal materials. These methods involve developing opto-mechanical models that concurrently satisfy a combination of measurements - equilibrium, steady-state optical transport, dynamic scattering, and rheological properties - for well-prepared uniform emulsions. These methods could be beneficial for quantitative microrheological characterization of materials like homopolymers or microgels, composed of soft, deformable, spherical particles that bear resemblance to droplets in emulsions. To explore the use of DWS microrheology to these systems, the gradual change in refractive index at colloidal interfaces, as opposed to the step change at droplet interfaces in emulsions, as well as the different pair-interaction potential profiles between colloids, might impose a higher degree of complexity in the interpretation. This complexity is a compelling area for further exploration.

Another area of future research could be the development of more sophisticated opto-mechanical models and simulations that capture the complexity of dense colloidal systems more accurately. This may include the use of three-dimensional models, the incorporation of different interaction potentials, and the consideration of additional factors such as collisions between colloids, thermal and vibrational fluctuations, and inhomogeneity in microscale structures. In addition to translational Brownian dynamics, one can also consider rotational Brownian dynamics for highly viscous droplets and even solid particles in the three-dimensional models. By refining these models, a deeper understanding of the underlying mechanisms governing the properties of dense colloidal emulsions can be achieved. In addition, the exploration of novel molecular detection techniques for passive microrheology holds promise for advancing the field. Developing and validating new methods that complement current techniques, such as diffusing wave spectroscopy, may allow for a more nuanced understanding of the rheological properties of emulsions and other colloidal systems.

In conclusion, this dissertation has made significant advances in the understanding of dense colloidal emulsions; yet there remains ample opportunity for future research to further explore and expand upon the findings presented here. As the field continues to evolve, the knowledge gained from these investigations will contribute to the development of novel materials and technologies, ultimately benefiting a wide range of industries and applications.

REFERENCES

1. Russel, W. B., Saville, D. A., and Schowalter, W. R. *Colloidal Dispersions.* Cambridge University Press, Cambridge, UK, 1989.

2. Hunter, R. J. *Foundations of Colloid Science.* Oxford University Press, Oxford, UK, 2001.

3. Berg, J. C. *An Introduction to Interfaces & Colloids: The Bridge to Nanoscience.* World Scientific, Singapore, 2010.

4. Schramm, L. L. *Emulsions, Foams, Suspensions, and Aerosols: Microscience and Applications.* John Wiley & Sons, Weinheim,Germany, 2014.

5. McClements, D. J. *Food Emulsions: Principles, Practices, and Techniques.* CRC press, Boca Raton, Florida, 2015.

6. Sarkar, D. K. *Pharmaceutical Emulsions: A Drug Developer's Toolbag.* John Wiley & Sons, West Sussex, UK, 2013.

7. Albert, C., Beladjine, M., Tsapis, N., Fattal, E., Agnely, F., and Huang, N. "Pickering emulsions: Preparation processes, key parameters governing their properties and potential for pharmaceutical applications." *J. Control. Release*, **309**:302–332, 2019.

8. You, H., Yang, S., Ding, B., and Yang, H. "Synthesis of colloidal metal and metal alloy nanoparticles for electrochemical energy applications." *Chem. Soc. Rev.*, **42**(7):2880–2904, 2013.

9. Taylor, K. C. and Nasr-El-Din, H. A. "Water-soluble hydrophobically associating polymers for improved oil recovery: A literature review." *J. Pet. Sci. Eng.*, **19**(3-4):265–280, 1998.

10. Kim, H. S. and Mason, T. G. "Advances and challenges in the rheology of concentrated emulsions and nanoemulsions." *Adv. Colloid Interface Sci.*, **247**:397–412, 2017.

11. Mason, T. G. and Weitz, D. A. "Optical measurements of frequency-dependent linear viscoelastic moduli of complex fluids." *Phys. Rev. Lett.*, **74**(7):1250–1253, 1995.

12. Squires, T. M. and Mason, T. G. "Fluid mechanics of microrheology." *Annu. Rev. Fluid Mech.*, **42**:413–438, 2010.

13. Leal-Calderon, F., Schmitt, V., and Bibette, J. *Emulsion science: basic principles.* Springer Science & Business Media, 2007.

14. Schuster, D. *Encyclopedia of Emulsion Technology: Applications*, volume 2. CRC Press, Boca Raton, Florida, 1985.

15. Schramm, L. L. et al. “Fundamentals and applications in the petroleum Industry.” *Adv. Chem.*, **231**:3–24, 1992.

16. Langevin, D., Poteau, S., Hénaut, I., and Argillier, J. “Crude oil emulsion properties and their application to heavy oil transportation.” *Oil Gas Sci. Technol.*, **59**(5):511–521, 2004.

17. Gutiérrez, J., González, C., Maestro, A., Solè, I., Pey, C., and Nolla, J. “Nano-emulsions: New applications and optimization of their preparation.” *Curr. Opin. Colloid Interface Sci.*, **13**(4):245–251, 2008.

18. Zhou, Y., Yin, D., Chen, W., Liu, B., and Zhang, X. “A comprehensive review of emulsion and its field application for enhanced oil recovery.” *Energy Sci. Eng.*, **7**(4):1046–1058, 2019.

19. Hussein, M. A., Mohammed, A. A., and Atiya, M. A. “Application of emulsion and Pickering emulsion liquid membrane technique for wastewater treatment: an overview.” *Environ. Sci. Pollut. Res.*, **26**:36184–36204, 2019.

20. Larson, R. G. *The Structure and Rheology of Complex Fluids*, volume 150. Oxford University Press, New York, 1999.

21. Mason, T. G., Bibette, J., and Weitz, D. A. “Elasticity of compressed emulsions.” *Phys. Rev. Lett.*, **75**(10):2051–2054, 1995.

22. Taylor, G. I. “The formation of emulsions in definable fields of flow.” *Proc. Royal Soc. Lond. A*, **146**(858):501–523, 1934.

23. Meleson, K., Graves, S., and Mason, T. G. “Formation of concentrated nanoemulsions by extreme shear.” *Soft Mater.*, **2**(2-3):109–123, 2004.

24. Mason, T. G., Wilking, J. N., Meleson, K., Chang, C. B., and Graves, S. M. “Nanoemulsions: formation, structure, and physical properties.” *J. Phys. Condens. Matter*, **18**(41):R635–R666, 2006.

25. Fryd, M. M. and Mason, T. G. “Advanced nanoemulsions.” *Annu. Rev. Phys. Chem.*, **63**:493–518, 2012.

26. Taylor, P. “Ostwald ripening in emulsions.” *Adv. Colloid Interface Sci.*, **75**(2):107–163, 1998.

27. Sonneville-Aubrun, O., Simonnet, J.-T., and L’alloret, F. “Nanoemulsions: a new vehicle for skincare products.” *Adv. Colloid Interface Sci.*, **108**:145–149, 2004.

28. Mason, T. G., Krall, A. H., Gang, H., Bibette, J., and Weitz, D. A. ““Monodisperse Emulsions: Properties and Uses”.” In Becher, P., editor, *Encyclopedia of Emulsion Technology*, volume 4, pp. 299–336. Marcel Dekker, New York, 1996.

29. Bibette, J. "Depletion interactions and fractionated crystallization for polydisperse emulsion purification." *J. Colloid Interface Sci.*, **147**(2):474–478, 1991.

30. Wilking, J. N. and Mason, T. G. "Irreversible shear-induced vitrification of droplets into elastic nanoemulsions by extreme rupturing." *Phys. Rev. E*, **75**(4):041407, 2007.

31. Scheffold, F. and Mason, T. "Scattering from highly packed disordered colloids." *J. Phys. Condens. Matter*, **21**(33):332102, 2009.

32. Mason, T. G. "New fundamental concepts in emulsion rheology." *Curr. Opin. Colloid Interface Sci.*, **4**(3):231–238, 1999.

33. Scheffold, F., Cardinaux, F., and Mason, T. G. "Linear and nonlinear rheology of dense emulsions across the glass and the jamming regimes." *J. Phys. Condens. Matter*, **25**(50):502101, 2013.

34. Lequeux, F. "Emulsion rheology." *Curr. Opin. Colloid Interface Sci.*, **3**(4):408–411, 1998.

35. Bernal, J. D. and Mason, J. "Packing of spheres: co-ordination of randomly packed spheres." *Nature*, **188**(4754):910–911, 1960.

36. Torquato, S., Truskett, T. M., and Debenedetti, P. G. "Is random close packing of spheres well defined?" *Phys. Rev. Lett.*, **84**(10):2064–2067, 2000.

37. Kim, H. S., Scheffold, F., and Mason, T. G. "Entropic, electrostatic, and interfacial regimes in concentrated disordered ionic emulsions." *Rheol. Acta*, **55**(8):683–697, 2016.

38. Mason, T. G. and Scheffold, F. "Crossover between entropic and interfacial elasticity and osmotic pressure in uniform disordered emulsions." *Soft Matter*, **10**(36):7109–7116, 2014.

39. Krall, A. H. and Weitz, D. A. "Internal dynamics and elasticity of fractal colloidal gels." *Phys. Rev. Lett.*, **80**(4):778–781, 1998.

40. Trappe, V., Prasad, V., Cipelletti, L., Segre, P. N., and Weitz, D. A. "Jamming phase diagram for attractive particles." *Nature*, **411**(6839):772–775, 2001.

41. Cates, M. E., Fuchs, M., Kroy, K., Poon, W. C. K., and Puertas, A. M. "Theory and simulation of gelation, arrest and yielding in attracting colloids." *J. Phys. Condens. Matter*, **16**(42):S4861–S4875, 2004.

42. Zaccarelli, E., Buldyrev, S. V., La Nave, E., Moreno, A. J., Saika-Voivod, I., Sciortino, F., and Tartaglia, P. "Model for reversible colloidal gelation." *Phys. Rev. Lett.*, **94**(21):218301, 2005.

43. Tsurusawa, H., Leocmach, M., Russo, J., and Tanaka, H. "Direct link between mechanical stability in gels and percolation of isostatic particles." *Sci. Adv.*, **5**(5):eaav6090, 2019.

44. Asakura, S. and Oosawa, F. "Interaction between particles suspended in solutions of macromolecules." *J. Polym. Sci.*, **33**(126):183–192, 1958.

45. Petsev, D. N., Denkov, N. D., and Kralchevsky, P. A. "Flocculation of deformable emulsion droplets: II. interaction energy." *J. Colloid Interface Sci.*, **176**(1):201–213, 1995.

46. Datta, S. S., Gerrard, D. D., Rhodes, T. S., Mason, T. G., and Weitz, D. A. "Rheology of attractive emulsions." *Phys. Rev. E*, **84**(4):041404, 2011.

47. Meller, A. and Stavans, J. "Stability of emulsions with nonadsorbing polymers." *Langmuir*, **12**(2):301–304, 1996.

48. Meller, A., Gisler, T., Weitz, D. A., and Stavans, J. "Viscoelasticity of Depletion-Induced Gels in Emulsion- Polymer Systems." *Langmuir*, **15**(6):1918–1922, 1999.

49. Aben, S., Holtze, C., Tadros, T., and Schurtenberger, P. "Rheological investigations on the creaming of depletion-flocculated emulsions." *Langmuir*, **28**(21):7967–7975, 2012.

50. Steiner, U., Meller, A., and Stavans, J. "Entropy driven phase separation in binary emulsions." *Phys. Rev. Lett.*, **74**(23):4750–4753, 1995.

51. Wilking, J. N., Graves, S. M., Chang, C. B., Meleson, K., Lin, M. Y., and Mason, T. G. "Dense cluster formation during aggregation and gelation of attractive slippery nanoemulsion droplets." *Phys. Rev. Lett.*, **96**(1):015501, 2006.

52. Lozsan, A. "Salt-induced fast aggregation of nano-emulsions: structural and kinetic scaling." *Colloid Polym. Sci.*, **290**:1561–1566, 2012.

53. Weihs, D., Mason, T. G., and Teitell, M. A. "Bio-microrheology: a frontier in microrheology." *Biophys. J.*, **91**(11):4296–4305, 2006.

54. Khan, M. and Sood, A. "Out-of-equilibrium microrheology using optical tweezers to probe directional viscoelastic properties under shear." *Europhys. Lett.*, **92**(4):48001, 2010.

55. Pine, D. J., Weitz, D. A., Chaikin, P. M., and Herbolzheimer, E. "Diffusing wave spectroscopy." *Phys. Rev. Lett.*, **60**(12):1134–1137, 1988.

56. Mason, T. G., Gang, H., and Weitz, D. A. "Diffusing-wave-spectroscopy measurements of viscoelasticity of complex fluids." *J. Opt. Soc. Am. A*, **14**(1):139–149, 1997.

57. Kim, H. S., Şenbil, N., Zhang, C., Scheffold, F., and Mason, T. G. "Diffusing wave microrheology of highly scattering concentrated monodisperse emulsions." *Proc. Natl. Acad. Sci. U.S.A.*, **116**(16):7766–7771, 2019.

58. Seager, C. R. and Mason, T. G. "Slippery diffusion-limited aggregation." *Phys. Rev. E*, **75**(1):011406, 2007.

59. Kim, H. S., Xu, Y., Scheffold, F., and Mason, T. G. "Self-motion and heterogeneous droplet dynamics in moderately attractive dense emulsions." *J. Phys. Condens. Matter*, **33**(17):175101, 2021.

60. Zaccarelli, E. "Colloidal gels: equilibrium and non-equilibrium routes." *J. Phys. Condens. Matter*, **19**(32):323101, 2007.

61. Trappe, V. and Sandkühler, P. "Colloidal gels—low-density disordered solid-like states." *Curr. Opin. Colloid Interface Sci.*, **8**(6):494–500, 2004.

62. Berthier, L. and Biroli, G. "Theoretical perspective on the glass transition and amorphous materials." *Rev. Mod. Phys.*, **83**(2):587–645, 2011.

63. Zhao, K. and Mason, T. G. "Assembly of colloidal particles in solution." *Rep. Prog. Phys.*, **81**(12):126601, 2018.

64. Dawson, K., Foffi, G., Fuchs, M., Götze, W., Sciortino, F., Sperl, M., Tartaglia, P., Voigtmann, Th., and Zaccarelli, E. "Higher-order glass-transition singularities in colloidal systems with attractive interactions." *Phys. Rev. E*, **63**(1):011401, 2000.

65. Bergenholtz, J., Poon, W. C. K., and Fuchs, M. "Gelation in model colloid- polymer mixtures." *Langmuir*, **19**(10):4493–4503, 2003.

66. Kroy, K., Cates, M. E., and Poon, W. C. K. "Cluster mode-coupling approach to weak gelation in attractive colloids." *Phys. Rev. Lett.*, **92**(14):148302, 2004.

67. Foffi, G., De Michele, C., Sciortino, F., and Tartaglia, P. "Arrested phase separation in a short-ranged attractive colloidal system: A numerical study." *J. Chem. Phys.*, **122**(22):224903, 2005.

68. Liu, A. J. and Nagel, S. R. "Jamming is not just cool any more." *Nature*, **396**(6706):21–22, 1998.

69. Torquato, S. and Stillinger, F. H. "Jammed hard-particle packings: From Kepler to Bernal and beyond." *Rev. Mod. Phys.*, **82**(3):2633–2672, 2010.

70. Pusey, P. N., Pirie, A. D., and Poon, W. C. K. "Dynamics of colloid-polymer mixtures." *Phys. A: Stat. Mech. Appl.*, **201**(1-3):322–331, 1993.

71. Segre, P. N., Prasad, V., Schofield, A. B., and Weitz, D. A. "Glasslike kinetic arrest at the colloidal-gelation transition." *Phys. Rev. Lett.*, **86**(26):6042–6045, 2001.

72. Pham, K. N., Puertas, A. M., Bergenholtz, J., Egelhaaf, S. U., Moussaıd, A., Pusey, P. N., Schofield, A. B., Cates, M. E., Fuchs, M., and Poon, W. C. K. "Multiple glassy states in a simple model system." *Science*, **296**(5565):104–106, 2002.

73. Saika-Voivod, I., Zaccarelli, E., Sciortino, F., Buldyrev, S. V., and Tartaglia, P. "Effect of bond lifetime on the dynamics of a short-range attractive colloidal system." *Phys. Rev. E*, **70**(4):041401, 2004.

74. Liu, J., Boyko, V., Yi, Z., and Men, Y. "Temperature-dependent gelation process in colloidal dispersions by diffusing wave spectroscopy." *Langmuir*, **29**(46):14044–14049, 2013.

75. Cipelletti, L., Manley, S., Ball, R. C., and Weitz, D. A. "Universal aging features in the restructuring of fractal colloidal gels." *Phys. Rev. Lett.*, **84**(10):2275–2278, 2000.

76. Cipelletti, L. and Ramos, L. "Slow dynamics in glassy soft matter." *J. Phys. Condens. Matter*, **17**(6):R253–R285, 2005.

77. Foffi, G., Zaccarelli, E., Buldyrev, S., Sciortino, F., and Tartaglia, P. "Aging in short-ranged attractive colloids: A numerical study." *J. Chem. Phys.*, **120**(18):8824–8830, 2004.

78. Romer, S., Bissig, H., Schurtenberger, P., and Scheffold, F. "Rheology and internal dynamics of colloidal gels from the dilute to the concentrated regime." *EPL*, **108**(4):48006, 2014.

79. Bibette, J., Roux, D., and Nallet, F. "Depletion interactions and fluid-solid equilibrium in emulsions." *Phys. Rev. Lett.*, **65**(19):2470–2473, 1990.

80. Zhu, X., Fryd, M. M., Huang, J.-R., and Mason, T. G. "Optically probing nanoemulsion compositions." *Phys. Chem. Chem. Phys.*, **14**(7):2455–2461, 2012.

81. Harich, R., Blythe, T. W., Hermes, M., Zaccarelli, E., Sederman, A. J., Gladden, L. F., and Poon, W. C. K. "Gravitational collapse of depletion-induced colloidal gels." *Soft Matter*, **12**(19):4300–4308, 2016.

82. Zakharov, P., Cardinaux, F., and Scheffold, F. "Multispeckle diffusing-wave spectroscopy with a single-mode detection scheme." *Phys. Rev. E*, **73**(1):011413, 2006.

83. Qiu, X., Wu, X. L., Xue, J. Z., Pine, D. J., Weitz, D. A., and Chaikin, P. M. "Hydrodynamic interactions in concentrated suspensions." *Phys. Rev. Lett.*, **65**(4):516–519, 1990.

84. Wyss, H. M., Romer, S., Scheffold, F., Schurtenberger, P., and Gauckler, L. J. "Diffusing-wave spectroscopy of concentrated alumina suspensions during gelation." *J. Colloid Interface Sci.*, **241**(1):89–97, 2001.

85. Zhang, C., Gnan, N., Mason, T. G., Zaccarelli, E., and Scheffold, F. "Dynamical and structural signatures of the glass transition in emulsions." *J. Stat. Mech.: Theory Exp*, **2016**(9):094003, 2016.

86. Jorjadze, I., Pontani, L.-L., and Brujic, J. "Microscopic approach to the nonlinear elasticity of compressed emulsions." *Phys. Rev. Lett.*, **110**(4):048302, 2013.

87. Cohen, I., Mason, T. G., and Weitz, D. A. "Shear-induced configurations of confined colloidal suspensions." *Phys. Rev. Lett.*, **93**(4):046001, 2004.

88. Dutta, S. K., Mbi, A., Arevalo, R. C., and Blair, D. L. "Development of a confocal rheometer for soft and biological materials." *Rev. Sci. Instrum.*, **84**(6):063702, 2013.

89. Weitz, D. A., Huang, J. S., Lin, M. Y., and Sung, J. "Dynamics of diffusion-limited kinetic aggregation." *Phys. Rev. Lett.*, **53**(17):1657–1660, 1984.

90. Bibette, J., Mason, T. G., Gang, H., and Weitz, D. A. "Kinetically induced ordering in gelation of emulsions." *Phys. Rev. Lett.*, **69**(6):981–984, 1992.

91. Bibette, J., Mason, T. G., Gang, H., Weitz, D. A., and Poulin, P. "Structure of adhesive emulsions." *Langmuir*, **9**(12):3352–3356, 1993.

92. Gisler, T., Ball, R. C., and Weitz, D. A. "Strain hardening of fractal colloidal gels." *Phys. Rev. Lett.*, **82**(5):1064–1067, 1999.

93. Manley, S., Skotheim, J. M., Mahadevan, L., and Weitz, D. A. "Gravitational collapse of colloidal gels." *Phys. Rev. Lett.*, **94**(21):218302, 2005.

94. Witten, Jr, T. A. and Sander, L. M. "Diffusion-limited aggregation, a kinetic critical phenomenon." *Phys. Rev. Lett.*, **47**(19):1400–1403, 1981.

95. Carpineti, M. and Giglio, M. "Transition from semiorder to disorder in the aggregation of dense colloidal solutions." *Phys. Rev. Lett.*, **70**(24):3828–3831, 1993.

96. Woodcock, L. V. "Glass Transition in the Hard-Sphere Model and Kauzmann's Paradox." *Ann. N. Y. Acad. Sci.*, **371**(1):274–298, 1981.

97. Bengtzelius, U., Gotze, W., and Sjolander, A. "Dynamics of supercooled liquids and the glass transition." *J. Phys. C: Solid State Phys.*, **17**(33):5915–5934, 1984.

98. Pusey, P. N. and van Megen, W. "Observation of a glass transition in suspensions of spherical colloidal particles." *Phys. Rev. Lett.*, **59**(18):2083–2086, 1987.

99. Götze, W. “Liquids, freezing and the glass transition.” *Les Houches Summer Schools of Theoretical Physics Session LI*, pp. 287–503, 1991.

100. Götze, W. *Complex dynamics of glass-forming liquids: A mode-coupling theory*, volume 143 of *International series of monographs on physics*. Oxford University Press, Oxford, 2008.

101. Szamel, G. and Löwen, H. “Mode-coupling theory of the glass transition in colloidal systems.” *Phys. Rev. A*, **44**(12):8215–8219, 1991.

102. Binder, K., Virnau, P., and Statt, A. “Perspective: The Asakura Oosawa model: A colloid prototype for bulk and interfacial phase behavior.” *J. Chem. Phys.*, **141**(14):140901, 2014.

103. Zaccarelli, E., Foffi, G., Dawson, K. A., Buldyrev, S. V., Sciortino, F., and Tartaglia, P. “Static and dynamical correlation functions behaviour in attractive colloidal systems from theory and simulation.” *J. Phys. Condens. Matter*, **15**(1):S367–S374, 2002.

104. Poon, W. C. K., Selfe, J. S., Robertson, M. B., Ilett, S. M., Pirie, A. D., and Pusey, P. N. “An experimental study of a model colloid-polymer mixture.” *J. Phys., II*, **3**(7):1075–1086, 1993.

105. Eckert, T. and Bartsch, E. “Re-entrant glass transition in a colloid-polymer mixture with depletion attractions.” *Phys. Rev. Lett.*, **89**(12):125701, 2002.

106. Dinsmore, A. D., Weeks, E. R., Prasad, V., Levitt, A. C., and Weitz, D. A. “Three-dimensional confocal microscopy of colloids.” *Applied Optics*, **40**(24):4152–4159, 2001.

107. Jorjadze, I., Pontani, L.-L., Newhall, K. A., and Brujić, J. “Attractive emulsion droplets probe the phase diagram of jammed granular matter.” *Proc. Natl. Acad. Sci. U.S.A.*, **108**(11):4286–4291, 2011.

108. Maret, G. and Wolf, P. E. “Multiple light scattering from disordered media. The effect of Brownian motion of scatterers.” *Z. Phys. B: Condens. Matter*, **65**(4):409–413, 1987.

109. Weitz, D. A., Pine, D. J., Pusey, P. N., and Tough, R. J. “Nondiffusive Brownian motion studied by diffusing-wave spectroscopy.” *Phys. Rev. Lett.*, **63**(16):1747–1750, 1989.

110. Pusey, P. N. and Van Megen, W. “Dynamic light scattering by non-ergodic media.” *Physica A*, **157**(2):705–741, 1989.

111. Xue, J.-Z., Pine, D. J., Milner, S. T., Wu, X.-L., and Chaikin, P. M. “Nonergodicity and light scattering from polymer gels.” *Phys. Rev. A*, **46**(10):6550–6563, 1992.

112. Schätzel, K. “Accuracy of photon correlation measurements on nonergodic samples.” *Applied Optics*, **32**(21):3880–3885, 1993.

113. Bizheva, K. K., Siegel, A. M., and Boas, D. A. “Path-length-resolved dynamic light scattering in highly scattering random media: The transition to diffusing wave spectroscopy.” *Phys. Rev. E*, **58**(6):7664–7667, 1998.

114. Scheffold, F. and Schurtenberger, P. “Light scattering probes of viscoelastic fluids and solids.” *Soft Mater.*, **1**(2):139–165, 2003.

115. Xu, Y., Scheffold, F., and Mason, T. G. “Diffusing wave microrheology of strongly attractive dense emulsions.” *Phys. Rev. E*, **102**(6):062610, 2020.

116. Derkach, S. R. “Rheology of emulsions.” *Adv. Colloid Interface Sci.*, **151**(1-2):1–23, 2009.

117. Pal, R. “Rheology of simple and multiple emulsions.” *Curr. Opin. Colloid Interface Sci.*, **16**(1):41–60, 2011.

118. Cohen-Addad, S. and Höhler, R. “Rheology of foams and highly concentrated emulsions.” *Curr. Opin. Colloid Interface Sci.*, **19**(6):536–548, 2014.

119. Helgeson, M. E. “Colloidal behavior of nanoemulsions: Interactions, structure, and rheology.” *Curr. Opin. Colloid Interface Sci.*, **25**:39–50, 2016.

120. Xu, Y. and Mason, T. G. “Complex optical transport, dynamics, and rheology of intermediately attractive emulsions.” *Sci. Rep.*, **13**:1791, 2023.

121. Chong, J. S., Christiansen, E. B., and Baer, A. D. “Rheology of concentrated suspensions.” *J. Appl. Polym. Sci.*, **15**(8):2007–2021, 1971.

122. Farr, R. S. and Groot, R. D. “Close packing density of polydisperse hard spheres.” *J. Chem. Phys.*, **131**(24):244104, 2009.

123. Ueda, T., Matsushima, T., and Yamada, Y. “Effect of particle size ratio and volume fraction on shear strength of binary granular mixture.” *Granul. Matter*, **13**(6):731–742, 2011.

124. Sweeny, K. H. and Geckler, R. D. “The rheology of suspensions.” *J. Appl. Phys.*, **25**(9):1135–1144, 1954.

125. Chang, C. and Powell, R. L. “Dynamic simulation of bimodal suspensions of hydrodynamically interacting spherical particles.” *J. Fluid Mech.*, **253**:1–25, 1993.

126. D’Haene, P. and Mewis, J. “Rheological characterization of bimodal colloidal dispersions.” *Rheol. Acta*, **33**(3):165–174, 1994.

127. Richtering, W. and Mueller, H. “Comparison between viscosity and diffusion in monodisperse and bimodal colloidal suspensions.” *Langmuir*, **11**(10):3699–3704, 1995.

128. Sikorski, M., Sandy, A., and Narayanan, S. “Depletion-induced structure and dynamics in bimodal colloidal suspensions.” *Phys. Rev. Lett.*, **106**(18):188301, 2011.

129. Erramreddy, V. V. and Ghosh, S. “Influence of emulsifier concentration on nanoemulsion gelation.” *Langmuir*, **30**(37):11062–11074, 2014.

130. Erramreddy, V. V. and Ghosh, S. “Influence of droplet size on repulsive and attractive nanoemulsion gelation.” *Colloids Surf. A Physicochem. Eng. Asp.*, **484**:144–152, 2015.

131. Pednekar, S., Chun, J., and Morris, J. F. “Bidisperse and polydisperse suspension rheology at large solid fraction.” *J. Rheol.*, **62**(2):513–526, 2018.

132. Lacasse, M.-D., Grest, G. S., Levine, D., Mason, T. G., and Weitz, D. A. “Model for the elasticity of compressed emulsions.” *Phys. Rev. Lett.*, **76**(18):3448–3451, 1996.

133. Mason, T. G., Lacasse, M. D., Grest, G. S., Levine, D., Bibette, J., and Weitz, D. A. “Osmotic pressure and viscoelastic shear moduli of concentrated emulsions.” *Phys. Rev. E*, **56**(3):3150–3166, 1997.

134. Graves, S. M. and Mason, T. G. “Transmission of visible and ultraviolet light through charge-stabilized nanoemulsions.” *J. Phys. Chem. C*, **112**(33):12669–12676, 2008.

135. Braibanti, M., Kim, H. S., Şenbil, N., Pagenkopp, M. J., Mason, T. G., and Scheffold, F. “The liquid-glass-jamming transition in disordered ionic nanoemulsions.” *Sci. Rep.*, **7**(1):13879, 2017.

136. Siano, D. B. “The log-normal distribution function.” *J. Chem. Educ.*, **49**(11):755–757, 1972.

137. Zhu, X. and Mason, T. G. “Nanoparticle size distributions measured by optical adaptive-deconvolution passivated-gel electrophoresis.” *J. Colloid Interface Sci.*, **435**:67–74, 2014.

138. Sanatkaran, N., Zhou, M., and Foudazi, R. “Rheology of macro-and nano-emulsions in the presence of micellar depletion attraction.” *J. Rheol.*, **65**(3):453–461, 2021.

139. Parella, T. “Pulsed field gradients: a new tool for routine NMR.” *Magn. Reson. Chem.*, **36**(7):467–495, 1998.

140. Stallmach, F. and Galvosas, P. “Spin echo NMR diffusion studies.” *Annu. Rep. NMR Spectrosc.*, **61**:51–131, 2007.

141. Appel, M., Fleischer, G., Kärger, J., Fujara, F., and Siegel, S. “NMR evidence of anomalous molecular diffusion due to structural confinement.” *EPL*, **34**(7):483–487, 1996.

142. Das, A., Jayanthi, S., Deepak, H. S. M. V., Ramanathan, K. V., Kumar, A., Dasgupta, C., and Sood, A. K. "Single-file diffusion of confined water inside SWNTs: an NMR study." *ACS Nano*, **4**(3):1687–1695, 2010.

143. Wassenius, H., Nydén, M., and Vincent, B. "NMR diffusion studies of translational properties of oil inside core–shell latex particles." *J. Colloid Interface Sci.*, **264**(2):538–547, 2003.

144. Geier, O., Snurr, R. Q., Stallmach, F., and Kärger, J. "Boundary effects of molecular diffusion in nanoporous materials: a pulsed field gradient nuclear magnetic resonance study." *J. Chem. Phys.*, **120**(1):367–373, 2004.

145. Naumov, S., Khokhlov, A., Valiullin, R., Kärger, J., and Monson, P. A. "Understanding capillary condensation and hysteresis in porous silicon: network effects within independent pores." *Phys. Rev. E*, **78**(6):060601, 2008.

146. Magin, R. L. "Models of diffusion signal decay in magnetic resonance imaging: capturing complexity." *Concepts Magn. Reson. Part A*, **45**(4):e21401, 2016.

147. Nakatani, A. I., Poliks, M. D., and Samulski, E. T. "NMR investigation of chain deformation in sheared polymer fluids." *Macromolecules*, **23**(10):2686–2692, 1990.

148. Callaghan, P. T. "Rheo-NMR: nuclear magnetic resonance and the rheology of complex fluids." *Rep. Prog. Phys.*, **62**(4):599–670, 1999.

149. Cormier, R. J., Schmidt, C., and Callaghan, P. T. "Director reorientation of a side-chain liquid crystalline polymer under extensional flow." *J. Rheol.*, **48**(4):881–894, 2004.

150. Williamson, N. H., Dower, A. M., Codd, S. L., Broadbent, A. L., Gross, D., and Seymour, J. D. "Glass dynamics and domain size in a solvent-polymer weak gel measured by multidimensional magnetic resonance relaxometry and diffusometry." *Phys. Rev. Lett.*, **122**(6):068001, 2019.

151. Kimmich, R. and Fatkullin, N. "Polymer chain dynamics and NMR." In *Advances in Polymer Science*, volume 170, pp. 1–113. Springer, Berlin, Heidelberg, 2004.

152. Callaghan, P. T. "Rheo-NMR and velocity imaging." *Curr. Opin. Colloid Interface Sci.*, **11**(1):13–18, 2006.

153. Mason, T. G. "Emulsiogenesis and the emergence of nanoemulsions." *Matter*, **1**(3):542–546, 2019.

154. Naseema, A., Kovooru, L., Behera, A. K., Kumar, K. P. P., and Srivastava, P. "A critical review of synthesis procedures, applications and future potential of nanoemulsions." *Adv. Colloid Interface Sci.*, **287**:102318, 2021.

155. Garasanin, T., Cosgrove, T., Marteaux, L., Kretschmer, A., Goodwin, A., and Zick, K. "NMR self-diffusion studies on PDMS oil-in-water emulsion." *Langmuir*, **18**(26):10298–10304, 2002.

156. Fryd, M. M. and Mason, T. G. "Cerberus nanoemulsions produced by multidroplet flow-induced fusion." *Langmuir*, **29**(51):15787–15793, 2013.

157. Packer, K. J. and Rees, C. "Pulsed NMR studies of restricted diffusion. I. Droplet size distributions in emulsions." *J. Colloid Interface Sci.*, **40**(2):206–218, 1972.

158. Hollingsworth, K. G. and Johns, M. L. "Measurement of emulsion droplet sizes using PFG NMR and regularization methods." *J. Colloid Interface Sci.*, **258**(2):383–389, 2003.

159. Peña, A. A. and Hirasaki, G. J. "Enhanced characterization of oilfield emulsions via NMR diffusion and transverse relaxation experiments." *Adv. Colloid Interface Sci.*, **105**(1-3):103–150, 2003.

160. Callaghan, P. T. *Translational Dynamics and Magnetic Resonance: Principles of Pulsed Gradient Spin Echo NMR.* Oxford University Press, 2011.

161. Malmborg, C., Topgaard, D., and Söderman, O. "NMR diffusometry and the short gradient pulse limit approximation." *J. Magn. Reson.*, **169**(1):85–91, 2004.

162. Bernewitz, R., Guthausen, G., and Schuchmann, H. P. "NMR on emulsions: characterisation of liquid dispersed systems." *Magn. Reson. Chem.*, **49**:S93–S104, 2011.

163. Callaghan, P. T., Coy, A., Halpin, T. P. J., MacGowan, D., Packer, K. J., and Zelaya, F. O. "Diffusion in porous systems and the influence of pore morphology in pulsed gradient spin-echo nuclear magnetic resonance studies." *J. Chem. Phys.*, **97**(1):651–662, 1992.

164. Hoang, V. "Melting of simple monatomic amorphous nanoparticles." *J. Phys. Chem. C*, **116**(27):14728–14735, 2012.

165. Fryd, M. M. and Mason, T. G. "Time-dependent nanoemulsion droplet size reduction by evaporative ripening." *J. Phys. Chem. Lett.*, **1**(23):3349–3353, 2010.

166. Codd, S. L. and Callaghan, P. T. "Spin echo analysis of restricted diffusion under generalized gradient waveforms: planar, cylindrical, and spherical pores with wall relaxivity." *J. Magn. Reson.*, **137**(2):358–372, 1999.

167. Meiboom, S. and Gill, D. "Modified spin-echo method for measuring nuclear relaxation times." *Rev. Sci. Instrum.*, **29**(8):688–691, 1958.

168. Khan, M. and Mason, T. G. "Local collective motion analysis for multi-probe dynamic imaging and microrheology." *J. Phys. Condens. Matter*, **28**(30):305201, 2016.

169. Lam, N. Q., Okamoto, P. R., and Li, M. “Disorder-induced amorphization.” *J. Nucl. Mater.*, **251**:89–97, 1997.

170. Pfeuffer, J., Flögel, U., Dreher, W., and Leibfritz, D. “Restricted diffusion and exchange of intracellular water: theoretical modelling and diffusion time dependence of ^{1}H NMR measurements on perfused glial cells.” *NMR Biomed.*, **11**(1):19–31, 1998.

171. Vermeir, L., Sabatino, P., Balcaen, M., Declerck, A., Dewettinck, K., Martins, J. C., and Van der Meeren, P. “Effect of molecular exchange on water droplet size analysis in W/O emulsions as determined by diffusion NMR.” *J. Colloid Interface Sci.*, **463**:128–136, 2016.

172. Mason, T. G., Ganesan, K., van Zanten, J. H., Wirtz, D., and Kuo, S. C. “Particle tracking microrheology of complex fluids.” *Phys. Rev. Lett.*, **79**(17):3282–3285, 1997.

173. Gittes, F., Schnurr, B., Olmsted, P., MacKintosh, F. C., and Schmidt, C. F. “Microscopic viscoelasticity: shear moduli of soft materials determined from thermal fluctuations.” *Phys. Rev. Lett.*, **79**(17):3286, 1997.

174. Xu, Y., Nelson, M. L., Seymour, J. D., and Mason, T. G. “Signatures of nanoemulsion jamming and unjamming in stimulated-echo NMR.” *Phys. Rev. E*, **107**(2):024605, 2023.

175. Uhlenbeck, G. E. and Ornstein, L. S. “On the theory of the Brownian motion.” *Phys. Rev.*, **36**(5):823, 1930.

176. Khan, M. and Mason, T. G. “Random walks of colloidal probes in viscoelastic materials.” *Phys. Rev. E*, **89**(4):042309, 2014.

177. Chandrasekhar, S. “Stochastic problems in physics and astronomy.” *Rev. Mod. Phys.*, **15**(1):1–89, 1943.

178. Khan, M. and Mason, T. G. “Trajectories of probe spheres in generalized linear viscoelastic complex fluids.” *Soft Matter*, **10**(45):9073–9081, 2014.

179. Crocker, J. C. and Grier, D. G. “Methods of digital video microscopy for colloidal studies.” *J. Colloid Interface Sci.*, **179**(1):298–310, 1996.

180. Kubitscheck, U. “Fluorescence microscopy: single particle tracking.” In *Encyclopedic Reference of Genomics and Proteomics in Molecular Medicine*, pp. 579–583. Springer, Berlin, Heidelberg, 2005.

181. Shen, Z. and Andersson, S. B. “Tracking nanometer-scale fluorescent particles in two dimensions with a confocal microscope.” *IEEE Trans. Control Syst. Technol.*, **19**(5):1269–1278, 2010.

182. Mladenova, B. Y., Chumakova, N. A., Pergushov, V. I., Kokorin, A. I., Grampp, G., and Kattnig, D. R. “Rotational and translational diffusion of spin probes in room-temperature ionic liquids.” *J. Phys. Chem. B*, **116**(40):12295–12305, 2012.

183. Oganesyan, V. S. “EPR spectroscopy and molecular dynamics modelling: a combined approach to study liquid crystals.” *Liq. Cryst.*, **45**(13-15):2139–2157, 2018.

184. Pagenkopp, M. J. *Exploring Novel Uses of Size-Fractionated Nanoemulsions.* PhD thesis, UCLA, 2019.

185. Pagenkopp, M. J. and Mason, T. G. “Surfactant partitioning in nanoemulsions.” *Langmuir*, **34**(35):10309–10320, 2018.

186. Aronson, M. P. and Petko, M. F. “Highly concentrated water-in-oil emulsions: Influence of electrolyte on their properties and stability.” *J. Colloid Interface Sci.*, **159**(1):134–149, 1993.

187. Wong, S., Lim, J., and Dol, S. “Crude oil emulsion: A review on formation, classification and stability of water-in-oil emulsions.” *J. Pet. Sci. Eng.*, **135**:498–504, 2015.

188. Fryd, M. M. and Mason, T. G. “Self-limiting droplet fusion in ionic emulsions.” *Soft Matter*, **10**(26):4662–4673, 2014.

189. Yaqoob Khan, A., Talegaonkar, S., Iqbal, Z., Jalees Ahmed, F., and Krishan Khar, R. “Multiple emulsions: an overview.” *Curr. Drug Deliv.*, **3**(4):429–443, 2006.